The University
Of
Sheffield.

# The Influence of Aerodynamic Stall on the Performance of Vertical Axis Wind Turbines

A Dissertation Submitted for the Degree of Doctor of Philosophy

by

Jonathan Mark Edwards

The University of Sheffield
Department of Mechanical Engineering
January 2012

# Summary

There is currently an increasing desire for local small-scale sustainable energy generation. This has lead to increased interest in the concept of the vertical axis wind turbine (VAWT), which is potentially well-suited to operation within the built environment.

This study investigates the performance and flow physics of a small-scale VAWT using experimental and computational methods. The experiments utilise the University's low-speed open-section wind tunnel. The design and use of a variety of existing and newly developed methods and apparatus is detailed, this includes the development of an entire VAWT-testing rig and associated measurement equipment. Also included, is a new method for the experimental determination of the power performance. A full performance curve is shown to be determined using a short test taking a few minutes.

The near-blade flow physics of the rotating blades were interrogated using particle image velocimetry (PIV) as part of a measurement campaign which goes beyond the existing literature in both the range of measurements taken and the subsequent analysis which is presented. Details of the effect of changes in azimuthal position, tip speed ratio and fixing angle on the flow physics are presented.

Comparable CFD simulations are first validated against the PIV measurements before they are used to provide additional information for the performance analysis. A new methodology for determining flowfield-corrected lift and drag polars from a CFD solution allows detailed examination of the performance-impact of the changes in the aerodynamic forces with azimuthal position and tip speed ratio.

Described in this dissertation is work performed in the Department of Mechanical Engineering, at the Univeristy of Sheffield between October 2008 and January 2012. I hereby declare that no part of this work has been submitted as an exercise for a degree at this or any other university. This dissertation is entirely the result of my own work and includes nothing which is the outcome of collaboration, except where stated otherwise. This dissertation contains 163 figures and approximately 60,000 words.

- Jonathan M. Edwards

# Publications

Relevant publications by the author:

**Edwards, J.M.**, Angelo Danao, L., Howell, R.J. PIV Measurements and CFD Simulation of the Performance and Flow Physics and of a Small-Scale Vertical Axis Wind Turbine. *Wind Energy*, Article In Press, Published online in Wiley Online Library (wileyonlinelibrary.com). DOI: 10.1002/we.1690.

Danao, L. A., **Edwards, J.**, Eboibi, O., Howell, R. A Numerical Study on the Effects of Unsteady Wind on Vertical Axis Wind Turbine Performance. *ASME 2013 International Mechanical Engineering Congress and Exposition.* San Diego, California, USA. 15th – 21st November 2013.

Danao, L. A.; **Edwards, J.**, Eboibi, O., Howell, R. A Numerical Investigation into the Influence of Unsteady Wind in the Performance and Aerodynamics of a Vertical Axis Wind Turbine. *Applied Energy*, 116 (2014), pp. 111–124.

Danao, L. A., **Edwards, J.**, Eboibi, O., Howell, R. A Numerical Investigation into the Effects of Fluctuating Wind on the Performance of a Small Scale Vertical Axis Wind Turbine. *Engineering Letters*, 21(3), pp. 149-157, August 2013.

Danao, L. A., **Edwards, J.**, Eboibi, O., Howell, R. The Performance of a Vertical Axis Wind Turbine in Fluctuating Wind - A Numerical Study. *International Association of Engineers, World Congress on Engineering*, London, UK. 3rd-5th July 2013.

Eboibi, O., Danao, L. A., Howell, R., **Edwards, J. M.** A Numerical Study of the Influence of Blade Profile and Solidity on the Performance of Vertical Axis Wind Turbines. *51st AIAA Aerospace Sciences Meeting including the New Horizons Forum and Aerospace Exposition*, Grapevine, Texas, USA, 7th –10th January 2013.

Danao, L. A., **Edwards, J.**, Eboibi, O., Howell, R. An Experimental Investigation into the Influence of Unsteady Wind on the Performance of a Vertical Axis Wind Turbine. *51st AIAA Aerospace Sciences Meeting including the New Horizons Forum and Aerospace Exposition*,

Grapevine, Texas, USA, 7th –10th January 2013.

**Edwards, J.**, Danao, L. A., Howell, R. J. Novel Experimental Power Curve Determination and Computational Methods for the Performance Analysis of Vertical Axis Wind Turbines. *Journal of Solar Energy Engineering, Transactions of the ASME*, 134(2), p. 031008, August 2012.

Howell, R., Qin, N., **Edwards, J.**, Durrani, N. Wind Tunnel and Numerical Study of a Small Vertical Axis Wind Turbine. *Renewable Energy*, 35(2), pp. 412-422, February 2010.

**Edwards, J.**, Durrani, N., Howell, R., Qin, N. Wind Tunnel and Numerical Study of a Small Vertical Axis Wind Turbine. *46th AIAA Aerospace Sciences Meeting and Exhibit*, Reno, Nevada, USA. 7th – 10th January 2008.

*Dedicated to my Dad*

# Nomenclature

**Symbols**

| | |
|---|---|
| $a$ | interference factor |
| $A$ | swept frontal area of turbine |
| $AR$ | blade aspect ratio |
| $B$ | blade length |
| $c$ | blade chord length |
| $C_d$ | section drag coefficient |
| $C_l$ | section lift coefficient |
| $C_{l-max}$ | maximum section lift coefficient |
| $C_m$ | section moment coefficient |
| $C_p$ | power coefficient |
| $C_{p-blade}$ | power coefficient (blades only) |
| $C_{p-max}$ | maximum power coefficient |
| $C_{p-min}$ | minimum power coefficient |
| $d_p$ | seed particle diameter |
| $D$ | turbine diameter |
| $F_d$ | drag force per unit length |
| $F_D$ | drag force |
| $F_l$ | lift force per unit length |
| $F_L$ | lift force |
| $F_n$ | normal force per unit length |
| $F_N$ | normal force |
| $F_t$ | tangential force per unit length |
| $F_T$ | tangential force |
| $I_{rig}$ | mass moment of inertia of turbine rig (without blades) |
| $I_T$ | mass moment of inertia of turbine |
| $k$ | reduced frequency |
| $N$ | number of blades |
| $P$ | power |
| $P_\infty$ | freestream wind power |

| | |
|---|---|
| $p_{atm}$ | atmospheric pressure |
| $R$ | turbine radius |
| $R_{gas}$ | specific gas constant |
| $Re$ | Reynolds number |
| $Re_{min}$ | minimum Reynolds number |
| $Re_{max}$ | maximum Reynolds number |
| $Re_{\omega}$ | rotationally-averaged Reynolds number |
| $S_t$ | Stokes number |
| $t$ | time |
| $t_p$ | characteristic time of seeding particle |
| $t_s$ | characteristic time of flow |
| $T$ | torque |
| $T_{app}$ | applied braking torque |
| $T_{atm}$ | atmospheric temperature |
| $T_{blade}$ | blade torque |
| $T_{net}$ | total torque |
| $T_{res}$ | blade torque |
| $T_l$ | turbulence length scale |
| $T_u$ | turbulence intensity |
| $V_R$ | relative resultant flow velocity |
| $V_t$ | wind velocity at turbine |
| $V_w$ | local wind velocity |
| $V_x$ | local wind velocity component in x-direction |
| $V_y$ | local wind velocity component in y-direction |
| $V_{R\omega}$ | blade velocity |
| $V_{\infty}$ | undisturbed freestream wind |
| $z$ | distance of laser sheet from blade mid-span |
| $\alpha$ | angle of attack |
| $\alpha_c$ | local flow-corrected angle of attack |
| $\alpha_g$ | geometrically-derived angle of attack |
| $\beta$ | blade fixing angle |
| $\lambda$ | tip speed ratio |
| $\mu$ | dynamic viscosity |
| $\mu_p$ | seed particle dynamic viscosity |
| $\xi$ | angular acceleration |
| $\rho$ | density |
| $\rho_p$ | seed particle density |
| $\sigma$ | rotor solidity |

| | |
|---|---|
| Φ | vorticity |
| $\psi$ | azimuth angle |
| $\omega$ | rotational velocity |

**Abbreviations**

| | |
|---|---|
| CFD | Computational Fluid Dynamics |
| DES | Detached Eddy Simulation |
| FOV | Field of View |
| HAWT | Horizontal Axis Wind Turbine |
| LES | Large Eddy Simulation |
| NLF | Natural Laminar Flow |
| PIV | Particle Image Velocimetry |
| URANS | Unsteady Reynolds-Averaged Navier-Stokes |
| VAWT | Vertical Axis Wind Turbine |

# Contents

# Chapter 1

# Introduction

## 1.1 The Need for Sustainable Energy Sources

The need to reduce global greenhouse gas emissions is well established. However, the majority of the vast and currently increasing energy demand from society is currently met by burning fossil fuels which are a major contributor to global $CO_2$ emissions. Climate considerations aside, fossil fuels are a limited resource: they take millions of years to form, a few days to dig up, and seconds to burn. The reduction of greenhouse emissions and the replacement of fossil fuel-based energy sources with sustainable or nuclear alternatives is now central to the policies of governments across the world.

As a sustainable energy resource, wind energy is important in many national responses to the pressure to avoid or at least reduce the potential harmful consequences of climate change. The UK has substantial wind and marine energy resources, and relatively poor solar and hydro-energy potentials. In the UK in 2010, onshore and offshore wind farms generated 10,200 GWh of energy, with hydro (3,600 GWh) and various waste and biomass combustion processes (11,900 GWh) making up the remainder of the total renewable energy contribution of 25,700 GWh (3.3%) to the UK's overall energy consumption [1].

Within the national development of sustainable energy sources, there is an increasing desire for local small-scale sustainable energy applications which is driven by energy-performance related building regulations and the desire for a business, group or an individual to be energy efficient and live sustainably. Increasing in popularity, relatively small-scale wind turbines (rated power <100kW) are becoming a consideration for rural locations and also sites within the built environment. Approximately 16 GWh of the UK's energy was generated by small-scale wind in the UK in 2008 [2].

## 1.2    Types of Wind Turbines

Wind turbines are usually divided into two main groups of drag-driven and lift-driven devices. The drag-driven wind turbine (Figure 1.1a) involves the creation of large regions of separated flow and the rotor tip speed must be below that of the wind. As a result, drag-driven devices can generate high-torque but only at low rotational speeds. Such a device is therefore more suited to applications such as water pumping, rather than electricity generation. The lift-driven wind turbine (Figures 1.1b and 1.1c), relies on blades creating lift via the creation of streamline curvature in the surrounding flow field. An aerofoil profile is usually chosen for the blade cross-section. A lift-driven wind turbine is capable of generating forces comparable to the drag-driven device at higher rotational speeds, leading to a higher power potential. A lift-driven design configuration is chosen for almost all electricity-generating wind turbines.



(a) Drag-driven anemometer        (b) Lift-driven HAWT        (c) Lift-driven VAWT
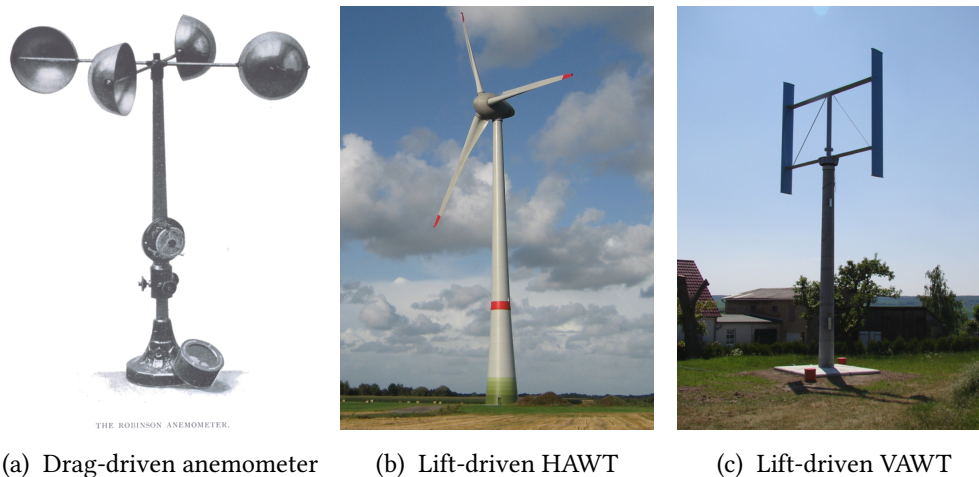
Figure 1.1: Examples of main types of wind turbines: a) The Robinson Anemometer [3], b) Enercon 126m diameter rotor HAWT[1], c) GreenEcosys Tassa 5KW[1] VAWT.

The lift-driven wind turbine category can also be split into two sub-categories of horizontal axis wind turbines, HAWTs (Figure 1.1b) and vertical axis wind turbines, VAWTs (Figure 1.1c), which have substantial fundamental differences in their operation. The horizontal axis design is well-understood and is highly developed: the HAWT design is used in all current large scale wind farms, as well as for numerous smaller-scale applications in rural locations. As is discussed in the following sub-section, the VAWT design results in a complicated aerodynamic and structural engineering problem. Understanding and optimising the VAWT is difficult, research and development of wind turbines has favoured HAWTs, and therefore the VAWT design concept is considerably less-developed.

The crucial difference between the HAWT and VAWT designs lies in the relative blade velocity and angle of attack experienced by a blade during rotation in each case: The HAWT

---

[1]image file from the Wikimedia Commons, licensed under the Creative Commons Attribution-ShareAlike 3.0 License

blade, rotating steadily in a plane perpendicular to the incoming flow, experiences a resultant blade velocity which is constant in both magnitude and direction. However, in the VAWT case, the alignment of the rotational plane and incoming flow leads to a resultant blade velocity which changes dramatically in both magnitude and direction throughout a rotation. The vertical axis design is perhaps more usefully described as a 'cross-flow' device, as it is really the fact that the VAWT's axis of rotation is perpendicular to the incoming flow direction that leads to the main operational differences between the VAWT and the HAWT. However, most publications refer to 'VAWTs' rather than 'cross-flow' turbines, and this convention is maintained for this study.

The earliest lifting-blade VAWT designs are detailed in Georges Jean Marie Darrieus's 1931 US patent 1,835,018. The patent covered various design configurations including straight-bladed VAWTs however the term "Darrieus VAWT" is usually applied to devices which feature blades of a trospokien shape (the shape of a spun rope) to minimise blade bending forces (Figure 1.2). Darrieus's invention received little attention until it was re-invented by Canadian researchers in the early 1970s. The 1973 Arab oil embargo forced the U.S.A to review its reliance on foreign energy sources, and funding was quickly fed into research of potential domestic energy sources. A significant proportion of research on VAWT design was carried out in the late 1970s and early 1980s, most notable is the research by the USA Department of Energy at Sandia National Laboratories, the reports of which are referred to many times in a review of the literature which is presented in Chapter 2. Recent interest in wind energy in the



Figure 1.2: A Darrieus-type VAWT: the "34m Test Bed" of Sandia National Laboratories [4]

built environment has led to a renewed interest in the VAWT design. In the built environment, the VAWT potentially presents several advantages over the more common HAWT:

- No requirement to yaw (turn to face the wind).

- Low sound emission (due to operation at lower tip speed ratios [5]).

- Increased performance in skewed flow [6].

- The manufacturing cost for VAWT blades has the potential to be lower than that of the blade of an equivalent HAWT, if simpler straight blades of constant cross-section are employed.

- From a mechanical point of view, the VAWT is more able to withstand higher winds through changing stalling behaviour, offering a potential operational safety advantage during gust conditions.

- It has even been suggested that the VAWT has "better aesthetics due to its three-dimensionality (more suitable for integration in some architectural projects, since it follows the concept of volume of the building)" [7], although this point is probably contentious.

The potential disadvantages of the VAWT design over the HAWT include:

- Complex aerodynamics (discussed in Section 1.3), which result in constant and rapid changes to the rotor forces during operation, this leads to:

  - challenging aerodynamic design optimisation.

  - structural and fatigue-related design issues.

- The VAWT is generally not a self-starting device, usually the generator is briefly used as a motor to achieve a suitable start-up rotational speed.

- There is no theoretical reasoning which suggests that the HAWT should outperform the VAWT, or vice versa. However, current VAWT designs would typically under-perform a HAWT counter part (in steady wind). Presumably, this is due to the relatively much larger efforts made in researching and developing the HAWT design over recent decades.

An additional point worth noting is that the VAWT concept is potentially more suited to very large scale devices [8], as the variation in the gravitational loads on a HAWT may become too severe to deal with as the rotor size increases. Such loading on a VAWT would be practically constant, although the engineering team would still need to contend with the problem of the varying aerodynamic loading. Research on the very large-scale potential of the VAWT is currently limited, and is not dealt with in this study.

## 1.3 Main Features of the VAWT Operation

The operational characteristics of the VAWT present a complicated aerodynamic problem: the direction of the undisturbed free-stream wind, $V_\infty$, is perpendicular to the axis of rotation,

as the turbine rotates the blades experience a large and rapid change in angle of attack, $\alpha$. During a single revolution the blades may operate in both stalled and unstalled conditions, and encounter their own wakes and the wakes of other blades and the shaft.

A diagram is presented in Figure 1.3 which shows the velocity and force vectors acting on the blade of a VAWT rotating at constant rotational velocity, $\omega$. The vector addition of the wind velocity, $V_w$, and the blade velocity, $V_b$ (=R$\omega$), establishes a relative resultant flow velocity, $V_R$, which is seen by the blade. This resultant flow is incident on the blade at an angle
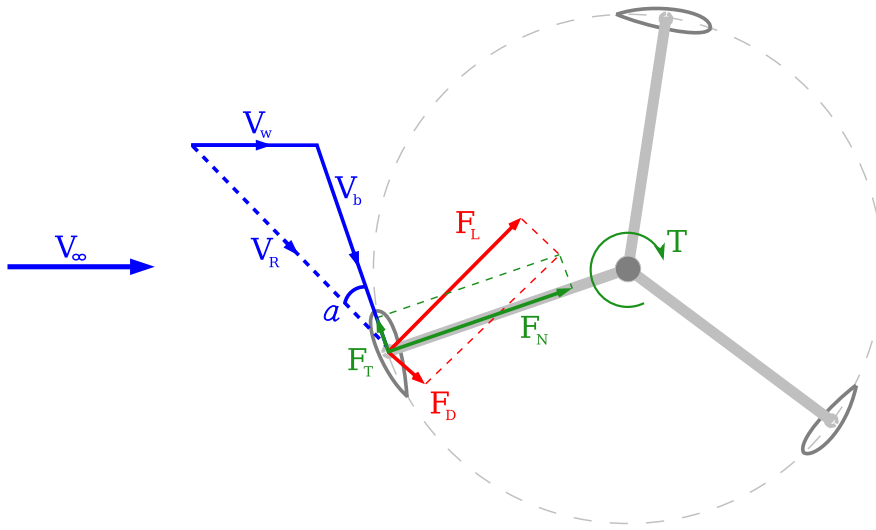


Figure 1.3: A diagram of the blade velocity and force vectors

of attack.

**Neglecting the rotor effects on the incoming freestream flow**, the consideration of the circular path traced by the blade as the azimuthal position, $\psi$, varies yields a sinusoidal variation in $V_R$ (Figure 1.4a) which has an amplitude of $V_\infty$ and a mean value equal to $V_\infty\lambda$, where $\lambda$ is the tip speed ratio which compares the blade speed to the wind velocity (Equation 1.3).

$$V_R = \left(V_\infty{}^2 + (R\omega)^2 - 2V_\infty R\omega \cos(180 - \psi)\right)^{\frac{1}{2}} \tag{1.1}$$

or, in terms of $\lambda$...

$$V_R = \left(V_\infty{}^2(1 + \lambda^2 - 2\lambda \cos(180 - \psi))\right)^{\frac{1}{2}} \tag{1.2}$$

where...

$$\lambda = \frac{R\omega}{V_\infty} \tag{1.3}$$

The resultant variation in $\alpha$ represents a skewed sinusoid, the amplitude and skewness of which reduces with increasing $\lambda$ (Figure 1.4b).

$$\alpha = \tan^{-1}\left(\frac{\sin\psi}{\lambda + \cos\psi}\right) \tag{1.4}$$
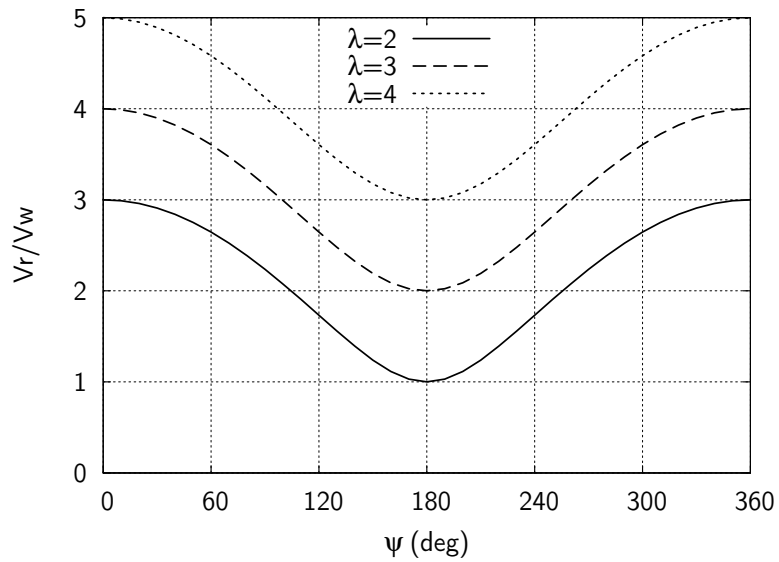
(a) $V_R$ vs. $\psi$
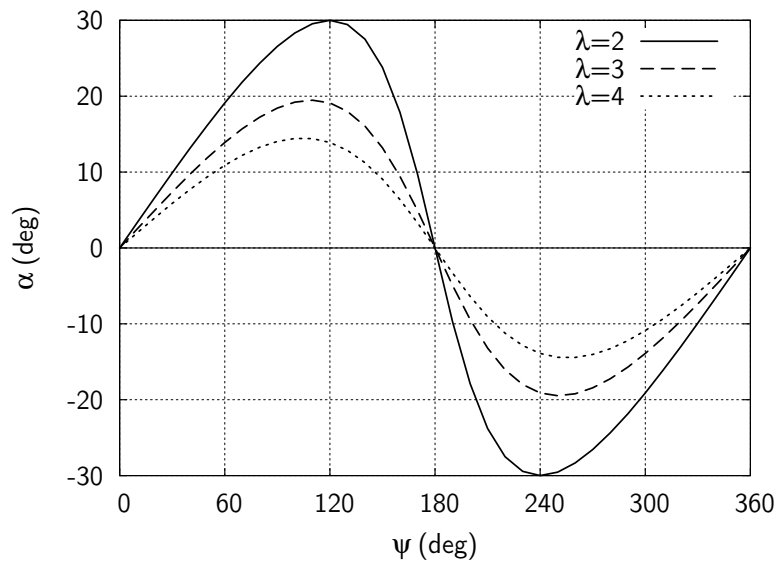


(b) $\alpha$ vs. $\psi$

Figure 1.4: Geometric calculations of the variation of angle of attack and relative blade velocity with blade azimuthal position.

The flow, incident on the blade at an angle of attack, gives rise to aerodynamic lift, $F_l$, and drag, $F_d$, forces. These forces are more usefully resolved into tangential, $F_t$, and normal, $F_n$, components. The contribution of the aerodynamic moment to torque, which depends on the chord-wise mounting position of the blade, is usually ignored as it is small and has opposing effects in the upwind and downwind parts of the rotation (defined in Figure 1.5).

$$F_n = F_l \cos\alpha + F_d \sin\alpha \tag{1.5}$$

$$F_t = F_l \sin\alpha - F_d \cos\alpha \tag{1.6}$$

$F_t$ acts at a radius, $R$, creating a torque, $T$, about the rotation axis (Equation 1.7), thus causing the turbine, with a total of $N$ blades, to rotate and produce power (Equation 1.8). The efficiency is usually expressed as a power coefficient, $C_p$ (Equation 1.9), which compares the power of the turbine with the available power in the free-stream wind, $P_\infty$, across the swept frontal area of the VAWT, $A$. For a straight-bladed VAWT: $A = RB$, where $B$ is the length of the blade.

$$T = F_t R \tag{1.7}$$

$$P = N\omega \frac{1}{2\pi} \int_0^{2\pi} T(\psi)d\psi \tag{1.8}$$

$$C_p = \frac{P}{P_\infty} = \frac{P}{\frac{1}{2}\rho A V_\infty{}^3} \tag{1.9}$$

Further consideration of the simplified performance dynamics, which have been described above, reveals the following important observations:

1. From a power-performance point-of-view $F_n$ has no contribution and is of no concern for this study of the performance aerodynamics. However, if considering the structural loading both forces must be included and it should be observed that, except at very small $\lambda$, $F_n$ is usually much larger than $F_t$.

2. Except at very small $\lambda$, where extremely large angles of attack may be experienced, the tangential resolution of the lift and drag forces results favours the drag force contribution, as $\alpha$ is below 30° when $\lambda > 2$. As a result, it is usually the case that a drop of $x\%$ in drag would yield a larger improvement in the overall VAWT torque than the same percentage increase in lift.

3. Another important consideration is that the aerodynamic forces will vary approximately with the square of relative blade velocity (the change in Reynolds number will also have an effect). Figure 1.4a shows that $V_R$ varies significantly throughout a rotation, the aerodynamic forces will vary both with $V_R$ and $\alpha$.

4. As $V_R$ varies throughout the rotation, so does the blade Reynolds number. To allow a simple comparison between VAWTs, it is common to use the rotationally-averaged Reynolds number, as defined in Equation 1.10:

$$Re_\omega = \frac{\rho(R\omega)c}{\mu} \tag{1.10}$$
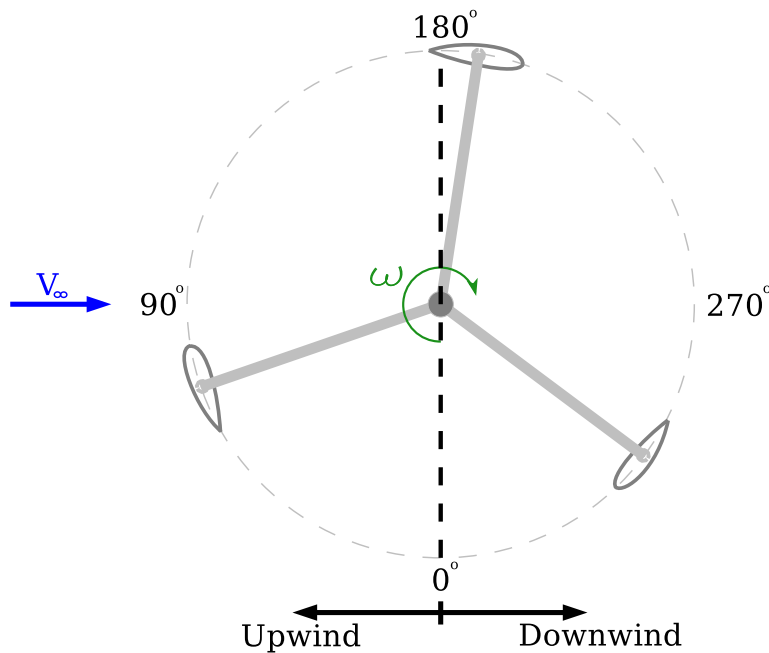
Figure 1.5: Diagram showing the definition of the upwind and downwind parts of the rotation, 'upwind' refers to $0° \leq \psi \leq 180°$, 'downwind' to $180° \leq \psi \leq 360°$.

The fundamentals of the VAWT operation have been explained in the simplistic analysis above. However, a significant simplification was made in that the rotor effect on the freestream wind was not considered. The rotor presence in the freestream effects the actual wind velocity 'seen' by a blade. This is particularly significant for the downstream part of the rotation where the flow velocity may be significantly lower than the freestream due to the energy-extraction of the upwind part of the rotation. In the downstream part of the rotation, the resultant angle of attack may be much lower than predicted in the simplified analysis above. Turbulent wakes of the shaft and blades further complicate the flowfield, resulting in blade forces and VAWT performance which vary significantly from the simplified descriptions which have been presented above. As performance and the flowfield are interdependent, a prediction of a rotor's efficiency is therefore usually made using some kind of iterative numerical scheme. Due to the complex flowfield, and resulting difficulty in modelling the VAWT behaviour, experimental study has made a significant contribution to VAWT research literature.

## 1.4 Thesis Outline and Synopses of Chapters

This thesis aims to improve upon the current understanding of VAWT performance in order to allow better designs to be created in the future. The research presented evaluates the flow physics in greater detail through experimental and modelling methods. Both performance measurements and flow visualisations are obtained in a series of wind tunnel tests and

companion simulations are also carried out using computational fluid dynamics. The study has an impact on the understanding of the aerodynamic performance of the VAWT and also upon experimental and modelling methods. The thesis is divided into 8 Chapters, a synopsis of each is given is the following paragraphs:

Chapter 1 has introduced the fundamentals behind basic VAWT operation, and has also given a very brief account of the VAWT's research history and current place in society's development of sustainable alternatives to fossil fuels.

Chapter 2 presents a review of the main VAWT-related research literature, including a review of the main principles and findings of mathematical model-based research, the specific research findings of factors influencing performance, and more recent investigations of the flow physics using advanced experimental techniques and computational fluid dynamics (CFD).

In Chapter 3 the design, set-up and use of a wind tunnel-based performance testing assembly is described, and the development of a new method to obtain the VAWT performance is detailed.

In Chapter 4 the apparatus and methods are detailed for a Particle Image Velocimetry (PIV) measurement campaign which aims to capture images of the near-blade flowfield throughout a whole rotation. The methods for a comparable CFD model are also presented, and a new methodology is described which allows the determination of a corrected local angle of attack, and subsequent lift and drag polars.

The results of the experimental power-curve measurement for a 'Reference Case' is presented in Chapter 5. PIV visualisations of the near-blade flowfield are used to explain the flow physics behind the performance changes with tip speed ratio. The experimental measurements and visualisations are also compared to a CFD simulation.

In Chapter 6 the 'Reference Case' is further investigated and a detailed analysis is made of the changes in the aerodynamic forces throughout a rotation at different tip speed ratios.

Using experimental measurements and PIV visualisations the significant effects of small changes to the blade fixing angle are analysed in Chapter 7.

Chapter 8 concludes the findings gained from the experimental and computational measurements. Following this, several suggestions for topics requiring further work are presented based on the experiences and results gained from the experimental and computational measurement campaign.

# Chapter 2

# Literature Review

## 2.1   Introduction

This chapter aims to place the research presented in this thesis into context by carrying out a review of the relevant literature. The review is divided into three main sections, each of which contains an assessment of the gains and impact of the publications discussed within it.

Research into the VAWT concept began in the early 1970s, with several researchers establishing basic mathematical models motivated by the fact that if the VAWT could be successfully modelled then its performance could be examined, understood and improved with greater ease than physical testing would likely provide. Subsequent research used these models and experimental study to develop understanding of some of the parametric effects of performance (rotor solidity, aerofoil profile, blade fixing angle...etc). More recently, CFD simulation studies have been published, allowing a closer modelling of the VAWT flow physics. The advancement and availability of PIV equipment (roughly in parallel to CFD use) has provided useful validation data for CFD models and a start has been made into establishing a detailed understanding of the VAWT flow physics.

The research presented in this thesis evaluates the flow physics in greater detail, and has an impact on the understanding of the aerodynamic performance of the VAWT and also upon experimental and modelling methods, including both CFD simulations and mathematical models based on the modification of aerofoil datasets.

## 2.2   Mathematical Models

A significant amount of early research on VAWTs focused on the development and use of mathematical models and much of current understanding is drawn from the use of these models. When compared to a CFD simulation, a mathematical model is relatively quick and simple to solve. When compared to an experimental study, a mathematical model is likely to be relatively low cost and can quickly yield results. A mathematical model is a good choice

when conducting any study requiring a large number of solutions, such as parametric studies or design optimisation. While a mathematical model was not utilised in this study, they are significant in the literature and so a summary of the most common forms of models and their assumptions is presented in this section. The main aim of a mathematical model is to determine the torque, power and efficiency of a proposed VAWT design. In order to do this, a model typically seeks to do the following:

- compute the induced velocity field.

- determine the relative blade velocity and angle of attack.

- look-up $C_l$, $C_d$ and $C_m$ data from an external source, usually experimental aerofoil data.

As discussed in Chapter 1, the interdependency between the VAWT performance and the induced velocity field means a solution must usually be found by iteration. Further modifications may be added to account for additional effects such as those due to finite blade span, dynamic stall, blade sweep, and supporting structure.

### 2.2.1 Momentum Models

As part of work begun in the 1960s by the NRC of Canada, R.J. Templin is credited with some of the earliest analysis of the VAWT: publishing a single streamtube momentum model in 1974 [9]. Templin's single streamtube model was an adaption of actuator disk momentum theory, first applied to propellers by Glauert [10]. In the model, the VAWT is represented by a single 1D actuator disc, contained within a single streamtube as shown in Figure 2.1. The



Figure 2.1: A diagram of Templin's single streamtube model
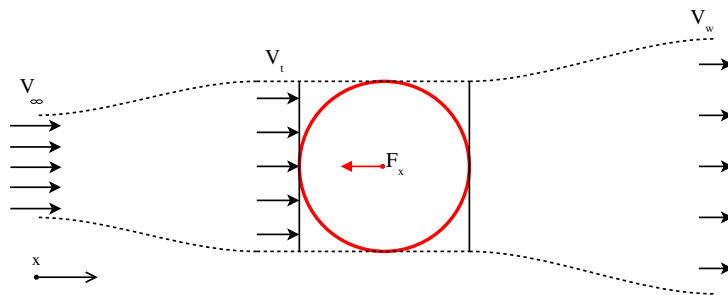
streamwise momentum change in the flow that passes though the VAWT rotor is equated to the streamwise force applied by the rotor. The VAWT rotor and its wake reduce the flow velocity passing through the rotor, from the free stream velocity, $V_\infty$, to a lower value, $V_t$. From this, a flow interference factor, $a$, is defined:

$$a = 1 - (V_t/V_\infty) \tag{2.1}$$

As previously discussed in Chapter 1, as the VAWT blade rotates its angle of attack continuously changes, dramatically so at certain conditions. The forces exerted by the blade on the freestream may vary significantly with $\psi$, so the assumption of a constant interference factor is not appropriate when the rotor loading becomes high, such as at high $\lambda$ or $\sigma$, or for any design configurations seeing large changes in aerodynamic forces as $\psi$ varies [11].

To begin to account for variation in streamwise force with $\psi$, a multiple streamtube model was implemented by Strickland [11] (after being first introduced by Wilson and Lissaman in 1974 [12]). In Strickland's model, the original principles as used by Templin are applied, but this time the control volume is split into a number of streamtubes (Figure 2.2). In addition to allowing for varying $a$ with $\psi$, wind shear can also be modelled. A detailed account of the
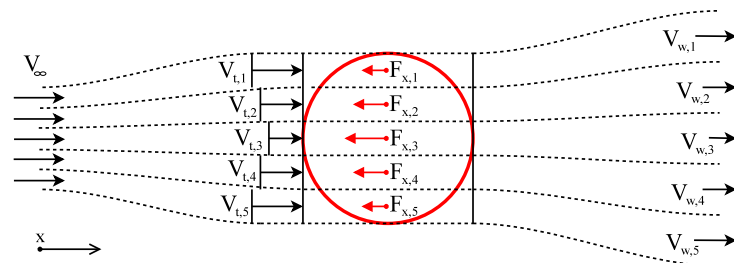


Figure 2.2: A diagram of Strickland's multiple streamtube model

method for obtaining a solution for a certain design configuration at desired values of $\psi$ and $V_\infty$ is given in [11], but the process may be summarised as follows:
At each $\psi$ increment...

1. initially, set the interference factor $a$ to 0

2. calculate the blade angle of attack $\alpha$

3. look-up $C_L$ and $C_D$ from data tables

4. calculate $V_R$

5. calculate the force exerted by the blade on the streamtube

6. re-calculate $a$

7. find new $\frac{V}{V_\infty}$ ratio and feed back into step 2.

Steps 2 to 7 are repeated until the value of $a$ converges to the required degree of accuracy. The rotor torque due to the blades passing through the streamtube, is then found and the sum through the full range of $\psi$ yields the the time-averaged rotor torque over a full rotation, from which the power and power coefficient can be determined.

(a) three-blade VAWT　　　　　　　　　(b) two-blade VAWT
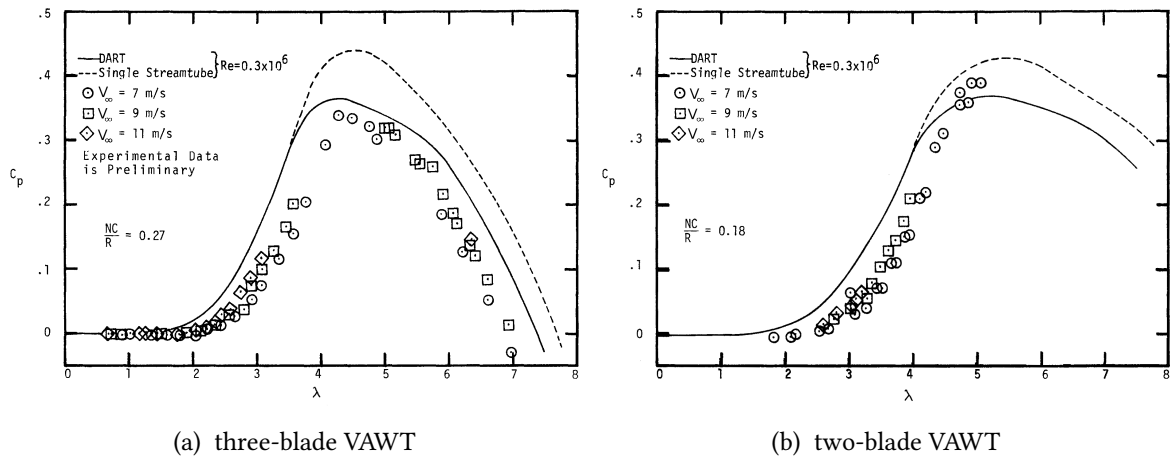
Figure 2.3: Results of Strickland's momentum model (DART) plotted against a single streamtube model and experimental results [11] (Figure b has been modified slightly to match axes of figure a).

When compared to wind tunnel tests on a 2m diameter Darrieus rotor, Strickland showed that the multiple streamtube model was capable of providing a reasonable prediction of $C_p$ [11] (Figure 2.3).

In Figure 2.3, the difference in prediction between single and multiple streamtube models is clearly visible. A greater difference between the single and multiple streamtube models is observed for the three-blade VAWT. This is consistent with the assumptions of both approaches becoming invalid as solidity is increased. Solidity being a ratio which compares the frontal areas of the blades with the overall rotor frontal area. For a VAWT, solidity is usually defined as:

$$\sigma = Nc/R \tag{2.2}$$

This equation relates to the Darrieus-type rotor, for a straight-bladed VAWT the denominator should really be $2R$; however, the definition above is generally adopted for all VAWT rotors.

The single streamtube model is particularly unable to deal with high solidity and so its prediction is less accurate for the three-blade case. For the multiple streamtube model, some inconsistency is shown as the model over-predicts performance for the three-blade VAWT but under-predicts for the two-blade. The overall form of the performance curve is reasonably well-matched for the three-blade case, unfortunately experimental results do not extend to the point of peak performance so it is hard to assess this case.

Whilst the multiple streamtube model's prediction is not 'spot-on' it is shown to function well enough to provide a useful tool for analysing some of the fundamentals of the Darrieus VAWT, and some useful plots are generated showing the influence of solidity (Figure 2.4 - discussed in Section 2.3.2) and the contribution of the trospokien blade shape to overall rotor power (Figure 2.5). It is shown that the roots of each blade contribute very little to the overall power of the VAWT, due to the small radius, it can be seen in Figure 2.5 that approximately

90% of the peak power comes from the central 60% of the overall blade length.
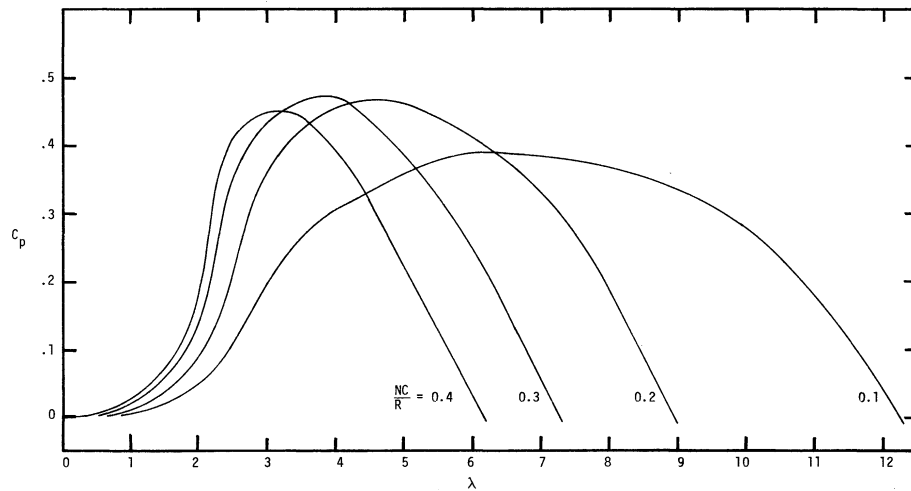


Figure 2.4: Solidity effect on performance from Strickland's multiple streamtube model [11]
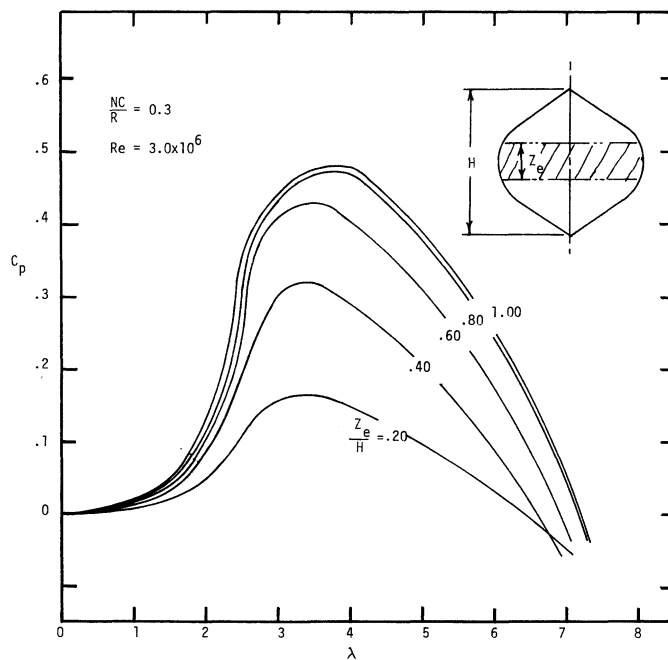


Figure 2.5: Contribution of blade section to overall VAWT power from Strickland's multiple streamtube model [11]

Strickland acknowledges the limitations of the overall approach: specifically, the break-down at high blade loading and the fact that streamtube distortion and interaction are not modelled are cited as key downfalls of the model. The prediction's dependence on two-dimensional data gained from experiment is also highlighted as a problem. The blade Reynolds

number changes during a rotation and with changing $\lambda$, and $\alpha$ may extend to very high angles which would not have been tested in most aerofoil characterisation experiments (usually aimed at aviation use). Finding the required range of reliable aerofoil data from literature may be difficult due to the Re and $\alpha$ variation and specific tests may be required to generate suitable data. It is also questionable how applicable two-dimensional aerofoil data is to the behaviour of a VAWT blade. Effects such as blade-wake interactions, centrifugal effects and dynamic stall at different $\dot{\alpha}$ are difficult to account for. On a straight-bladed VAWT, end effects and blade-structure interactions would further complicate the aerodynamics.

In 1981, Paraschivoiu [13] introduced a double multiple streamtube model which separately carried out the analysis of the upwind and downwind halves of the rotation cycle. The interference factor was considered constant across each half, avoiding the need for iteration and making the model similar to Templin's model, but split into the two halves. The model makes an important step in that it recognises the significance of the relative power contributions of the upstream and downstream halves of the rotation cycle. Comparison of the $C_p$ results of the model against a set of experimental results [14] are good, see (Figure 2.6).
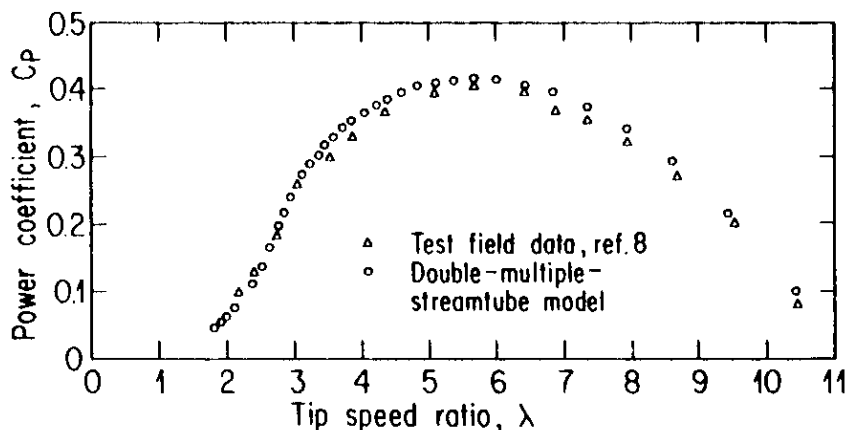


Figure 2.6: Double multiple streamtube model results from Paraschivoiu [13] showing $C_p$ prediction compared to experimental measurements.

The next generation of Paraschivoiu's model [15] assumed a cosine-type variation in $a$ with azimuth angle, and included the use of a dynamic stall model to modify the lift and drag data gathered from two-dimensional static aerofoil tests. Results of the variation of $F_t$ and $F_n$ are compared against experimental measurements (Figure 2.7), $F_t$ prediction in the original and the modified model shows a different change with azimuth angle and is some way off the experimental results. This indicates that the good $C_p$ correlation, as shown in Figure 2.6 is not a result of the blade performance being mapped out correctly through the rotation.
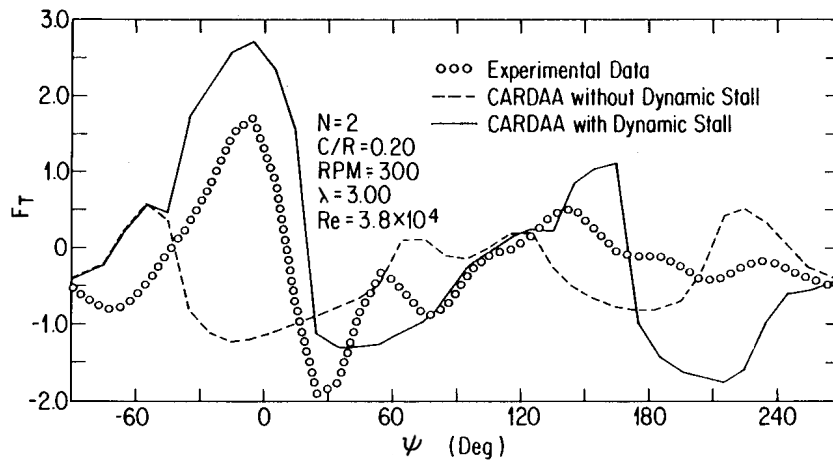
Figure 2.7: Double multiple streamtube model predictions by Paraschivoiu [15] (with and without dynamic stall) as compared to experimental results.

## 2.2.2 Vortex Models

The other main alternative to the momentum model representation of the VAWT is a vortex model. In a vortex model, a turbine blade is represented by bound (lifting-line) vortices, the strength of which being determined from an aerofoil coefficient data using the appropriate values of $V_R$ and $\alpha$, as calculated from the induced velocity field. The strength of the bound vortex changes with time as the VAWT blade rotates, and at each time interval a spanwise vortex is shed which has the same strength as the change in bound vortex strength. Each portion of the shed vortex system (known as a vortex filament) is convected at the local fluid velocity, and over a number of rotations the wake of the VAWT is built-up (see Figure 2.8). The local velocity at any point is determined from the sum of the wind velocity and the velocity induced by all of the vortex filaments in the flowfield. As the induced velocity field is determined from the influence of vorticity in the wake of the blade(s) an iterative approach must be employed to obtain a solution. As with the momentum models, the aerofoil coefficient datasets on which the model depends are usually derived from two-dimensional static aerofoil experiments.

The earliest vortex models were formulated by Larsen [17], Walters et al. [18] and Wilson [19] These models laid the foundations of the vortex method, but were of limited use due to considerations such as blade angle of attack being limited to low values, and lightly-loaded rotors [20]. Strickland et al. [21] presented a more useful development of the vortex method, the results of which were compared with experimental data.

Predictions of $C_p$ from Strickland's vortex model appear to match experimental data quite well, as shown in Figure 2.9. However, further analysis of the torque variation using data from [22] shows poor comparison between vortex model and experimental measurements (Figure 2.10). The prediction seems worse in the downwind region, particularly for the higher-
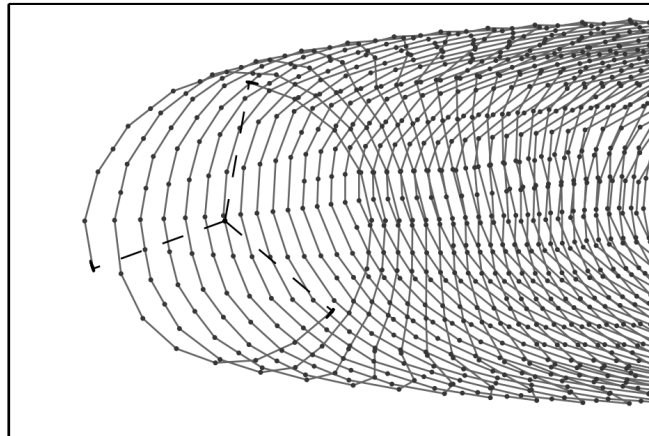
Figure 2.8: An example of the wake structure built up by a three-blade VAWT using the vortex model of McIntosh [16] after 16 rotations at $\lambda = 6$.

solidity three-blade case. The accuracy of the downwind prediction depends on the accuracy of the upwind prediction, as well as the method in general. It should also be observed that the experimental measurement are quite challenging and errors in the experiment may account for some of the differences observed in both the predictions of Strickland's vortex model and Paraschivoiu's double multiple streamtube model.
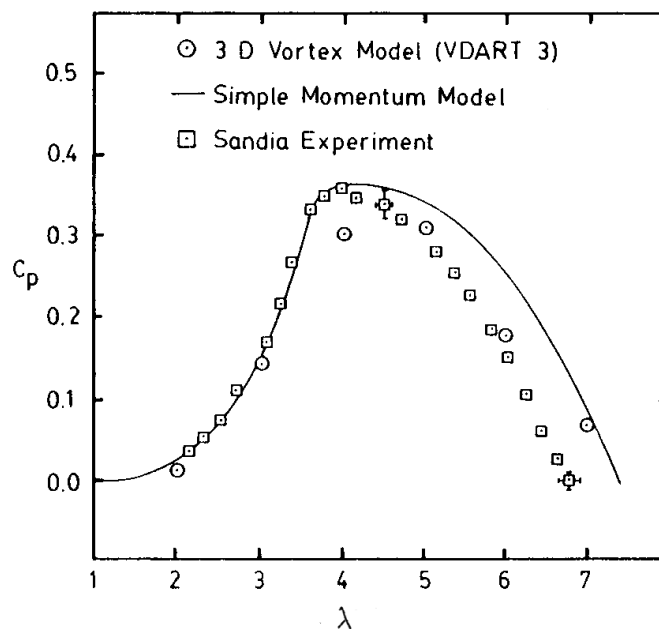


Figure 2.9: Vortex and momentum model $C_p$ prediction comparison with experimental data [21].
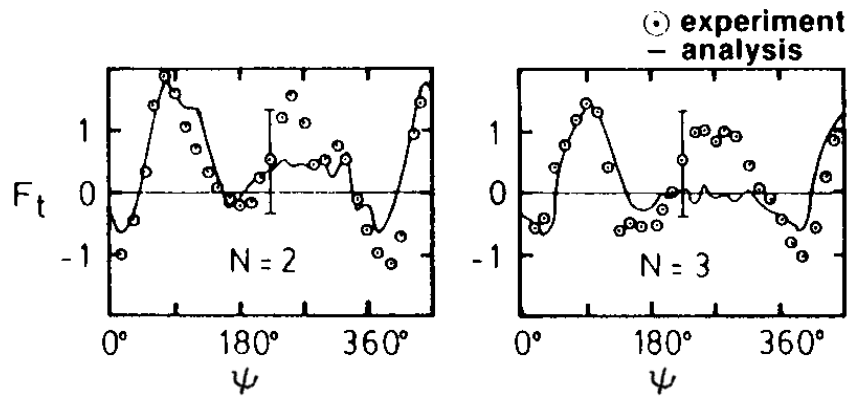
Figure 2.10: Vortex model prediction of tangential force comparison with experimental data [21].

Strickland's model is a free-wake model, the individual vortex filaments are convected at the induced velocity calculated from the whole vortex filament system. Other vortex models [23] [24] use a momentum model to prescribe the rate at which the wake is convected in order to save on the computational efforts. These models are known as fixed or prescribed wake vortex models.

### 2.2.3 Summary of Mathematical Models

The section above has covered only the basic foundations of the two most popular and influential forms of mathematical models. There exists other forms of mathematical model for the VAWT, as well as several adaptations and modifications of those already detailed above. In fact, a significant proportion of the literature is concerned with the development of mathematical models.

It was shown early on in the first modelling papers, as referenced above, that even the fairly basic formulations were adequate enough to give a general indication of a VAWT's performance. Whilst the importance of an adequate mathematical model is not disputed, it is the Author's opinion that there exists an imbalance in the literature with too many studies offering improved modelling approaches and too few yielding improved understanding of the VAWT performance, as shown in the following sections of the Literature Review. Perhaps this is in-part due to the fascinating mathematical problem that the VAWT provides and also to the difficultly of design analysis (an in-depth study may have much dependence on acquiring extensive library of experimental aerofoil data).

## 2.3   Performance Fundamentals

To be able to anticipate and tailor the performance of a VAWT the influence of the many design variables needs to be understood. This is not a straight forward process because one variable will often have an effect on another, or have more than one effect on performance. For example, adjusting the blade chord will adjust the c/R ratio which has an effect on both solidity (Section 2.3.2) and flow curvature effects (Section 2.3.5), as well as adjusting the blade Reynolds number (Section 2.3.7). This section reviews the current state of understanding of the main design parameters effecting performance. In many cases, the understanding is drawn from both mathematical models and experimental studies.

### 2.3.1   Fixing Angle

VAWT blades are usually mounted so that the position vector from the axis of rotation intersects the blade chord in the region of 25-50%$c$; this region will be close to the stalled and unstalled centres of pressure and the centre of mass, so that twisting forces along the blade axis will be minimised during operation. The angle between the support arm is an important design parameter, referred to as the fixing angle, $\beta$. As the fixing angle is varied, the range in $\alpha$ experienced by the blade throughout the rotation will be be altered. In this thesis, a negative fixing angle is defined as one that pitches the blade leading edge toward the VAWT axis (see Figure 2.11). A negative fixing angle would reduce the range in $\alpha$ experienced in the upwind part of the rotation, but increase it in the downwind part.
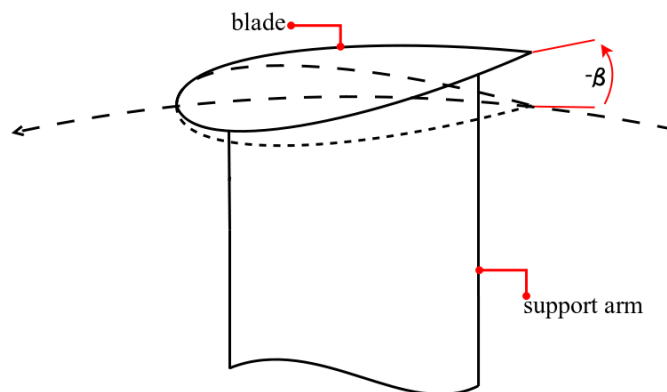


Figure 2.11: Diagram showing a negative fixing angle.

Klimas was one of the first to look at the influence of blade pitching angle on VAWT performance [25]. In outdoor wind tests on a 5m diameter Darrieus with two NACA0015 blades ($\sigma$ = 0.122) the fixing angle was varied by adjusting the chord-wise mounting point of the blades at the shaft (Figure 2.12) altering the performance due to two sources: 1) $\alpha$ variation with $\psi$ will change. 2) The blade normal force is more able to contribute to the turbine torque.
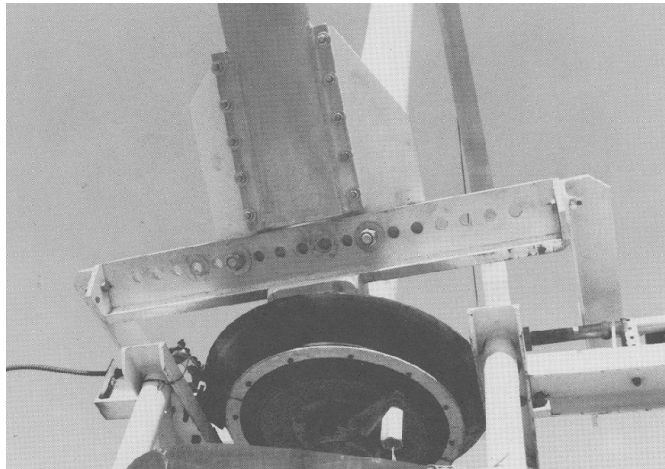
Figure 2.12: Image showing method of fixing angle adjustment as used by Klimas on a Darrieus rotor [25], chord-wise mounting point of blade root is varied at the shaft.

In Klimas' analysis a positive fixing angle is one that pitches the blade leading edge toward the VAWT axis. It is noted from Figure 2.13 that a small variation in fixing angle can lead to significant differences in performance. Small negative angles improving performance slightly, a positive angle does not seem to improve performance, and its degrading effect as the angle increases is greater than with negative angles. -1/2 and +1 degree adjustments seem to move performance to higher $\lambda$. Due to the two effects mentioned previously Klimas's analysis is not a true test of pitching angle effect, although it is likely to be the more dominant of the two effects. Also, as with many of the Sandia/DOE tests, readings are taken at fixed rotational speed so Re and stall effects are not properly quantified. Nevertheless, their results show a performance that is clearly influenced by a pitching angle change.

A more detailed explanation of the effects of blade fixing angle is given by Coton et al. [26] who use a fixed-wake vortex model to inspect the variation of torque throughout a rotation. It is shown in Figure 2.14 that the shift in $\alpha$ variation with $\psi$ results in positive pitch (defined as pitching the leading edge away from the VAWT shaft) delaying stall to higher azimuth angles where the orientation of the lift is such that it may make a larger contribution to torque, whilst in the downwind part of the rotation stall is reached earlier. As the downwind part of the rotation has a lower wind speed it is beneficial to enhance the upwind torque peak. However, this benefit is said to only exist for small positive fixing angles, with Coton et al. showing a slight increase in performance for a +2deg fixing angle (Figure 2.15). The analysis of Coton et al., being based on a vortex model, is constrained as per the limitations discussed in Section 2.2.2. Wake interactions and increased flow unsteadiness in the downwind portion are not properly modelled and the assessment of the effect of altering upwind performance may not be properly accounted for. However, the results are consistent with those observed experimentally by Klimas in that they show a small increase in $C_p$ for a fixing angle that pitches the blade leading edge outward.
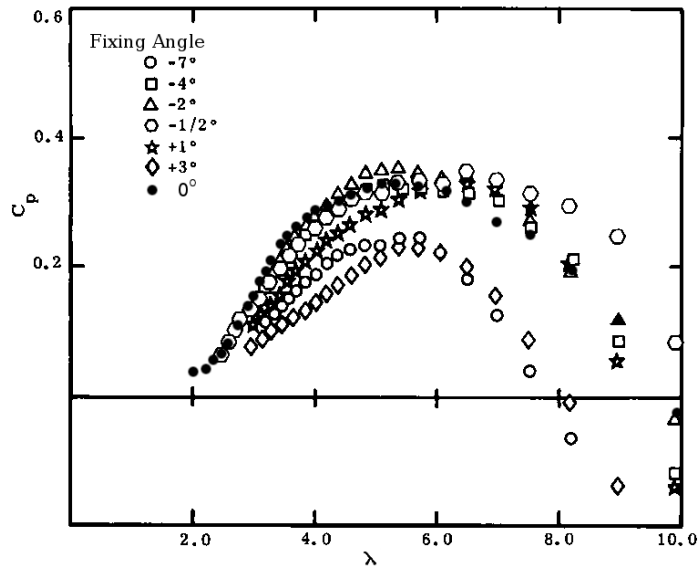
Figure 2.13: Effect of fixing angle adjustment on $C_p$ vs tip speed ratio, from [25] with 0° measurements added from [27].

## 2.3.2   Solidity

Solidity has a strong influence on VAWT performance, effecting $C_p$ variation with $\lambda$ and the maximum efficiency. High solidity machines reach optimum efficiency at low $\lambda$ and efficiency drops away quickly either side of this optimum, giving a sharp peak to the $C_p - \lambda$ curve. Low solidity machines have a $C_{p-max}$ located at higher $\lambda$ and a slower move away from optimum efficiency with changes in $\lambda$, giving a flatter $C_p - \lambda$ curve (Figure 2.16). High solidity machines
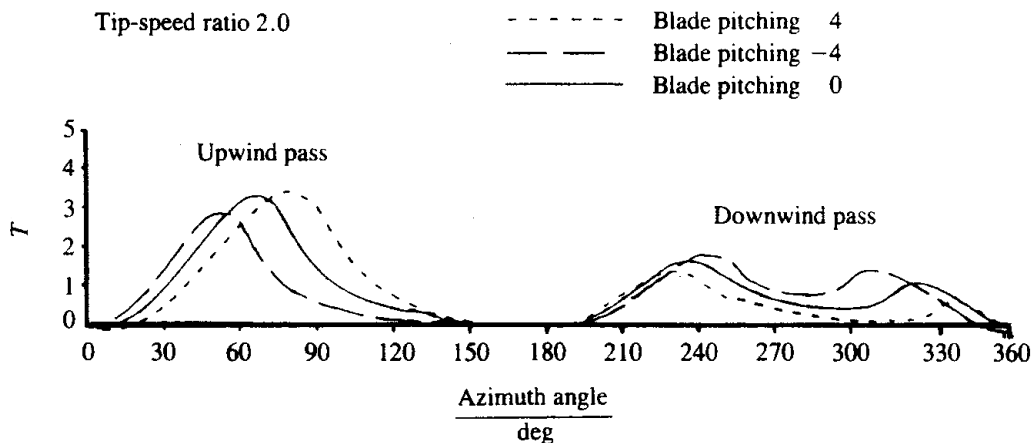


Figure 2.14: The effect of the variation of fixing angle on torque throughout a rotation, from [26].
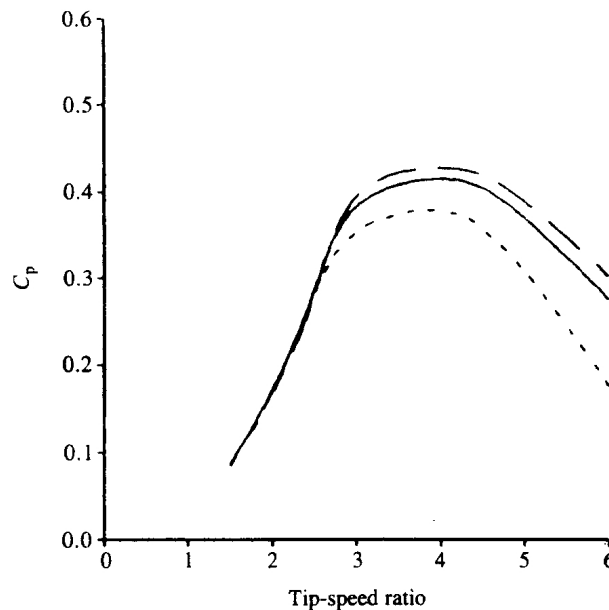
Figure 2.15: The effect of the variation of fixing angle on $C_p$, from [26].

typically produce more torque at a lower $\lambda$ than low solidity machines.

One way to alter solidity is to change the number of blades, and in doing so curvature and blade Reynolds number remain the same between cases; however, the number of blade-wake interactions will change. A number of authors have investigated solidity effects, one of the most useful studies was carried out by Consul et al. [28] who used a two-dimensional CFD model, and varied the number of blades to study the source of performance changes due to solidity. Consul et al. state that VAWT power output is proportional to the thrust that the turbine exerts on the flow; larger thrust gives greater flow impedance[1], lowering the flow velocity and energy flux through the turbine and also influencing the variation of $\alpha$ with $\psi$; the correct solidity and tip speed ratio is sought so the VAWT presents the most efficient impedance to the flow, and delivers the best possible performance. Two- and four-blade configurations tested by Consul et al. (Figure 2.17) show an increased $C_{p-max}$ for the higher solidity case, and a narrowing and shift to lower $\lambda$ of the overall $C_p$ - $\lambda$ curve. The results are consistent with experimental results from studies at Sandia National Laboratories [22], [29] and another computational study by Vassberg et al. [30].

CFD solutions can be probed for many details, and this advantage is taken by Consul et al. who examine the flow impedance and torque variation in a rotation: the four-bladed turbine is found to present a larger impedance, resulting in a reduction in streamwise flow velocity between the lower and higher solidity configurations of between 14% and 26% depending on the tip speed ratio. The effect of impedance on $C_p$ depends on $\lambda$. At high $\lambda$, an increase in

---

[1]For this thesis, impedance is broadly defined as the flow-retarding effect of the rotor's presence in the streamtube (analogous to the interference factor as defined in Equation 2.1 on page 12).

solidity leads to higher impedance, resulting in a decrease in power as $\alpha$ is low and a higher impedance reduces it further, leading to reduced lift and torque. Lift is further reduced by the reduction in the flow velocity from the increased impedance. At low $\lambda$, increasing solidity increases the VAWT power, as a low solidity device may experience significant stall at low $\lambda$, whilst a higher solidity turbine may not due to decreased streamwise velocity.

The solidity effect on the individual blade performance in the study of Consul et al. must be taken into account along with the number of blades. To accomplish this they plot single blade torque variation with $\psi$ (Figure 2.18). At $\lambda$=3, the higher solidity case is shown to result in less stall, with the low solidity case showing evidence of full separation and vortex shedding (Figure 2.18a). Torque per blade is similar for both cases, but the resulting $C_p$ for the $\lambda$=3 case (Figure 2.17) is much higher due to the increased blade number. For $\lambda$=4, both solidities appear to have attached flow for the full rotation, but the increased impedance results in lower torque per blade for the higher solidity case (Figure 2.18b). However, the reduced torque per blade is compensated for by the increased blade number, and the higher solidity case has a higher $C_p$ (Figure 2.17). At $\lambda$=8, the increased impedance severely reduces the torque per blade for the higher solidity case (Figure 2.18c), and the increased blade number is no longer a benefit (Figure 2.17).
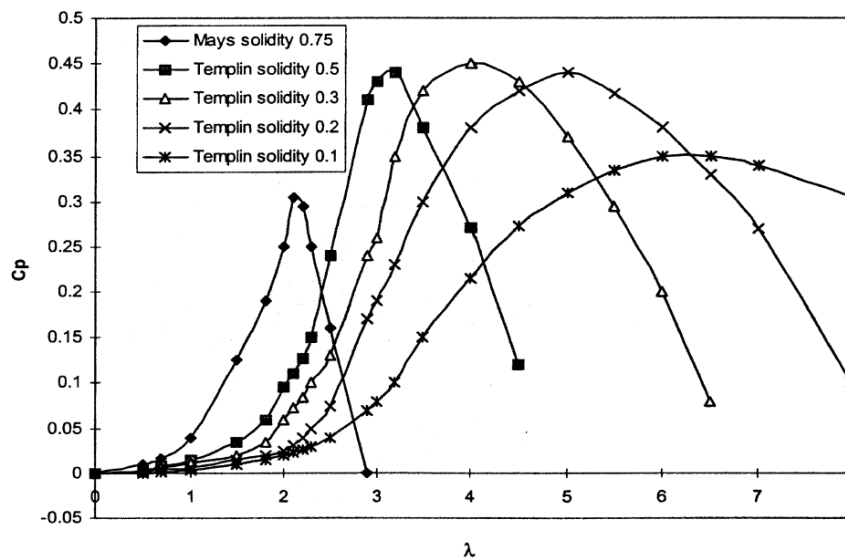


Figure 2.16: The effect of solidity on performance, from [31].

### 2.3.3 Blade Number

From an overall design point of view, the choice of number of blades is not one that only concerns solidity. The number of blades has a strong influence of the variation in loading on the VAWT structure. The variation of torque is shown to be significantly reduced with three or four blades, rather than two, which is shown in work by Consul et al.[28] and McIntosh et al.
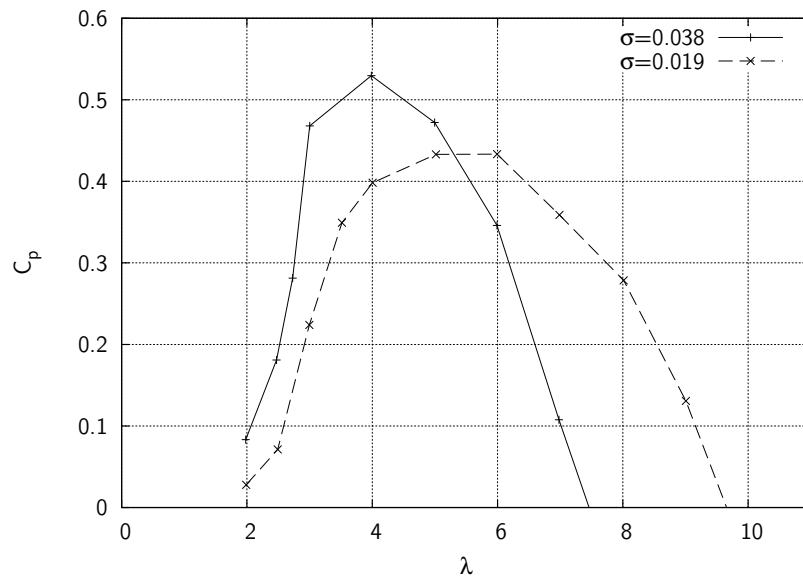
Figure 2.17: $C_p$ - $\lambda$ curves for two- and four-blade configurations of Consul et al. [28].
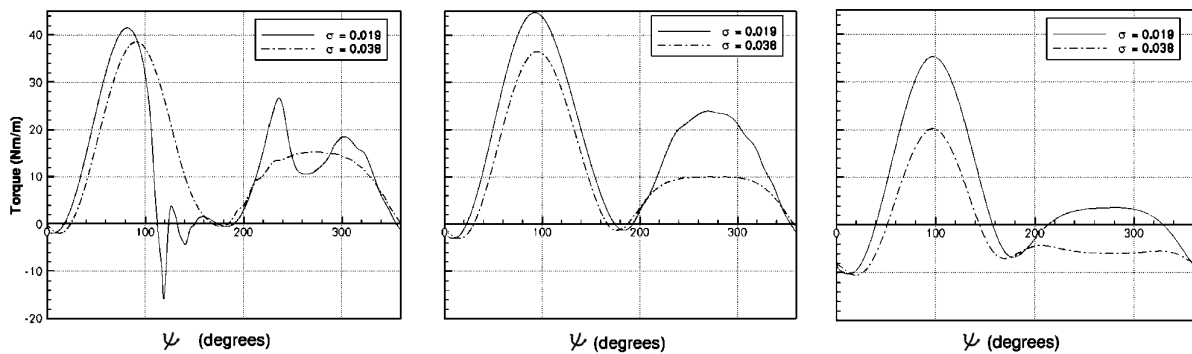


Figure 2.18: Single-blade torque variation within a rotation for two- and four-blade configurations of Consul et al. [28] at $\lambda$ = 3, 4 and 8.

[32]. Varying loads are an inherent part of VAWT operation due to the unsteady aerodynamics, and fatigue was a serious design issue with early VAWTs [33]. The form of the VAWT rotor may be dictated as much by fatigue and structural aspects as it is by aerodynamic benefits.

## 2.3.4 Blade Sweep

The influence of blade sweep has been a recently addressed design feature. By sweeping the blades at an angle to the vertical, the torque produced will be smoother than with a vertical blade which should help improve fatigue lifetimes of the turbine components. In addition, self-starting ability may be improved. McIntosh et. al [16] examined the effect of sweep on

rotor forces and turbine efficiency using a vortex model. Blade sweep was implemented as a simple correction by using the chord-wise blade velocity and assuming span-wise component to have no effect. McIntosh et. al showed, for their NACA0021-bladed rotor, that moderate sweep angles of up to 30° significantly smoothed rotor forces (Figure 2.19a) whilst having a small effect on $C_{p-max}$ (Figure 2.19b).



(a) effect of sweep angle on force [16].

(b) effect of sweep angle on $C_p$ [16].
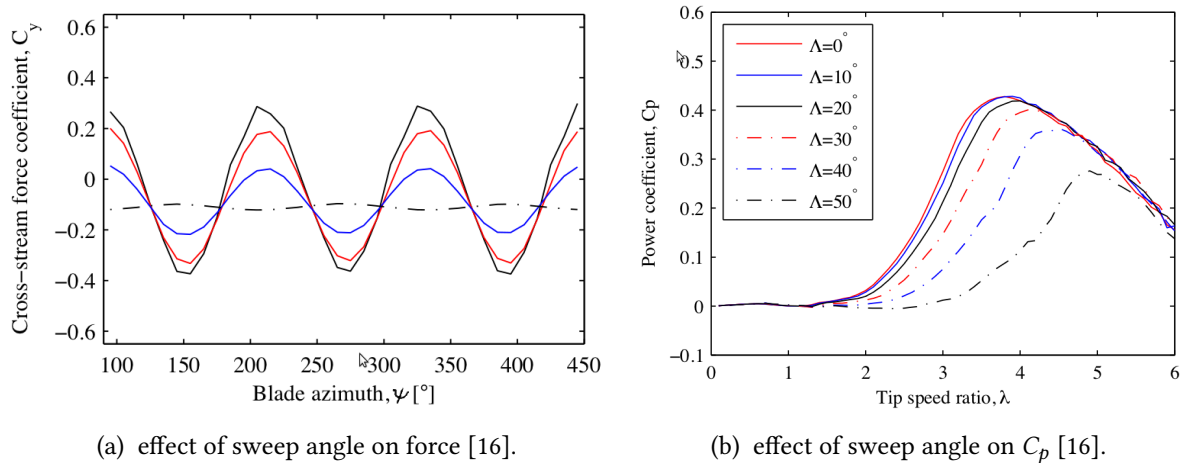
Figure 2.19: The effect of blade sweep.

### 2.3.5  Curvature Effects

VAWT blades move in a curvilinear flow and in this their behaviour may differ significantly from that in a rectilinear flow. It is common practice to define $V_R$ and $\alpha$ as occurring at the point of attachment of the turbine blade to its support arm. In reality, they are unique at any point along the blade chord, as the radial distance from the turbine axis of rotation to the blade chord line varies along the chord line itself. Migliore et. al [34] showed that the flow curvature effects become more pronounced at the $c/R$ ratio increases: in an example, at $\lambda$=6, and with $c/R$=0.26 the difference in $\alpha$ between leading and trailing edge was close to 12° and for $c/R$=0.11 the difference was close to 5°. For $c/R$=0.11, the solidity of two- and three-blade turbines $\sigma$ would be 0.23 and 0.34 respectively, which is in the noted optimum region for a VAWT. So flow curvature effects may be important, particularly when translating 2D aerofoil data for VAWT modelling purposes.

Migliore shows how 'conformal mapping' may be used to transform an aerofoil in curvilinear flow to an equivalent aerofoil in rectilinear flow. Local $V_R$, and $\alpha$ are preserved in the process so that the transformed aerofoil in rectilinear flow should exhibit the same behaviour as the original aerofoil in curvilinear flow. Transformed aerofoils have virtual camber and virtual incidence (Figure 2.20) these result in the $C_l$ curve being shifted up and toward lower $\alpha$ (Figure 2.21) stall therefore occurs at lower angles of attack than expected. Curvature is shown to degrade performance if not considered, the potential undesirable effects are:

- A reduced stall angle, therefore the portion of the rotation which sees stall is increased.

- At small negative $\alpha$, $C_l$ is positive for the virtual aerofoil producing negative torque.

- At larger negative $\alpha$ the negative value of $C_l$ is lower, and so the negative camber has poor performance at negative $\alpha$.
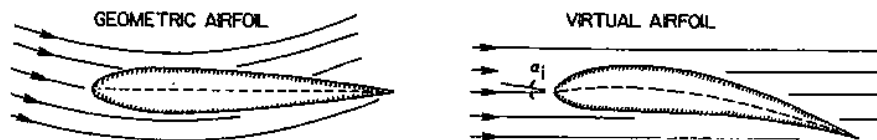


Figure 2.20: Diagram from [34] showing the resulting aerofoil profile from a conformal mapping process.
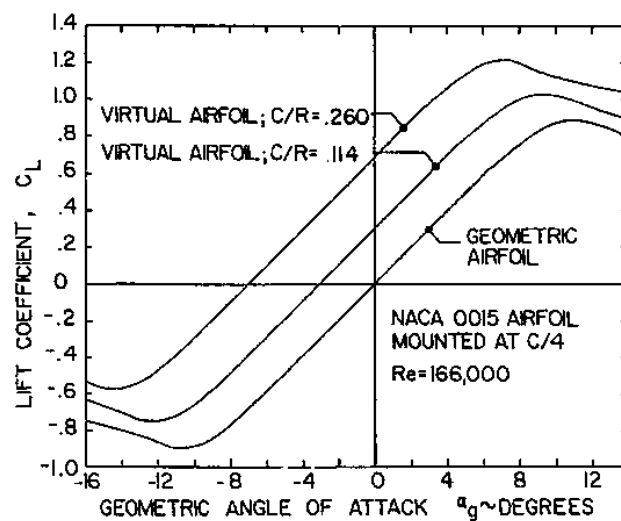


Figure 2.21: Diagram from [34] showing the effect of flow curvature for two different $c/R$ ratios.

It is interesting to note that despite these effects theoretical models using standard data without modification are seen to work reasonably well in many cases (see Section 2.2). Many models do however seem to have trouble at higher solidities and most models seem to over-predict performance in general, curvature effects could account for this somewhat. Perhaps the curvature effects are over predicted above, or maybe the $c/R$ ratio in most cases was not large enough to cause a problem, certainly for higher $\sigma$ machine you would expect performance to be effected. Unfortunately, the majority of the research literature does not appear to consider curvature.

### 2.3.6 Aerofoil Profile

Most of the research literature concerning VAWTs features symmetrical NACA 00xx profiles, in particular NACA0012 and NACA0015. These were chosen as their performance was well understood and data was available covering the wide range of conditions encountered in a VAWT, as is necessary for a mathematical model. The modern consensus appears to be that NACA0012 or 0015 are not necessarily the best profiles for VAWT design and that different ones, perhaps with increased thickness and/or camber, might provide better performance. Several papers attempt to review different aerofoils; however, in most cases, the studies are not thorough enough to draw a firm conclusion.

**Natural Laminar Flow Aerofoils**

It was observed using an aerofoil design code that the for the equatorial elements of a Darrieus blade (i.e. the part of the blade at greatest radius), aerofoils with thickness of 15-21%$c$ and large extents of laminar flow were desirable [35]. A set of aerofoils were developed with the objective of maintaining a laminar boundary layer over as much of their length as possible, known as natural laminar flow (NLF) aerofoils. Analysis by Kilmas et al. [36] showed that the NLF aerofoil SAND0015/47 led to a lower maximum efficiency as stall occurred earlier. Masson et al. [37] showed that for the 17m Sandia machine, held at constant rotational speed, the SAND0015/47 aerofoil gave a small performance enhancement, relative to a NACA0015 baseline, only at low wind speeds. The improved performance at low wind speed really means better performance at higher $\lambda$ as the machine had a fixed rotational speed. Lift and drag data showed the SAND0015/47 to be superior at low $\alpha$ but earlier stall resulted in better performance for the NACA0015 at moderate to high $\alpha$.

**Camber**

The VAWT rotation has upwind and downwind parts from which it is required to generate torque over a wide range of both negative and positive angles of attack; a symmetrical aerofoil profile is obvious first choice to test. However, the upwind part of the rotation is seen to generate a high proportion of the power, which is understandable as the flow speed received by the downwind part of the rotor is reduced. This has led to proposals, e.g. by Baker [38], to maximise upwind energy capture by cambered or angled blades.

One of the first studies of the effect of blade camber was conducted by Healy in 1978 [39]. Healy's study concluded that camber was not an advantage stating: "the closer the profile is to symmetric, the higher the output". However, Healy used a multiple streamtube model which is limited as discussed in section 2.2.1, and it is debatable whether a good study of camber can be carried out with such a model, as the problem essentially boils down to a good assessment of relative upwind and downwind performances. In contrast to Healy's conclusion, studies by Kirke [31], who also used a multiple streamtube model, showed that a cambered S1210 aerofoil gave a higher $C_{p-max}$ and much improved self-starting performance. Kirke also

suggested that cambered aerofoils such as those used on model aircraft may perform better than traditional symmetric aerofoils, the performance of which being known to suffer at low Reynolds numbers.

In what is mostly a review paper, Islam et al. [40] seem to suggest improved performance in given by cambered aerofoils S1210, NACA4415, NACA LS(1)-0417 and NACA NLF(1)-0416 relative to a NACA0015 baseline case. However, only torque curves at one condition are presented which do not take account of the VAWT aerodynamic environment as they are derived from $C_l$ and $C_d$ data generated from XFoil code [41]. More recent publications by Islam et al. [42] [43] also feature analysis on cambered aerofoils, but the analysis suffers from the same downfalls and is of limited use.

**Thickness**

A thicker blade profile may be more beneficial to the VAWT structural engineer trying to create a blade with good bending resistance, and so aerofoil thickness effect on the aerodynamic performance were examined in early VAWT literature. Healy conducted an investigation of thickness in 1978 [44] using a multiple streamtube model and a library of aerofoil data for NACA profiles 0009, 0012, 0015, and 0018 at Reynolds numbers ranging from $2 \times 10^5$ to $2 \times 10^6$. At all but the highest Re, the thicker profiles were shown to have better performance, particularly so at the lowest Re where the performance of NACA0015 and 0018 profiles were significant improvements compared to that of the thinnest aerofoil profile, NACA0009. The improved resistance to stall of the thicker aerofoils was stated as the reason for improved low-Re performance. Islam et al. [40] also state some other potential advantages of thicker aerofoils, such as improved starting performance and lower noise generation. On the whole, it is likely the work published so far on the effect of blade thickness would leave a prospective VAWT designer in need of some additional analysis.

**Summary**

In general, the VAWT literature features a somewhat patchy discussion relating to aerofoil profile choice. In the Author's opinion, the main aspect that has prevented a more conclusive analysis regarding aerofoil choice has been the lack of good understanding regarding the VAWT flow physics. Work done using the mathematical models as discussed in Section 2.2 has allowed some insight into how to make a suitable aerofoil choice and has given an idea of which profiles might offer a better performance. However, with important aspects of the VAWT dynamics missing from such models, such as effectively simulated upwind-downwind behaviour, only a partially-complete picture has been gained of how to make a suitable study of aerofoil choice. With a typical blade likely to experience low Reynolds numbers in many cases, the matter is further complicated...

### 2.3.7 Reynolds Number Considerations

A sensible point is made by Berg [35] who suggests that the approach of utilising aerofoils designed with aviation use in-mind has limited potential for wind turbines, and that this is particularly so on smaller scale turbines where the Reynolds numbers for the blades are low. This is shown in Table 2.1 which indicates approximate Reynolds number ranges for a number of hypothetical VAWTs. Indeed, it is clear that even for a relatively large VAWT the Reynolds number may be fairly low for low $\lambda$, low $V_\infty$ cases.

| Radius (m) | Rated Power $V_w$=12m/s, $C_p$=0.3 | Start-up $Re$ $\lambda$=1, $V_w$=4m/s | Typical $Re$ $\lambda$=3, $V_w$=6m/s | Rated Power $Re$ $\lambda$=5, $V_w$=12m/s |
|---|---|---|---|---|
| 0.5 | 300 W | 13,000 | 60,000 | 200,000 |
| 1 | 1.2 kW | 27,000 | 120,000 | 400,000 |
| 5 | 30 kW | 130,000 | 600,000 | 2,000,000 |
| 10 | 120 kW | 270,000 | 1,200,000 | 4,000,000 |

Table 2.1: Table indicating the Reynolds numbers range experienced by a hypothetical three-blade VAWT of $\sigma$=0.3 with different rotor sizes (for simplicity, rotor height=rotor diameter).

Low Reynolds number behaviour is a particular concern when assessing starting performance and many of the publications which address low-$Re$ VAWT aerofoils do so with the purpose of assessing self-starting capabilities. Baker [38] was one of the first to analyse self-starting behaviour and suggested that as "laminar separation is inevitable at the suction peak for aerofoils at low $Re$, a section that encourages the formation of a separation bubble will stall later than one that does not." Camber near the leading edge, and that the leading edge should be rounded, are stated as features which encourage the re-attachment of a separated flow.

In his thesis, Kirke [31] showed that the improved low-Re behaviour of a S1210 relative to a NACA0015 aerofoil gave a higher $C_{p-max}$ and much improved self-starting performance. Islam et al. also suggest in their review paper [40] that cambered aerofoils have better low-$Re$ performance. In a publication referenced by Islam, Miley [45] states that a "type-3" aerofoil (Figure 2.22) which has lift generation more influenced by a high-pressure on the lower surface is the most suitable candidate for low-Re applications, as the lower adverse pressure gradient on the upper surface helps to prevent separation of the laminar boundary layer.

Swamy et al. [46] showed, albeit using a simple single streamtube model, substantial differences in performance using data for NACA0012 at Reynolds numbers across three orders of magnitude, $4\times10^4$ to $4\times10^6$ although there is no description of the aerofoil behaviour which relates to the performance changes.

A useful paper by Selig and McGranahan [47] features wind tunnel tests on six aerofoils with their use on wind turbines in mind, the aerofoils are designed for various low $Re$ applications, with $Re$ ranging from 100,000 to 500,000. A variety of Reynolds number-related effects are shown by the lift and drag polars: At the lowest values of $Re$ all of the aerofoils show reduced lift and higher drag. On some of the aerofoils the laminar separation at low angles
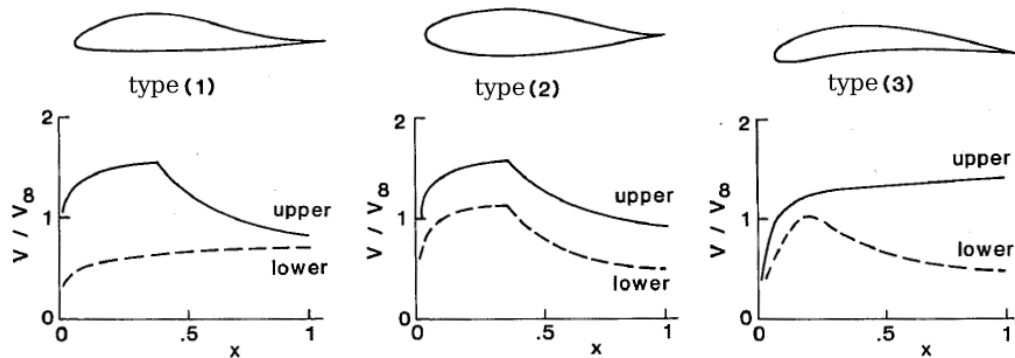
Figure 2.22: Velocity distributions on three types of aerofoil, showing upper and lower contributions to lifting pressure, from Miley [45]

does not reattach to the aerofoil surface whilst at moderate $\alpha$ it does, this results in a kink in the typically straight ($2\pi\alpha$) region of the lift curves. How this behaviour may effect a VAWT blade has yet to be addressed, but the Reynolds number at which it is observed in Selig and McGranahan's results ($Re$=1x10$^5$) would suggest it may be important to small to medium scale rotors (see Table 2.1). A laminar separation bubble is almost always shown to cause higher drag, and a shifting of the lift curve downward. A boundary layer trip is shown to reduce these effects by causing earlier transition; however, for some of the profiles the trip is beneficial in terms of reducing bubble length but it can also reduced the maximum lift. The SH3055 profile is effected severely by a low $Re$, showing much reduced lift and a high drag; with boundary layer trips the lift performance at low $Re$ is better, but is degraded at higher Re. The E387 profile shows little lift-sensitivity to the trip, Selig and McGranahan state that a leading edge separation bubble can result in the near-complete immersion of the boundary layer trip in the re-circulating region of the bubble and thus the trip has little effect. It is also interesting that the measurements of Selig and McGranahan show greatest errors (when compared to another set of test data) at the lowest Reynolds numbers; this illustrates the difficulty in testing aerofoils, and wind turbines, at low $Re$.

A recent paper by Cao et al. [48] features low $Re$ ($Re$=5.5x10$^4$ to 1.5x10$^5$) wind tunnel tests on a "prospective candidate vertical axis wind turbine airfoil", the S1223 profile. Turbulence intensity, $T_u$, and length scale, $T_l$, are varied and the corresponding lift and drag forces are measured. The main body of the paper focuses on the difference between $T_u$ = 4% and 9% cases; the $T_u$=9% case shows a more gentle stall characteristic as would be expected for a high-$Re$ trailing-edge-type stall, the $T_u$=4% case shows a more sudden drop in lift at stall which would be usually associated with a sudden separation occurring at the leading edge, often a feature of low-$Re$ behaviour (Figure 2.23). The two length scales tested show little effect on the behaviour, expect that the larger $T_l$ case has slightly higher $C_{l-max}$. Strangely, a significant discussion is absent from the paper: the discussion of the $T_u$=0.5% "smooth" flow case relative to the higher turbulence intensity cases. Re-plotting the data of Cao et al. (Figure 2.24) shows

a significant change in aerofoil behaviour with changing *Re* for the $T_u$=0.5% case, whereas for the higher $T_u$ cases *Re* has little effect on the lift and drag polars. This could be highly significant, as a wind tunnel section turbulence intensity would be expected to lie close to this value, rather than the $T_u$ = 4% and 9% cases.
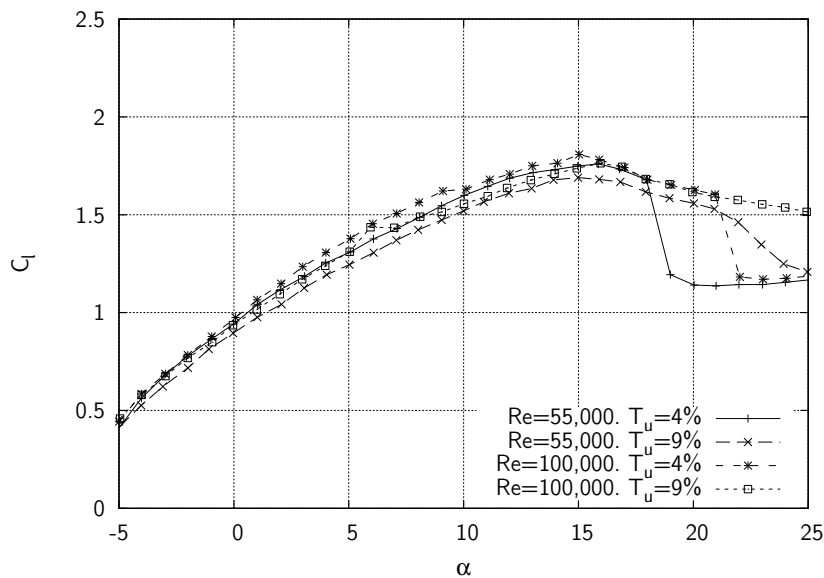


Figure 2.23: Effect of turbulence intensities of 4% and 9% on the lift coefficient of a S1223 aerofoil at two Reynolds numbers, data from [48].

**Surface Roughness**

The surface roughness of VAWT blades is dependent on manufacturing methods and may be altered during operation through wear and tear and from contamination due to insects and other particles present in the local atmosphere. Contamination by some kind of atmospheric particles would be hard to avoid over the long lifetimes expected of a VAWT, so the effect of the associated surface roughness change on performance needs to be quantified.

Real-wind data for the 34m diameter Sandia VAWT from a report by Ashwill [49] shows a noticeable effect when the blades became contaminated with "bug residue". The dirty blades underperformed the clean blades by up to 7% for $V_\infty$ < 11m/s (fixed rotational speed - low wind speed => high $\lambda$) and in fact the percentage effect is worse for very low wind. The dirty blades then outperform the clean blades by a significant amount at higher wind speeds (low $\lambda$). It is suggest by Ashwill that the insects are acting as tiny vortex generators, tripping the boundary layer into turbulent flow and helping the flow remain attached to the aerofoil surface for longer – which would support the improved results at low $\lambda$ where stall becomes significant. Indeed, the Sandia machine is stall-regulated and the bugs appear to be providing an unwelcome performance increase; raising rated power by around 20%, which might be a
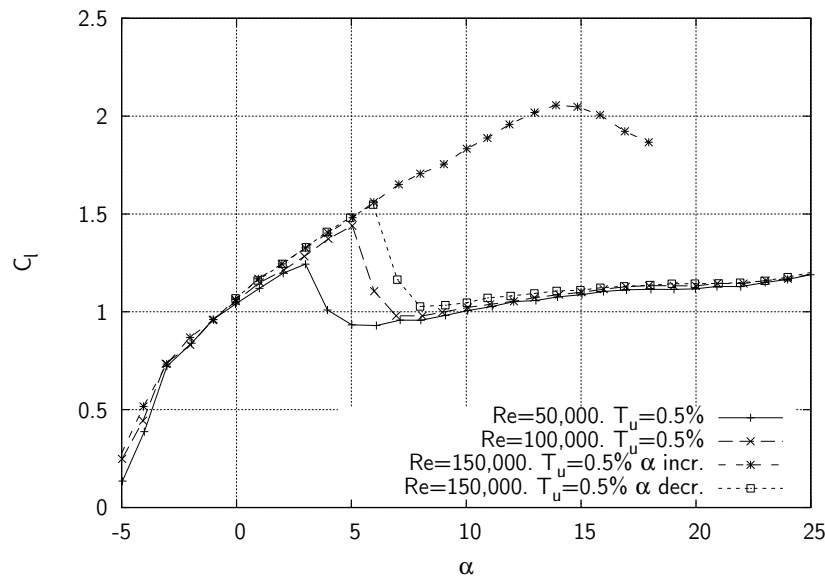
Figure 2.24: Lift coefficient vs $\alpha$ for S1223 aerofoil at three Reynolds numbers, data from [48]

concern for some of the machine components. A similar effect was observed by Dodd et al. [50] due to flaking paint on the SNL 34m diameter Darrieus which led to a series of small steps of approximately 0.25mm height ($c$= 0.91m), which acted as small boundary layer trips. The Author also tested the effect of blade surface roughness on a small VAWT (in a fairly crude fashion) and observed similar behaviour, with improvements at low $\lambda$, and degradation at higher $\lambda$ [51]. The scale of turbine and of the roughness, as well as solidity, was quite different to the Sandia machine so it is hard to draw anything more from the results. A more structured study is needed, perhaps with flow visualisation so predictions of flow attachment may be validated.

### 2.3.8 Dynamic Stall

The importance of dynamic stall behaviour to VAWT performance was shown by early generations of mathematical models which incorporated dynamic stall models [15] [52] [53] [54] in order to improve the performance prediction derived from static aerofoil datasets. Later publications have set-out to visualise the resulting flowfield through experimental techniques and CFD simulation, as discussed in Section 2.4.

Above a certain critical angle of attack, $\alpha_{ss}$, an aerofoil is usually observed to stall, with the flow separation from the surface resulting in a loss of lift and a large increase in drag. For an aerofoil undergoing a rapid increase in $\alpha$, the onset of stall can be delayed to incidences above $\alpha_{ss}$ resulting in different behaviour of the aerodynamic forces, including a higher value of $C_{l-max}$. Beyond stall, a rapid decrease in $\alpha$ leads to a delayed reattachment of the flow. The overall result is a significant hysteresis in the aerodynamic force curves. For the inherently

unsteady VAWT blade aerodynamics, the effects of dynamic stall must be correctly assessed in order for performance to be successfully evaluated.

As shown in Chapter 1, the VAWT blade experiences an skewed-sinusoidal change in angle of attack through the rotation. The study of aerofoils experiencing a sinusoidal variation in $\alpha$ has been the subject of a large number of studies which address dynamic stall (for example: [55] [56] [57] [58]), one reason for this is that such a variation is experienced by a helicopter rotor in forward flight. For the test case of an aerofoil oscillating about some mean value of $\alpha_0$, with amplitude $\alpha_a$, such that $\alpha(t) = \alpha_0 + \sin(\omega t)$, the dynamic stall process is characterised by the following sequence of events, as explained below (numbers refer to the positions shown in Figure 2.25):

1-2 Shortly after the angle of attack exceeds $\alpha_{ss}$, a thin layer of reversed flow develops at the bottom of the boundary layer. On trailing-edge stalling aerofoils, this starts at the rear of the aerofoil and moves forward toward the leading-edge. On leading-edge stalling profiles, the separation region develops rapidly just downstream of the suction peak.

3-4 Within the separated region, a vortex begins to roll-up and grows as it is convected toward the rear of the aerofoil at a speed below that of the freestream. The aerodynamic moment is effected, and drag also starts to rise, lift continues to increase at the same rate until the vortex is well-past the mid-chord point, overshooting static maximum value.

4-5 As the vortex nears the trailing-edge the aerodynamic forces reach their largest values, though not necessarily at the exact same time, before falling significantly as the vortex leaves the aerofoil surface.

5 Depending on the depth of stall, the roll-up and convection of subsequent vortices may produce further fluctuations in the aerodynamic forces, but generally at reduced levels relative to the initial vortex at stall.

5-6 As $\alpha$ decreases, the flow will begin the process of reattachment from the leading edge, with the reattachment point moving toward the trailing edge at a rate below the freestream velocity, eventually resulting in a recovery of the aerodynamic forces at some value below $\alpha_{ss}$.

In order to relate the period of the transit of flow structures over the blade to the period of oscillation, a non-dimensional reduced frequency, $k$, needs to be defined: For aerofoil undergoing oscillations which lead to a sinusoidal variation in $\alpha$, $k$ is usually defined as:

$$k = \frac{\omega c}{2U_\infty} \tag{2.3}$$

For a VAWT, the motion of the flow relative to the blade is due to a combination of the freestream velocity and the blade's motion due to rotation (see Chapter 1). However, Ferreira et
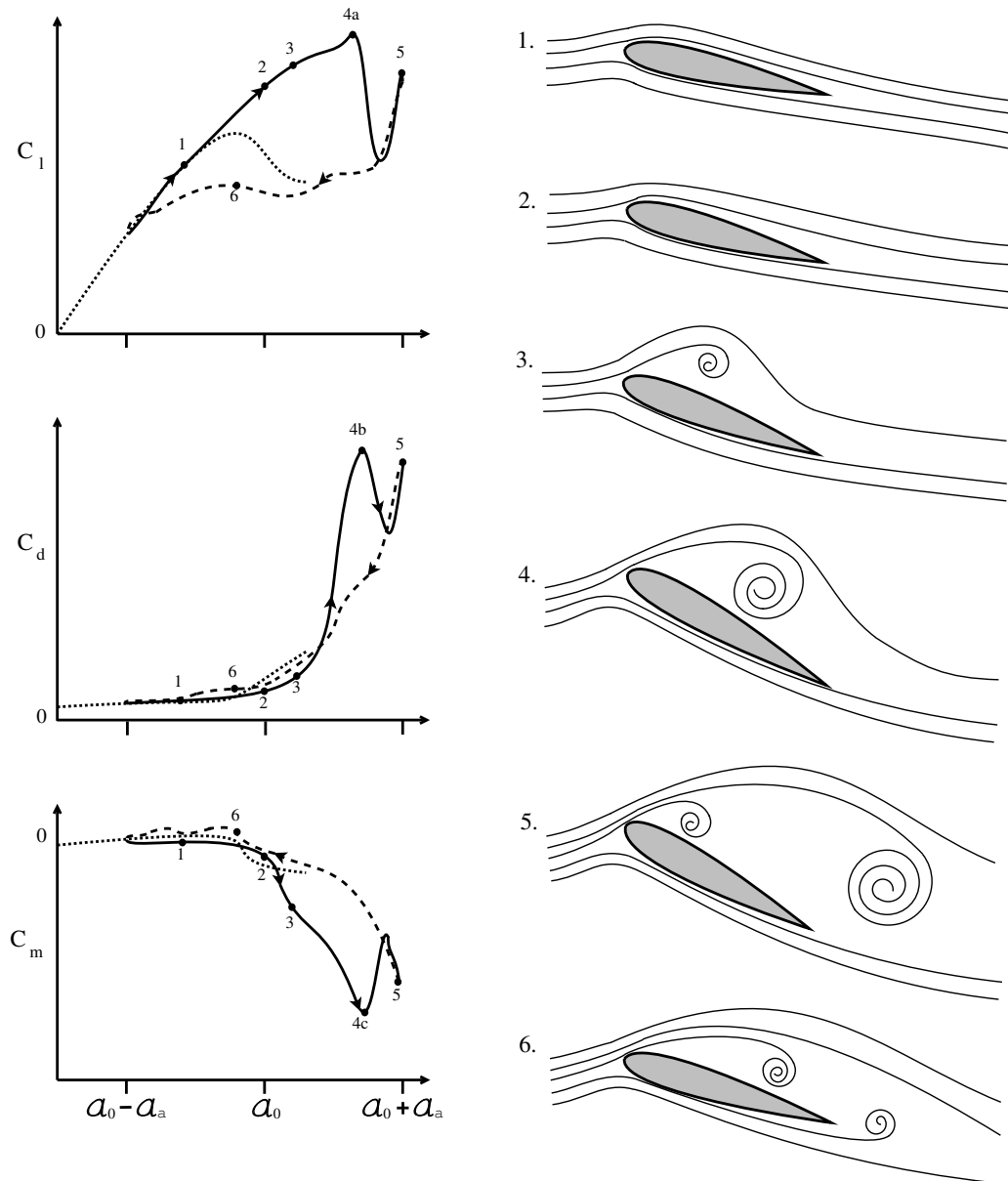
Figure 2.25: Plots of the aerodynamic force coefficients and diagrams illustrating a typical dynamic stall and reattachment process as produced by a large sinusoidal variation in $\alpha$, that goes beyond $\alpha_{ss}$. Plots are derived from those shown by McCroskey [59]. 4a, 4b, 4c do not necessarily occur at exactly the same instant in time.

al. [7] simplify the VAWT case by using the rotationally-averaged blade speed, = $R\omega$ (ignoring induction), and using the same definition as Equation 2.3 this leads to:

$$k = \frac{\omega c}{2R\omega} = \frac{c}{2R} \tag{2.4}$$

Which shows that for a VAWT, the reduced frequency depends only on the $c/R$ ratio. So, as far as the VAWT blade is concerned, dynamic stall behaviour is largely a function of:

- the reduced frequency (approximately dependant on the $c/R$ ratio),

- the amplitude of the variation in $\alpha$ (controlled by $\lambda$, see Equation 1.4),

- aerofoil profile,

- and Reynolds number.

In terms of the assessment of VAWT performance, the most important effects of dynamic stall are the sizes of the over- and under-shoots of the aerodynamic forces, and when they occur in the rotation. A secondary consideration is the effect of the large vortices which are shed at one azimuth position but may have an effect on another as they are convected downstream and through the path of the rotor.

### 2.3.9   Summary of Performance Fundamentals

Despite the significant number of studies conducted over some 40 years and even with large investments such as the Sandia 17m and 34m programs, some fundamental aspects of VAWT performance are still not clearly understood. This point is best illustrated by taking a look at the timeline of the literature, it is only in recent years that publications on fundamental design aspects such as solidity [28] and aerofoil profile [47] [48] have been published. Many performance aspects have previously been dealt with using mathematical models that are not capable of yielding a full understanding of an aspect of design such as blade camber or fixing angle. Perhaps better progress could have perhaps been made using such models, with very short run-times many design configurations could have been tested with the momentum and vortex-based models that have been developed. However, few authors have published good data illustrating performance trends associated with design parameters, the limited studies on solidity would be one example of this.

Some of the recent literature has begun to take a better approach with studies into the flow physics have starting to emerge. Aided by the continued use and development of CFD and the improvement of experimental capabilities such as PIV, researchers are beginning to gain a better understanding of the influence of fundamental design parameters on VAWT performance.

## 2.4   Flow Physics

Much of the parametric analysis referred to in Section 2.3 has been evaluated without explicitly examining the flow field. Design changes, for example: to aerofoil profile or number of blades, result in performance changes due to a change in the the VAWT's interaction with the flow. By monitoring the characteristics of the flow physics the true reasons behind a performance change can be understood and more effective design changes can be made.

VAWT flow dynamics are governed by the following operational characteristics:

1. As the VAWT rotates, each blade experiences continuous changes in angle of attack and relative flow velocity, these variations becoming most notable at low $\lambda$ where the magnitude of variation in $\alpha$ is largest.

    - A continuously changing $\alpha$ which reaches high values gives rise to dynamic stall behaviour.

    - Reynolds number also varies throughout the rotation.

2. Each blade sheds a wake which is swept downstream by the oncoming flow and may interact more than once with other blades and indeed the blade which produced it.

    - The wake may contain strong vortices originating from deep stall.

    - The wake may affect the performance of downwind blade positions, e.g. hitting a wake originating from an upwind blade position may induce stall early in downwind positions.

3. The fact that energy is extracted from the wind at the upstream blade positions results in lower wind velocity at downstream blade positions, giving rise to an inherent difference in operating conditions between upwind and downwind blade positions.

    - This further complicates the variation in $\alpha$ and *Re* across a rotation.

    - $\lambda$ effectively varies throughout a rotation because of this.

The unsteady characteristics described above are dependent on a non-deterministic flow behaviour; the roll-up and subsequent shedding of vortices into the blade wake, is an example of VAWT phenomena that is difficult to analyse mathematically. The understanding of the relationship between flow behaviour and VAWT performance therefore has been strongly led by experimental techniques. The flow characteristics may be difficult to monitor or physically observe, technological advancements in the last decade or so have allowed experimental techniques such as PIV and CFD, as well as older techniques such as smoke visualisation, to provide important insight. Such techniques are discussed in the following sections.

### 2.4.1 Rotor Wake

Some of the first experimental VAWT rotor wake visualisations were obtained by Strickland et al. for the purpose of validating a vortex model [21]. A dye was released from the trailing edge of one of the blades in a water tunnel test. The total number of blades was varied from $N$=1 to $N$=3, at $\lambda$ = 5. In Figure 2.26, the effect of increased $\sigma$ is clearly seen: with increasing blade number the downstream convection rate of the wake is slower resulting in a greater number of blade wakes present within the rotor volume. An increased number of blade-wake interactions would result from this, as well as from the increased number of blades. Figure 2.26a shows the blade to interact with its own wake three times, Figure 2.26b shows five interactions, Figure 2.26c appears to show seven athough with the increased turbulence and slower convection rate the distinction of each individual wake becomes increasingly difficult. It is worth remebering that in the cases of Figures 2.26b and 2.26c there are additional wakes from the other blades which do no have a dye streakline and so are not visible in the images. In the most extreme of the three test cases, $N$=3, $\lambda$ = 5, in the region of 20 blade-wake interactions must occur in the downwind case.

Strickland's dye-visualisation images show that the flow in the downwind region may be highly unsteady; aerofoil performance is likely to be effected by this and this poses questions over the validity of using 2D smooth-flow aerofoil data as part of a mathematical model, particularly for upwind versus downwind assessments such as those studying camber or fixing angle. Indeed, the tangential force predictions of Strickland's vortex model (previously shown in Figure 2.10) show poor downwind predictions in comparison with experimental measurements.



(a)  $N$=1                    (b)  $N$=2                    (c)  $N$=3
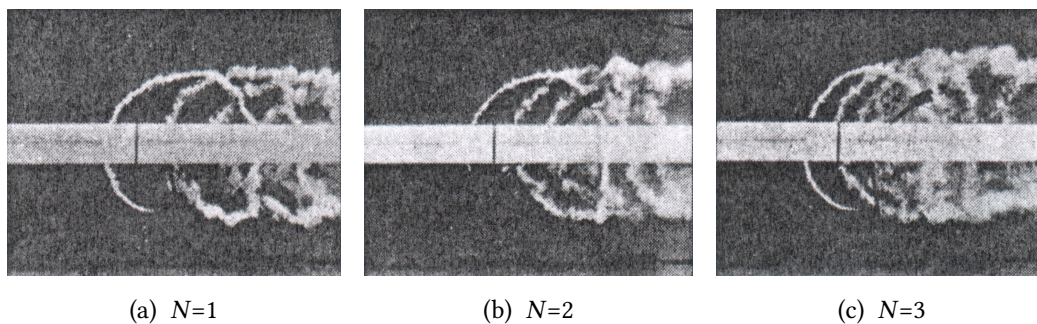
Figure 2.26: Water tunnel streakline visualisation on the wake from one blade, with varying total blade number, from [21]

Using smoke visualisation, Ferreira et al. [60] showed that the trajectory of a vortex shed from the blade tip at the most upwind position was orientated at an angle to the vertical rotor xz-plane, as shown in Figure 2.27, revealing that the wake is not perpendicular to the unperturbed wind direction, i.e. there is an asymmetry in the wake across the xy-plane. A similar vortex movement was also shown in earlier water tunnel studies by Fujisawa and Shibuya [61]. Neither Ferreira et al. or Fujisawa and Shibuya offer an explanation of why

this movement occurs. With greater aerodynamic forces in the first quadrant of the rotation, due to the favourable resultant angle of attack a greater momentum loss would result in the flow, with the consequence of a greater expansion of the wake. The streakline dye-traces of Fujisawa and Shibuya [61] appear to show this (Figure 2.28), and a prediction by Dixon et al. [62] using a free-wake panel method also showed a wake asymmetry.
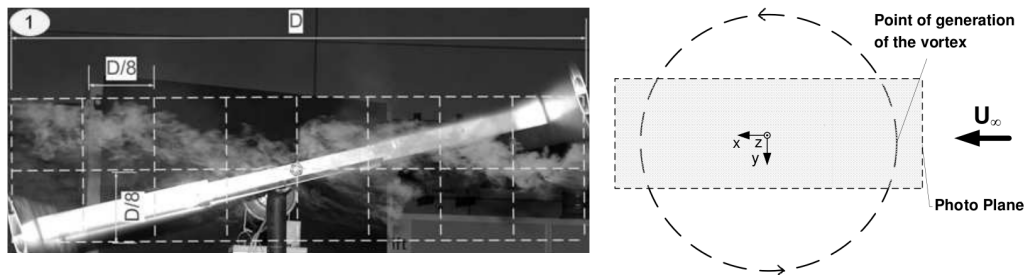


Figure 2.27: Smoke visualisation of the convection of a tip vortex shed at the $\psi=90°$ position, adapted from [60]



| (a) $\psi=45°$ | (b) $\psi=90°$ | (c) $\psi=135°$ | (d) $\psi=180°$ |

Figure 2.28: Water tunnel streakline visualisation on the wake of a small scale VAWT from a fixed reference point-of-view, from [61] (VAWT blade positions added)

From a side-on view Ferreira's smoke visualisation analysis in skewed flow showed the tip vortex shed from the downstream tip to move with increasing speed towards the turbine centre, downstream of the rotor. Interaction between the area of the wake generated upwind and the part of the wake generated downwind of the axis of rotation was cited as an explanation for the observed acceleration of the curvature rate. This seems to be a contrast to the movement with respect to the xz plane; this time the faster convecting part of the wake that has interacted with only the downstream blade is moving inbound. This may be due to the flow returning to equilibrium downstream of the rotor once the wake has expanded, the effect of the wake expansion will fade further downstream which would explain the rate of movement of the vortex core accelerating as it progresses further downstream. Dixon's analysis [62] shows how the wake structure begins to break down, with faster sections merging

with slower sections after approximately one diameter downstream of the rotor. Additional work by Hofemann et al. [63] on a non-skewed VAWT also showed inbound movement of the tip vortices using stereo-PIV measurements. In all three of these studies discussed, the work concentrates on giving a description of the wake phenomena observed but with little relation to performance, and so the studies appear to be somewhat academic as far as the VAWT designer is concerned.

### 2.4.2 Near-blade Wake

For the purposes of aerofoil selection, as well as the wider understanding of the VAWT performance dynamics, the near-blade fluid is often of most interest to a flow physics investigation. Due to the inherently unsteady $\alpha$, dynamic stall is a feature of the VAWT, and the understanding of the effect on performance has been the focus of several stuides investigating VAWT flow physics, not least because the adaption of 2D static aerofoil data to include dynamic effects is difficult and is a potential reason for inaccuracies in various models [15], [37], [52].

Dynamic stall on a VAWT was first visualised by Fujisawa and Shibuya [61] in water tunnel tests using both streakflow visualisation and PIV measurements in both stationary and rotating frames of reference. The generation of two pairs of stall vortices in one cycle of turbine rotation was observed (Figure 2.28). The mechanism for this was said to be the successive generation of flow separation over the inner surface of the blade, followed by the roll-up flow motion from the outer surface to the inner surface through the trailing edge of the blade. The $\psi$ at which these stall vortices are shed and their development was said to be influenced by the $\lambda$, as would be expected due to a smaller range in $\alpha$ with increasing $\lambda$. The structure of the stall vortices was noted as being approximately independent of these parameters (Figure 2.29). The interaction between stall vortices and the downwind blade positions was not examined. It is also interesting to observe the reduced wake convection rate shown with increasing $\lambda$. Although no performance measurements are presented, maximum performance for a rotor of $\sigma$ = 0.33 would be expected to occur around $\lambda$=3 or 4, and so an increasing momentum drop across the rotor would be expected as $\lambda$ increases from 1 to 3 for such a rotor. The rotor used for the experiments was very small indeed, $R$= 0.03m, so $Re$=500 to 1500 for tests at $\lambda$=1 to 3. At such low Reynolds numbers it is clearly questionable whether the observed fluid dynamics would be representative of a realistically sized VAWT. This point is also made by Ferreira et al. who suggest that smaller vortex pairs would be shed at higher $Re$ [7].

At a higher $Re$ values of $5 \times 10^4$ and $7 \times 10^4$ Ferreira et al. [7] show the influence of $\lambda$ on dynamic stall vortex shedding behaviour through PIV measurements (Figure 2.30). Although the convection of the shed vortices is not shown, the roll up and magnitude of the vortices is clearly effected by $\lambda$, with large separations at $\lambda$=3 and $\lambda$=2 (not shown) but the flow remains almost completely attached flow for the part of the $\lambda$=4 case expected to feature the highest $\alpha$. As is the case with the work of Fujisawa and Shiubya, there are no corresponding performance measurements so relation of the dynamic stalling behaviour to performance cannot be made.

An interesting paper also by Ferreira et al. attempts to determine the blade aerodynamic

(a) $\lambda$=1        (b) $\lambda$=2        (c) $\lambda$=3
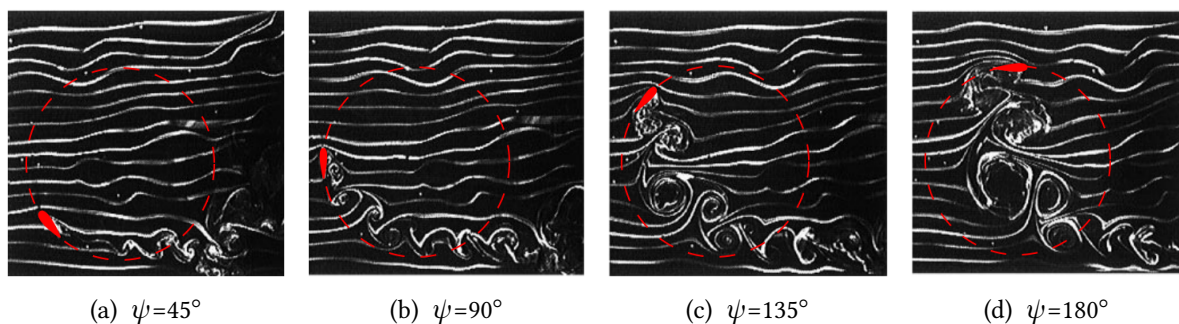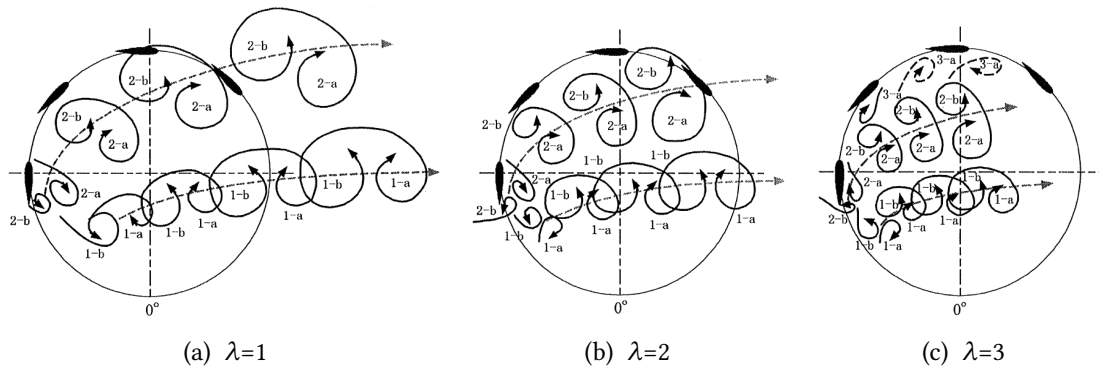
Figure 2.29: Schematic illustrations based on water tunnel streakline visualisations on the wake of a small scale VAWT from a fixed reference point-of-view, adapted from [61]



(a) $\lambda$=3                   (b) $\lambda$=4
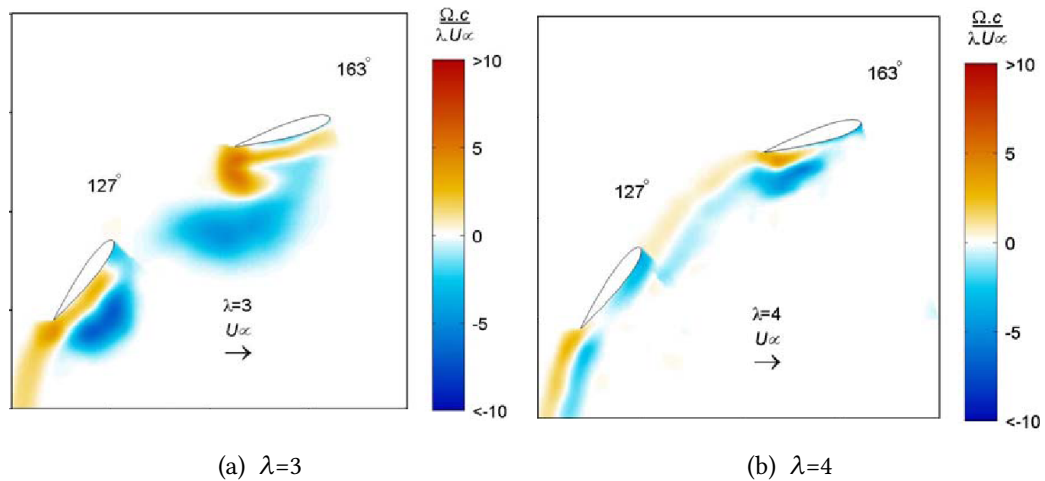
Figure 2.30: Images obtained by PIV showing vorticity shed from a VAWT blade of a single-blade rotor, from [7]

forces from PIV data [64]. An integration process of the velocity field around a contour enclosing the blade is used to determine the blade forces from the PIV data. The method is first tested successfully on a CFD solution, where the velocity flow field and corresponding blade forces are already known. The application of the method is shown for one PIV case, with three different contours around the same blade comparing well. However, only one experimental case is presented, and it is for a $\lambda$=4, $\psi$=20° case where the flow is attached as $\alpha$ is very low. The question of whether the method can be extended to other $\lambda$ and $\psi$ remains unanswered. *If* the method could be shown to be reliable it would be very worthwhile, as measuring the blade forces directly is quite difficult, particularly on a small VAWT where the centrifugal and vibrational forces may likely far outweigh the aerodynmic forces, leaving the experimenter with the unenviable error-prone task of accurately extracting a small value from the measurement of a much larger value.

### 2.4.3 Computational Fluid Dynamics

Some of the previously discussed downfalls of the mathematical models and the practical difficulties of experimental testing can be avoided by using a CFD model to simulate the flow around a rotating VAWT blade or a whole rotor. The downside is that a large unsteady simulation involves a significant amount of computation, requiring a large computational resource or a long computational time. It is only the last decade that has seen computational advancements significant enough to allow CFD simulations of the VAWT to become feasible for a typical academic institution. In addition, commercial CFD packages have been developed with the aim of making it easier and more approachable to generate useful models.

Currently, it would be expensive or time consuming to run large numbers of simulations, such as for an optimisation study. CFD is better placed to aid the understanding of the flow physics: a single simulation can be probed in detail, the aerodynamic forces and the corresponding flow field are easily available, and an understanding of how flow physics and performance are linked can potentially be gained. As with the mathematical models, the CFD solution must first be validated in order to be useful. Establishing a model that is adequate is challenged by the following aspects of VAWT operation in dynamic stall, as noted by Ferreira [65]:

- Unsteady flow requires a time accurate model, adding an extra dimension (time) to the numerical grid.

- The rotor geometry does not allow for important spatial/time grid simplifications to be applied e.g. radial symmetry.

- The large amount of shed vorticity implies that the model could be sensitive to numerical dissipation. In order to avoid numerical dissipation, the spatial resolution of the grid must be fine not only in the immediate vicinity of the blades but over the entire rotor.

- Blade-vortex interaction at the downwind passage means that the development of the shed vorticity must be correctly modelled inside the rotor diameter to model performance correctly.

- Lift and drag forces on the blade vary significantly, resulting in instants during the rotation where the VAWT is being decelerated by drag forces far larger than lift. The correct use of a turbulence model and near-wall models is essential in these situations. This is particularly important at low $\lambda$, where the power output of the VAWT may be negative; the performance in this region is highly important for determining start-up behaviour and the response to large gusts that cause a sudden drop in $\lambda$.

In addition, low Reynolds numbers at start-up or for small scale VAWTs and a boundary-layer that is detaching and reattaching are challenging flow physics to simulate, and so the first publications on the CFD simulation of VAWTs have concentrated on attempting to get a valid solution.

Some of the earliest studies of a VAWT are conducted by Horiuchi et al. in 2003 [66] and Vasseberg et al. in 2005 [30]. Neither of these studies are particularly useful: Horiuchi et al. concentrate their study on comparing velocity changes across the rotor, and do not specifically address power performance. Vasseberg et al. do use their model to generate a power curve and a curve of $T$ vs $\alpha$. However, their description of the structure of their model and the mesh are not clear, there are no plots of the flow field, and very little information on VAWT performance is gained. More useful studies were carried out by Ferreira et al. [65] [67] who used their PIV flowfield visualisations of the vorticity field (discussed previously in Section 2.4.2) as a validation case with the aim of determining the best turbulence model for the VAWT case. Confusingly, these two very similar papers from Ferreira et al. show different results for what appears to be the exact same model and test condition: very different flowfield plots and force coefficients reported for the Spalart-Allmaras (S-A) and $k$-$\epsilon$ turbulence models. The results in [65] (published at a later conference) look much more in-line with what would be expected as the tangential force change with $\psi$ is much more representative of what is shown by experimental results and mathematical models, and so the analysis of [67] will be disregarded for the purposes of this literature review.

The mesh used by Ferreira et al. was composed of four structured sub-grids of quadrilateral elements (Figure 2.31), three of which composed a rotor grid which rotates with an outer domain (a similar approach was used in an earlier paper by Klaptocz et al. [68]). Dividing the rotor space in three sub-grids was said to allow efficient use of a structured grid, as a quadrilateral structured grid allows better control of grid refinement.



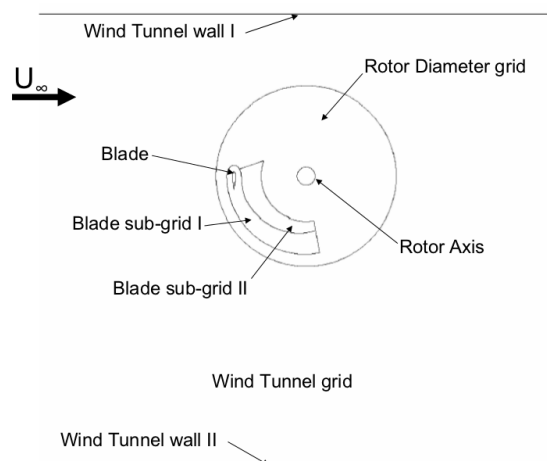Figure 2.31: Computational grid domains as used by Ferreira et al. [67]

Three types of CFD simulation are carried out: Unsteady Reynolds-Averaged Navier-Stokes (URANS) simulations solve the Reynolds averaged form of the Navier-Stokes equations (see Section 4.3) in order to reduce the computational time. For the URANS simulations, two popular eddy-viscosity-type turbulence models are tested, the one equation Spalart-Allmaras

(S-A) model and the two equation k-$\epsilon$ model. In addition, large eddy simulations (LES) are also tested, for which the equations are not Reynolds-averaged in time, but averaged in volume. Computational requirements are increased, but a sub-grid scale model (SGS) is used to model the sub-grid sized turbulence to keep grid density to sensible levels. Finally, a Detached Eddy Simulation (DES) is carried out; a hybrid method of LES and URANS, with the near-wall region being modelled with a URANS model and the outer region with LES.

According to Ferriera et al., the S-A model predicts a later onset of vorticity generation (Figure 2.33a) compared to the PIV data (Figure 2.32a). Roll-up of trailing edge vorticity is not shown at the $\psi$=120° position (Figure 2.33e). The more computationally expensive k-$\epsilon$ model, appears to have a better prediction of the onset of stall (Figure 2.33b), the scale of the leading edge vortex appears to be well matched to the experiment, but the expected roll-up of trailing edge vorticity (as shown in the PIV measurements, Figure 2.32b) is not visible in Figure 2.33f. LES analysis shows shedding of leading edge vorticity and the roll-up of the trailing edge wake are simulated. However, the vorticity shed at the leading edge (Figure 2.33c) covers a larger region than shown in the experimental results and appears to be a series of small vortices rather than one large dynamic stall vortex. Roll-up of the trailing edge wake also occurs too early in the rotation (Figure 2.33g). The DES is said to present the best simulation relative to the experiment, although the onset of stall appears to be predicted to occur much earlier than the experiment: Figure 2.33d shows a leading-edge vortex has been shed before $\psi$=90°; early stall would have a significant effect on the predicted performance.

Aerodynamic forces are compared between the two models; unfortunately, the tangential and normal components are plotted on the same axes making it hard to assess the differences in torque prediction between the cases. It appears though that the S-A model predicts a particularly high torque peak, at a relatively large $\psi$. The delay in the onset of stall (Figure 2.33a) and the delayed convected of the stall vortex away from the upper aerofoil surface (Figure 2.33e) for the S-A model would account for this. LES and DES simulations show a maximum tangential force at lower $\psi$ which would also be expected given the previously discussed vorticity plots.

One criticism of the work by Ferriera et al. is that it would have been more useful if the experimental performance had been measured in addition to the flow characteristics. It would have been interesting to see how the apparent differences in flow characteristics between CFD models and the PIV results effected the quality of the performance prediction. Based on much of the literature review in this chapter, the Author suspects that the $\psi$ at which stall is predicted, as well as the lift and drag prediction in general are more important, in terms of an accurate $C_p$ estimation, than the particular post-stall flow physics which occur.

More recent CFD studies of the VAWT include work by Tullis et al. [69], Beri and Yao [70] and Castelli et al. [71]. The most interesting of these studies is the work by Castelli et al. which shows a comparison of the CFD-simulated power curve against an experimental equivalent and provides a detailed description of the CFD model set-up. A very similar trend in the change of $C_p$ with $\lambda$ is predicted. However, the 2D CFD significantly over-predicts the

(a) leading edge vorticity
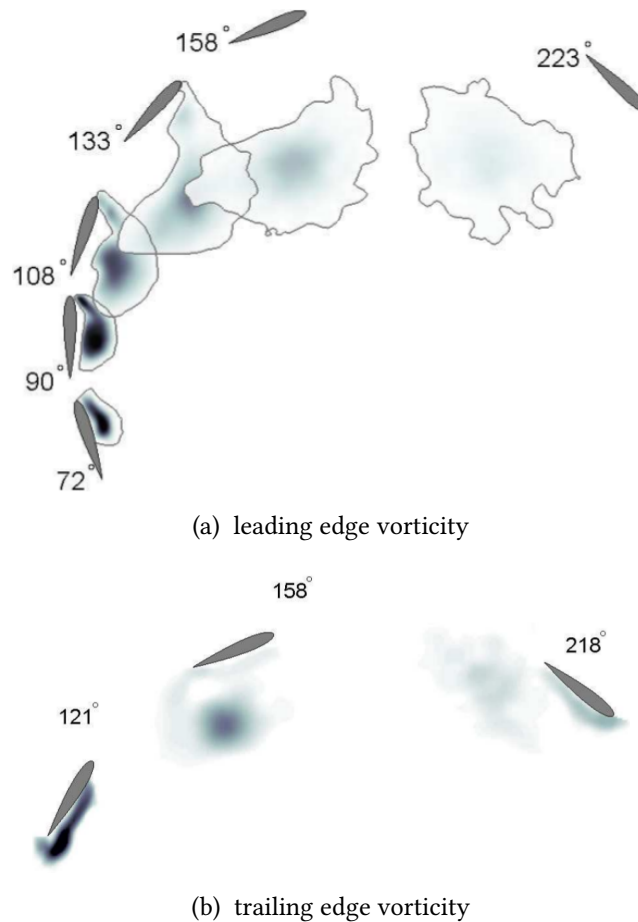


(b) trailing edge vorticity

Figure 2.32: Images obtained by PIV showing evolution of shed vorticity at upwind stall, adapted from [65]

$C_p$ and a $C_{p-max}$ twice that of the experiment is simulated, with the combined effects of finite blade length and spoke drag cited as the main reason for the differences. In a paper from an earlier study, for which the Author conducted the experimental tests, the results suggest that the match between a 3D CFD solution and an experimental case might be considerably better than for a 2D CFD solution [51]. However, the VAWT in this case had a particularly high aspect ratio ($AR = 4$), and so this result is perhaps not surprising. How the performance of a VAWT with a more sensible aspect ratio (>10) differs with 2D and 3D CFD simulations is still yet to be shown, no studies have been found which do this in the Author's own search of the literature.

### 2.4.4   Summary of Flow Physics

Particularly in recent years, there has been some good quality investigations into some aspects of the VAWT flow physics. Improved experimental technologies have played a major part in this, but the wide availability of computing resources capable of allowing detailed simulation

(a) S-A model, $\psi$=90°    (b) k-$\epsilon$ model, $\psi$=90°    (c) LES model, $\psi$=90°    (d) DES model, $\psi$=90°

(e)    S-A    model, $\psi$=120°    (f) k-$\epsilon$ model, $\psi$=120°    (g) LES model, $\psi$=120°    (h) DES model, $\psi$=120°
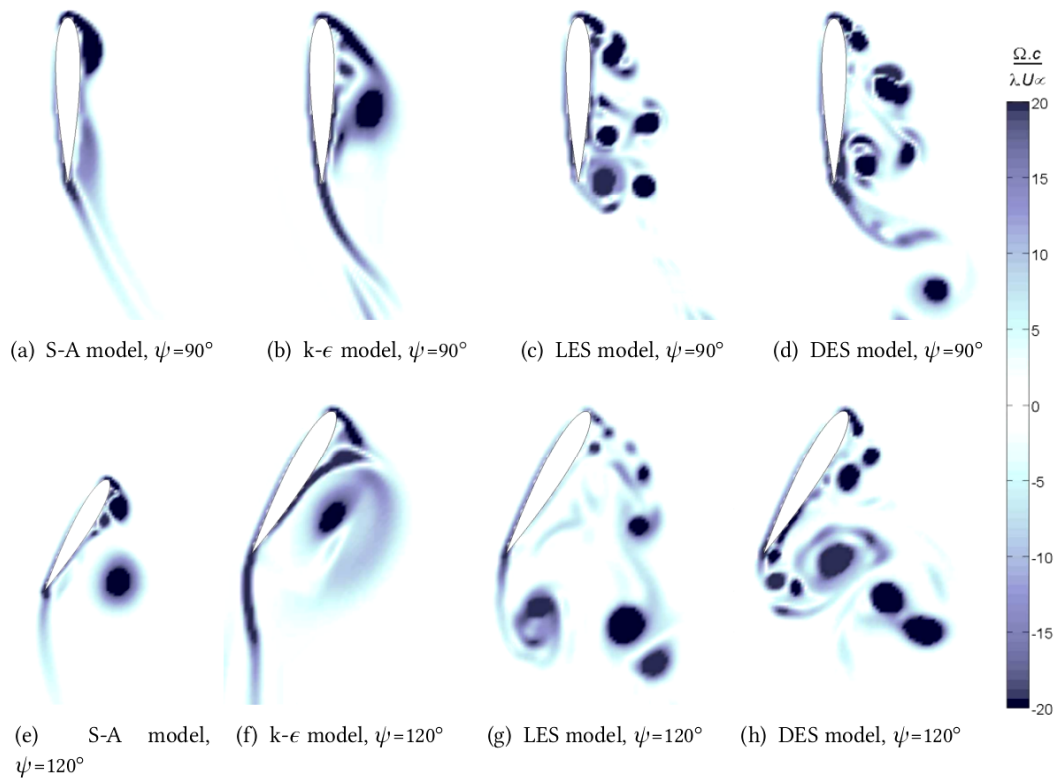
Figure 2.33: Images obtained by CFD showing vorticity shed from a VAWT blade of a single-blade rotor, adapted from [65]

will perhaps prove to be the most significant development in terms of allowing researchers to probe the VAWT flow physics in more detail. A picture of the flow characteristics of the blade and overall rotor wake is beginning to emerge. However, strong links between the observed physics and the earlier, often mathematically modelled behaviours have yet to emerge. This thesis aims to significantly improve the link between the observed flow physics and the aerodynamic performance of the VAWT.

## 2.5   Summary

In essence, the three major sections into which this review has been divided appear to exist somewhat in the history of the literature itself: The early publications have set-out the basics principles of the main types of mathematical models, and studies following on from these utilise the models, and experiments, to investigate the fundamentals of performance. The most recent papers have attempted to address the flow physics using advanced experimental techniques and computational fluid dynamics. There is, of course, some cross-over within the general historical trend, with some recent papers addressing fundamental issues such as solidity.

There are numerous configurations of mathematical models, although many are based around the fundamental momentum or vortex principles as outlined in Section 2.2. Many papers look at the improvement of these models, some are little more than a demonstration of their use which, although useful for adding a tool the VAWT researchers toolbox, do not in themselves advance design or understanding. Using a combination of experiment and modelling some of the fundamental performance characteristics have been examined, with varying degrees of success. These have been detailed in Section 2.3. It has been shown that there is still some work to be done in this area, for example: even a well-read VAWT designer would still have difficulty in selecting a suitable aerofoil without conducting his own tests first. Finally, work examining the physics of the flow through the rotor and around a blade have been presented. These studies are, on the whole, relatively recent and they have yet to be linked through to some of the earlier work, and most significantly to the performance fundamentals that have been previously addressed using mathematical models.

There are many areas of the VAWT literature that might be considered candidates for further research development. In the Author's opinion, the most important thing is that a VAWT produces the energy output that is required of it. This may take the form of improved self-starting ability, or a smooth power output for fatigue considerations. More often, it is the energy extraction potential of the design that is most important. To yield improved knowledge of the VAWT design, and ultimately to give better energy yields, the following areas of the literature are judged to be those most in need of development.

1. Performance Fundamentals

   - Aerofoil selection capabilities must be improved, current studies do not give sufficient information for a designer to make a knowledgeable choice of an appropriate profile.

   - The variation of $C_p$ with variables such as $\sigma$ and $\lambda$ must be better understood before a rotor and the control and operation strategies can be chosen.

   - If smaller scale VAWTs are to be utilised within the urban environment, then the understanding of Reynolds number and turbulence effects must be improved.

2. Flow Physics

   - Better understanding of the blade fluid dynamics would feed into aerofoil selection, current understanding is often based on 2D static aerofoil tests.

   - The effect of upstream shed vortices and flow induction needs to be understood before upwind versus downwind performance can be properly assessed.

   - CFD is potentially very useful, but techniques and aspects such as turbulence model selection need further research before CFD models can be used to assess the flow physics.

- Currently, the study of the VAWT flow physics is experimentally-led, improvement of experimental techniques is a priority for better understanding. Some of the downfalls of mathematical models could then be addressed, and those models improved.

# Chapter 3

# Methods: Performance Measurement

The work presented in this thesis utilised a range of apparatus and techniques, much of which required significant development during the study. To aid the reader, the explanations of the apparatus and methods are divided into two chapters. This first one addresses the wind tunnel apparatus and methods which were used for the VAWT performance measurements. Following this, in Chapter 4, the techniques (PIV and CFD) used to investigate the performance-related flow physics are described.

## 3.1   Introduction

There were no existing VAWT testing facilities at the University when the research for this study was started. In addition, the detail of the varied experimental methods and apparatus given in the literature does not readily allow a recipe for VAWT testing to be formed. The aim of this chapter is to take the reader from this blank-canvas starting point of the research, through the design and testing process, and up to the point at which working apparatus and measurement techniques are established.

In Section 3.2, the general design methodology is outlined and an explanation is given of the design process, which was used to guide the design of the apparatus and methods. A design brief for the apparatus is defined which sets out the essential characteristics and capabilities. Following this, in Section 3.3, the apparatus is described for the various components of the complete VAWT testing system. After which, the development of a new method for obtaining the VAWT power curve is detailed in Section 3.4. Finally, the potential effects of errors and uncertainties are discussed in Section 3.5

In general, the discussions of the apparatus and methods aim to be as full as is practical, so that a detailed record of them is made that is hopefully of use to other experimenters. In addition, for the separate sections in this chapter, a short summary of appropriate literature

has been collated and is presented within this methods chapter, rather than the main literature review.

## 3.2 Design

When faced with a need to undertake an experimental study, suggestions for appropriate apparatus and methods can usually be gained from literature. However, there are a series of easily over-looked steps required to turn ideas and suggestions into correctly functioning equipment. In the VAWT case, the number of experimental-based publications is fairly low and there is no consensus on the make-up of a suitable experimental set-up, or how measurements are best made. Additional work was therefore needed to generate the designs for the various equipment. To optimise the use of time, funding and resources, the design process was guided by a design methodology which is detailed below. A design brief set out the required characteristics of the equipment, providing constraint to the design process and helping to keep it focused. The design brief is also detailed below.

Whilst this section aims to lay out the overall design of the apparatus and methods in a clear manner with defined steps, in practice the design process was not always so structured: it was sometimes subject to unforeseen circumstances and requirements, and on occasions there was a need to iterate between different stages, or carry out two stages in parallel. The design brief and design methodology (detailed below) were most usefully employed as a set of guidelines, not rules.

### 3.2.1 Design Brief

The overall aim of this work was to further the understanding of the VAWT flow physics for the purposes of improved design and energy capture. An experimental strategy was chosen which reflected this, beginning with the design of a purpose-built VAWT model. Initially, the following criteria were laid out as a design brief:

1. The rotor geometry must be typical (relative to the literature):

    - $\sigma \approx 0.3$ ($\sigma = Nc/R$)
    - a symmetrical NACA00xx aerofoil profile
    - a suitable blade aspect ratio, $AR > 10$
    - two or three blades

2. The apparatus must allow:

    - $0 < \lambda < 6$
    - $T$ and $\omega$ measurement
    - adjustment of blade fixing angle and blade number

- components to be easily replaced when necessary

3. The rotor geometry should feature free blade ends to allow flow probes to be used in and around the rotor volume.

4. Aerodynamic forces to be measured should be as large as possible, and the system resistances as small as possible, to enable accurate measurements.

## 3.2.2   Modular Design

The first step of the design process was to modularise the design of the apparatus where possible, this allowed the concentration of the literature research and design efforts on one part of the assembly at a time, and also meant that most design changes could be applied to the particular module without requiring changes to other subsystems. Points at which the characteristics of one system were dependant on those of another were highlighted and used as design criteria for the module. The modules were prioritised so that at these shared design points one module could take priority over another, for example: the start-up motor specification was connected to the rotor size, but the rotor design took priority meaning that the motor was specified based on the chosen rotor design.

The VAWT apparatus was divided into the following modules and sub-modules, the overall system is shown in Figure 3.1, with the individual modules outlined for clarity:

- rotor assembly

- start-up mechanism

- measurement assemblies:

  - $T$ and $\omega$ measurement system
  - Wind velocity
  - PIV system (Laser and Camera)

- user area:

  - data logging
  - control

## 3.2.3   Design Methodology

A similar process was followed to generate the design for each module, this generalised process is shown in the form of a flow chart in Figure 3.2. Initially, related literature was collated and reviewed, and following this a 'brainstorm' of ideas was generated following the main design criteria. The ideas were then filtered by consideration of time and research budget
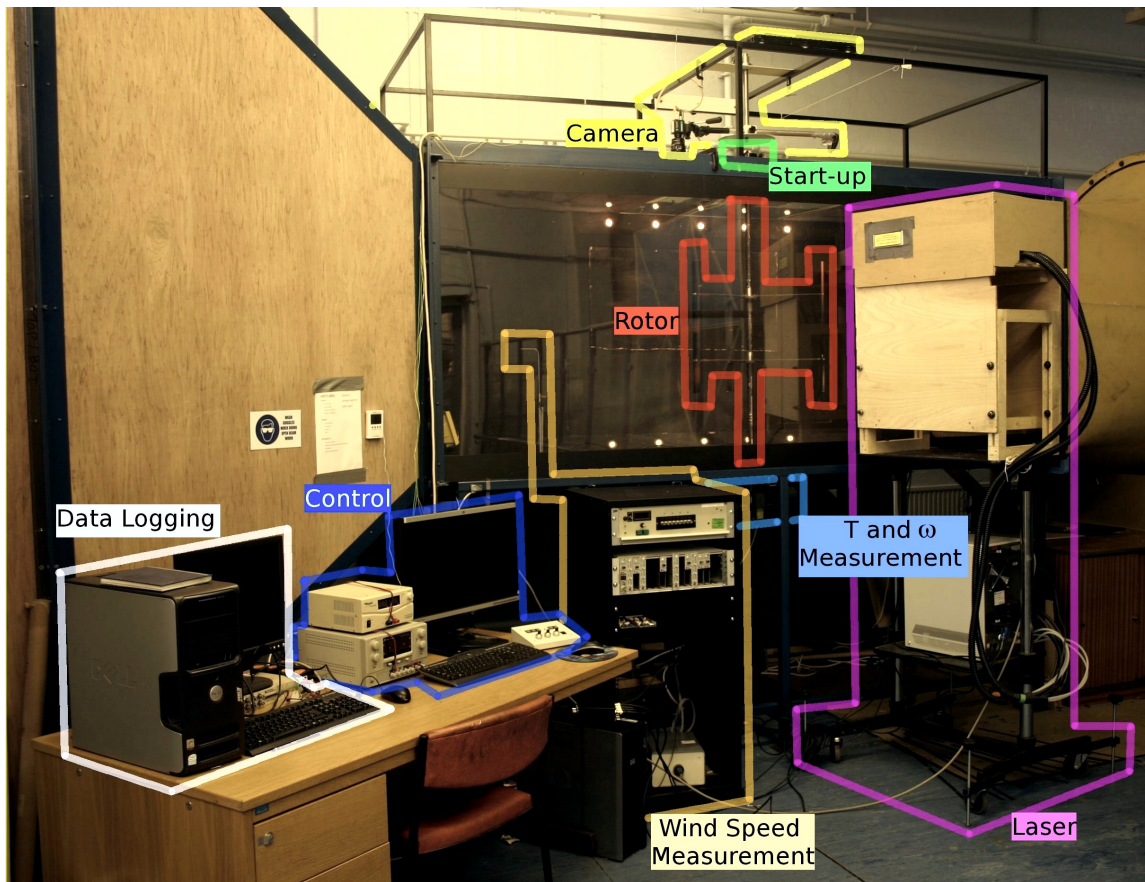
Figure 3.1: VAWT testing system, with individual design modules highlighted

and key components were identified, allowing the a basic design to be formed. Shared design points were then identified and the design was modified using the previously defined priorities. With the fundamental design established, a CAD model was made which allowed the module's geometric interface with the main assembly to be checked. Where possible, a simplified test was carried out to check the basic functioning of the manufactured equipment. Following this, the equipment was tested more rigorously using a real test situation. For example: the PIV system was initially tested on a straight known-velocity flow, then on a fixed VAWT blade, and finally the rotor was spun to test the real synchronised test situation. Some minor modifications were usually needed, but the earlier stages of the design process, such as CAD modelling, helped to reduce the likelihood of unanticipated problems with the design.

## 3.3   Apparatus

This section details the main apparatus used for the experiments, most of which was designed by the Author via the design process which has been outlined in the previous section. A short review of the literature relating to experimental VAWT testing is presented in the first
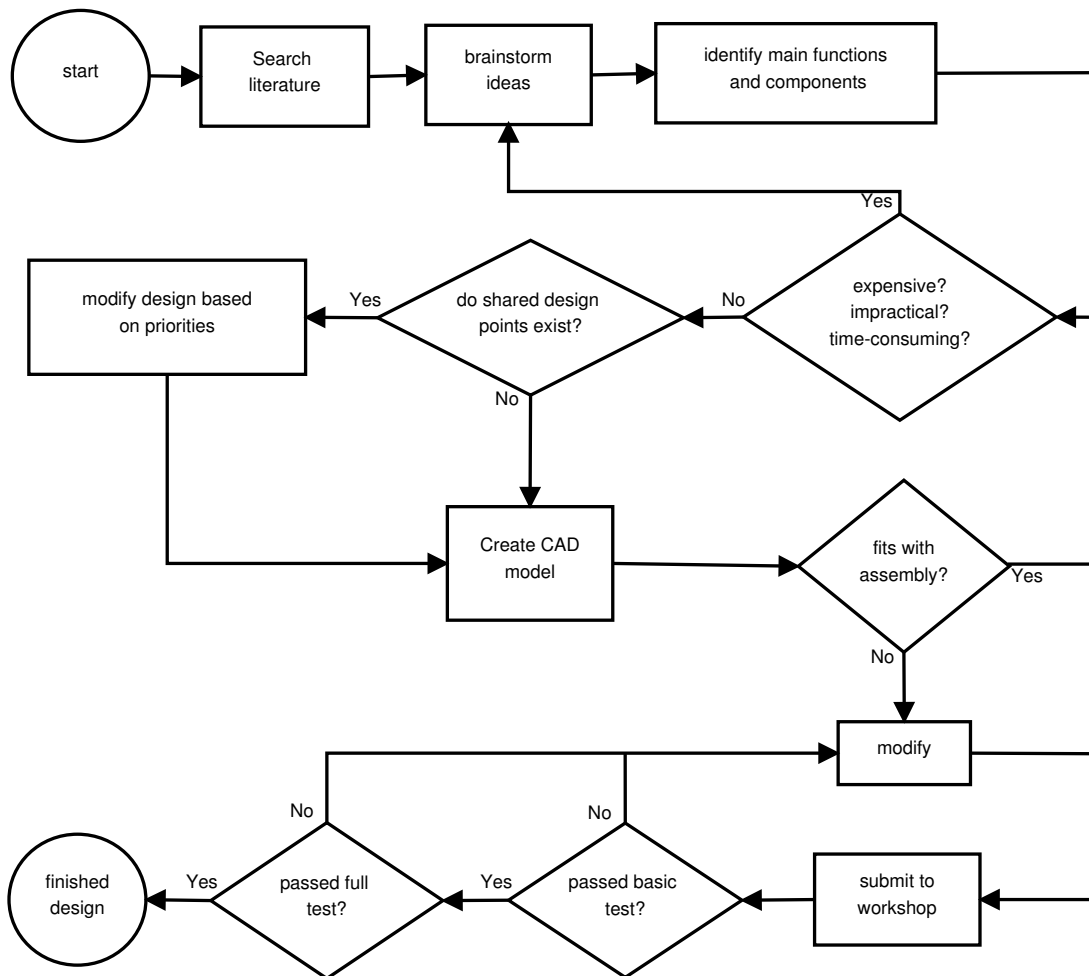
Figure 3.2: A flow chart showing the general design process for the apparatus modules

subsection.

### 3.3.1  Literature

**Rotor Geometry**

For most of the published wind tunnel experiments addressed in the following subsections, the rotor configurations under test usually have two or three blades, and solidities typically in the range of 0.15 to 0.4, although a one blade rotor (with a counterbalancing mass) was used by Ferreira et al. for their PIV testing [7][65], although the $C_p$ performance was not investigated.

In most cases, blades are usually supported by support arms connected to a central shaft via a hub. It is desirable for the structure to have a low-drag profile to minimise resistive torque, as well as aerodynamic effects on the blades. For the testing conducted by Vittecoq [72] and Laneville [73] the support arm contained a a strain gauge system which measured

the aerodynamic forces on the blades as the VAWT rotated. As an alternative, particularly for flow visualisation experiments, it may be desirable to support the blades using supporting discs rather than arms. Blade-supporting discs are utilised by several studies, including those by Fujisawa and Shibuya [61] and Ferreira et al. [64]. Van Brussel et al. [74] also used disc supports and had to add additional support to reduce the higher than expected bending of the blade due to centrifugal forces.

**Blades**

The blades are one of the most difficult and expensive components to manufacture for an experimental VAWT set-up, due to a requirement for a lightweight but stiff blade, and the need for an accurate aerofoil profile. The blade manufacture may be further complicated by the addition of twist or curvature. In particular for a small VAWT, the high rotational velocities required to set $\lambda$ may result in relatively high blade and structural loading due to centrifugal forces.

Both straight and curved bladed VAWTs have been investigated; in addition, skewed blades with twist have been manufactured and tested by several authors [74] [69] [75]. One possible method of manufacture is to machine blades from aluminium [22] [69] which has the advantage of being able to generate an accurate surface profile with equipment available to most academic institutions. The disadvantage of solid aluminium blades is that they are relatively heavy, which may result in structural and vibrational problems as encountered by some studies [76] [77], and may limit the rotational velocity. Lighter blades have been made by extruding a hollow profile also using aluminium [49] [50] [77] or by manufacture from carbon fibre [31] [75] but both of these techniques require facilities and expertise which may not be available to all but the most well-funded research projects, for example: the large curved blades as used by Sheldahl [77] were extruded, bent into shape and then stress-relieved which would certainly be a costly one-off manufacture. One possible low-cost method is to wrap an aluminium sheet around a profiled rib, as used by Kirke [31]. However, it would be difficult to achieve an accurate profile on small chord ($c$ <10cm) aerofoils using this method. Another lightweight, low-cost blade material is balsa wood which Vittecoq [72] and Laneville [73] used for their tests in which they measured the varying aerodynamic forces on a blade across a rotation. For this application, lightweight blades were essential in order to minimise the centrifugal forces which had to be deducted from the net force to give the aerodynamic forces. Again, achieving an accurate surface profile might be difficult, and certainly the material would not stand up to much wear and tear. However, a suitable surface coating might help to solve both of these problems.

**Fixing Angle**

Fixing the blade securely to the supporting structure whilst allowing the blade fixing angle to be varied requires a well-designed mechanism. The mechanism also needs to have a low

drag profile, as it is likely to be located near to the blade at maximum radius, where any drag has a large effect on the resistive torque on the rotor. For the Darrieus VAWT, the mechanism will be near to the shaft, where drag is not of much concern. Klimas' method of varying the fixing angle at this point has been previously discussed in Section 2.3.1. Klaptocz adjusted fixing angle on a straight blade VAWT using a pivot joint with a clamping mechanism, no description is given of the mechanism other that to saying that the angle of attack could be adjusted using "precision-wedges" [68]. Unusually, the blade chord is not given by Klaptocz, the turbine diameter was 0.9m. So, assuming $c \approx 40mm$, a displacement of the trailing edge of just 0.7mm ($0.017c$) would alter the fixing angle by a 1°, which illustrates that the fixing angle mechanism must indeed be precise, especially for a small VAWT. The method of fixing angle adjustment used by Armstrong and Tullis [78] appears to be similar; however, the joint used is a little cumbersome and would certainly have quite high drag (see Figure 3.3). In addition, the drag may vary as the wedges are changed, which would be difficult to account for when assessing the performance changes due to the fixing angle adjustment.



Figure 3.3: Armstrong and Tullis' blade support arm joint, as used to adjust fixing angle [78].

**Mounting the Rotor**

In relation to his wind tunnel tests on a 2m diameter Darrieus VAWT, Blackwell notes: "*Because of the importance of precise determination of torques, bearing selection and loading are critical*" [22]. Blackwell's rotor was supported by a double-row self-aligning ball bearing at the based of the shaft and a set of two single-row radial contact ball bearings held the top of the shaft. Affixing the shaft between bearings at the top and bottom of the shaft is the most practical way to mount a rotor shaft in a wind tunnel and several studies, including this one, have chosen to mount their VAWTs in this way [31] [74] [79]. The lightweight rotor used by Vittecoq [72] was supported in a double set of bearings only at the bottom of the shaft. For the full-scale testing of the commercial Quiet Revolution QR5 VAWT [75], the shaft and bearing assembly was attached directly to the wind tunnel force balance which enabled streamwise and side force measurements to be captured. In many cases, it may be more practical to mount the shaft horizontally which gives easier access to measurement equipment such as generators,

motors and encoders which are usually located the ends of the shaft. Gravitational loading variations mean that a horizontal shaft is only practical for two-bladed rotors, as tested by Ferreira et al. [60].

**Wind Tunnel**

Both open and closed circuit wind tunnels have been used for the testing of VAWTs, and towing water tanks have also been used. Open-section tunnels have been used by Vittecoq [72], Laneville [73] and Van Brussel et al. [76] in a bid to avoid blockage effects. Bertinyi's full-scale closed-circuit wind tunnel tests of a 3.1m diameter VAWT were corrected for blockage using the method developed by Glauert [10] and the experimentally measured streamwise force on the rotor. Blackwell, also corrects his results for blockage but in lieu of a streamwise force measurement, a rotor drag coefficient was assumed. Ferreira et al. suggested that for their closed circuit wind tunnel tests, CFD simulations had shown blockage to be negligible [7].

Other tests have been conducted in free air, such as those as part of the large scale Sandia program including tests by Ashwill [49], Sheldahl et al.[27] [77] and Worstell [14] [29], and other tests including those by Van Brussel et al. [76], Kjellin et al. [80] and Dabiri [81]. Free air testing is easily disrupted and restricted by the local weather conditions which may make it difficult to carry out a program of testing and, whilst not subject to blockage effects, testing in free air is subject to many other potential sources of error: measurement of the incoming wind velocity is a particular challenge, often the wind velocity is obtained from the interpolation of more than one velocity measurement taken from anemometers placed around the VAWT test position. A method of bins [80] may be used to log data and build up a database of test conditions from which performance can ultimately be assessed. To make use of data from outdoor tests, the effect of both large and small turbulence scales must also be understood, work looking at the potential effects of gusts has only recently been published by McIntosh et al. [82]. Ashwill also reports that contamination of the blade surface by "bug-residue" altered performance, presumably due to the increased surface roughness tripping the boundary layer flow.

In order to reach higher Reynolds numbers at small scales, water tunnels have been used in several studies. Fujisawa and Shibuya [61] used a water tunnel for their PIV and streakline analysis on a very small VAWT (0.06m diameter). A towing tank was used by Klaptocz [68] to investigate the effect of a ducted flow, and also by Strickland [21] to provide previously discussed performance and flow visualisations (See Section 2.4.1).

**Summary of Apparatus Literature**

The rotor configurations documented in the experimental studies of the literature are varied, as are specific design details such as blade manufacturing methods or fixing angle mechanisms. So far, too few experimental studies have been conducted to have allowed the development of

any kind of standardised set-up or common approach. As a result, it was more often the case that pieces of more than one publication were combined and used to make informed decisions during the design process for this study's apparatus.

### 3.3.2 Rotor Assembly

The chosen rotor assembly design was a compromise between the criteria outlined in Section 3.2.1, and the wind tunnel geometry and research budget available. The design work for each component was carried out by the Author, most of the components were then manufactured by technicians in the Department of Mechanical Engineering's workshop.

**Rotor Geometry**

In order to maximise the size of the forces to be measured, and the Reynolds number range that could be tested, the rotor was made as large as possible for the available wind tunnel section size. A blade length, $B = 0.6m$, and a rotor radius, $R = 0.35m$ were chosen as suitable rotor dimensions. This led to an area-based blockage ratio of 0.29. Matching $C_p$ values to far-field boundary equivalents was not the aim of this research, so the concern for blockage ratio had a lower weighting than the requirement for good-sized forces and flow features in order to aid measurement. Figure 3.4 shows the rotor layout and main dimensions.

Blades of 40mm chord length were manufactured in the Department of Mechanical Engineering's workshop from aluminium using a CNC milling machine to generate an accurate as possible profile. The selected blade chord length gave $\sigma$=0.22 or 0.34 for two or three blade rotor configurations respectively. A NACA0022 profile was chosen for the blades as it met the criteria for a symmetrical profile and, in addition, two Masters Degree studies carried out at the University by Smith [83] and Hamada [84] had suggested thicker profiles might give an improved performance, relative to the more popular 0012 or 0015 profiles. However, more recent work within the Howell research group [85] (started after the VAWT rotor was designed) has suggested the NACA0012 will give a higher $C_{p-max}$. From a practical point of view, the increased thickness gives a blade more resistant to bending and also allows easier fixing.

Low-drag profile support arms, based on a 30mm-chord NACA0026 section, were also manufactured out of aluminium. Two support arms held each blade, connected at the $\frac{1}{4}$ and $\frac{3}{4}$ positions along the blade to minimise bending forces on the blade. The blade fixing centre was set so that a radial line drawn from the rotor centre would intersect the chordline perpendicularly at the $0.5c$ position.

**Rotor Loading**

To balance to rotor, the individual blades and support arms were weighed and then arranged into three sets of approximately equal mass in order to minimise loading and vibrations during rotation. Structural calculations (detailed in Appendix A.1) determined that the rotor $\omega$ should

not be allowed to exceed 1000rpm due to excessive centrifugal force of the blades above this speed.
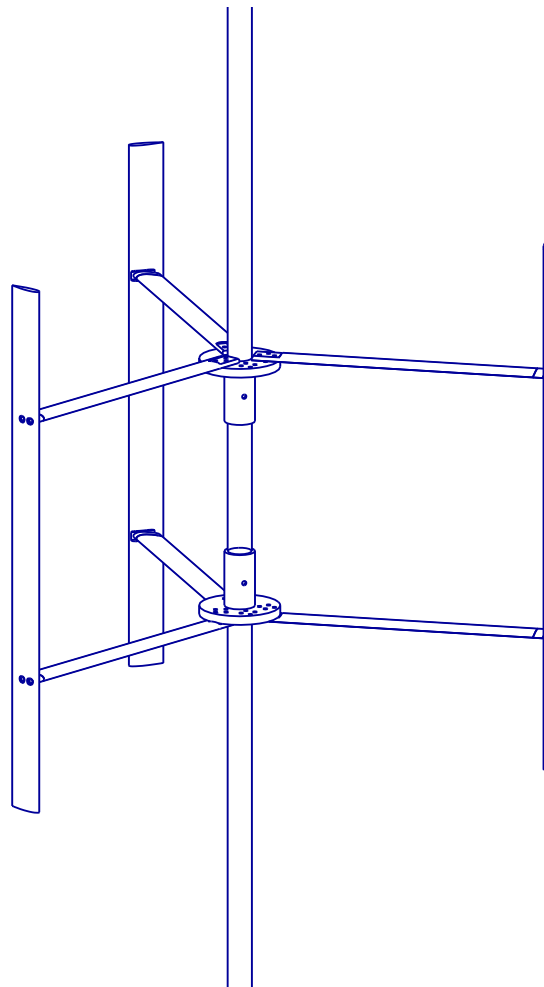
**Fixing Angle**

The literature shows that VAWT performance is sensitive to fixing angle changes (see Section 2.3.1). So, it was important that the blade fixing angle could be set accurately to a known value. A number of small inserts cut at different angles were used to control the fixing angle of the blade. The fixing angle inserts were also CNC machined from aluminium to the same profile as the support arm. The angle of the insert was cut so that the blade fixing angle pivoted about the leading edge (see Figure 3.5a). Error in positioning the support arm at the hub would lead to an effective change in fixing angle, so it was important the support arm fixing to the shaft allowed accurate and repeatable attachment. To facilitate this, the support arms connected to hubs which had fixing slots to locate the end of the support arm (see Figure 3.6). Two sets of slot positions were machined which allowed two and three blade rotor configurations.
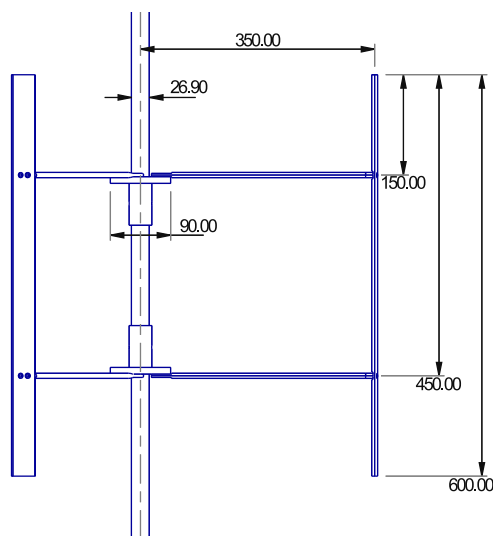
**Bearing Assembly**

For supporting the shaft, the overall aim was to mount the rotor as safely and rigidly as possible, but without causing excessive resistance to rotation. The rotor assembly was mounted on a shaft which was fixed between the top and bottom of the wind tunnel sections. The assembly hung on a tapered roller bearing (see Figure 3.7a) which was lightly push-fitted into a steel plate, which was in turn bolted to the steel frame of the wind tunnel working section. A ball-bearing supported the radial loads at the bottom of the shaft. To prevent the rig moving upward, an amount of pre-tension was added to the shaft assembly via a spring and bolt underneath the bottom bearing (see Figure 3.7b).
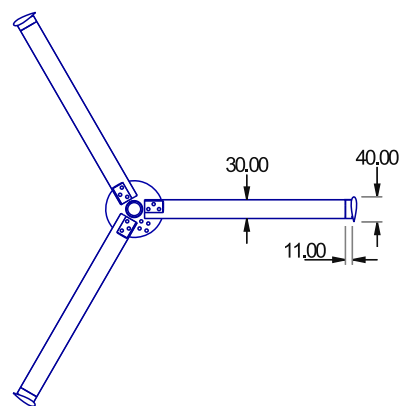
### 3.3.3 Wind Tunnel

The Department of Mechanical Engineering's low-speed wind tunnel (Figure 3.8) was used for all of the experiments detailed in this thesis. The tunnel is an open-circuit suction tunnel, with the flow being driven by an eight-blade axial fan located at the outlet. The wind tunnel has a total length of 8.5m, which includes the 3m-long working section. At the inlet, a honeycomb mesh (with cells 0.01m wide and 0.1m long) straightens the flow and breaks up any large scale flow structures present in the room. After the honeycomb the flow encounters a fine 1mm-cell mesh screen with a 80% free area ratio. The fine mesh breaks up flow structure scales that have passed through the honeycomb, and helps even-out any variations in the flow through the generation of small scale turbulence and a pressure drop. The settling section allows time for turbulence and flow non-uniformities to dissipate before the flow is accelerated by a 6.25:1 contraction which leads to the working section. For some measurements, a turbulence grid was placed at the start of the working section to generate near-homogeneous turbulence at the test position of known intensity and length scale.

(a) 3D view



(b) side view

(c) top view

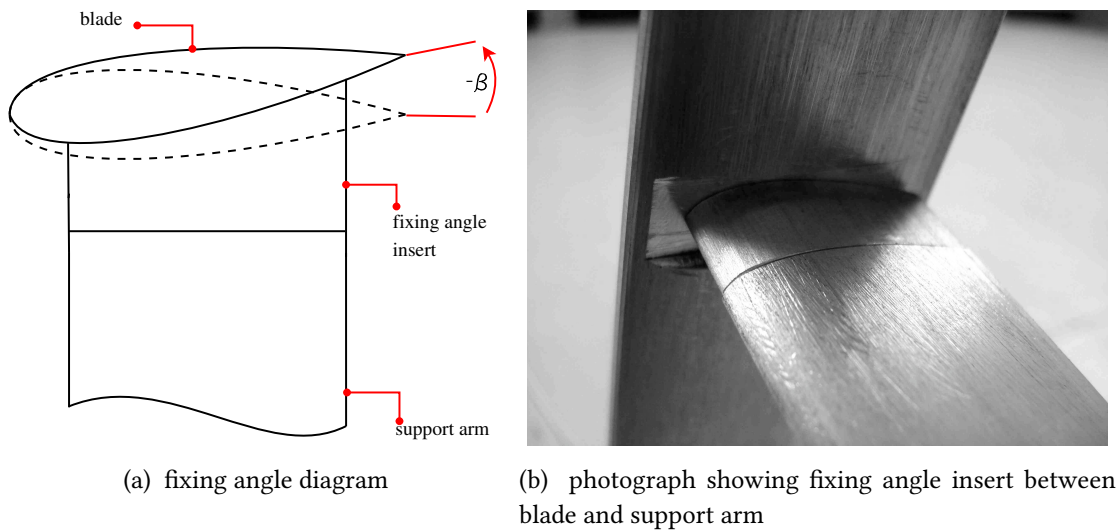Figure 3.4: Rotor design (dimensions in mm)

(a) fixing angle diagram

(b) photograph showing fixing angle insert between blade and support arm

Figure 3.5: Method of altering fixing angle of the blade



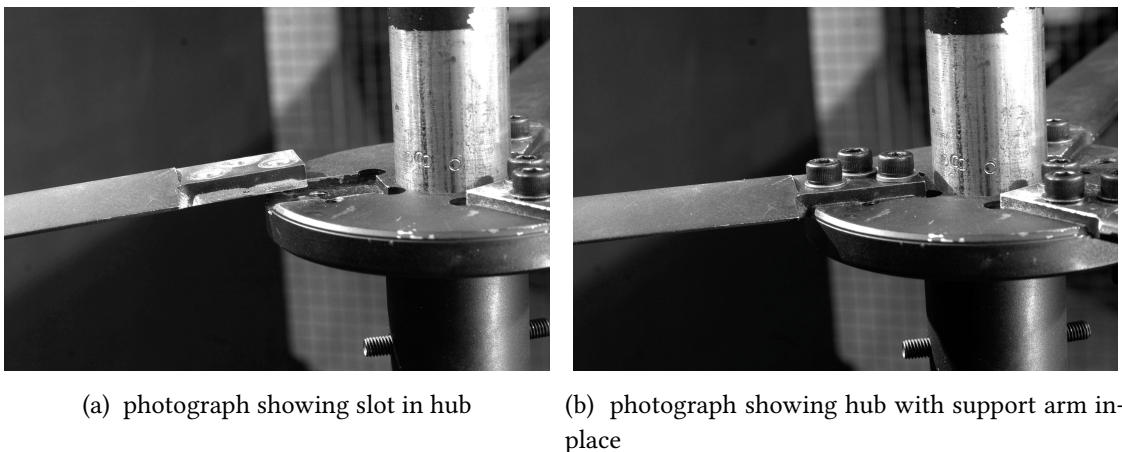(a) photograph showing slot in hub

(b) photograph showing hub with support arm in-place

Figure 3.6: Hub design

Existing steel supporting structures allowed the VAWT testing position to be set to 1.8m downstream of the start of the working section, this gave the grid-generated turbulence and any non-uniformities resulting from the contraction chance to even out, creating an inflow which was as close to uniform as possible with the facilities available. The remaining 1.2m of the working section, allowed a wake length of 1.8D to be established downstream of the turbine shaft position before the diffuser was encountered. The VAWT performance is dominated by the near-blade and near-rotor wakes (as discussed in Section 2.4), the distortion of the wake after 1.2m was not thought to have a significant effect on this investigation into the fundamental VAWT flow physics.

A reference Pitot-static tube was located at the start of the working section and was used to set the reference wind tunnel flow speed (as detailed in Section 3.3.5).
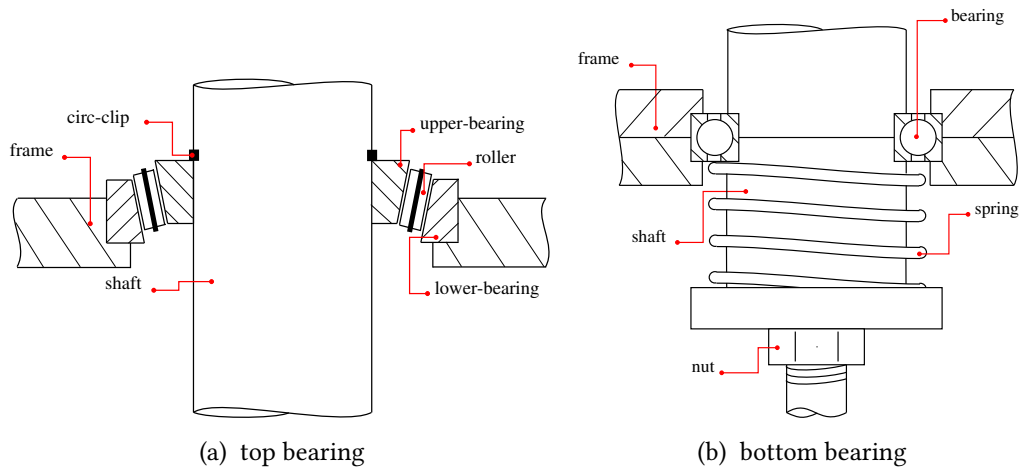
(a) top bearing
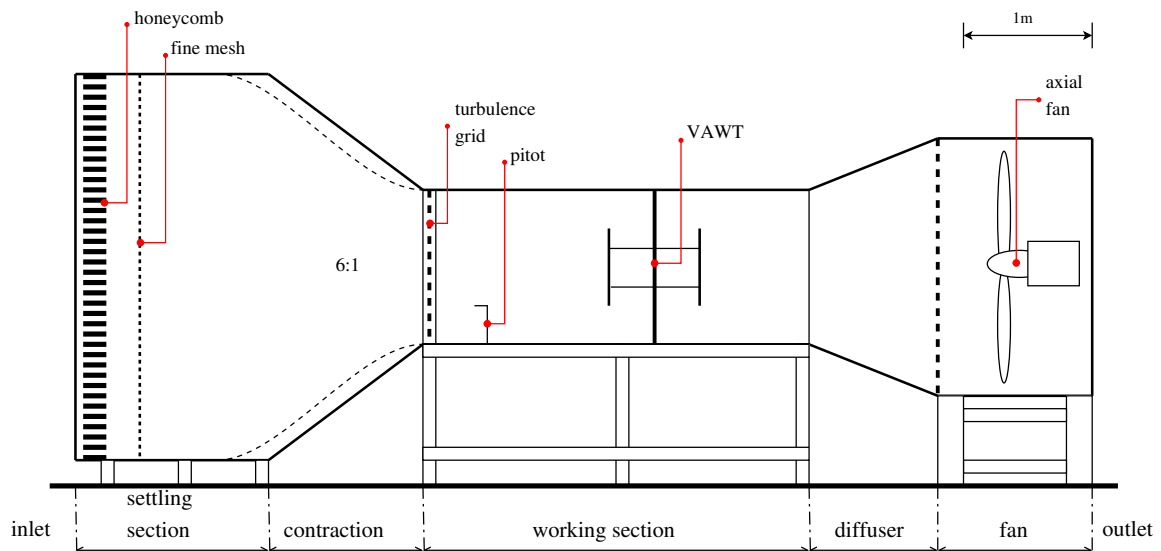
(b) bottom bearing

Figure 3.7: bearing set-up



Figure 3.8: Wind tunnel

### 3.3.4   Start-up Mechanism

Like most VAWTs, the wind tunnel testing model was not capable of self-starting in some configurations, and so a starting mechanism was required. This consisted of an 250W electrical motor and an electronic clutch (See Figure 3.9). The clutch completely disengaged the motor from the turbine once the required $\omega$ had been reached, therefore the start-up apparatus had no effect on the test measurements. For the PIV tests (detailed in Chapters 4 to 7), the start-up mechanism was employed to hold the VAWT at the required $\omega$ (below cut-in) by modulating the voltage on the motor.
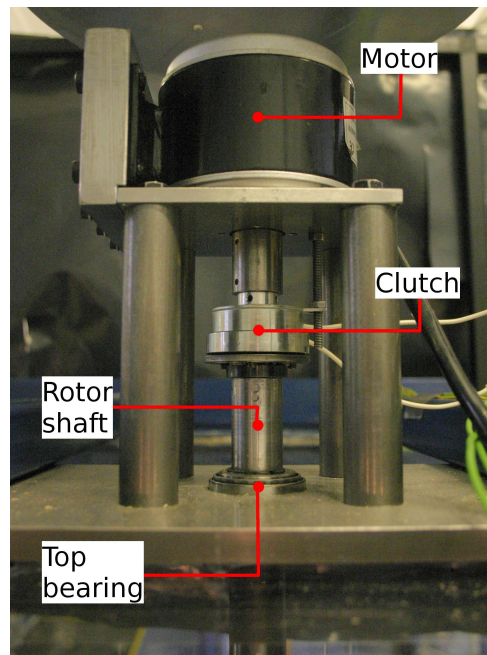
Figure 3.9: Starting mechanism

### 3.3.5 Measurement Apparatus

The two main measurements required for the rotor were those of torque and rotational velocity. In addition, wind velocity and turbulent characteristics were also needed. The assemblies used for these measurements were designed by the Author and are described in the following sub-sections...

**Rotational Velocity**

Rotational velocity measurement was accomplished using an Avago optical encoder (model: AEDA-3300-TAM) which gave 3000 pulses per rotation. The frequency of the pulses was counted using a program (VAWT-RPM.vi) written in the Labview programming language. The encoder output was connected to a standard PC via a National Instruments BNC 2090 connector block into a National Instruments PCI-6220 data acquisition card. For safety, the program was coded to highlight the maximum allowable $\omega$ of the rotor. Measurement variations in the frequency count were mean averaged over a short period of time; 0.1s was found to give both a good frequency measurement and a suitable resolution of the rate of change of $\omega$ for the power coefficient measurement detailed in Section 3.4.

**Torque**

For the experiments detailed in this thesis, torque was not directly measured but was instead inferred from measurements of rotational velocity variation with time, the methodology for

this is detailed in Section 3.4. For some test conditions it was necessary to apply an additional torque to the shaft which opposed that generated by the aerodynamic rotor loads. This additional torque, $T_{app}$, was applied by a Magtrol hysteresis brake (model: HB-140-M2) which had a maximum load capacity of 1Nm. The Magtrol hysteresis brake consists of a pole structure and a drag cup, which interacted magnetically to produce a braking torque. The fixed pole structure is formed by inner and outer parts, between which is a small air gap into which the rotating drag cup was suspended on a shaft by a set of integral bearings. The drag cup and shaft form the rotating member of the brake assembly, to which the VAWT rotor was connected. As current is applied to the coil, a magnetic field proportional to current is established within the air gap. The drag cup is magnetised and resists movement, creating a braking torque between the pole structure and drag cup. The transmitted torque responds to increases and decreases in coil current with corresponding increases and decreases in torque. Though a slight eddy-current effect is present in a hysteresis device, the torque is essentially provided independently of rotational speed. So, changes in $T_{app}$ were independent of changes in $\omega$. Manufacturer data could not be replied upon to give a good enough relation of $T_{app}$ to supplied current; So, the brake was mounted on a spring balance. A Sangamo DC miniature displacement transducer (model: DFG/2.5) measured the displacement of the balance at a radius from the brake, giving a voltage that was linearly proportional to the displacement. The measurement of transducer voltage was integrated into the VAWT-RPM.vi software, so that readings of time, $\omega$ and $T_{app}$ were logged simultaneously.

The brake and torque balance, and the optical encoder were mounted in a rigid frame (See Figure 3.10) which was separate to the VAWT rotor assembly. The measurement assembly was mounted to the wind tunnel structure and a flexible coupling linked it to the rotor assembly.
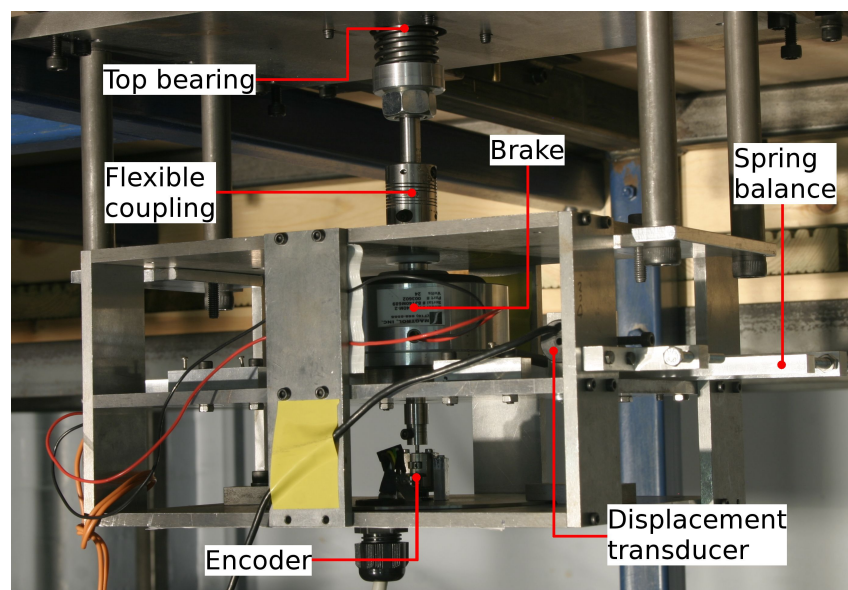


Figure 3.10: Measurement assembly

**Wind Velocity**

A Pitot-static probe was used to set the reference wind tunnel flow velocity for each test. The probe was located along the centre of the section, 0.4m downstream of the start of the working section and two turbine-diameters ahead of the VAWT shaft. The measurement height was 0.4m. This position was kept constant for all of the tests. The Pitot-static probe pressure difference was measured using a Furness Controls Micromanometer (model FC0510) with a stated measurement accuracy of 0.25% of the reading between 10% of lowest range and full scale (200Pa). Temperature and atmospheric pressure measurements were taken at the start of each set of tests to find the dynamic pressure corresponding to the required wind velocity.

A hotwire was traversed across the wind tunnel cross-section at the most upstream VAWT blade position, with the velocity being logged at high frequency to determine the turbulence intensity. The hotwire used was a Dantec 55P11 wire, which was connected to a Dantec 56C00 CTA system. A measurement period of 2 seconds was used for the measurements, this was sufficient as there were no large scale velocity variations observed over longer periods (such as those caused by surging, see Pope [86]). The voltage output from the anemometer was logged at 5kHz with the output low-pass and high-pass filters set to 3kHz and 1Hz respectively. The anemometer low-pass filter choices were limited to 1kHz, 3kHz or 5kHz. 3kHz was chosen as it was closest to matching the Nyquist folding criteria for signal measurement, which states that a signal of a certain frequency should be measured at sample rate at least twice that frequency to avoid aliasing. As only a mean and RMS value of velocity was required from the hotwire the breakdown of frequencies was not necessary for the work, but it was considered good practice to consider the anemometer filtering anyway. With no turbulence grid in-place, the turbulence intensity was measured at 0.4%. Also, across the section, a variation of less than 2% in the mean velocity was measured, this was around the error in the velocity measurement itself, and was not expected to have any notable effect on this fundamental flow physics study.

As the VAWT rotational speed changed, the flow received by the wind tunnel fan was altered as the fan was situated in the wake of the VAWT. As a result, the fan would have received flow of lower velocity and higher turbulence; this had the consequence of altering the set flow speed, causing it to drop by as much as 10%. A hotwire was used in place of the reference Pitot-static tube so that the reference flow velocity could be logged at a high enough rate.

Much like the blockage considerations, the exact determination of wind velocity for accurate $C_p$ measurement was not the main priority for the tests. The testing concentrated on examining fundamental flow physics and comparing one set of tests with another. So, setting a flow velocity consistently between one test and another was more important than accurately setting a certain value of flow velocity. Potential error related to wind speed measurement is discussed in Section 3.5.2.

## 3.4 Power Measurement

Directly measuring the power produced by a VAWT involves measurement of both torque and rotational speed, the product of which is power. As an alternative, the electrical power output from the generator may be measured, but the characteristics of the generator must be known if the actual input power from the VAWT is to be deduced. In any case, it is ideal if both positive and negative torque contributions that arise from the system components (e.g. blades, support structure, bearings...etc) are measured separately so that the influence of the design of each component is not blended into the overall power measurement. This is useful, not only from a design point of view, but also for comparing results in the literature - where one set-up inevitably varies from another.

### 3.4.1 Spin-Down Method

When testing small wind turbine models a number of problems may be encountered that would perhaps not occur in a practically-sized 'real-world' device:

- At a desired $\lambda$ or $Re$, a small VAWT rotates at high speed resulting in large centrifugal forces relative to the turbine size; the apparatus, being required to withstand such loading, may give system resistances which outweigh the positive torque generated by the blades, i.e. the turbine does not 'cut-in'.

- Typically, a VAWT will have a band of $\lambda$ for which net positive performance occurs, i.e. useful torque is produced. Outside of this band, performance will be negative and the turbine must be driven in order to maintain rotation.

- Only parts of the $T$-$\lambda$ curve with negative gradient can be measured without a control system to sense rotational speed and adjust opposing torque accordingly.

A method is therefore required that allows the useful blade torque to be measured so that the blade performance can be evaluated and a comparison can be made between varying cases such as 2D CFD, where only the blades may be analysed, and literature, where the structure to which a blade is mounted may be different. The method explained below provides measurement of both negative and positive blade torque, $T_{blade}$, and, in doing so, it also provides a measurement of the system resistive torque, $T_{res}$, often referred to as 'tare torque' in the literature.

For this work, a new method was devised to generate the $C_p$ curves. The method was based on carrying out two spin-down tests:

1. Without the blades in place, the system resistive torque, $T_{res}$, is determined by a spin-down test.

2. With the blades in place, the test is repeated to determine the total turbine torque, $T_{net}$.

By knowing the mass moment of inertia of the turbine, $I_T$, in each case the aerodynamic blade torque could be deduced via the following method:

For a VAWT spinning down from high $\omega$, the torque balance is defined as in Equation 3.1. Any additional torque applied by the brake, $T_{app}$, is known. $I_T$, is calculated from the mass and geometry of the rig. The angular acceleration, $\xi$, is calculated for two readings of rotational speed, $\omega_1$ and $\omega_2$, and knowing the time between the readings taken at, $t_1$ and $t_2$, the deceleration is easily calculated using Equation 3.2.

$$T_{net} = T_{blade} + T_{res} + T_{app} = I_T \xi \tag{3.1}$$

$$\xi = \frac{\omega_1 - \omega_1}{t_1 - t_2} \tag{3.2}$$

In order to quantify $T_{res}$, a spin-down test was first carried out by spinning the rig without blades up to high rotational speed and logging measurements of time and $\omega$ from which $\xi$ was calculated. $T_{res}$ could then be deduced via Equation 3.3, again the moment of inertia of the rig without blades, $I_{rig}$, is calculated from the mass and geometry of the rig.

$$T_{res} = I_{rig} \xi \tag{3.3}$$

$T_{res}$ varies continuously $\omega$ decreases, however, it must be assumed constant across the measurement interval $t_1$ to $t_2$; as the encoder produced 3000 counts per revolution, the accuracy of this assumption was more than adequate. A series of readings could therefore be taken as the turbine decelerated, mapping out the $T_{res}$ versus $\omega$ curve. With all other variables in Equation 3.1 now being known, $T_{blade}$ can be deduced. The method is extended to positive net torque conditions by simply applying greater braking torque, $T_{app}$, such that the VAWT is prevented from cutting in.

Plots of $\omega$ vs time are shown for the two tests in Figure 3.11. In the second test (Figure 3.11b) the influence of the blades is clearly shown, an additional load has been applied by the hysteresis brake which prevents the VAWT cutting-in. The resulting torque curves are shown in Figure 3.12, the steady load of $T_{app}$ is shown to result in $T_{net}$ being shifted to negative values for the whole test, enabling the spin-down test to be carried out.

So by first determining $T_{res}$ from a spin-down test without the blades attached, $T_{blade}$ is then found from a second test on the complete turbine. However, this assumes that the addition of the blades has no effect on the resistive forces, there are potentially several reasons why this might not be the case:

- The increased weight of the rig might alter the amount of bearing friction.

- The blade-support arm junction will give rise to an additional and unaccounted for source of drag. Conversely, the fact that the ends of the support arms are no longer free may reduce the drag.
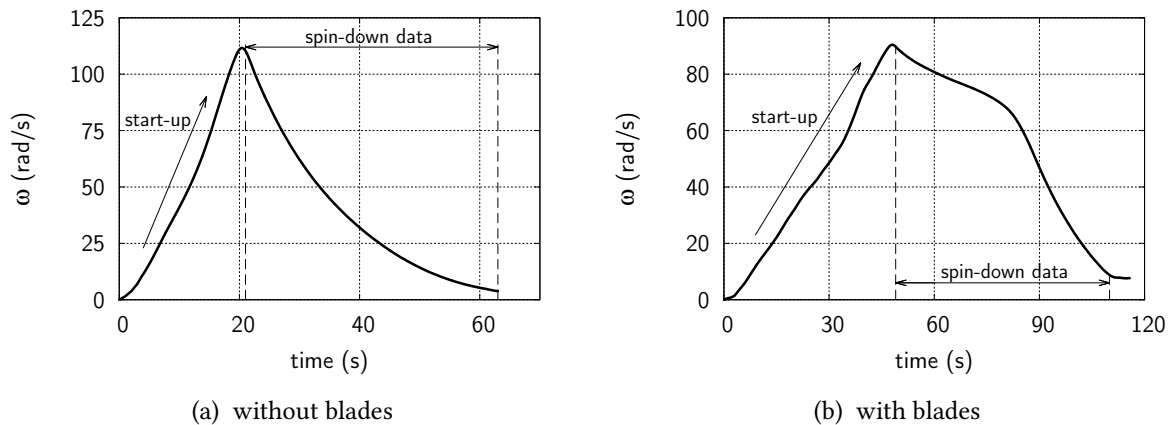
(a) without blades

(b) with blades

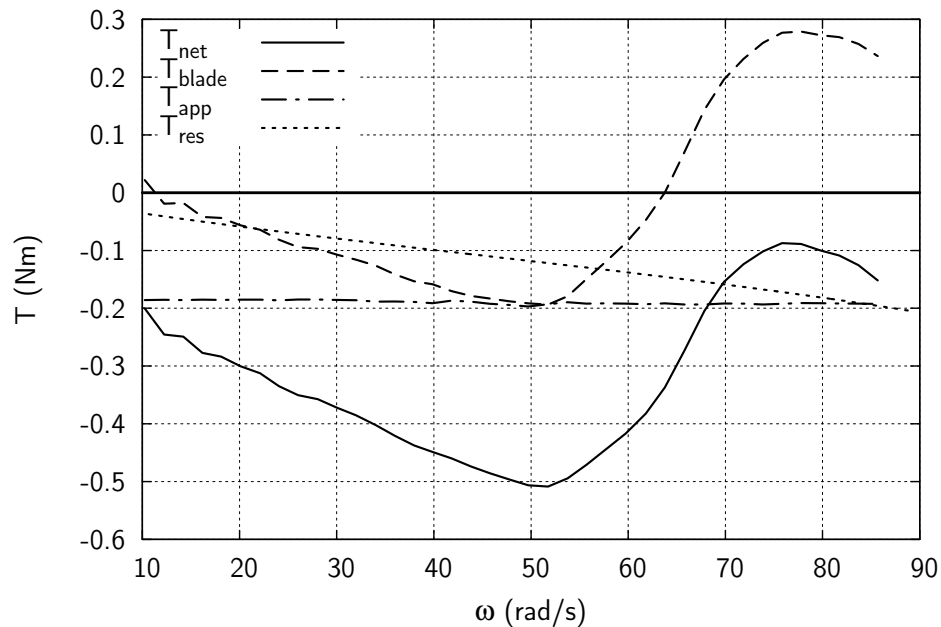Figure 3.11: Example plots showing $\omega$ vs time for the two spin-down tests, $V_\infty = 8\,m/s$.)



Figure 3.12: A plot showing the resulting values for $T_{net}$, $T_{blade}$, $T_{app}$, $T_{res}$ vs $\omega$ as determined from the two spin-down tests at $V_\infty = 8\,m/s$.

- With the blades in place, the flow speed in the rotor volume will be slower; therefore the drag force on the support arms may be lower with the blade attached. The blades also create turbulence in the flow ahead of the support arms which could have a positive or negative impact.

Assessing the influence of each of the above effects is difficult; it is likely though that each of these potential effects has a fairly small influence on the overall value of $T_{res}$, and the subsequent determination of $T_{blade}$. As the value of $T_{blade}$ is determined from the difference

between the two tests, a change in $T_{res}$ could potentially be included within the value determined for $T_{blade}$. A validation study is conducted in the next section which addresses the effect of the increased rotor mass, and the reduced flow speed in the rotor volume. The effects of the blade-support arm junction and increased rotor-volume turbulence were neglected as they were very difficult to address and were unlikely to dominate rotor performance.

In addition to the effects listed above, there is another aspect of the test that needs to be addressed: in normal operation, a VAWT would be expected to hold a steady condition where the operational characteristics of $T$ and $\omega$ are in equilibrium with the fluid domain, including the wake of the blades and the turbine as a whole. The wake at this point will be fully-developed. For test procedure outlined above, the operational characteristics of the turbine are continuously varying (it is decelerating) and therefore the wake will also be varying. For each $T$-$\omega$ reading to be valid, the variation of the conditions need to be such that it can be considered insignificant, i.e. the condition can be considered quasi-steady, the wake at that point in time being effectively fully-developed and the turbine effectively steady. This is also addressed in the following validation section...

### 3.4.2   Spin-Down Method Validation

The most effective way to validate the spin-down torque measurements would have been to instrument the rotor with accurate transducers which would give measurements of blade and total torque. However, this would be a difficult and expensive process and was not considered possible within the time and funding constraints of this study. Instead, a series of validating tests were devised in order to assess the quality of the spin-down measurements. Firstly, the general form of the $C_p$-$\lambda$ curve was briefly reviewed against expectations based on the literature. After this initial method assessment, two validation tests were carried out to assess the method in detail.

**Expected Curve-shape**

Whilst not a validation test, an indication of the spin-down test's performance is given by simply considering the general form of the measured $C_p$ curve. The $C_p$ resulting from the blades only, $C_{p-blade}$ is presented in Figure 3.13. The curve bears a form which is typically characteristic of VAWT performance:

1. Initial low (drag driven) performance at very low $\lambda$.

2. Performance falls away initially with rising $\lambda$ giving a negative trough.

3. With a further rise in $\lambda$, the $C_{p-blade}$ rises up to a peak value.

4. When $\lambda$ reaches very high values $C_{p-blade}$ again begins to fall away.

A fairly low peak $C_{p-blade}$ performance of 0.22 is observed at a $\lambda$ = 3.8, the curve also has quite a narrow peak, and the area of negative performance seems particularly deep. However,
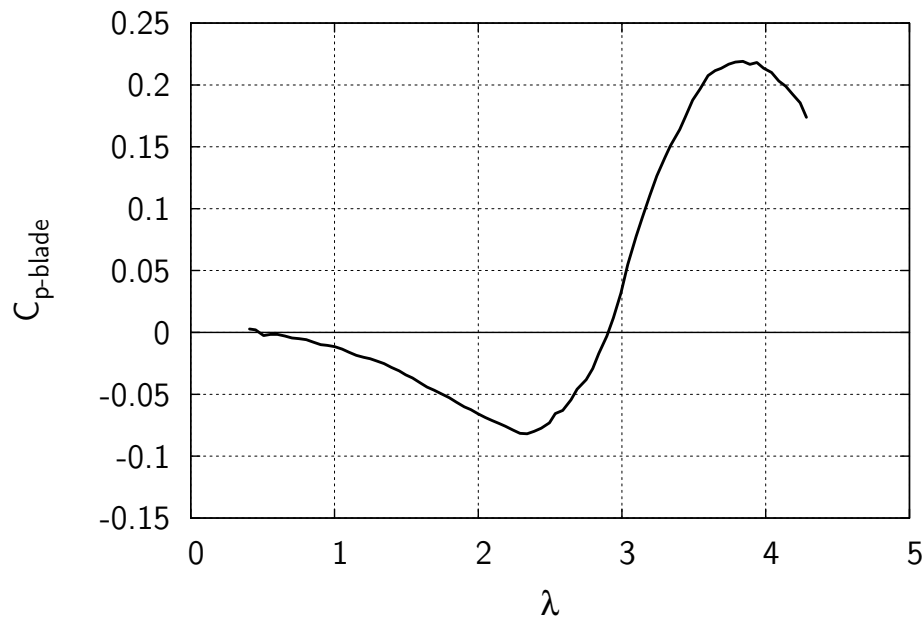
Figure 3.13: Plot of $C_{p-blade}$ vs $\lambda$ for $V_\infty = 8\,m/s$.

analysis presented later in Section 5.3 shows that the low performance, narrow peak and deep negative trough are due to a low-Reynolds number performance and are not a product of the spin-down test. The general shape of the curve is in-line with what is expected, and serves as an early indication that the method is adequate and appropriate. The results of later tests also show that the method is capable of capturing resulting performance changes due to fixing angle adjustment (Chapter 7) and free-stream turbulence (Chapter 6).

**Expected Cut-out**

The separate spin-down tests gave measurements of blade and resistive torques, and so it was possible to determine the rotational speed at which 'cut-out' should occur. At rotational speeds above cut-out, the positive blade torque starts to exceed the negative resistive torque, resulting in a positive net torque which accelerates the rotor if unopposed.

The rotational speed at which cut-out occurred was assessed in the following way:

1. The VAWT rotor was spun to a high rotational speed (above cut-out) using the start-up mechanism.

2. The clutch then disengaged the motor and the VAWT was left to settle to a steady $\omega$, where rotor torque and resistive forces were in-balance.

3. A braking load was then applied to reduce $\omega$.

4. After a short time the braking load was released, and the VAWT was observed to speed back-up towards the previously attained steady-value of $\omega$.

5. This braking processing was repeated, each time slowing the VAWT to lower $\omega$ until finally the value of $\omega$ at which cut-out occurred was determined.

For $V_\infty = 8\,m/s$, the steps detailed above were performed to find the value of $\omega$ at which cut-out occurred was determined. Figure 3.14 shows a plot of $\omega$ vs time for one test. As slowing the rotor to precise values of $\omega$ was not possible, the test was repeated five times to obtained a cut-in value accurate to within $\pm 0.5$rad/s. A value of $\omega_{cut-out} = 68$ rad/s was determined.
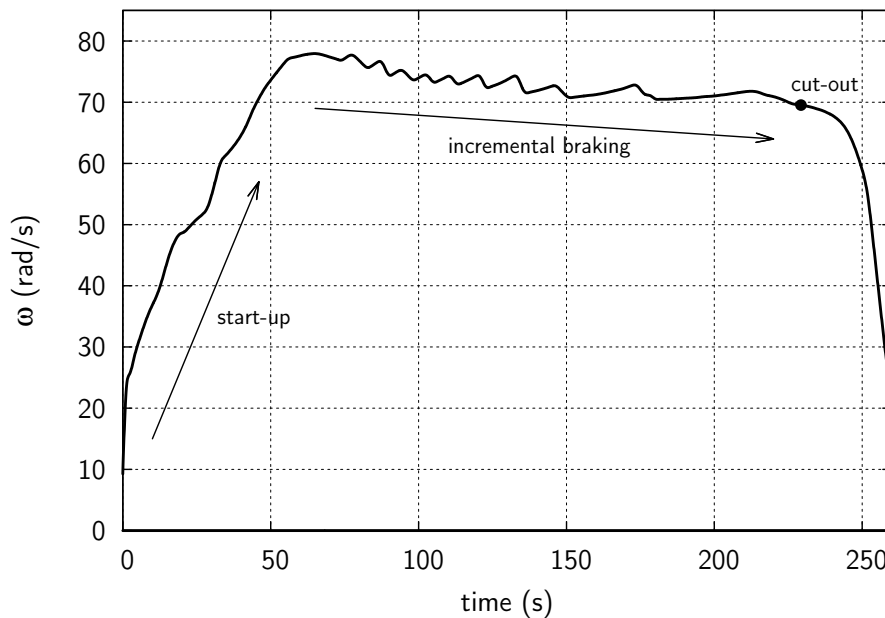


Figure 3.14: Plot of rotational speed versus time showing the stages of the cut-out test.

From separate spin-down tests, the blade and resistive torques were measured, a plot of $T_{res}$ and $-T_{blade}$ vs $\omega$ (Figure 3.15) shows that the cut-out point, at which the blade and resistive torques are equal and opposite, is 68.3 rad/s. This compares very well with the value of $\omega$ at which cut-out was actually observed to occur in the incremental-braking test, and indicates that the spin-down process and the subsequent data processing is giving an acceptable measurement of the blade and resistive torques.

**Change in Rotor Mass**

The method used to determine the blade torque assumes that the addition of the blades has no effect on the resistive forces between the two spin-down tests. As discussed above, there are several reasons why this might not be the case. In particular, the addition of the
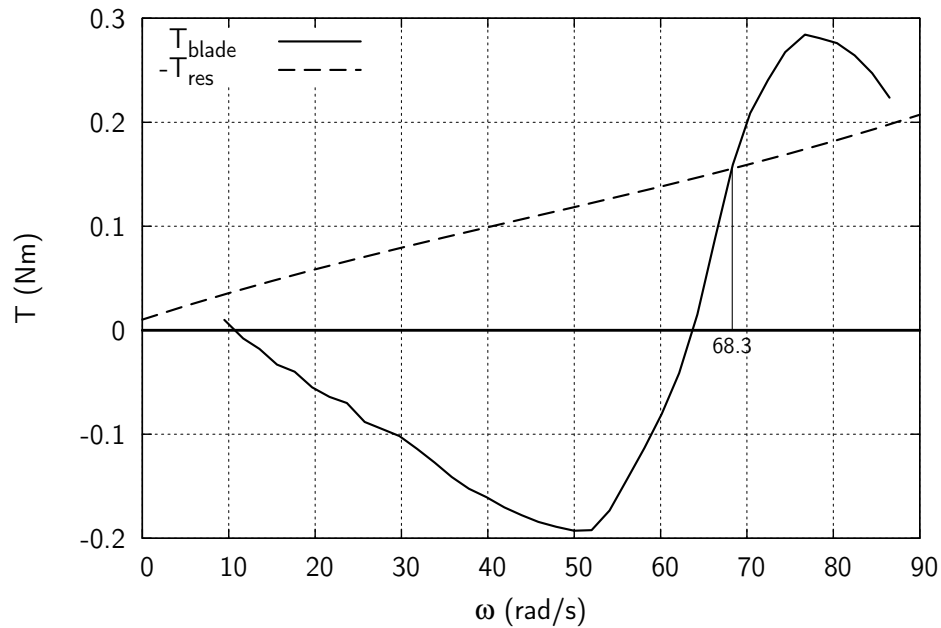
Figure 3.15: Plot of blade and resistive torques versus rotational speed for $V_\infty = 8\,m/s$.

blades increases the mass of the rotor, with an increase in bearing friction being a possible consequence. The effect of an increased rotor mass was simulated using the pre-tensioning spring in the lower bearing assembly (see Figure 3.7b). The compression of the spring placed an additional load along the shaft, equivalent to the addition of mass to the rig. The effect of this on the determined value of $T_{res}$ is shown in Figure 3.16. A negligible difference measured in $T_{res}$ with and without this load, which shows the added mass of the blades is not significant in terms of the overall system resistances.

**Reduced Flow Velocity**

With blades in place, the flow velocity in the rotor volume will be somewhat slower when compared to the first spin-down test. As a result, the drag force on the support arms may be lower with the blade attached, which would in turn lower the resistive torque of the rig. The spin-down test for $T_{res}$ was repeated at wind velocities of 5, 6, 7 and 8m/s. Very small differences were measured in $T_{res}$ as the flow velocity was reduced (Figure 3.17), showing that the resistive torque on the rig is dominated by $\omega$ and the bearing resistance.

**Spin-Down Rate**

As previously discussed, the torque measurements taken using the spin-down method were only valid if the condition could be considered quasi-steady. This was assessed by repeating a test several times using different values of $T_{app}$ to alter the rate of deceleration. In each case
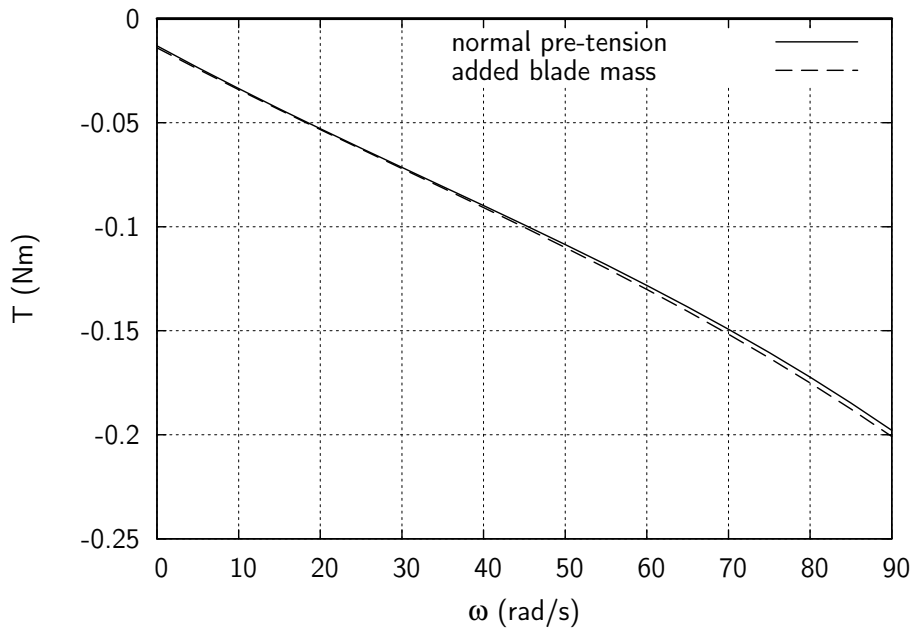
Figure 3.16: Plot of resistive torque versus rotational speed for $V_\infty = 8m/s$ showing the result of an additional load along the shaft (equivalent to added blade mass).
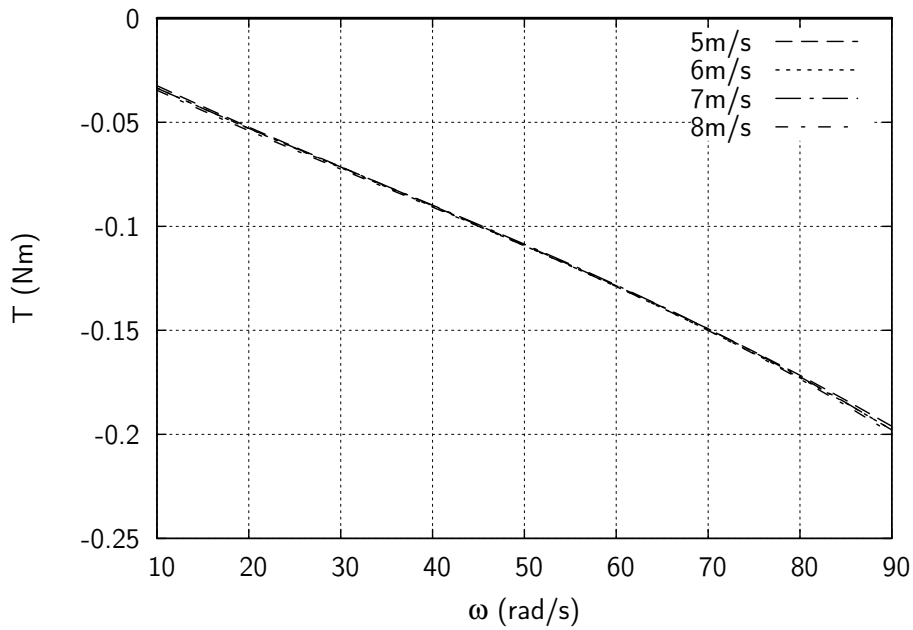


Figure 3.17: Plot of resistive torque versus rotational speed for varying $V_\infty$.

the value of $T_{app}$ is known and the value of $T_{res}$ is assumed not to be effected by spin-down rate. The results of the test show that only small differences are measured in blade torque for a range of spin-down rates (Figure 3.18). The observed differences arise when the rotor spins down at the highest rates which are 4 and 5 times the original rate.

The original spin-down rate required a test lasting only a couple of minutes. The small differences in the results indicate that it would have been possible to use a faster rate; however, the shortened times actually made the test and data logging procedure difficult to execute, and so the original spin-down rate was reverted to for the remainder of the testing.
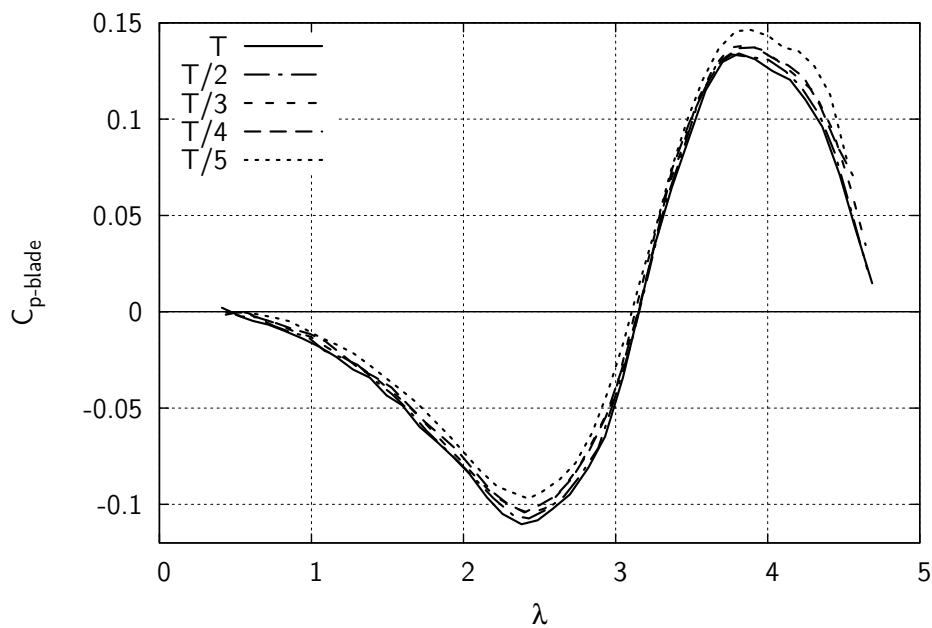


Figure 3.18: Plot of $C_{p-blade}$ vs rotational speed for varying rates of spin-down at $V_\infty = 7\,m/s$. T is the original time taken for $\omega$ to drop from 800 to 100 RPM.

## 3.5 Errors and Uncertainties

A number of measurements were made during the experimental campaign using a variety of apparatus and equipment, the expected influence of errors and uncertainties is discussed in the following sections.

### 3.5.1 Accuracy of Geometry

**Blade Profile**

The blades were manufactured in the Mechanical Engineering workshop. After manufacturing. a laser scan was made of the blades by the Author to assess the accuracy of the profile;

using a Matlab script (also written by the Author) the actual profile surface coordinates were found to deviate by less than 0.05mm from those of the prescribed 8.8mm thick aerofoil, which was not thought to be a concern.

**Blade Position**

As the blades had a short chord length (40mm), setting an accurate fixing angle was challenging; as a result, particular care was taken in designing and manufacturing the mechanism for setting the fixing angle. The fixing inserts were manufactured in the Mechanical Engineering workshop, a maximum machining error was estimated at $\pm$ 0.05mm which lead to a potential $\pm$ 0.2° error in fixing angle. Results shown in the Literature Review (see Section 2.3.1) have shown that a small change of fixing angle of only a degree can bring about a notable change in performance, so potentially an error of $\pm$ 0.2° is significant and was taken into account when reviewing the results of Chapter 7. Another effect on the position of the blade relates to the position of the support arm at the hub, the support arms were connected to hubs which had fixing slots to locate the end of the support arm (see Figure 3.6). With the same machining error the effect on blade position was negligible relative to the error in the fixing angle inserts.

**Bearings**

Earlier attempts to mount the bearings in split-circle clamps seemed to be affected by the exact position in the clamp and the clamping force used, which gave slightly varying bearing resistances. The lightly push-fitted bearings and the spring and nut pretension system was found to be more reliable: between one installation and another no differences in resistance could be observed in the measurements, showing any changes to bearing resistance were negligible.

### 3.5.2   Measurement Accuracy

**Torque**

The balance was calibrated giving a maximum error $\pm$0.01Nm (see Appendix A.2.2), which largely originated from the bearings supporting the brake in the measurement assembly. $\pm$0.01Nm corresponds to a maximum error of $\pm$5% in the maximum $C_p$ value determined for tests at $V_\infty = 7\,m/s$, this was the lowest wind speed for which the brake was used and therefore represented the most error-prone case.

**Wind Speed**

A Pitot-static probe was used to set the reference wind tunnel flow velocity for each test. The probe was located along the centre of the section, 0.4m downstream of the start of the working section and two turbine-diameters ahead of the VAWT shaft. The measurement height was

0.4m. This position was kept constant for all of the tests. The Pitot-static probe pressure difference was measured using a Furness Controls Micromanometer (model FC0510) with a stated measurement accuracy of 0.25% of the reading between 10% of lowest range and full scale (200Pa). With the accuracy of the Pitot-static tube at an estimated 1%, the total accuracy of the wind speed measurement was an estimated 1.25%.

### Rotational Speed

Rotational velocity measurement was accomplished using a 3000 pulse-per-rotation optical encoder. The pulses were counted using a program (VAWT-RPM.vi) written in the Labview programming language, the frequency count was mean averaged over a short period of time (0.1s). So at a typical rotational speed of 500-900RPM, 2500-4500 pulses were counted for every 0.1s measurement interval. With such a high resolution of the frequency pulse measurement, error in the determination of rotational speed was negligible.

### Atmospheric Conditions

A measurement of air density was required to calculate the power available to the rotor which was required to obtain a $C_p$ value. The air density was calculated using the ideal gas law (Equation 3.4) and measurements of pressure and temperature in the lab. The temperature measurement was accomplished using an Atech RE54J digital thermometer which was accurate to $\pm 0.1°C$. At the start of each lab session an atmospheric pressure measurement was taken using a Griffin BHL-300-T mercurial manometer, with an accuracy of $\pm 100Pa$. The maximum error in the density is therefore approximately $\pm 0.0016 kg/m^3$ ($\pm 0.13\%$).

$$\rho = \frac{P}{RT} \qquad (3.4)$$

Where R is the specific gas constant for dry air = 287.058 J/(kgK)

### Calculation of Power Coefficient

For the calculation of $C_p$, the rotor area, rotational speed and power, the air density and the power in the wind must all be known (see Chapter 1), the error in each of these quantities combine to give the potential error in $C_p$. Any variation in the measurement of flow velocity is particularly significant as $P_\infty$ varies with $V_\infty{}^3$.

The power in the wind, $P_\infty$ is given by:

$$P_\infty = \frac{1}{2}\rho A V_\infty^3 \qquad (3.5)$$

Taking the potential measurement errors for wind velocity and density into account this yields a maximum potential error of $\pm 2.1\%$ for the available power in the wind (calculated for a typical test at 7m/s).

The power of the rotor is the product of the measured torque and the rotational speed, neglecting any error in rotational speed measurement results in a maximum potential error of ±5%. The combined potential maximum error in the $C_p$ measurement is therefore ±7.25%. Using the experience gained from running many tests during the course of the experimental campaign The Author suggests this value is a fairly good approximation, but is perhaps a little on the high side: A set of datum tests, repeating the velocity setting process taken on different days (varying atmospheric conditions) was found to compare well. In summary, the variability of the VAWT performance measurement was considered to be adequate for this fundamental flow physics investigation.

# Chapter 4

# Methods: PIV Visualisation and CFD

## 4.1   Introduction

In this study, experimental PIV measurements and CFD simualtions are used as tools to investigate the performance-related flow physics, with the main aim being that of linking the observed flow characteristics to the performance measurements. The main purpose of this chapter is to detail the apparatus and methods which are developed and used.

In Section 4.2, the PIV methodologies are discussed with reference to the necessary equipment. The data processing techniques and the verification of the required settings are also presented.

In Section 4.3, the CFD model is discussed, this includes: details of the model domain and mesh settings, and validation of settings used for the turbulence model and convergence monitoring. In addition, an entirely new methodology is presented which allows the determination of a local corrected angle of attack variation with azimuth from a CFD solution.

## 4.2   Particle Image Velocimetry

### 4.2.1   Introduction

One way to examine the flow physics of the VAWT is to visualise the fluid flow around the blade by some means. This has been attempted by several authors in the past, as is discussed in the Literature review in Chapter 2 (with specific experimental details given in Section 4.2.2). In this study, PIV was utilised for this purpose, a discussion of the apparatus and methods employed is discussed in the following sections.

The general principle of PIV is simple: the fluid is seeded with particles which are assumed to faithfully follow the flow dynamics, a light sheet illuminates a plane of particles and two

images are captured a short time apart. The motion of the seeding particles between the first and second images is then used to calculate the velocity field of the flow.

For this study, PIV was used to visualise the flow in the near-blade region. Flowfield images were obtained throughout a full rotation, which, as far as the Author is aware, has not been attempted by any other published studies. In this Section, the apparatus and methods used are presented, and the required settings are verified. A brief summary of the related literature and the fundamentals of PIV are also presented.

### 4.2.2 Literature

Fujisawa and Shibuya [61] conducted what appears to be the first study of the VAWT flow physics using PIV, they also obtained visualisations by dye-injection, the results from both techniques have been previously discussed in Section 2. In their water tunnel experiments, Fujisawa and Shiubya used plastic micro-spheres of $40\mu$m diameter as tracer particles. The single blade rotor had dimensions of $B$=135mm, $R$=30mm, $c$=10mm, $V_{\infty}$=50mm/s, and so $\omega$ varied from 7 to 14RPM between $\lambda$=1 to 4 resulting in a maximum $Re$=1500. The light sheet was produced by two stroboscopes and was 5mm thick, with each flash lasting for $20\mu$s. The field of view (FOV) was 22mmx22mm and was resolved using a 512x512 pixel CCD camera giving 23.3 pixels/mm. 30x30 pixel interrogation windows were used. The time interval was 2 or 3ms between pulses, corresponding to a 3.5 or 5.2 pixel displacement based on the freestream velocity. The rotor was supported at only one end, with the camera positioned looking along the free end of the blade, this would probably not be practical on larger rotors, or when rotating a rig at higher speeds. Interestingly, images from the blade point of reference were captured by rotating the camera at the same rotational speed as the blade. The number of images gathered per position is not given. The results obtained matched well with the comparison streaklines obtained using dye-injection.

Ferreria et al. [7] [64] also conducted PIV analysis on a larger scale VAWT in a wind tunnel. Particles of $1\mu$m diameter generated by a fog machine were used as tracer particles. The single blade rotor dimensions were $L$=1.0m, $R$=0.2m, $c$=50mm, $V_{infty}$=3.7 to 10.5m/s, $\omega$ was set to either 75 of 105rad/s resulting in a $Re$ range from 25,000 to 52,000 between $\lambda$=2 to 4. The light sheet was produced by a laser with 200mJ/pulse and was 2mm thick. The FOV was 120mmx100mm and was resolved using a 1,374x1,040 pixel CCD camera giving 11 pixels/mm. 32x32 pixel interrogation windows were used. The time interval was set such that particles would give a 8 pixel displacement assuming the a particle speed of $U = 4V_{\infty}$. Approximately between 30 and 100 samples are acquired per azimuthal position, which was said to give an average sufficient to allow analysis of the flow which focuses on the strength and distribution of vortical structures, instead of individual point velocities.

### 4.2.3 PIV Fundamentals

**Correlation**

For common PIV measurements, greyscale image pairs are obtained and spilt into interrogation areas. Cross-correlation is then used to obtain the velocity vector for each interrogation area by correlating pixel intensity with particle distances (Equation 4.1). The most likely particle movement can then be found as that which has the highest cross-correlation function, $R$. The process is illustrated below in a simple 1D example (See Figure 4.1). In this example, pixels have a binary intensity value, I=1 for seed, I=0 for background. This also shows that small numbers of particles (in this case, one) passing through the sheet can easily generate significant noise.

$$R(\delta x) = \sum I_1(x)I_2(x + \delta x) \tag{4.1}$$

A displacement vector, obtained from an initial correlation using larger interrogation windows, may be used to shift the interrogation area on the second image. The aim of this being to follow the approximate path of the particles and help maintain consistent particles between the respective interrogation areas of image one and two. The process may be repeated a number of times until the difference between passes is considered small enough. This is known as Adaptive Multi-pass Correlation.
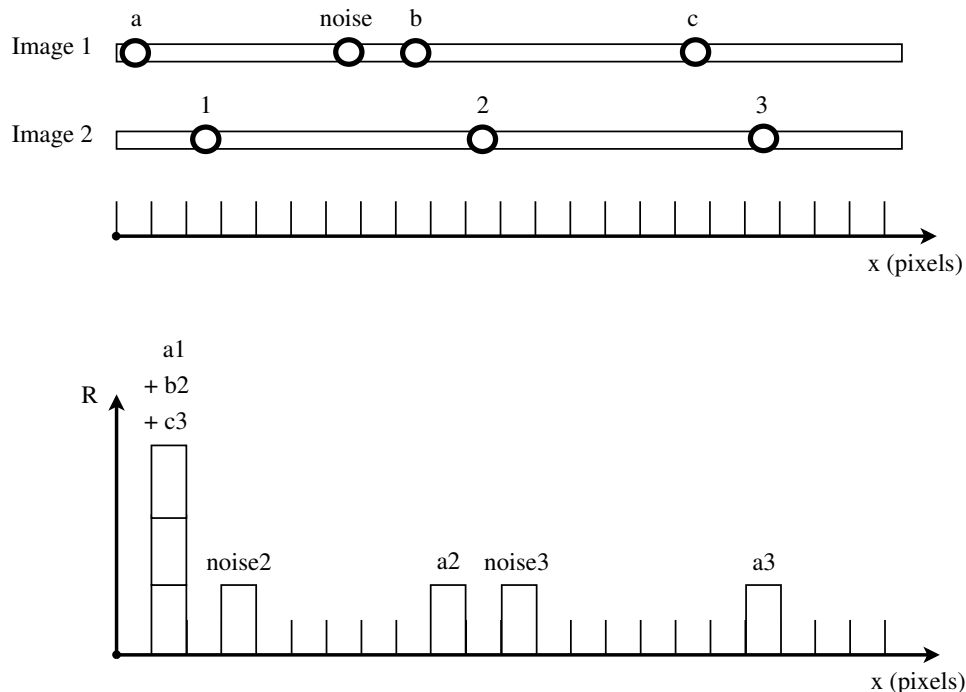


Figure 4.1: 1D example illustrating the cross-correlation process [? ].

**Timing**

The laser pulse duration may be much shorter than the image exposure time, this permits variable pulse timing between images (see Figure 4.2). The choice of an appropriate time between pulses is a compromise between getting particle distances short enough so that individual particle pairs can be identified but long enough to get an accurate enough velocity measurement. Two lasers are usually used to allow very small times between pulses $\sim O(10^{-6})$s).
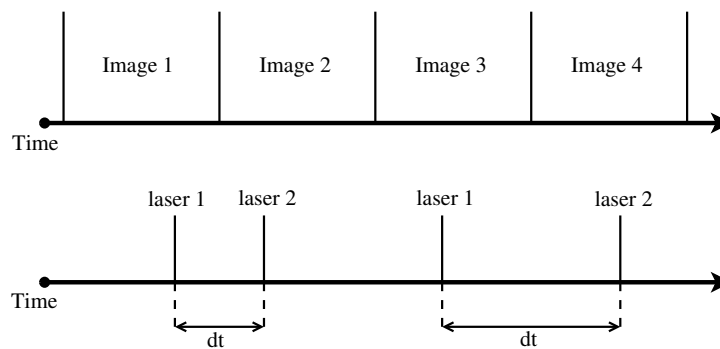


Figure 4.2: Diagram showing the possible variance of timing of laser pulses with image exposure.

**Sub-pixel accuracy**

The intensity of the particle images can be approximated closely by a Gaussian distribution. If a partial image spreads across 2-3 pixels, a Gaussian curve can be fitted to $R$ and the mean position of the correlation peak can be measured to sub-pixel accuracy. Particle displacement measurements accurate to $0.05 - 0.1$ pixels are achievable.

**Laser Sheet**

A laser is an ideal light source, having an ability to produce a high-power light beam with a short pulse duration. The sheet thickness varies, converging upon a focal length before diverging. This may have an impact on the accuracy across images, and when the imaged region is moved to another part of the rotor the sheet thickness focal length may need adjusting. Reduced thickness increases the likelihood of particles, with some z-component of velocity, appearing in one image but not the other. Increased thickness may give particle densities that are too high, risk particle overlap in the correlation, or lead to the intensity of the reflected light being too low to get good contrast in the acquired images.

**Spatial Resolution**

The spatial resolution is limited by the size of the interrogation area. If the interrogation area is too small then there will be too few particle pairs and a correlated displacement will not be found. The seeding density therefore also influences the minimum size of interrogation area. The requirement to have particles across two or three pixels limits the total image size, for a given particle size.

## 4.2.4 Apparatus

A Dantec Dynamics integrated 2D PIV system was used for the tests. The system was based around a Litron Nano-S-65 Nd:YAG laser which emitted light at a wavelength of 520nm (green) with a maximum energy of 65mJ per pulse. A Dantec Dynamics FlowSense 4M CCD camera with a resolution of 2048x2048 pixels was used to capture the images via a Nikon AF Micro-Nikkor 60mm f/2.8D lens. Dantec DynamicStudio v3.14 software was used to manage the PIV system via a National Instruments PCI-E 1427 DAQ Card and a Dantec Dynamics timer box which was controlled by a National Instruments PCI 6602 timer board.

**Seeding: Stokes Number**

The Stokes number, $S_t$, is a measure of flow tracer ability to track the flow. If $S_t \ll 0.1$, the particles should follow fluid streamlines closely giving tracing accuracy errors of below 1% [87]. A TSI 9306A Six-Jet Atomiser provided olive oil droplets as the tracer particle. The resulting spherical particles were approximately $2\mu$m in diameter. For the oil particles in air, the $S_t$ was calculated via Equation 4.2:

$$S_t = \frac{t_p}{t_f} \tag{4.2}$$

where $t_p$ and $t_f$ are the characteristic times of the seeding particles and flow respectively...

$$t_p = \frac{\rho_p d_p^2}{18\mu_f} = 1.1 \times 10^{-5} \tag{4.3}$$

High velocities were contained within the shed vortices, and correct particle tracing in this region was needed in order to correctly capture the stalling behaviour. The highest vorticity recorded in the PIV measurements was around $4000s^{-1}$, which was used to give a characteristic time of $t_f = 5 \times 10^{-4}$s. This led to $S_t \approx 0.02$, which shows that the oil droplets can correctly be assumed to faithfully follow the fluid dynamics for the experiments conducted for this study.

**Seeding: Density and Distribution**

A suitable number of particles per interrogation window are required in order to obtain a good correlation, and so an even seeding density is required across the field of view to ensure each window has approximately the same number of particles within it. It was found to be

difficult to achieve this by introducing particles upstream of the test position. The wind tunnel laboratory was relatively small, the total volume of the room was $\approx 700\,m^3$; and so, at a wind speed of 7m/s one lab's worth of air passed through the tunnel in just over 1 minute. So, it was found to be easy enough to seed the entire room, which gave an effectively perfect seeding distribution. Even in a larger room, the prospect of seeding the whole room is unlikely to be a problem, as only a tiny amount of olive oil is actually used: it is roughly estimated that less than 100ml was used for more than 60 hours of testing time.

At the start of a test the room was seeded for 8 minutes. The seeding was then topped-up with an additional 1 minute of seeding for every 30 minutes of testing in order to maintain an approximately constant amount of seeding across the whole of a test. Before the full range of tests were carried out, a test of the effect of seeding density on the correlation was carried out, the results of which are discussed in Section 4.2.5.

**Laser**

The laser was mounted on an adjustable-height wheeled platform (see Figure 4.3) which was positioned outside the wind tunnel. A cylindrical lens turned the laser beam into a sheet which passed through the polycarbonate side window of the wind tunnel. The laser sheet plane was aligned with the main flow direction and was perpendicular to the blade(see Figure 4.4). The correct sheet position for each $\psi$ was achieved by wheeling the platform into an appropriate position. Pre-marked positions on the floor made this a quick process. A spirit level on top of the laser and height-adjustable feet on the platform ensured the laser sheet was kept level as the platform was moved over the slightly uneven laboratory floor. The effect of the laser sheet thickness on the quality of the results was evaluated before the full range of tests was carried out (see Section 4.2.5, which allowed the ideal thickness to be maintained throughout testing.

**Camera**

A rig was designed by the Author for the camera which was mounted on top of the wind tunnel (see Figure 4.5) giving a view along the blade length, perpendicular to the laser sheet. The camera was mounted on a rotating arm at such a radius that the blade was in the centre of the image, this minimised potentially damaging laser reflections entering the lens. The camera arm was mounted on a shaft, which was in-line with the VAWT shaft, and so the camera could be set to a known position via a simple angular measurement. Thus, images at different $\psi$ could be gathered quickly and easily. In addition, the focus, blade position, and FOV size would be consistent between images, which made the processing of the PIV images more manageable by a scripted process. The camera angle setting was estimated to be set within a maximum error of $\pm 0.2$deg.

As the laser sheet and camera were maintained at consistent heights between different azimuthal positions, no re-focusing of the camera was needed. The focus was set so that the particles were slightly blurred over at least 2-3 pixels to allow particle displacements to be
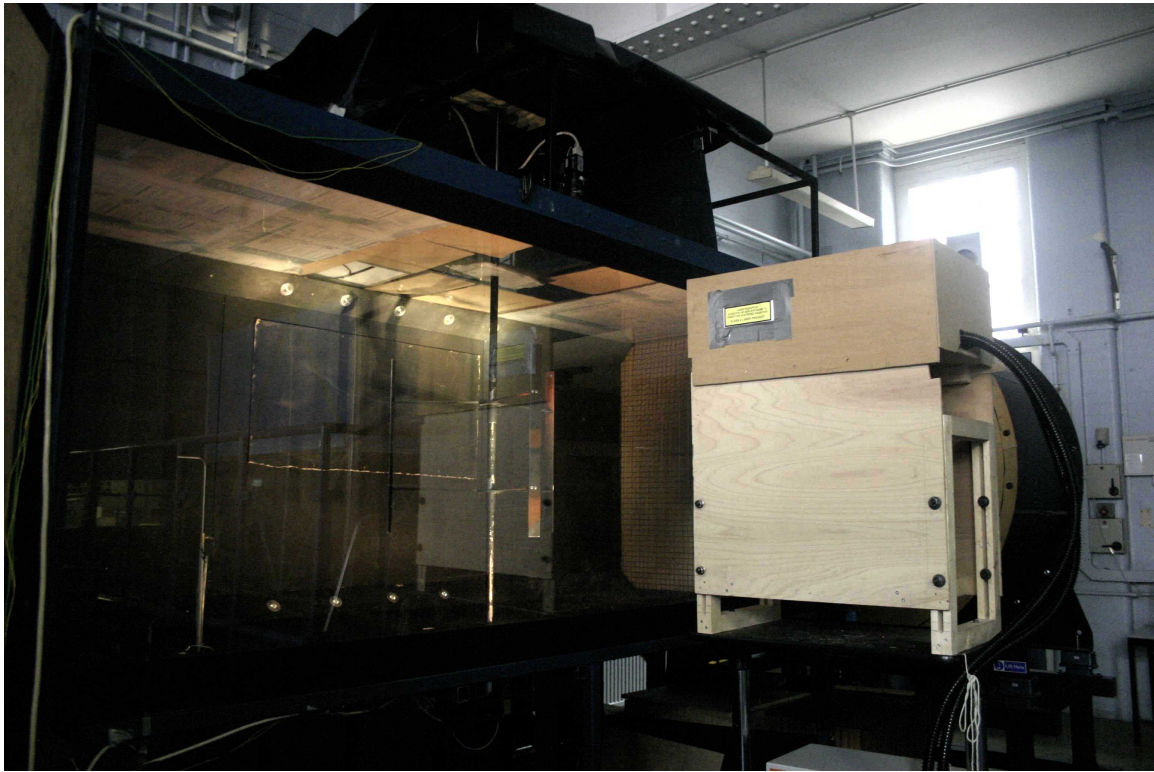
Figure 4.3: Photograph showing laser platform next to wind tunnel working section.

determined to a sub-pixel level of accuracy.

### Triggering

The laser and image acquisition needed to be synchronised to the position of one of the VAWT blades in order to capture images at the required position. The encoder used for the rotational velocity measurement had an additional channel which produced a once-per-rev pulse which was used to trigger the image acquisition. The encoder shaft was fixed to the rotor shaft so that the location of the index slot was aligned with one of the blades. The body of the encoder (holding the reader) was mounted on a rotating disc, so that the azimuth angle at which the reader encountered the index pulse could be altered (see Figure 4.6). Markings on the disc enabled the angle to be set to within an accuracy of ±0.1deg. The encoder pulse was estimated to vary by at most ±0.1deg, which resulted in a maximum error of ±0.2deg in the value of $\psi$ at which an image pair was acquired.

### Reflections

Reflection of the laser light from the blade surface can result in measurement errors caused by poor particle-background contrast and the illumination of particles which are not in the plane of measurement. Strong reflections could also cause irreversible damage to the camera's CCD
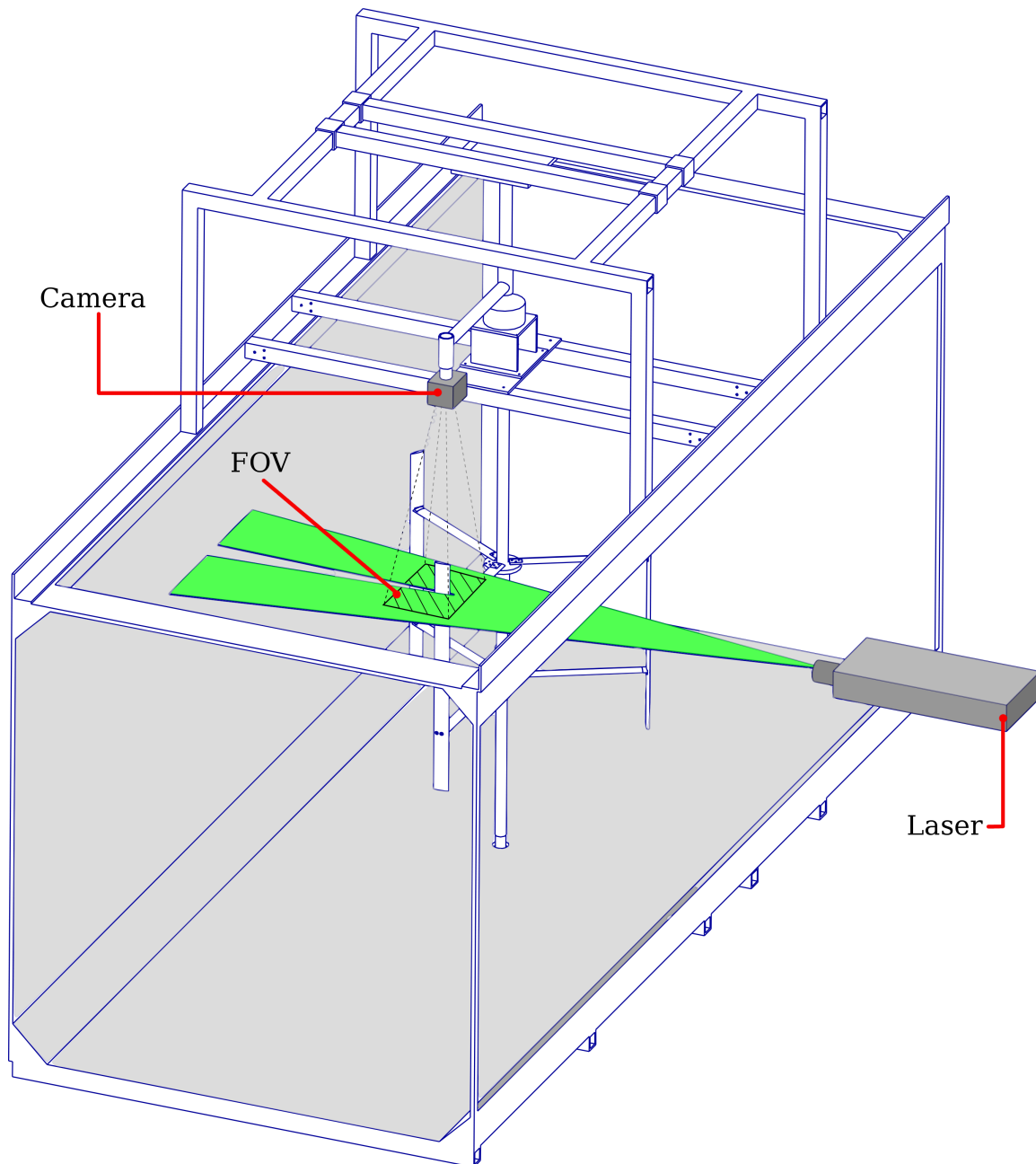
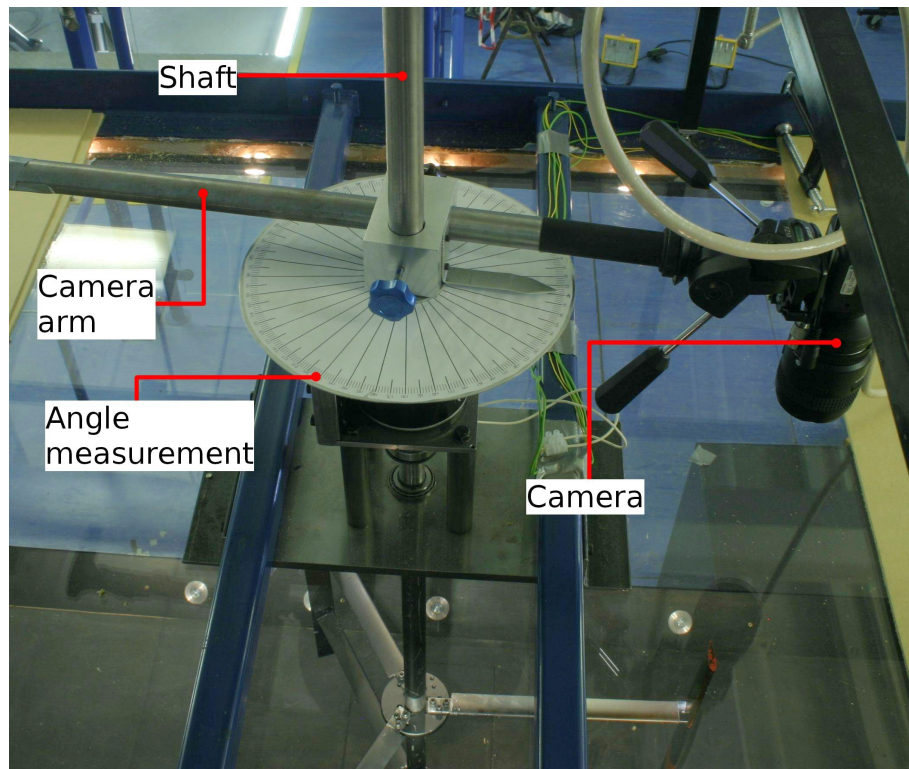Figure 4.4: Diagram showing laser sheet, camera and rotor arrangement.

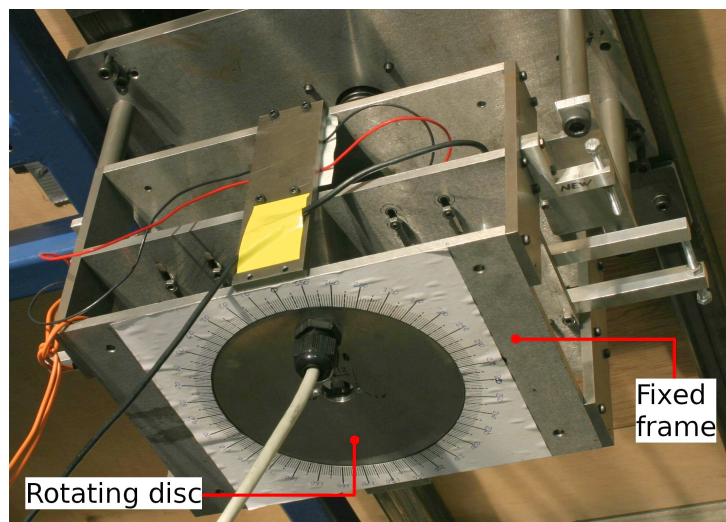Figure 4.5: Photograph showing camera rig above wind tunnel working section.



Figure 4.6: Photograph showing rotating disc to which encoder body was mounted to enable angle adjustment for triggering.

sensor. The requirement for measurements near to the blade surface region meant that it was not possible to avoid hitting the blade with the laser sheet.

To reduce the visible reflections, the blade surface and support arm were treated with an anti-reflection paint made from Rhodamine 6G dye mixed with a clear varnish (approx. 250mg Rhodamine 6G per 25ml of varnish). Green light is absorbed by Rhodamine 6G, and the resulting emission is slightly shifted to a longer wavelength. By fitting a narrow-band green-pass filter to the camera lens, much of the unwanted reflections were cut out, at the small expense of a slight dimming of the useful green light which was reflected from the seed particles. Three thin coats of the anti-reflection paint were applied to the surfaces, and the aerodynamic effect on the profile was deemed to be negligible. Figure 4.7a shows that the amount of light reflected from the blade surface onto the support arm was significant for the untreated surfaces: very poor particle-background contrast was shown which would give error-prone measurements in this region, this was not acceptable as it would have made the upwind stalling process hard to inspect. With paint applied only to the blade surface, Figure 4.7b already shows a much improved particle-background contrast. Once the support arm was also coated, the amount of undesirable reflections in the image was much reduced and the best possible contrast was obtained, as shown in Figure 4.7c



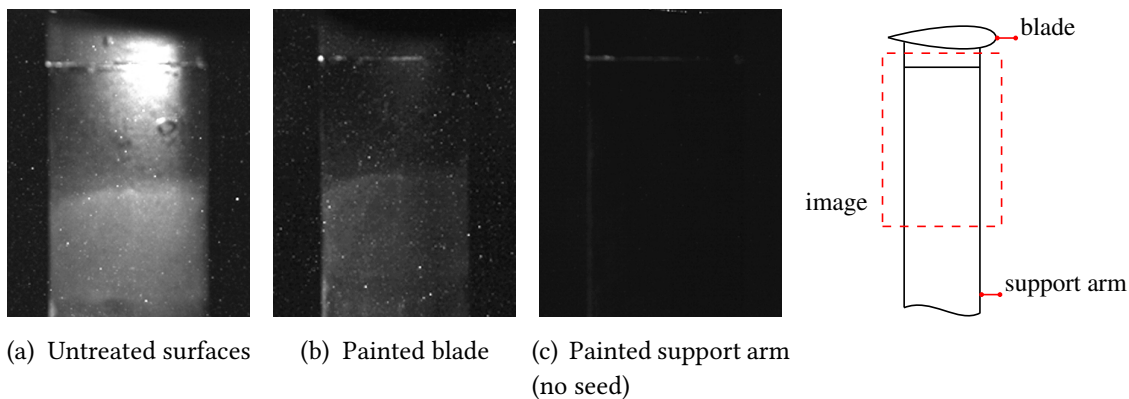(a) Untreated surfaces      (b) Painted blade      (c) Painted support arm (no seed)

Figure 4.7: Photographs showing the reduction of undesirable reflections using Rhodamine 6G paint and a narrow-band green-pass filter.

### Data Processing

The overall aim of the PIV measurement campaign was to capture main flow features, precise point-by-point velocities were not required. The quality of the image to flowfield-data processing was a compromise between producing the best possible flowfields and using the shortest processing times. To map out a whole rotation at three different tip speed ratios, 28 azimuth angles were inspected, with 100 images acquired for each condition in order to obtain a reasonable ensemble average. Therefore, the mapping of one rotor condition required the processing of 8400 image-pairs, which took a total of around 7 hours using the chosen data

processing sequence on a standard dual-core PC.

An adaptive correlation process with one iteration step was used with a 32x32 pixel interrogation area, which corresponded to a 2.2x2.2mm physical area in the field of view. The interrogation areas overlapped by 25% which resulted in the 140mmx140mm field of view being mapped out by a grid of 85x85 vectors (24 vectors to a blade chord length). Deforming windows were enabled in the software to help prevent particles appearing in one of the image-pair but not the other. Spurious vectors were removed within the iteration step using a moving average validation to identify vectors with a magnitude differing by more than 20% from the average of the neighbouring vectors over a 3x3 vector window.

With the camera positioned with a view along the blade length, the flow very close to the blade surface was obscured by the blade tip itself. In addition, the blade and laser sheet interaction resulted in a shadow region on one side of the blade. Both of these regions were masked out in the software such that interrogation windows with areas more than 50% covered by the mask were excluded from the data set. These aspects are discussed in more detail in Section 4.2.6. The blade position and invalid region are marked in an example image shown in Figure 4.8. Throughout this study, plots are used to identify key flow behaviour and dominant features. A non-standard range of contour intervals has been used which contains extra intervals at low levels, enabling the low vorticity of the previous blade's wake to be shown alongside strong vortices shed by the blade on which the view is centred. The scale, which is shown in Figure 4.8, is used throughout the study, it shows vorticity, $\Phi$, ranging from -4000 to 4000 /s, split into intervals of $\pm$ 0|25|50|100|200|400|600|800|1000|1500|2000|2500|3000|3500|4000 /s.

The vector map resulting from the PIV analysis is a discrete regular grid, velocity gradients are estimated by comparing neighbouring vectors to one another. In the Dantec DynamicStudio v3.14 software, whenever possible a central difference scheme is used and the resulting gradient corresponds to the slope of a second-order polynomial fit to 3 neighbour velocities (Equation 4.6). If only one valid neighbouring vector can be found, a forward or backward difference scheme will be used instead. If no valid neighbouring vectors can be found, velocity gradients are set to zero, but tagged as invalid. Vorticity at a point is defined as the local rotation or curl of the 3D velocity field:

$$\overline{\Phi} = curl(\overline{U}) = \nabla \times \overline{U} = \left(\frac{\partial W}{\partial y} - \frac{\partial V}{\partial z}\right)\overline{i} + \left(\frac{\partial U}{\partial z} - \frac{\partial W}{\partial w}\right)\overline{j} + \left(\frac{\partial V}{\partial x} - \frac{\partial U}{\partial y}\right)\overline{k} \qquad (4.4)$$

For the planar data resulting from the 2D PIV set-up, gradients in the z-direction cannot be calculated, so only vorticity around the z-axis is determined:

$$\Phi_z = \frac{\partial V}{\partial x} - \frac{\partial U}{\partial y} \qquad (4.5)$$

In the Dantec DynamicStudio v3.14 software, using a central difference scheme, this is carried out for each vector located at point (m,n):

$$\Phi_z = \left(\frac{V_{m+1,n} - V_{m-1,n}}{x_{m+1,n} - x_{m-1,n}}\right) - \left(\frac{U_{m,n+1} - U_{m,n-1}}{y_{m,n+1} - y_{m,n-1}}\right) \qquad (4.6)$$
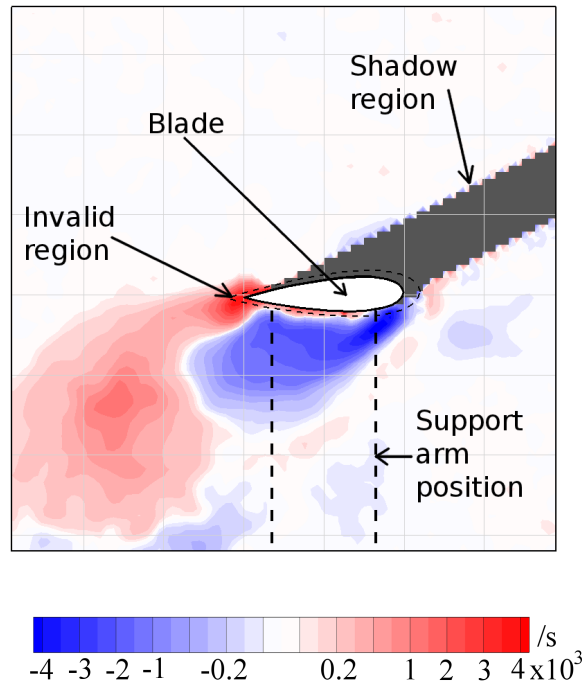
Figure 4.8: An example plot of vorticity showing the invalid areas of the flowfield data set caused by the blade-tip and shadow regions

The flowfield for each sample was smoothed using an averaging filter, this process replaced each vector with the average of its closed neighbours and reduced errors in the determination of the direction of the vector which was shown to contribute to error in the vorticity calculation. The averaging filter also smoothed the desirable gradients in the flow field, meaning that vorticity was slightly dissipated. A 3x3 vector window was chosen as the best compromise between smoothing-out errors whilst avoiding excessive vorticity dissipation. The results of the smoothing on one sample are shown for two tip speed ratios at $\psi=90°$ in Figure 4.9, at both $\lambda=2$ and $\lambda=4$ the error in the flow away from the blade is much reduced by using the averaging filter. The shed vortices at the $\lambda=2$ condition (Figures 4.9c and 4.9d) are also better resolved using the filter to remove errors. The unwanted dissipation effect is most evident in the wake of the blade at $\lambda=4$ where the small vortices are shown to be notably dissipated in Figure 4.9d when compared to Figure 4.9c.

**Test Procedure**

Preliminary experiments used a tripod to support the camera and a free standing platform to support the laser. The encoder trigger pulse was adjusted simply by rotating the coupling between the VAWT shaft and the measurement assembly. Around 20 minutes per condition were needed for adjustment of the camera FOV and focus, trigger pulse, and laser sheet positions. However, development of the camera rig, angle measurement devices, and pre-
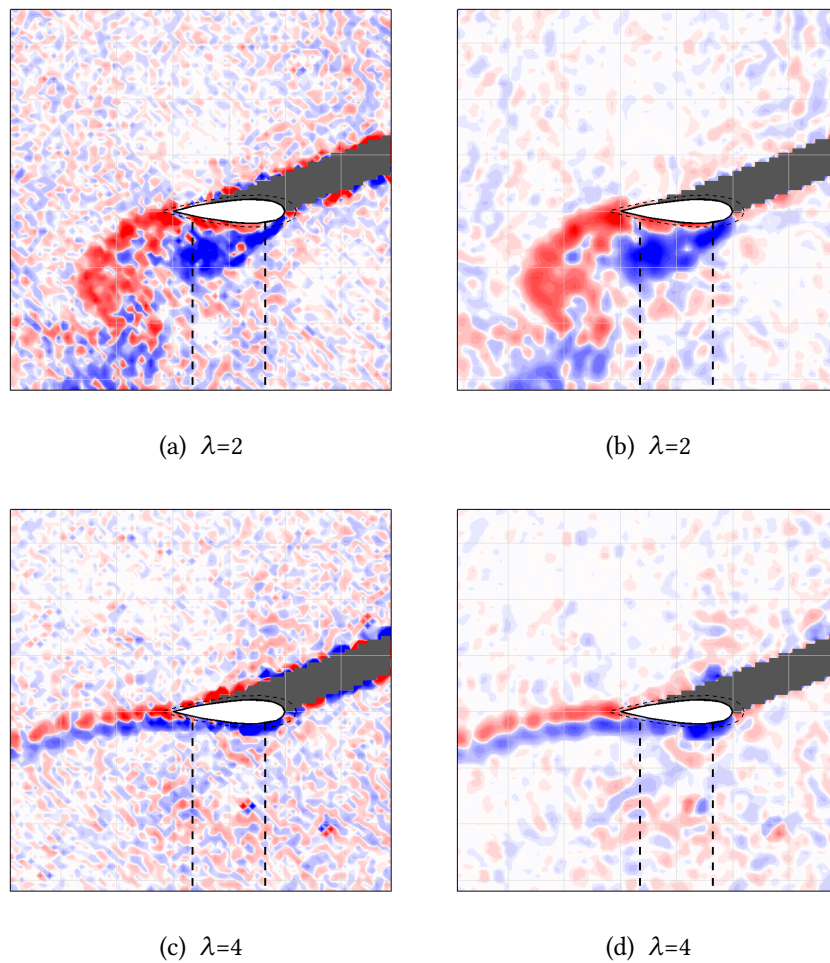
(a) $\lambda$=2                              (b) $\lambda$=2

(c) $\lambda$=4                              (d) $\lambda$=4

Figure 4.9: Plots of vorticity showing the effect of using 3x3 window averaging filter for the $\psi$=90° position.

marked laser positions reduced this process to a minute or two. In addition, a greater degree of consistency was maintained between measurements at different positions. With the physical adjustments minimised, the software's data capture and recording process was the main factor governing the time taken for the full test. The general test procedure is shown in Figure 4.10.

## 4.2.5  Verification of Settings

In order to determine the various settings required to give the best possible flowfield data, a series of short tests were carried out. It was not possible to simultaneously assess the effects of all of the experimental variables such as seeding density, sheet thickness...etc. Instead, a series of quick trial and error tests were first used to establish reasonable settings. Following this, a test of the impact of varying each setting was conducted by adjusting that particular setting, whilst maintaining all others. It was assumed that the optimum value determined for one setting would not differ considerably from the adjustment of another.
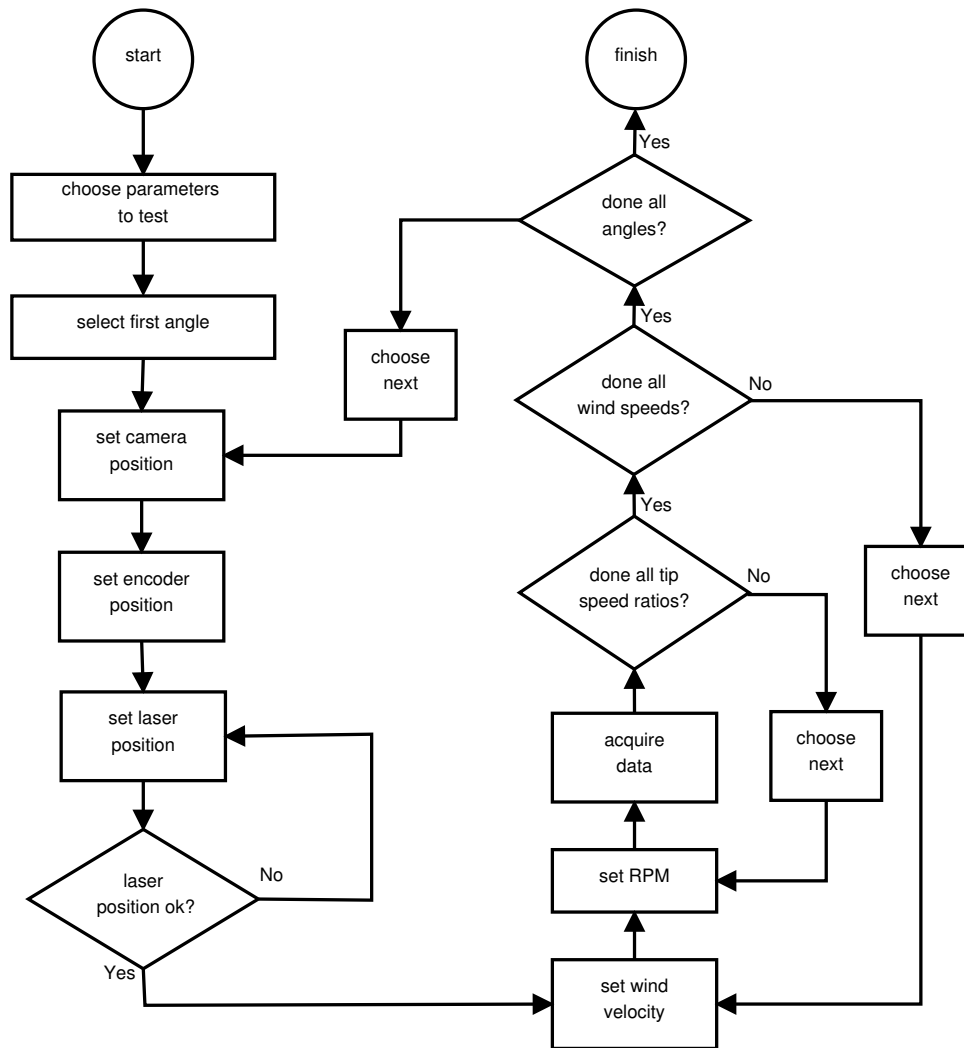
Figure 4.10: Flow chart illustrating PIV testing sequence.

**Seeding Density**

The effect of seeding density on the correlation accuracy was quantified so that the correct density could be set and the best correlation obtained from the experiments. Tests with varying amounts of seeding were carried out for one condition: $V_\infty = 7\,m/s$, $\lambda = 2$, $\psi = 90°$, which was chosen as it was a mid-range wind velocity and the condition also included highly separated flow which was considered to be potentially difficult to capture. In order to determine the quality of the correlation, a moving average validation was used with each vector being compared to the average of its neighbouring vectors over a 3x3 vector window. If the magnitude of vector and the neighbouring average differed by more than 10% the vector was marked as invalid. For each seeding test the average number of invalid vectors was noted for 15 samples. A simple cross correlation was used with a 32x32 pixel interrogation window.

The seeding density was varied by running the atomiser for different lengths of time. Figure
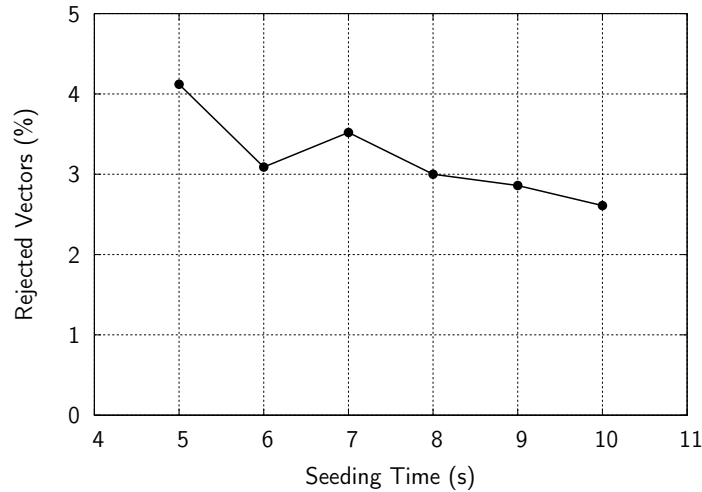


Figure 4.11: Plot showing the effect of seeding density on the number of poorly correlated vectors

4.11 shows that a doubling of the seeding density dropped the number of rejected vectors from an already reasonable 4.1% down to 2.7%. There was less than 1% difference in the number of rejected vectors for 6 to 10 minutes of seeding, indicating that a reasonable range in seeding density could be tolerated by the correlation process. So, setting seeding density with a high accuracy during the testing was not necessary. 8 minutes was chosen as a suitable length of seeding time for the rest of the testing.

**Laser Sheet Thickness**

The effect of the laser sheet thickness was assessed with the same moving average validation as for the seeding density assessment. The laser sheet thickness was difficult to measure, so instead the ideal position of the sheet focal length was determined by carrying out repeated tests with the focal length simply varied by adjusting the laser lenses. The $\lambda$=2, $\psi$=90° was chosen for consistency and also because the blade at this condition was situated in the middle of the tunnel working section, which was a sensible place to optimise the sheet thickness.

The results (Figure 4.12) show clearly that when the sheet focal length is around 1m the number of rejected vectors is particularly high. The blade at $\psi$=90° was 0.9m away from the laser and so the result actually shows that the minimum sheet thickness gives a poor correlation accuracy. This is expected due to the increased likelihood of cross-plane displacements resulting in particles appearing in only one of the paired interrogation areas. Bringing the focal point before or after the measurement region, which thickened the laser sheet, gave a much improved correlation. 2m was chosen as the ideal setting as it produced the lowest number of errors and small differences in setting the focal length would not

dramatically effect the correlation due to only slightly higher errors being recorded for ±0.5m of this setting.
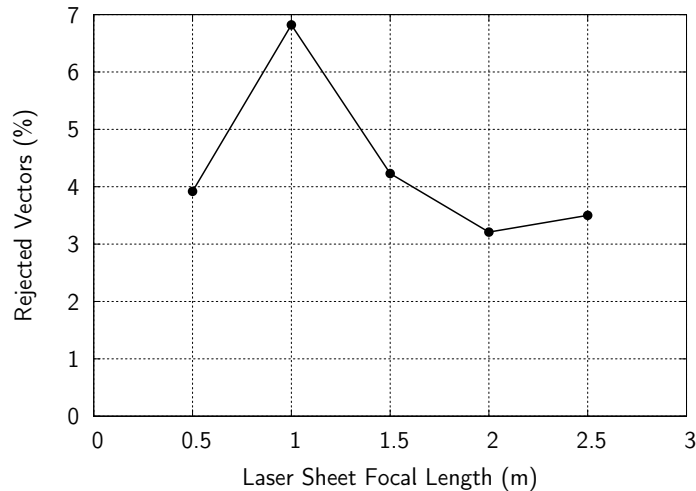


Figure 4.12: Plot showing the effect of laser sheet focal position on the number of poorly correlated vectors

**Time Between Pulses**

For reasons already discussed in Section 4.2.3, the time between pulses needed to be set to an appropriate value. To assess the impact of adjusting the time interval, the same moving average validation was used as for the previously discussed tests. Figure 4.13 shows that the percentage of rejected vectors falls below an acceptable 3% with time intervals below $30\mu s$. The correlation appears to improve the lower the time interval used, but the moving average validation does not give a full picture: images of the vorticity field for a single sample (Figure 4.14) show that at the smallest time intervals of $5\mu s$ (Figure 4.14a) and $10\mu s$ (Figure 4.14b) actually give a significant amount of error due to the difficulty of assessing the exact direction of the particle displacements, which have become very small. A value of $15\mu s$ was chosen as a good compromise between avoiding errors in the slower moving regions away from the blade whilst allowing faster regions of flow, such as shed vortices, to be captured.

In a paper by Ferreira et al. [64], the authors suggest setting the time interval such that particles would give a 8 pixel displacement assuming the a particle speed of $U = 4V_{\infty}$. For the tests described above, the wind velocity was 7m/s and, taking into account the camera settings used, this correspond to a time interval of 19.5us based on $U = 4V_{\infty}$. This is close to the 15us which was selected based on the Author's own tests (detailed above).
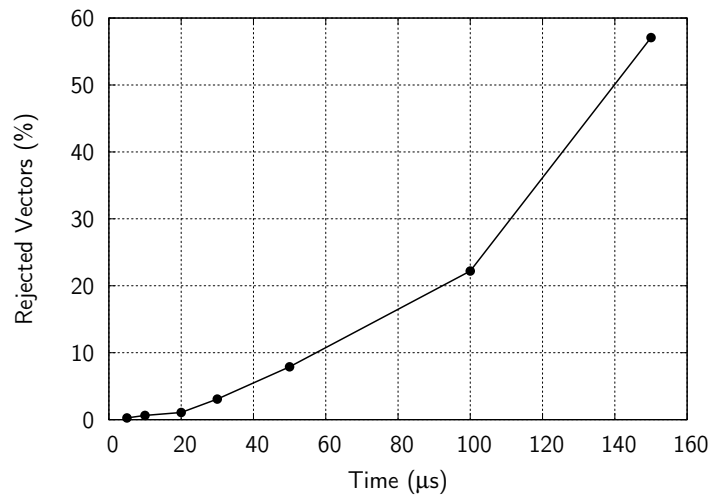
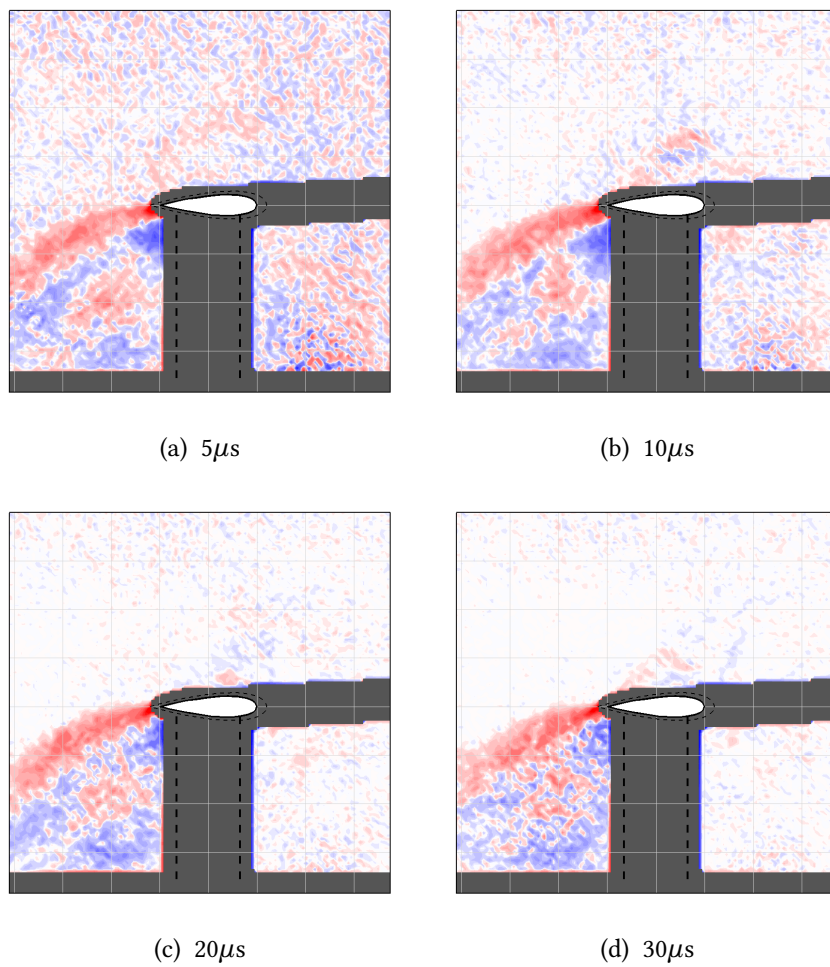Figure 4.13: Plot showing the effect of time interval on the number of poorly correlated vectors



(a) $5\mu s$



(b) $10\mu s$



(c) $20\mu s$



(d) $30\mu s$

Figure 4.14: Plots of vorticity showing the effect of time interval

**Laser Sheet Position**

The fundamental flow physics of the VAWT occur due to the fact that the rotation axis is perpendicular to the free-stream flow direction. For a rotor with straight blades, the same flowfield may be assumed at any slice across the rotor-axis by neglecting the free blade-ends, support arm junctions and streamtube expansion. This is the case for basic mathematical models [9] [11], 2D CFD simulations [51] [69] and previous PIV studies [61] [65]. In reality, the problem *is* three-dimensional: in addition to the neglected blade ends and support arm junctions, the flow separation and vortex shedding may also deviate from the quasi-2D simplification [88] [89].

    The objective of the PIV measurement campaign for this study was to build upon the initial work of Fujisawa and Shibuya and Ferreira et al. (see Section 2.4.1) and reveal further detail of the fundamental flow physics. It was therefore considered adequate to continue with the assessment on a quasi-2D basis. In order to do this, the flow variation along the blade was assessed in order to find the required laser sheet position such that the PIV measurements avoided strong influences of the support arm junctions and free blade ends. The symmetry of the rotor and wind tunnel arrangement allowed measurements to be taken at several positions (Figure 4.15) for one half of the blade at the $V_\infty = 7\,m/s$, $\lambda = 2$. The blade at this tip speed ratio experiences both attached and highly separated flow during a rotation. Three azimuth positions were monitored to capture the effect of the support arms and free blade-ends on the near-blade flow: the onset of stall occurs at $\psi = 60°$, a dynamic stall vortex-pair are shed at $\psi = 90°$ and deep-stall vortex shedding is shown at $\psi = 120°$.
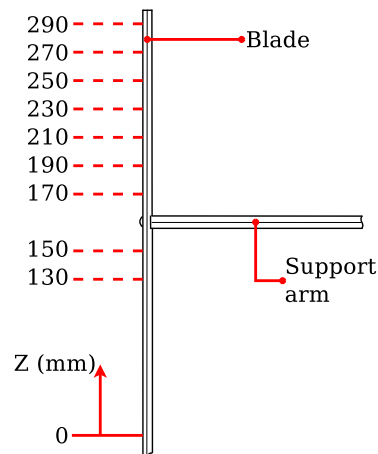


Figure 4.15: Diagram showing the positions along the top-half of the blade at which PIV measurements were taken for three azimuth angles.

    PIV visualisations at the mid-span position are shown to be partially obscured by the support arm in Figure 4.16. However, the gap in negative shed vorticity from the suction surface of the blade suggests the roll-up of a dynamic stall vortex over the surface. At $\psi = 90°$,

vortices are shown to be shed from the blade surface, and this continues at $\psi = 120°$.



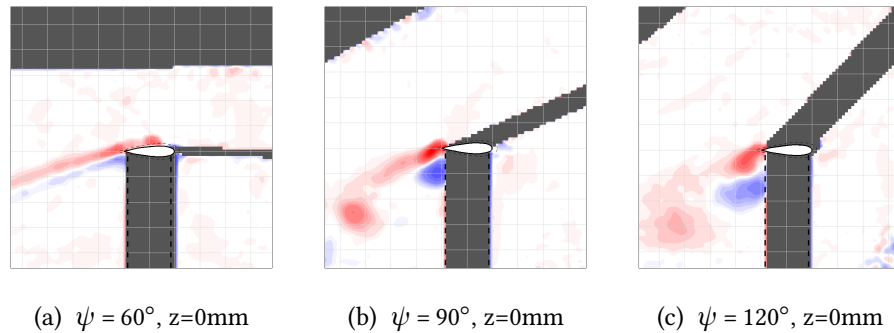| (a) $\psi = 60°$, z=0mm | (b) $\psi = 90°$, z=0mm | (c) $\psi = 120°$, z=0mm |

Figure 4.16: Contour plots of vorticity showing the flowfield at the mid-span position for $\psi = 60°$, $90°$ and $120°$ at $V_\infty = 7\,m/s, \lambda = 2$.

The flow visualisations at the mid-span (Figure 4.16) are shown to be reasonably well-matched to the upper region of the blade between the tip and the support arm junction, as shown in Figure 4.17. A larger distance is observed between shed vortices for the mid-span position at $\psi = 90°$ (Figure 4.16b); however, the phase of vortex shedding is fairly well-matched. The $z$=250mm position shows some differences, particularly at $\psi = 90°$ (Figure 4.17h) where the blade tip effects appear to have effected the vortex structures.

As the measurement position moves closer to the free blade-end (Figure 4.18) the visualisations show increasingly different vortex shedding patterns compared to those at the mid-span. At z=290mm (only 0.25c from the blade-end) the flow is shown to be detached at all three of the inspected azimuth positions (Figures 4.18d to 4.18f), and overlapping wakes from the pressure and suction surfaces indicate a tip-vortex structure which cannot be properly captured using 2D-PIV measurements. Tip vortices can reduce the effective angle of attack on an wing [89]; results at z=250mm (Figures 4.17g to 4.17i) and z=270mm (Figures 4.18a to 4.18c) appear to show a later stall which progresses more slowly than for the measurements further away from the blade tip.

Measurements close to the support arm junction (Figure 4.19) show there is a flow separation present at all three of the inspected azimuth positions at z=170mm (Figures 4.19a to 4.19c). Relative to the mid-span position, a closer-matched phase of vortex shedding is shown for z=190mm, although the shed vortices are shown to still be effected by the support arm and less-clear structures are observed as a result in Figures 4.19d to 4.19f. Similar flowfields were observed for the same laser sheet positions below the support arm (z=110 and 130mm).

A sketch showing a summary of the approximate extent of the influence of the blade-tips and support arm junctions on the near-blade flow is shown in Figure 4.20. Base on PIV visualisations (discussed above), the support arm and free blade-end have a significant effect on the flow around the blade: Within approximately 0.5c of the support arm or the blade tip the flow is most strongly effected, and was separated for all three azimuth angles. Within approximately 1c of the support arm or the blade tip, the onset of stall is not significantly
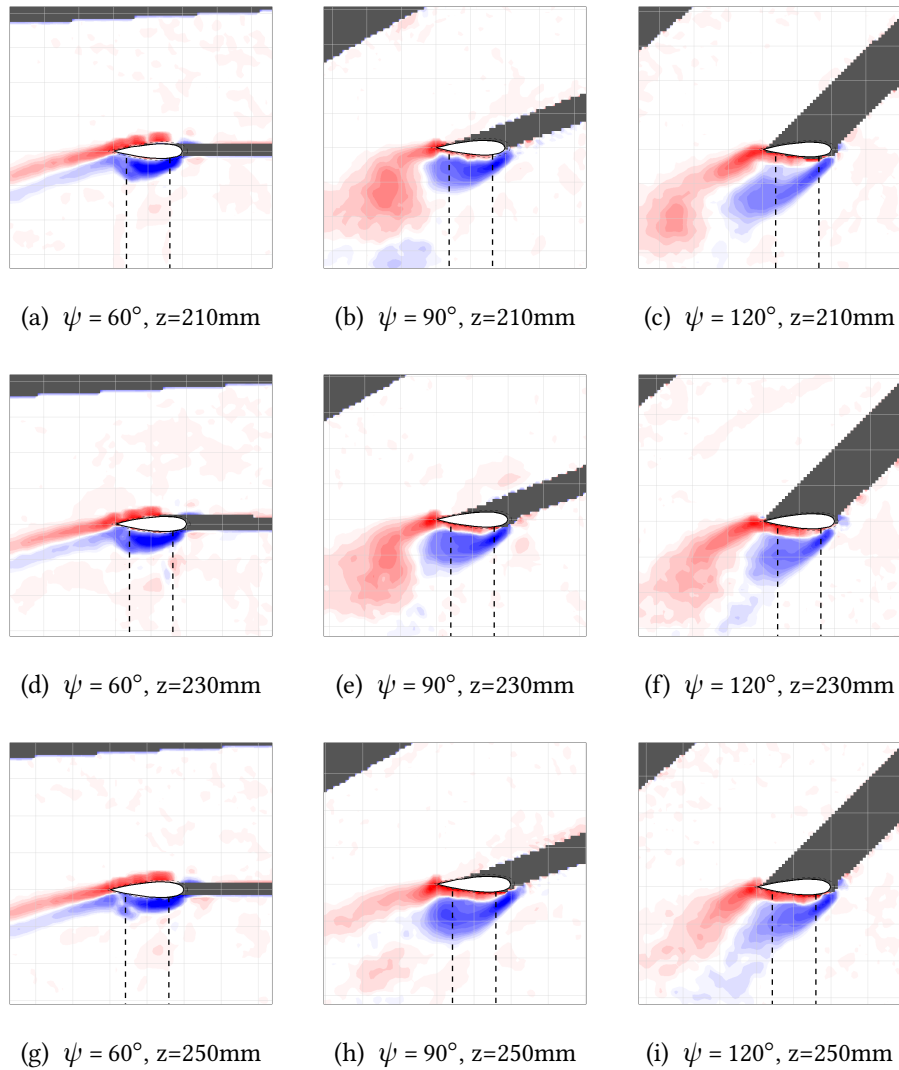
(a) $\psi = 60°$, z=210mm     (b) $\psi = 90°$, z=210mm     (c) $\psi = 120°$, z=210mm

(d) $\psi = 60°$, z=230mm     (e) $\psi = 90°$, z=230mm     (f) $\psi = 120°$, z=230mm

(g) $\psi = 60°$, z=250mm     (h) $\psi = 90°$, z=250mm     (i) $\psi = 120°$, z=250mm

Figure 4.17: Contour plots of vorticity showing the comparison between the mid-span and upper-blade regions for $\psi = 60°$, $90°$ and $120°$ at $V_\infty = 7\,m/s$, $\lambda = 2$.

effected but the subsequent shed vortices are distorted by z-component velocities in the wake. However, far enough between the tip and support arm junction, the flow has been shown to be reasonably representative of that at the mid-span. With the rotor supporting structure obscuring much of the mid-span flowfield it was considered most appropriate to continue tests at z=220mm. Further study of the effect of the support arms and free blade-ends is left as a subject for future study, and is discussed further in Chapter 8.4.

(a) $\psi = 60°$, z=270mm

(b) $\psi = 90°$, z=270mm

(c) $\psi = 120°$, z=270mm

(d) $\psi = 60°$, z=290mm

(e) $\psi = 90°$, z=290mm

(f) $\psi = 120°$, z=290mm
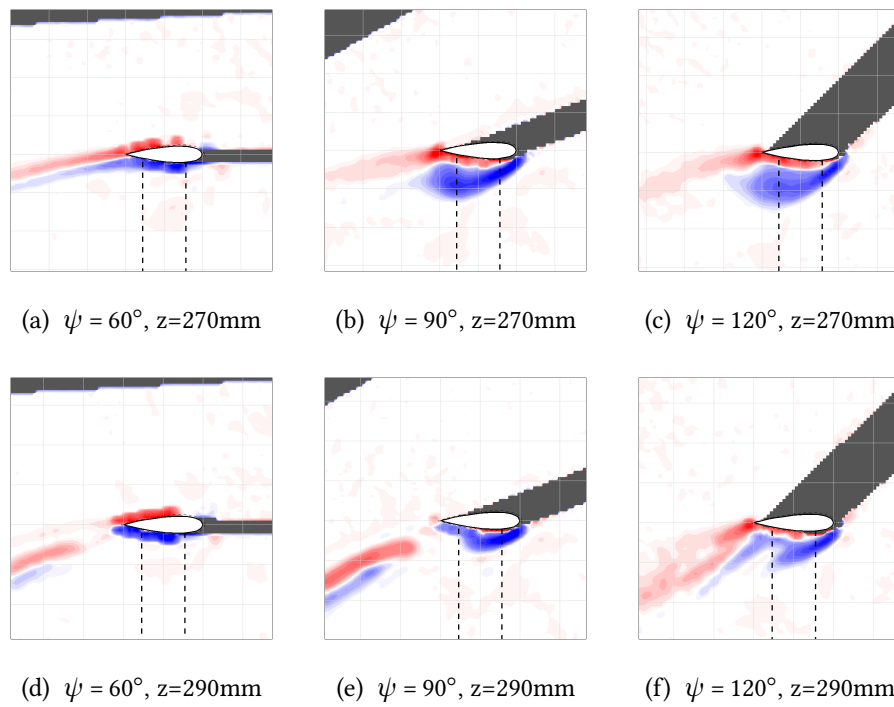
Figure 4.18: Contour plots of vorticity showing the effect of the free blade-end for $\psi = 60°$, $90°$ and $120°$ at $V_\infty = 7\,m/s, \lambda = 2$.



(a) $\psi = 60°$, z=170mm
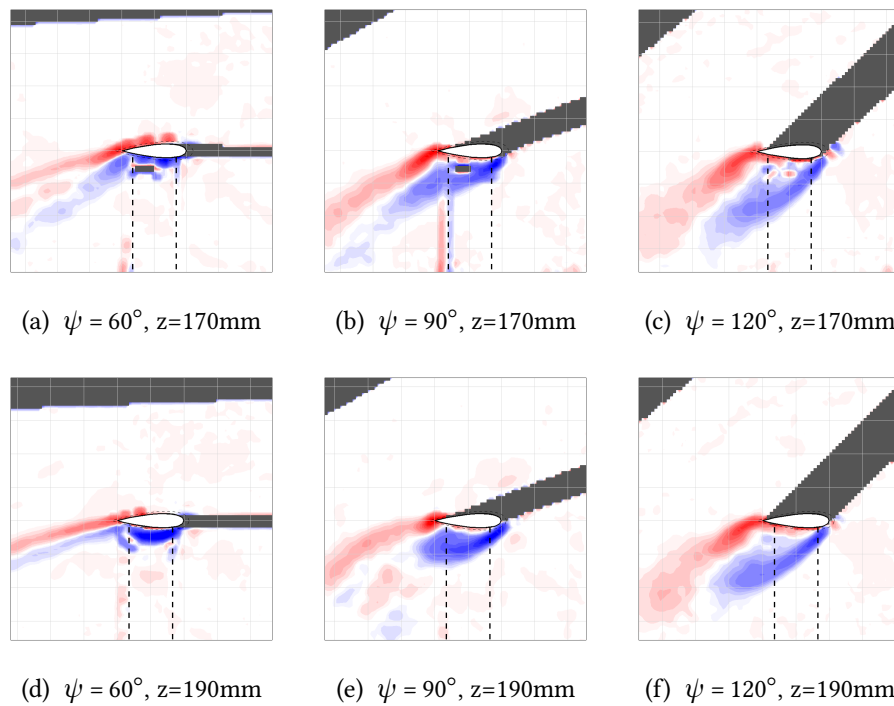
(b) $\psi = 90°$, z=170mm

(c) $\psi = 120°$, z=170mm

(d) $\psi = 60°$, z=190mm

(e) $\psi = 90°$, z=190mm

(f) $\psi = 120°$, z=190mm

Figure 4.19: Contour plots of vorticity showing the effect of the support arm junction for $\psi = 60°$, $90°$ and $120°$ at $V_\infty = 7\,m/s, \lambda = 2$.
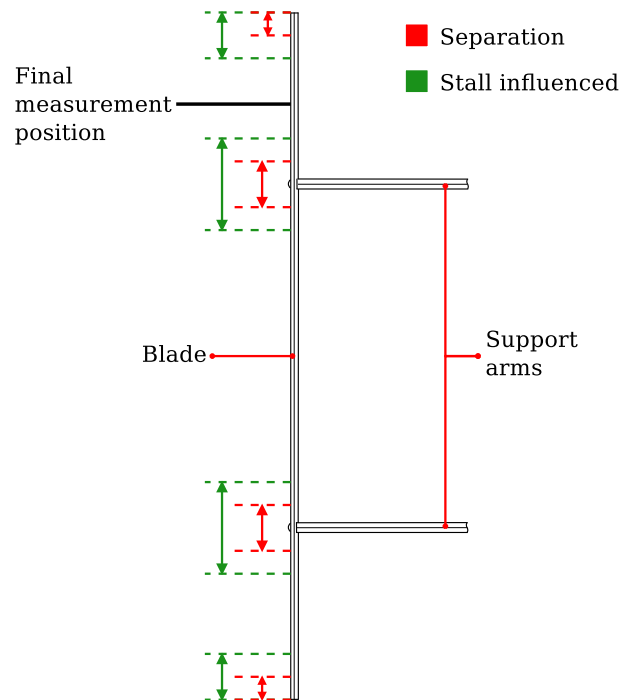
Figure 4.20: Diagram summarising the approximate extent of the influence of the blade-tips and support arm junctions on the near-blade flow.

### 4.2.6 Error and Uncertainties

**Number of Samples**

The aim of the PIV measurement campaign was to capture the main aspects of the flow physics, such as assessing whether or not the blade had stalled, and visualising the path of large vortices. Obtaining precise point-by-point averaged velocity values from a large number of samples was not anticipated to be necessary. The effect of averaging from a varying number of samples was assessed for the $V_\infty = 7\,m/s, \lambda = 2, \psi = 90°$ by comparing plots of vorticity. The flow at this point is highly separated and the blade sheds large vortices which was thought to represent one of the more difficult conditions to obtain a good average of the flowfield.

The first six samples of a total of 100 are shown in Figure 4.21. One sample was acquired every rotation. Some small phase differences are shown between the individual rotations, with the greatest differences observed between Figures 4.21a and 4.21d; however, the same basic flow physics are shown in each image. The error in the flow field away from the blade surface is shown in each image as small blobs of vorticity resulting from errors due to the difficulty of assessing the exact direction of the particle displacements. It is thought that the same reasons account for the somewhat fragmented appearance of the vortex structures.

Plots of vorticity are shown in Figure 4.22 for averages obtained from varying $n$, the number of samples. As is expected from the similarity of the individual samples shown in
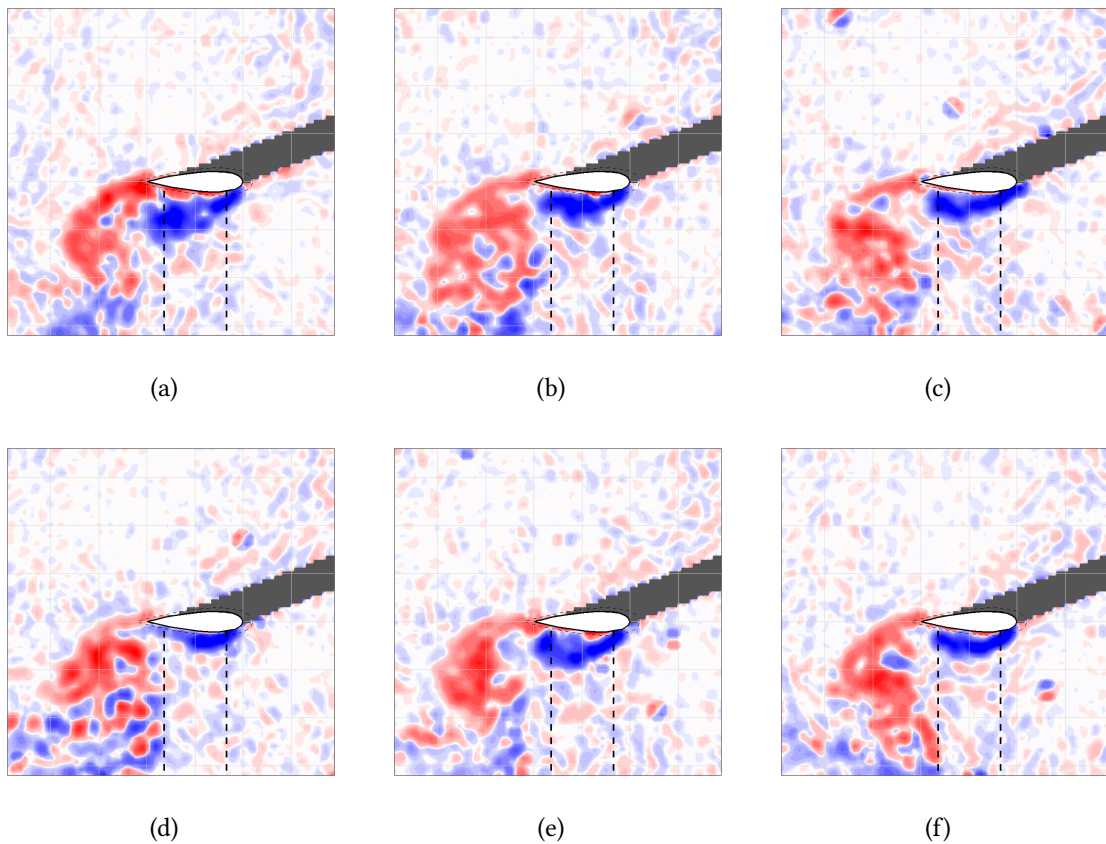
Figure 4.21: Plots of vorticity showing six samples at $\psi$=90°.

Figure 4.21, all of the plots obtained from averages of varying numbers of samples show the same basic flow patterns. The error in the regions away from the blade is quickly reduced with the averaging of only 5 samples (Figure 4.22b) and with 30 or more samples the errors in these regions becomes very small and changes little as the number of samples is increased. The definition of the shed vortices improves significantly as the number of sample increases from 1 to 30 (Figure 4.22b to 4.22e); between 45 and 100 samples the shed vortices show some small changes but overall the images of the flowfield are shown to change very little (Figure 4.22f to 4.22i).

Overall, based on the tests carried out for this condition, around 50 samples is shown to be an adequate number for mapping out the general flowfield in the near-blade region. As the acquisition process in the lab took only a few minutes per condition, it was decided that 100 samples should be used to give a factor of safety over the 50 samples deemed necessary from the tests discussed above.

**Blade Position and Near-surface Measurements**

Obtaining ensembles for each condition and azimuthal position was challenged by the fast rotation of the rotor. Whilst the rig was supported as rigidly as possible, the high speed of
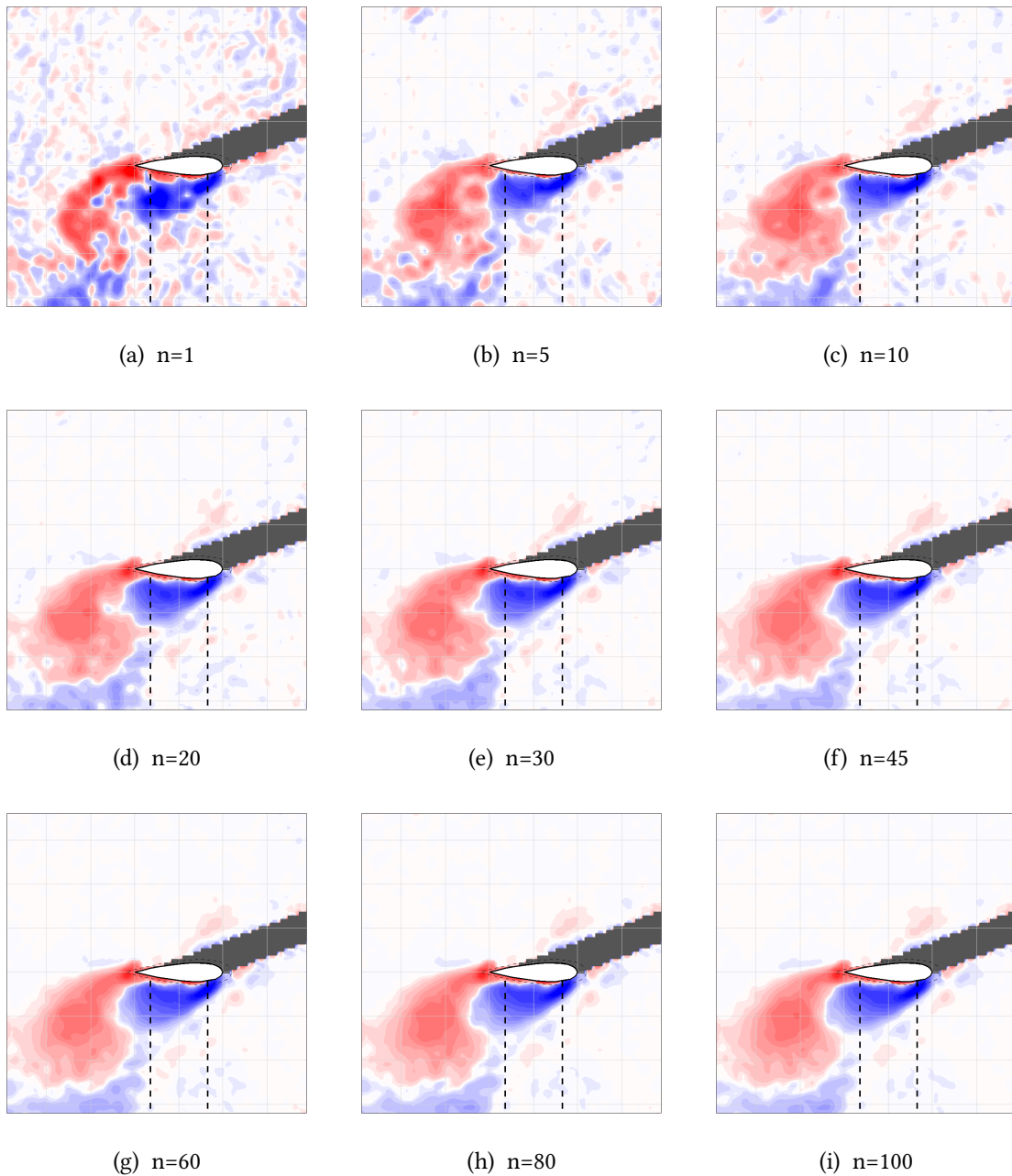
(a)  n=1

(b)  n=5

(c)  n=10

(d)  n=20

(e)  n=30

(f)  n=45

(g)  n=60

(h)  n=80

(i)  n=100

Figure 4.22: Plots of vorticity showing average flowfields obtained from varying *n*, the number of samples at $\psi$=90°.

rotation and the relatively heavy blade resulted in some vibration of the rig that slightly varied the position of the blade between ensembles. In addition, at higher rotational speed the blade deformed due to the centrifugal force. Reflections from the surface meant that information very close to the blade was lost. In addition, the grid of interrogation windows placed across the image resulted in some windows being partially masked out by the blade. The software was set to neglect a window if more than 50% of the window was within the masked area. All of these factors combined to increase to area of potentially invalid data close to the blade surface (Figure 4.8) which was already present due to the camera perspective along the blade length (discussed in the following sub-section). Some annotated example images are shown in Figure 4.23, also indicated are areas where secondary reflections from the blade bolt heads and support arm can cause additional reflections. Whilst results are plotted in the region fairly close to the surface, the reader is advised to consider the above-mentioned potential error and uncertainty for the near-surface regions. The discussions in this thesis generally refer to significant features, such as large stall vortices, in regions away from the blade surface, so uncertainty in this region has negligible effect as far as this study is concerned.
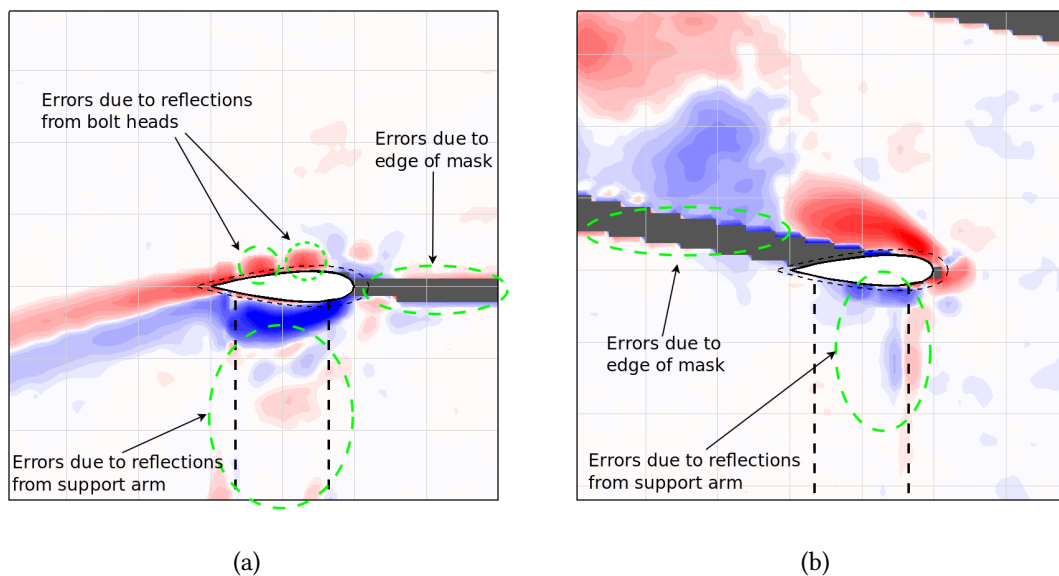


Figure 4.23: Plots of vorticity showing areas most prone to error and uncertainty.

In addition to factors discussed above it was also essential to reliably trigger the laser at the same azimuth angle for each ensemble, as the index pulse on the encoder was narrow (1/3000th, 0.12°) so an accidental trigger on the following rather than the leading edge would make very little difference. The vibration of the shaft did affect the encoder, but the effect was small so that triggering usually occurred on the leading edge of the encoder index pulse and always within ±0.05°. The mechanisms used to position the encoder index pulse and the camera were accurate to with ±0.2° (see Section 4.2.4) giving a total blade azimuthal position accuracy of ±0.25°.

**Camera Perspective**

Figure 4.24 illustrates a potential problem resulting from the camera perspective: as the edge of the image is slightly further away from the camera than the image centre, the scaling factor used to calibrate the flow velocity is not constant across the image. However, in the case of the measurements detailed in this study the camera was 0.9m away from the FOV, which resulted in difference of only 0.3% between the scaling factor for the centre and edge of the image. The perspective problem was therefore neglected for all of the tests. Also shown in Figure 4.24 is the shadow region cast by the blade tip, which obscured the very-near blade surface. This was not a problem for this study which does not focus on the flow close to the blade surface. In any case, as is discussed above, the near surface region is troubled by a range of problems and was not the main region of interest for this study. For these experiments, the tip-shadow region was actually quite useful as it helped to prevent potentially damaging direct reflections entering the camera lens.
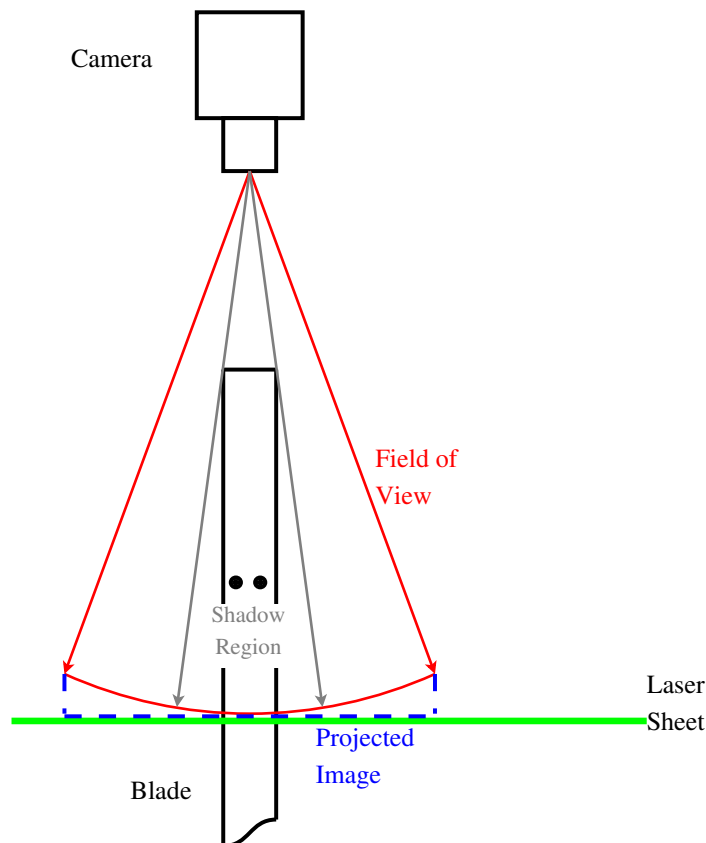
Figure 4.24: Diagram showing an exaggerated view of the camera perspective.

## 4.3 CFD

### 4.3.1 Introduction

CFD is well placed to aid the understanding of the VAWT flow physics due to the high level of detail that can be extracted from a single simulation. The aerodynamic forces, pressure distributions and the corresponding flowfield are easily available, and an understanding of how flow physics and performance are linked can potentially be gained.

The development of the finer details of CFD modelling techniques are not one of the aims of this study. However, the flow physics understanding that can be gained from a simulation is potentially a very useful addition to this experimentally-led investigation. A CFD model has been generated within the same research group as the Author, with the majority of the model development being carried out by Mr Louis Angelo Danao [85]. Later, in Chapters 5 and 6, the model is used by the Author to give some additional insight into the VAWT flow physics, with the simulation showing good matches to experimental flow visualisations by PIV. The model is also used to provide a more realistic estimation of the angle of attack of the incident flow onto the blade. A new technique was developed for this purpose (see Edwards et al. [90]) and is explained in Section 4.3.6.

A summary of the model and its development is presented in the following sections in order to give a foundation for the use of the model in later chapters.

### 4.3.2 Model Definition

The widely-used commercial CFD code Ansys Fluent 12.1 was used for all of the simulations detailed in this study. The Fluent 12.1 documentation [91] provides details concerning the governing equations and solver formulation which are not repeated in this thesis. Unless stated otherwise, the recommended values were used for solver settings and model coefficients. The pressure-based solver was used with absolute velocity formulation and a second order implicit transient formulation. The coupled pressure-velocity scheme was used, and a second order upwind discretisation was used for all solution variables. All solutions were initialised using the inlet conditions, where a turbulent intensity of 1% and length scale of 0.01m were applied. The following sections detail the geometry and mesh, turbulence model and time step selection, and the convergence monitoring.

### 4.3.3 Geometry and Mesh

Previously studies by Howell et al. [51], Ferreira et al. [65], Tullis et al. [69] and Hamada et al. [92] have shown that the main flow characteristics of the VAWT can be represented using a two-dimensional CFD model. Such a model is unable to account for the effects of the support arms or the blade tip losses on performance; however, as this study is concerned with the main flow physics of the VAWT these are secondary effects. The computation time for

a three-dimensional simulation would be many times greater and was adjudged to be more appropriate for future studies concerned with higher-level details.

The grid generation software Gridgen was used to create the model geometry and the mesh. The domain consists of two mesh zones: an inner rotor zone and an outer zone (Figure 4.25). The inner rotor zone contains the rotor geometry and the mesh rotates together with the blades and the central shaft. The outer domain is fixed and has a rectangular outer boundary (representing the wind tunnel) and a hole in the centre which accommodates the inner rotor zone. As the inner mesh rotates, at each time step the solution is interpolated between the inner and outer zones across the sliding interface boundary.
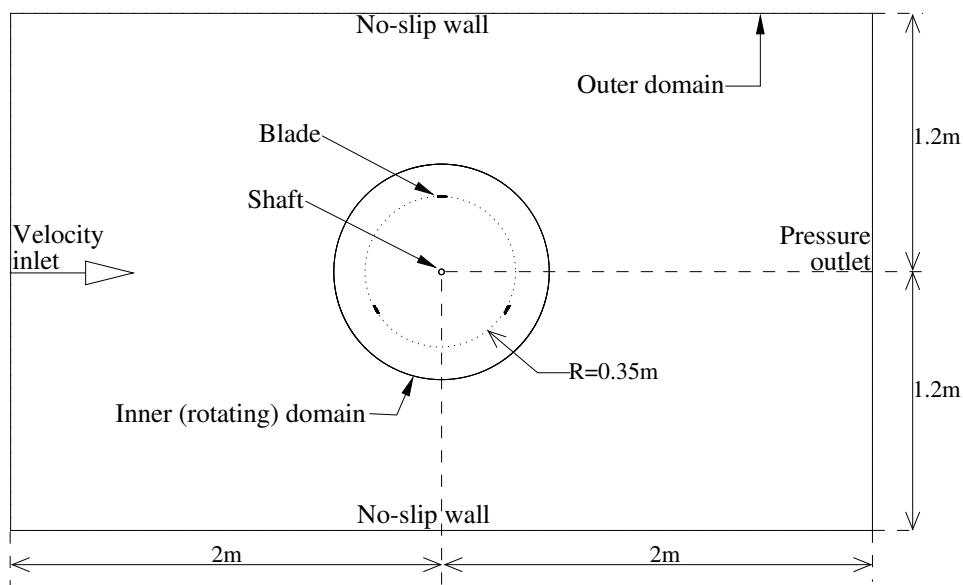


Figure 4.25: Diagram showing the construction of the overall two-dimensional simulation domain.

The geometry represented a mid-blade slice of the wind tunnel rotor: three NACA0022 blades were set 120° apart around a circular rotation path of 0.35m. The meshing strategy used was developed jointly between Mr Danao and the Author. A structured O-type mesh was constructed around each blade (Figure 4.26) which extended outward towards the interface, the VAWT shaft, and to the space between adjacent blades (Figure 4.27). With the wide range of angles of attack expected, the direction of the blade wake would vary greatly and stall was anticipated to involve the shedding of large vortices. A wider refinement of the wake region was therefore necessary to resolve important flow structures, this was more easily accomplished using an O-type, rather than a C-type mesh. To minimise computation time, the outer domain was meshed relatively coarsely (Figure 4.28) this dissipated high gradients in the wake, such as shed vortices. The general velocity deficit was still captured (see Section 4.3.6) and so the effect on the computation of the blade aerodynamics was not thought to be
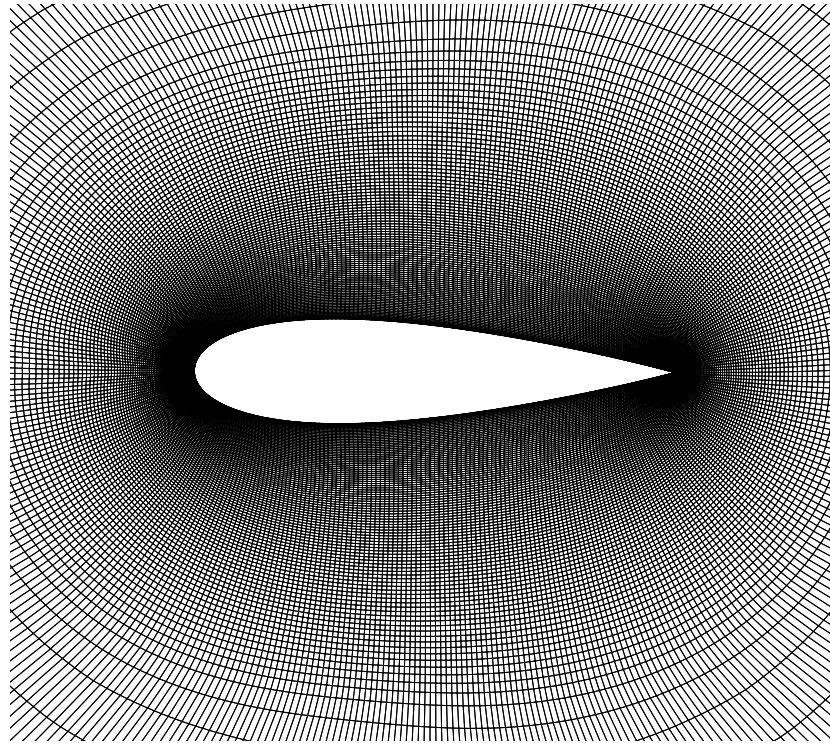
significant.



Figure 4.26: Image showing the near-blade mesh.

As has been discussed in the Literature Review (Chapter 2), there is little published work addressing blockage effects for a VAWT wind tunnel experiment. The simulation of a simple 2D-slice of the wind tunnel set-up would result in a significant over-estimation of blockage, as the ratio between the rotor and wind tunnel widths would not allow for the additional space above the rotor that exists in the wind tunnel case. A closer blockage approximation was achieved by matching the ratio of the rotor and wind tunnel widths in the CFD model to that of the rotor and wind tunnel cross-sectional areas in the experiment. In each case the wall interference effects may differ due to the increased distance between the blades and the wall, the minimum of which was $6.35c$ and $21.25c$ for the two cases. However, this simple approximation was thought to take a large step to addressing the increased effective velocity due to the impeded expansion of the streamtube, and the basic flow physics were not expected to differ significantly between the two cases. More extensive study, both experimentally and computationally, is needed before blockage can be addressed in detail, such study being beyond the scope of this fundamental flow physics investigation.

The effect of mesh density on the solution accuracy was extensively studied by Mr Danao and was not addressed by the Author. The meshing strategy resulted in the mesh density being related to the number of nodes around the aerofoil surface, Figure 4.29 which shows results obtained by Mr Danao using three differing mesh densities. It is observed that even
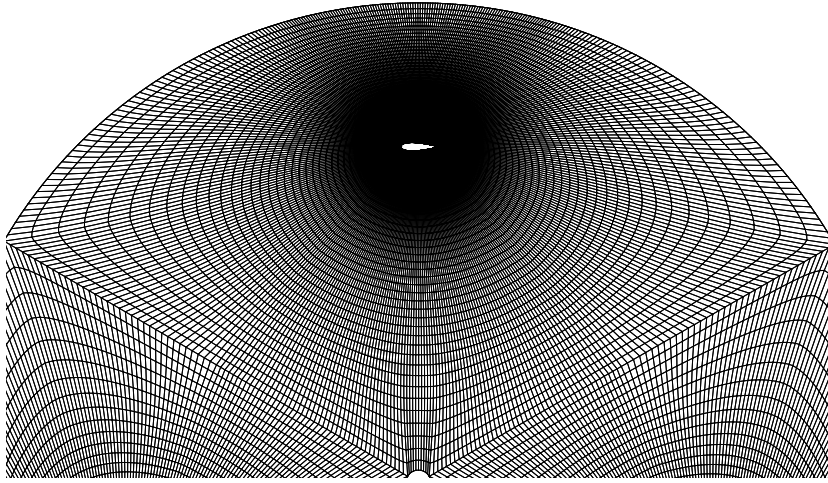
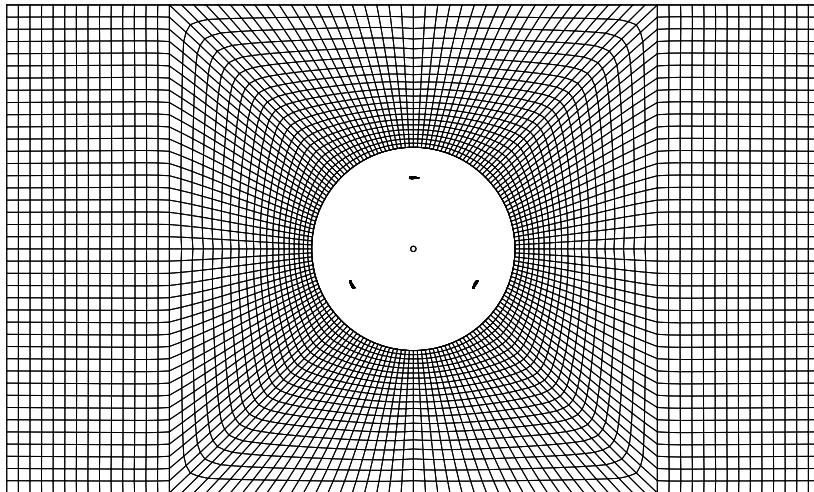Figure 4.27: Image showing one third of the the inner rotor mesh.



Figure 4.28: Image showing the outer domain mesh.

the coarsest mesh, based on 100 points around the surface, is fairly close to the other two simulations with 4 times and 8 times the number of elements. In all cases the performance is fundamentally similar suggesting that the same basic flow physics are exhibited by each model, which is the most important requirement for this study. The 400-surface-points mesh was used for the simulations presented in this thesis.

With separation and reattachment expected as part of the VAWT blade flow physics, correct modelling of the boundary layer was essential. A near-wall modelling approach was chosen over the treatment of the near-wall region by wall function. For each solution the wall Y-plus values were checked to ensure that they were within the recommended region of 1-5
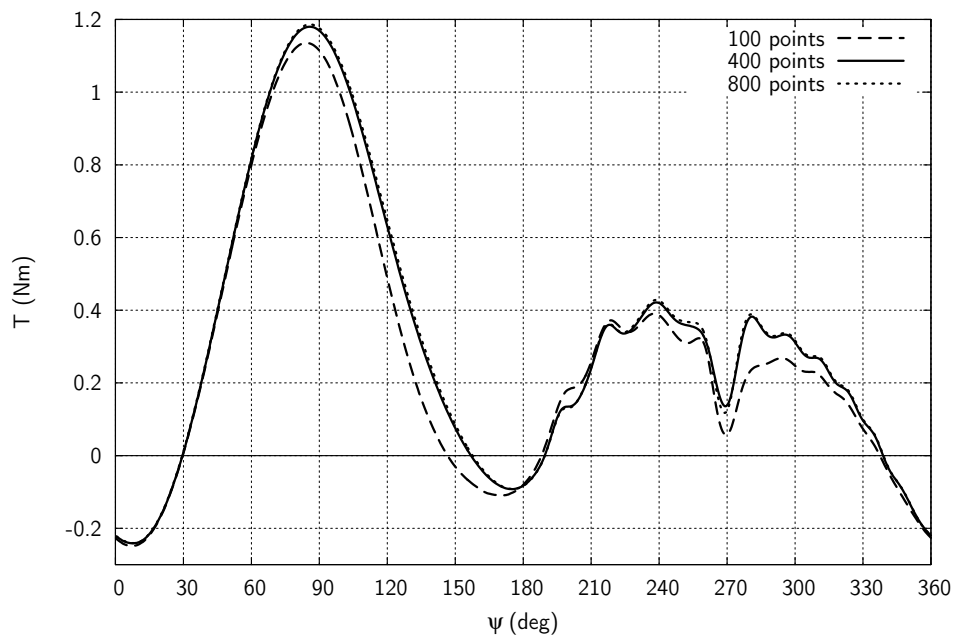
Figure 4.29: A plot showing the resulting torque change with azimuth for three difference mesh densities, where the mesh density is controlled by the number of points around the aerofoil [85].

[Fluent2010], and all solutions were found to have Y+ below 2.2.

### 4.3.4   Turbulence Model Selection

Work to select an appropriate turbulence model was carried out by Mr Danao as part of a published joint study with the Author, see [90]. The adequacy of the turbulence model is later verified by the Author through the comparison of CFD and PIV flowfields, as presented in Chapter 5. The turbulence model selection was carried out by attempting to match flowfield visualisation and force measurements of a pitching aerofoil study, conducted by Lee and Gerontakos [58]. The lift and drag predictions of the three most suitable models are shown in Figures 4.30 and 4.31. Of the available turbulence models in Fluent 12.1 the SST k-$\omega$ model was shown to give the closest match [90].

### 4.3.5   Time Step and Convergence

The unsteady simulation was stepped forward in time, with a number of iterations carried out at each time step to achieve convergence. The chosen size of the time step and the number of iterations were a compromise between solution accuracy and computation time. A higher number of iterations and smaller time step would contribute to a longer overall computation time for each simulation. The rotational position has the most significant influence on the
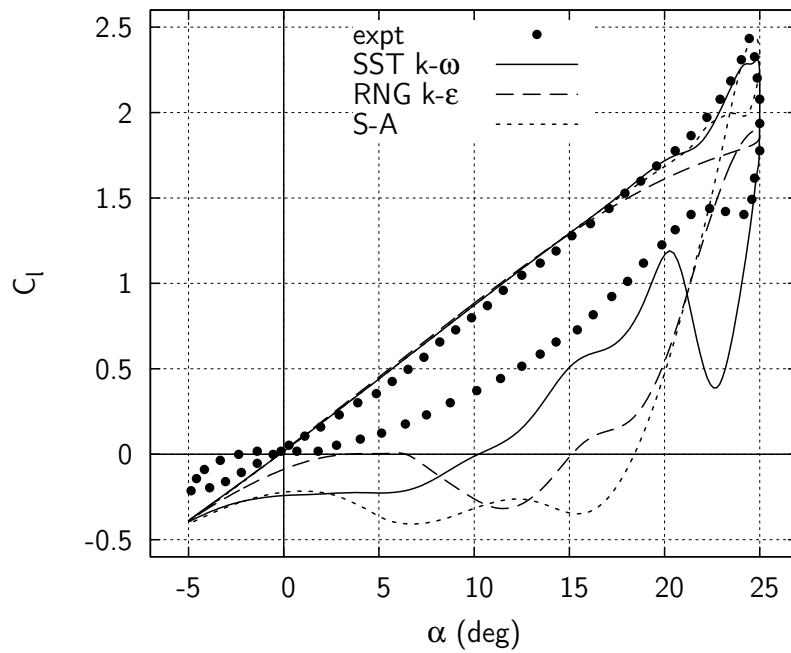
Figure 4.30: A plot showing the pitching aerofoil lift coefficient prediction by three turbulence models, from [90].
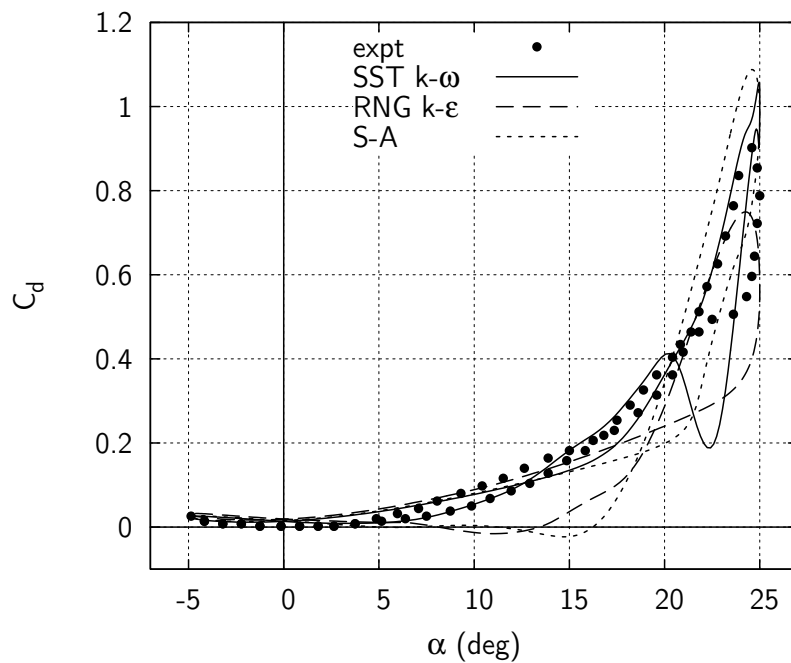


Figure 4.31: A plot showing the pitching aerofoil drag coefficient prediction by three turbulence models, from [90].

VAWT blade flow physics, and so the solution was stepped forward using a time interval corresponding to a particular azimuthal increment. Preliminary studies carried out by the Author, and series of simulations carried out by Mr Danao, indicated reasonably similar torque histories for time steps which corresponded to increments of less than 3°. A time step corresponding to an azimuthal displacement of 0.5°, at the particular $\omega$ being simulated, was chosen as the best compromise between solution accuracy and computation time, this value was used for all of the simulations presented in this study.

The solution was initiated using the inlet velocity value, with a turbulent intensity of 1% and length scale of 0.01m defined in order to approximately match the wind tunnel case. A large starting vortex resulted from the onset of the rotation of the VAWT, a number of rotations needed to be completed before the initial conditions were convected out of the domain. To check for convergence the torque curve history was plotted for the whole solution. Convergence of the forces was usually shown to occur in 5 to 10 rotations depending on $\lambda$. At higher $\lambda$, a higher number of rotations were completed before the initial condition were convected out of the domain. The example case shown in Figure 4.32 shows convergence after 6 rotations. The solution residuals were also checked to ensure that they were reduced by 6 orders of magnitude at the point at which the torque curve convergence was observed.
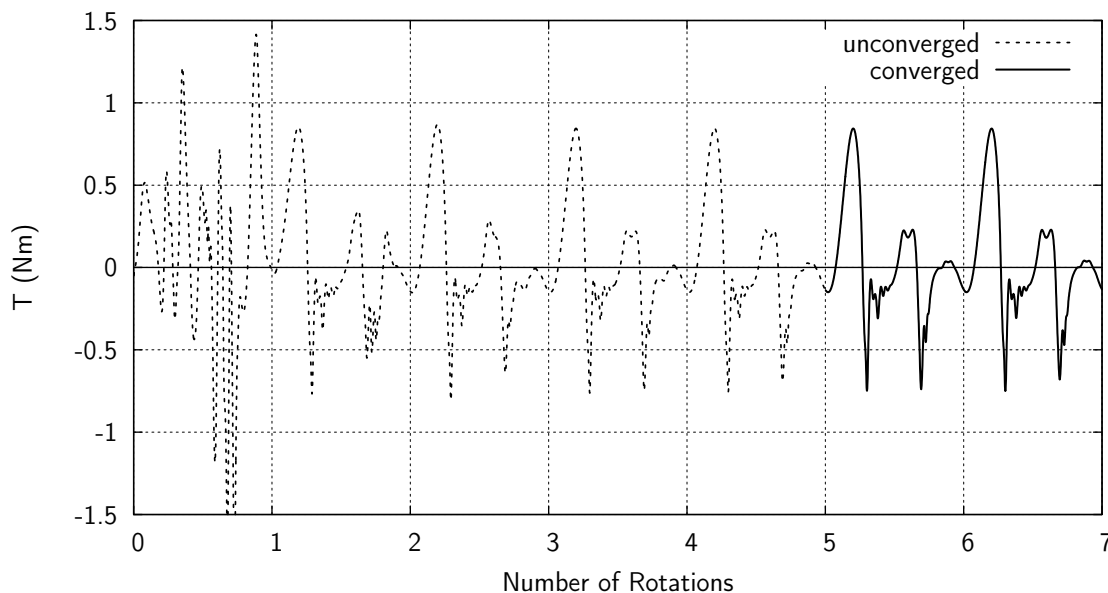


Figure 4.32: A plot showing the convergence of torque for one blade with increasing number of rotations.

### 4.3.6 A New Method for the Calculation of a Corrected Angle of Attack

In order to resolve tangential and normal blade forces into lift and drag forces, an angle of attack, $\alpha$, must be defined, and to determine the corresponding lift and drag coefficients the resultant blade velocity, $V_R$, must also be known. In several studies the determination of $\alpha$ and $V_R$ is achieved for the VAWT blade by considering the geometrical relationship between the blade velocity ($R\omega$) and freestream velocity vectors. However, this does not account for the effect that the rotor has had on the incoming flow: the presence of the VAWT in the freestream results in a streamwise force being exerted on the streamtube, which is slowed down and expands as the mass flow rate must be conserved. The actual incoming velocity is therefore not equal to the freestream, nor is it travelling on the original straight path (see Figure 4.33a). In addition, the upstream blade passes will capture some of the energy of the flow and result in a further reduced flow velocity received by the blades in the downstream part of the rotation. For these reasons the geometrically-derived values of $\alpha$ and $V_R$ may be some way from the actual case, and so the values of lift and drag, and the resulting coefficients, cannot be correctly found.

Attempts to determine the actual $\alpha$ have been made using various mathematical models [62] [93] [94] as the determination of $\alpha$ is a necessity for the use of experimental aerofoil data. Extracting $\alpha$ from a CFD solution is less straight forward, but is necessary if a detailed analysis is to be done respective to traditional terms, i.e. the consideration of lift and drag polars. In later chapters, the CFD simulations are used to establish a better approximation of the variation in $\alpha$ and $V_R$ that a VAWT blade sees during a rotation. Working together with Mr Danao, a new method was established by the Author for extracting a corrected angle of attack, $\alpha_c$, and resultant velocity, $V_{Rc}$ [90]. The method is summarised in the following steps:

1. Flow velocity components in the $x$ and $y$ directions, $V_x$ and $V_y$, were taken from the flowfield at thirty six positions of the blade around one full rotation from which a mean average flowfield was calculated (Figure 4.33).

2. The near-blade flowfield is distorted by the blade itself and also is effected by the shed vorticity (Figure 4.33b), data within a ring containing the blade and the large-scale shed vortices, with $R_{inner} = (R - 2c)$ and $R_{outer} = (R + 2c)$, was cut out of the dataset (Figure 4.34b).

3. Linear interpolation in the radial direction of $V_x$ and $V_y$ was performed for the cut–out region (Figure 4.34c).

4. The interpolated values of $V_x$ and $V_y$ along the blade path were then used to compute the local $\alpha_c$ and $V_{Rc}$ around the rotation.

5. The resulting changes in $\alpha_c$ and $V_{Rc}$ are smoothed with a moving average filter in order to remove any remaining influence of the shed vortices, most significant for low $\lambda$

(Figure 4.35).



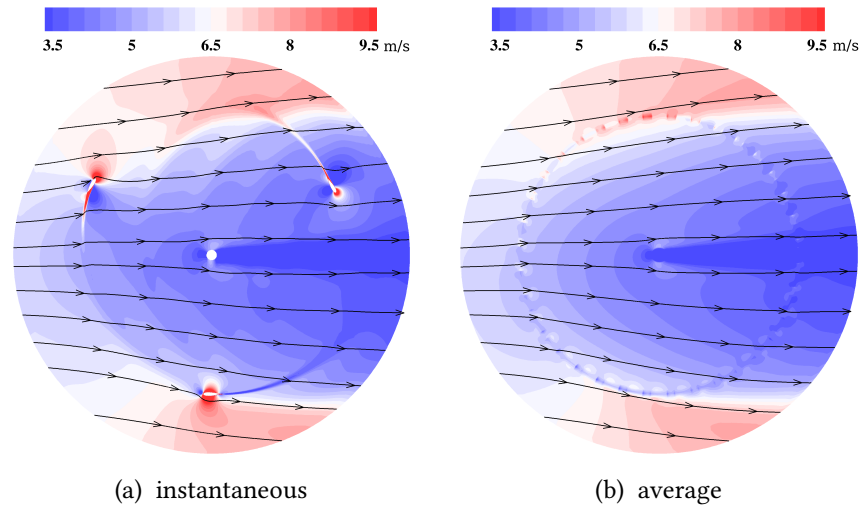(a) instantaneous · · · (b) average

Figure 4.33: Plots showing velocity magnitude contours and streamtraces for instantaneous and averaged flowfields for the near-rotor region at $V_\infty = 6.5\,m/s$, $\lambda = 4$.
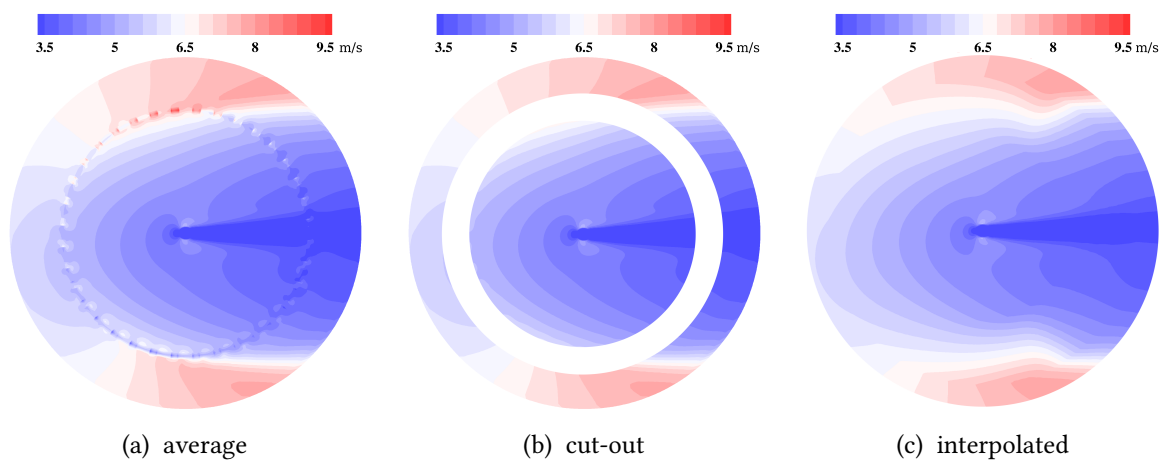


(a) average · · · (b) cut-out · · · (c) interpolated

Figure 4.34: Plots showing velocity magnitude contours for the cut-out process at $V_\infty = 6.5\,m/s$, $\lambda = 4$.

The final result yields the angle of attack and resultant blade velocity that results from the main influence of the presence of the VAWT rotor in the freestream flow, some of the unsteadiness of the VAWT flowfield that exists within a rotation has been neglected; however, the effect on the accuracy of the estimation is considered to be secondary to that of the overall flowfield induction. The method used is an approximation, but one that takes a large and relatively simple step toward a better understanding of the variation of $\alpha_c$ and $V_{Rc}$ with $\psi$.

The technique is verified by the results at $\lambda = 2$ (Figure 4.36a) which show that the value of $\alpha_c$ extracted from the flowfield lies close to the geometrically-derived value. This is expected
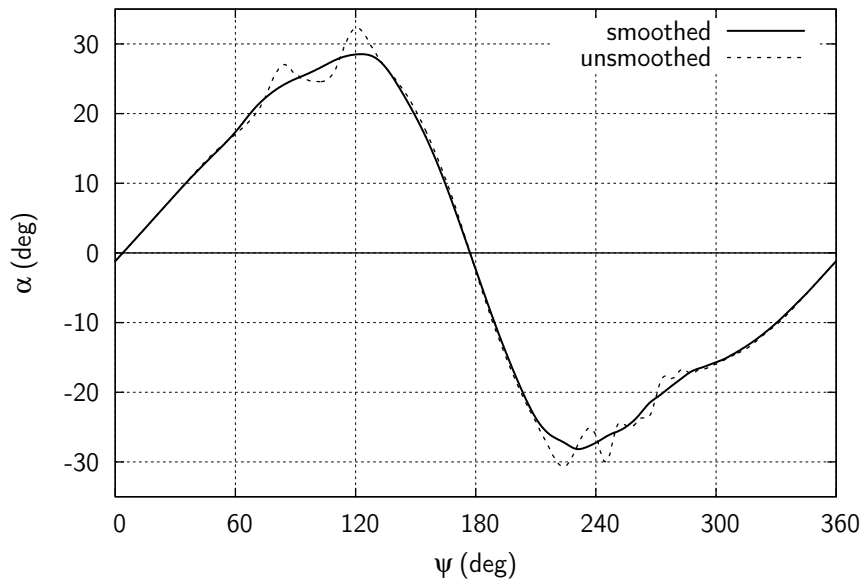
Figure 4.35: A plot showing the effect of moving average smoothing on the value of $\alpha_c$ for $\lambda = 2$

as performance at this tip speed ratio is low and little energy is extracted, therefore little momentum loss would be expected across the rotor. Results at $\lambda = 4$, where significant energy extraction takes place, show a notable difference between $\alpha_c$ and the geometrically-derived value, particularly for the downwind part of the rotation (Figure 4.36b).

The significance of neglecting the influence of the rotor on the flowfield is clearly shown when comparing plots of $C_l$ vs $\alpha$ (Figures 4.37a and 4.37b) and $C_d$ vs $\alpha$ (Figures 4.38a and 4.38b) as derived from geometric and corrected values of $\alpha$ and $V_R$. For both $\lambda = 2$ and 4, the greatest differences are shown for the downwind part of the rotation. In this region, the hysteresis loops are exaggerated if the force coefficient values are calculated with the geometrically-derived value of $V_R$ and $\alpha$, both of which are over-predicted if the rotor effect on the freestream is neglected. At $\lambda = 4$, the rotor has a significant effect on the freestream and it is important to correct for the streamtube expansion: the plot of $C_l$ incorrectly shows non-zero values for the symmetric aerofoil at $\alpha = 0^o$ for the geometrically-derived values (Figure 4.37b). Also shown for $\lambda = 4$, the general over-estimation of geometrically-derived value of $\alpha$ results in an incorrect resolution of the normal and tangential forces which most significantly effects the drag force and leads to an over-predicted drag force in both the upwind and downwind parts of the rotation. An in-depth discussion of the variation of $C_l$ and $C_d$ with $\alpha$ in relation to the flow physics is presented in Section 6.
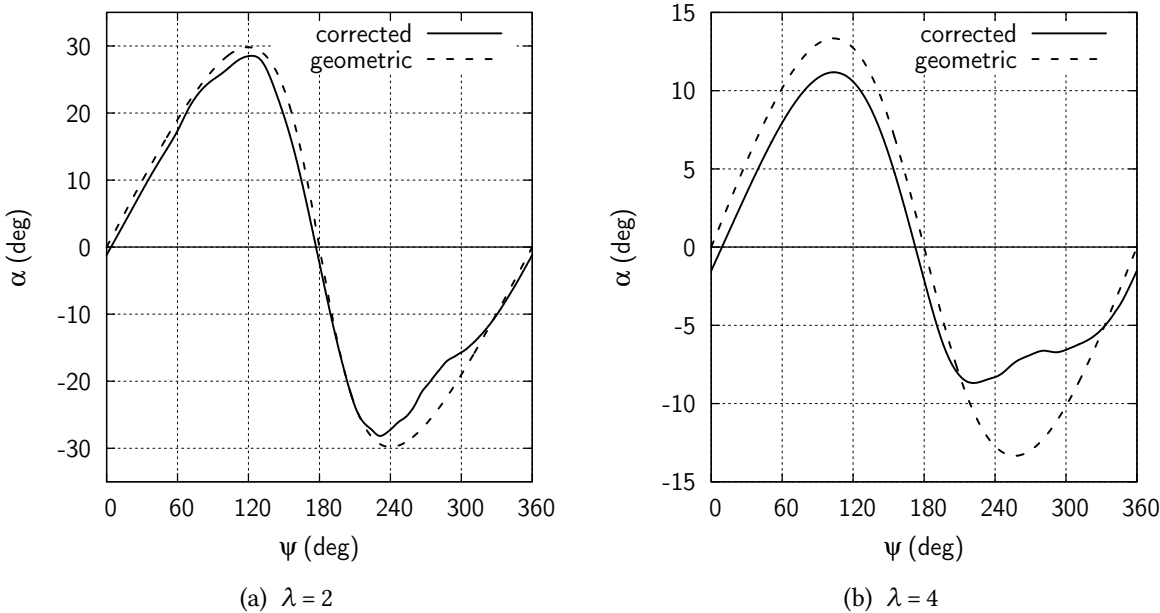
(a) $\lambda = 2$        (b) $\lambda = 4$

Figure 4.36: Plots showing the difference between $\alpha_c$ and the geometrically-derived value for $\lambda = 2$ and 4.
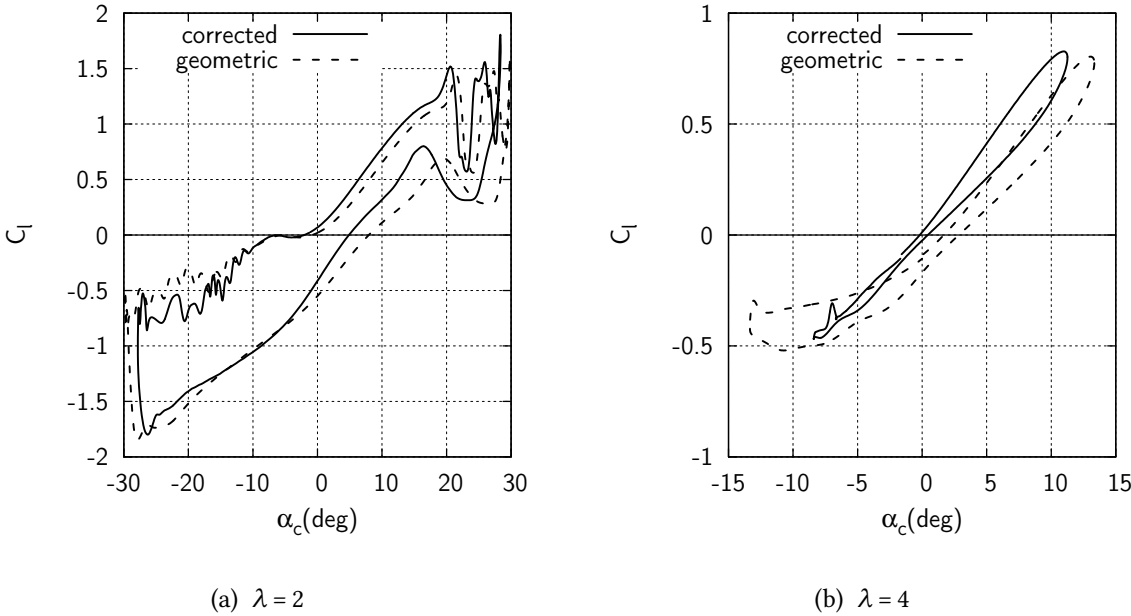


(a) $\lambda = 2$        (b) $\lambda = 4$

Figure 4.37: Plots showing the difference between values determined for $C_l$ when using corrected and the geometrically-derived values for $\alpha_c$ and $V_{Rc}$ at $\lambda = 2$ and 4.
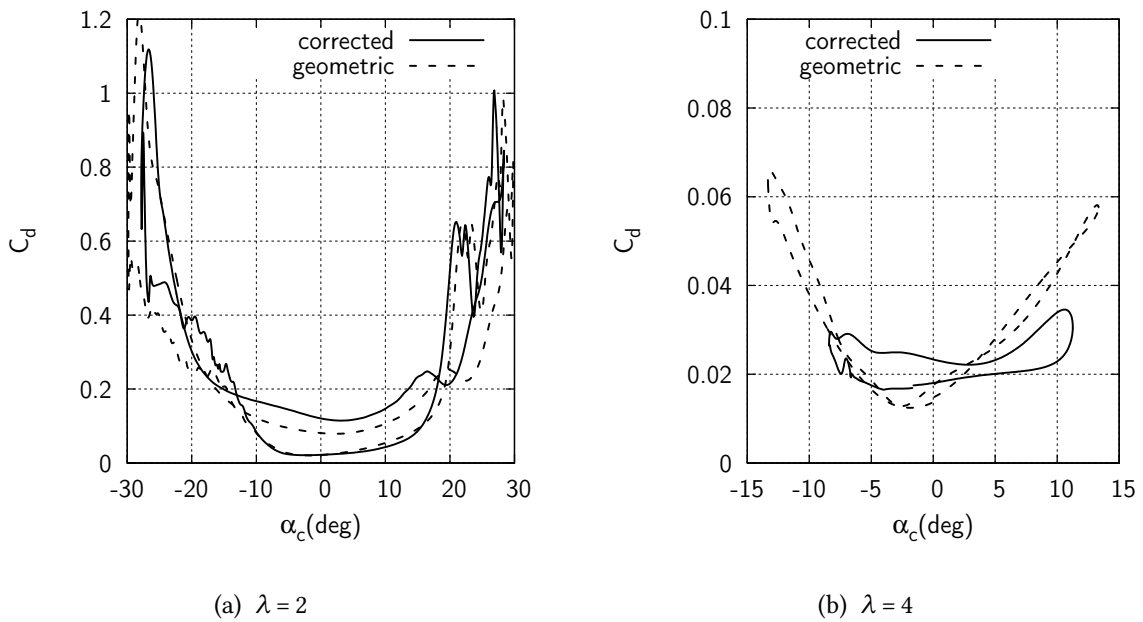
(a) $\lambda = 2$

(b) $\lambda = 4$

Figure 4.38: Plots showing the difference between values determined for $C_d$ when using corrected and the geometrically-derived values for $\alpha_c$ and $V_{Rc}$ at $\lambda = 2$ and 4.

# Chapter 5

# Reference Case: Flow Physics and Performance

## 5.1   Introduction

In this chapter, the $C_p$ performance with changing $\lambda$ is investigated for the rotor model which has been described in Chapter 3, this is done for one case which is labelled the Reference Case. In Section 5.2, the choice of the Reference Case is detailed. Following this, the power performance at the reference conditions is examined in Section 5.3. For the first time, visualisations of the near-blade flow physics over a whole rotation are presented in Section 5.4, and are correlated to the changing performance of the VAWT at three different tip speed ratios. Finally, a validation of the CFD model is carried-out using the experimental performance measurements and visualisations.

## 5.2   Choice of a Reference Case

Using the spin-down test (detailed in Section 3.4) the $C_p$ performance with changing $\lambda$ was measured for several different wind tunnel flow velocities. For each test the reference wind velocity was set whilst the rotor was stationary. When the rotor was spun the wind velocity dropped due to interference effects on the wind tunnel fan (discussed in Section 3.3.5), the calculation of $C_p$ and $\lambda$ was corrected for the relevant drop in wind velocity for each measurement.

The VAWT performance was found to vary significantly depending on the wind tunnel flow velocity (Figure 5.1a). At a wind velocity of 5m/s the entire performance curve was negative, except at very low $\lambda$ where a small positive region was measured where drag-driven performance occurred. With the flow velocity doubled to 10m/s, performance increased by a substantial amount and a maximum $C_{p-blade}$ of over 0.3 was measured, the exact peak could not be determined due to a structural safety limit on the maximum allowable rotational

velocity. The curves at 1m/s intervals between 5 and 10m/s appeared to show a convergence trend toward the highest wind velocity power curve, with reducing differences between the curves observed with each 1m/s increase in the wind velocity.

The dramatic change in efficiency is due to a change in aerofoil performance due to the changing blade Reynolds number. Generally speaking, a transition from a laminar to a turbulent flow might usually be expected to occur for an aerofoil somewhere around $Re \approx 70,000$ [95] [96], although this number may vary significantly from one aerofoil to another. The tested conditions spanned widely across this value with a minimum $Re_{r\omega} = 13,000$ observed when $V_\infty = 5$m/s and $\lambda = 1$, and a maximmum $Re_{r\omega} = 133,000$ when $V_\infty = 10$m/s and $\lambda = 5$ (Table 5.1). This suggested that a laminar to turbulent transition would be quite likely to occur somewhere within the measurement range. To test this, experiments at a higher level of freestream turbulence ($T_u = 1.0\%$) were conducted to cause earlier transition. An increased performance, which was most significant when $V_\infty$ and/or $\lambda$ were low, was observed for all of the tested wind speeds as shown in Figure 5.1b. The 10m/s case changed only slightly when $\lambda < 3$ and the 5m/s case showed the largest change except for when $\lambda \rightarrow 5$. A review of all of the conditions tested showed that the freestream turbulence increase had the most significant effect between $Re_{r\omega} = 30,000$ and 80,000.



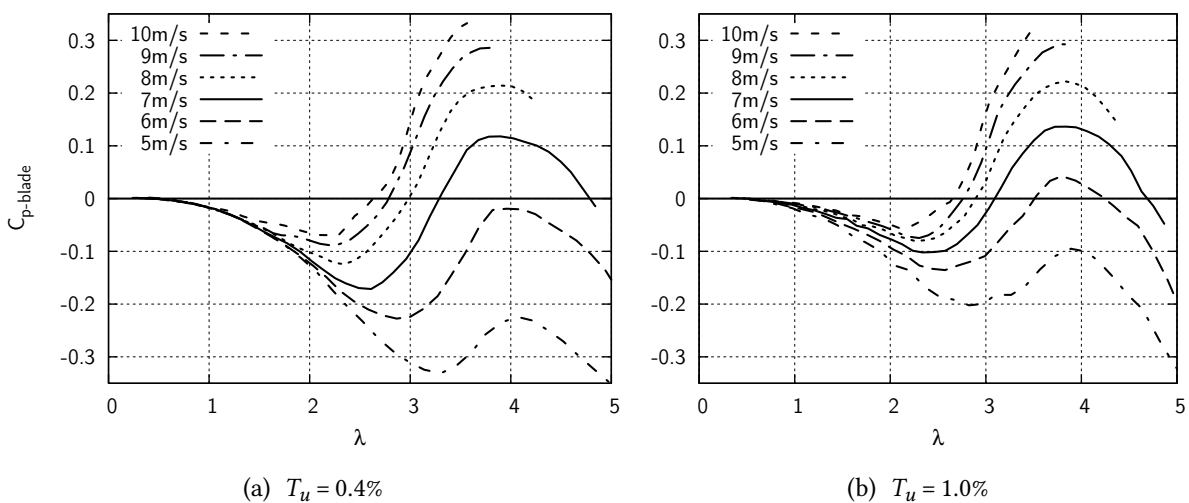(a) $T_u = 0.4\%$        (b) $T_u = 1.0\%$

Figure 5.1: Plots showing $C_{p-blade}$ measurements for varying wind speed and freestream turbulence levels.

In order to perform the detailed flow physics analysis, which is presented in the following chapters, a single reference condition needed to be selected on which to focus the work. It was decided that the highest Reynolds numbers should be tested in order to match as closely as possible the performance of other VAWT rotors in the literature which where mostly of a larger or similar scale to the model of this study. The structural safety limit on the maximum allowable rotational velocity ruled out conditions where $V_\infty \geq 8$m/s, as only a partial curve could be obtained at these wind velocities. The $V_\infty = 7$m/s, $T_u = 1\%$ case was chosen as the

| | $Re_\omega$ | | 1 | 2 | 3 | 4 | 5 |
|---|---|---|---|---|---|---|---|
| | | | | | $\lambda$ | | |
| | 5 | | 13,000 | 27,000 | 40,000 | 53,000 | 67,000 |
| | 6 | | 16,000 | 32,000 | 48,000 | 64,000 | 80,000 |
| $V_\infty$ | 7 | | 19,000 | 37,000 | 56,000 | 75,000 | 93,000 |
| (m/s) | 8 | | 21,000 | 43,000 | 64,000 | 85,000 | 107,000 |
| | 9 | | 24,000 | 48,000 | 72,000 | 96,000 | 120,000 |
| | 10 | | 27,000 | 53,000 | 80,000 | 107,000 | 133,000 |

Table 5.1: Table showing the approximate range in Reynolds numbers for the cases tested at wind velocities of 5 to 10m/s and $\lambda$ from 1 to 5.

next available condition, where the highest Reynolds number was reached and also a full curve could be tested safely.

## 5.3  $C_p$ **Performance of the Reference Case**

For the Reference Case, the approximate range in blade $Re$ is shown in Table 5.2 for the range of tip speed ratios which were tested. The wind velocity was set to 7m/s with the rotor at rest and a minimum wind speed of 6.3m/s was measured at the maximum tip speed ratio, $\lambda$=5 where the interference effects on the wind tunnel fan were most significant. For each data point, both the calculation of $C_p$ and $\lambda$ were corrected for the relevant drop in wind speed. The blade fixing angle was set to zero, but was later altered for tests which are detailed in Chapter 8. The turbulence level was set with the low turbulence grid to 1% intensity; removing the grid would allow the turbulence levels to be lowered if required.

| $\lambda$ | | 1 | 2 | 3 | 4 | 5 |
|---|---|---|---|---|---|---|
| $Re_{max}$ | | 37,000 | 56,000 | 75,000 | 93,000 | 112,000 |
| $Re_{min}$ | | 0 | 19,000 | 37,000 | 56,000 | 75,000 |
| $Re_\omega$ | | 19,000 | 37,000 | 56,000 | 75,000 | 93,000 |

Table 5.2: Table showing the approximate range in Reynolds numbers for the Reference Case at $\lambda$ from 1 to 5. $Re_{max}$ and $Re_{min}$ are the Reynolds numbers resulting from the blade travelling into the wind (at $\psi = 0°$), and with the wind ($\psi = 180°$) respectively.

The results presented in Figure 5.2 show the $C_p$ resulting from the blades only, $C_{p-blade}$, the resistive torque due to bearings and structure was removed from the result using the method discussed in Chapter 3. The form of the resulting curve shows the following typical characteristics of VAWT performance:

1. Initial low (drag driven) performance at very low $\lambda$.

2. Performance falls away initially with rising $\lambda$, giving a negative trough.

3. With a further rise in $\lambda$, the $C_{p-blade}$ rises up to a peak value.

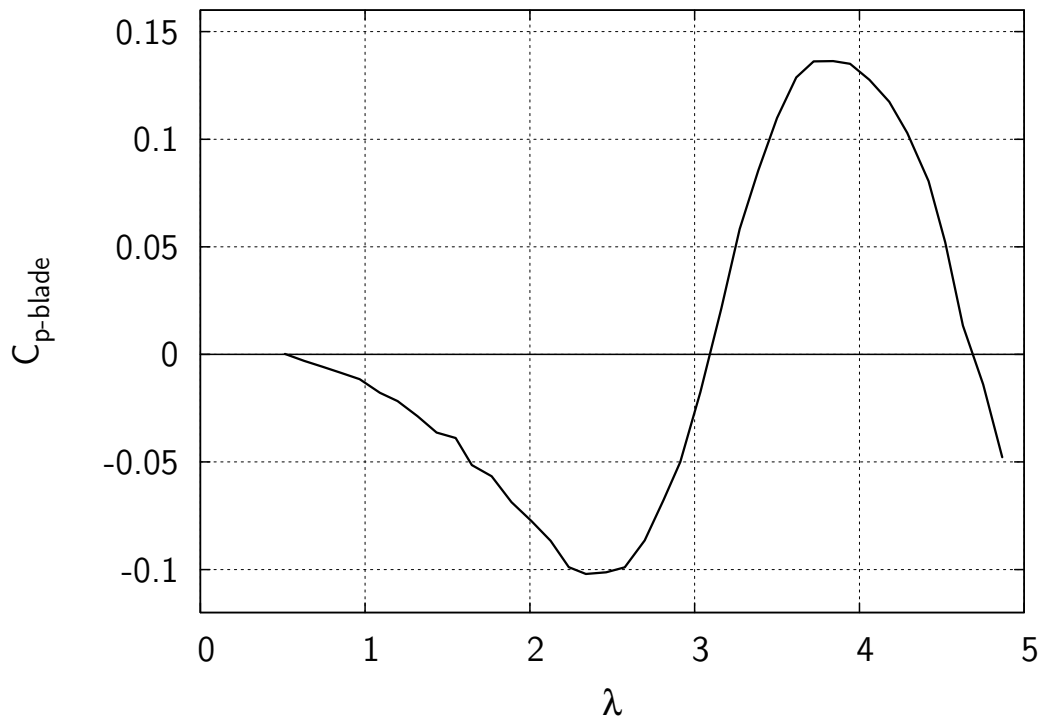4. When $\lambda$ reaches very high values, $C_{p-blade}$ again begins to fall away.



Figure 5.2: $C_{p-blade}$ vs $\lambda$ for the reference 7m/s case.

A fairly low peak $C_{p-blade}$ performance of 0.14 is observed at a $\lambda = 3.8$. This is particularly low when considering that the addition of an amount of structural drag and bearing resistance would further reduce this on a real VAWT. The curve also has quite a narrow peak, and the area of negative performance seems particularly deep when compared to published curves for other VAWTs, as shown throughout the literature review (Chapter 2). Negative performance for a certain band of $\lambda$ was studied for the purpose of improving VAWT self-starting capabilities by Baker who labelled it the 'dead band' [38]. Baker's studies showed that good low-Reynolds number performance was desirable to minimise the dead band. In his thesis, Kirke [31] analysed the effect of Reynolds number on the dead band using a multiple streamtube model with aerofoil data from Sheldahl and Klimas [97] which covered a wide range of Reynolds numbers. Kirke showed that lowering the Reynolds number had the effect of reducing overall performance (Figure 5.3), including a deepening of the dead band and a narrowing of the $C_p$ performance peak, both of which are shown by the measured experimental data in Figure 5.2. Parametric studies by McIntosh [32] show that a curve of this shape can be obtained with poor lift and drag performance and a low stalling angle, such characteristics would be typical for a

low Reynolds number aerofoil. For the VAWT model under test, the blade Reynolds numbers range from 20,000 to 110,000 (Table 5.2). So, a low Reynolds number aerofoil performance is expected and the literature shows that this can lead to a correspondingly low $C_p$ (e.g. Figure 5.3), which is indeed what is observed in the results for this Reference Case (Figure 5.2).

The tests conducted at a higher Re showed an improved performance of the current configuration but, most importantly for this study, the fundamental form of the curve (outlined above) was not observed to change with increasing Re. So, despite the relatively low $C_p$, the model and its performance make a suitable test case for performance analysis.
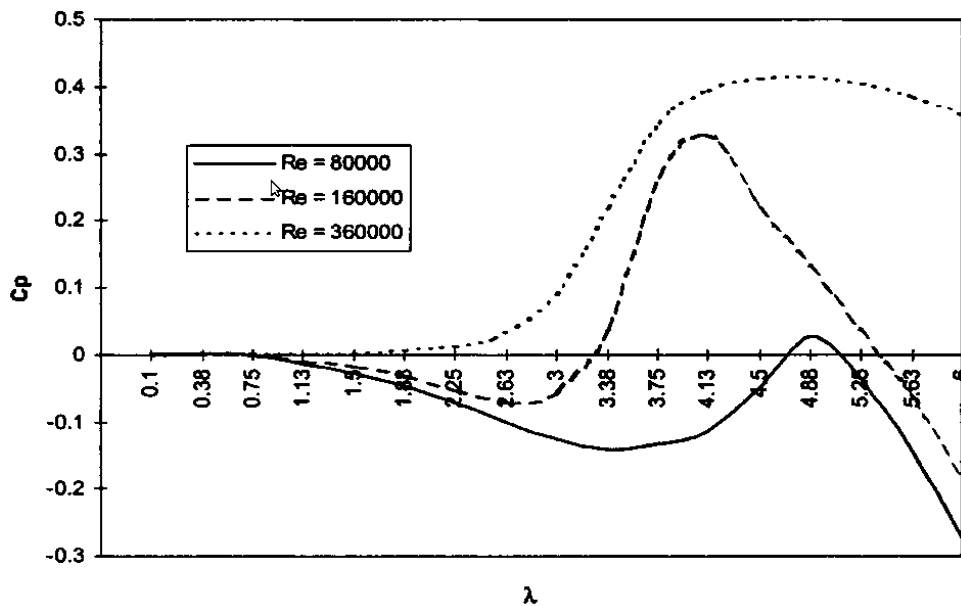


Figure 5.3: Kirke's investigation [31] showing the effect of low Reynolds number performance on the shape of the $C_{p-blade}$-$\lambda$ curve.

## 5.4   PIV Visualisation

The experimental power curve measurements have shown that $C_{p-blade}$ varies significantly with $\lambda$, as would typically be expected for a VAWT. To reveal the flow physics at work and to begin to understand the mechanisms behind the performance changes with $\lambda$, flowfield visualisations of the near-blade region were obtained using PIV. Visualisations were obtained throughout a full rotation, which, as far as the Author is aware, has not been attempted by any other published studies. The PIV measurements concentrated on three tip speed ratios, which covered the key regions of the $C_{p-blade}$-$\lambda$ curve:

1.  $\lambda = 2$ is near the minimum $C_p$,

2.  $\lambda = 3$ is on the part of the curve where the $C_p$ is rapidly increasing with increasing $\lambda$,

3. $\lambda = 4$ is near to $C_{p-max}$.

Measurements were taken at 10° $\psi$ intervals, following one of the blades through a whole rotation, as illustrated in Figure 5.4. The the blade was centred in the FOV which was 140mm x 140mm. Contours of vorticity are used to visualise the near-blade wake, with the same levels being maintained for all images: clockwise-rotating vortices are represented by blue contours, anti-clockwise by red, as previously defined in Section 4.2.4). As the discussion refers mainly to the position of vortices, a colour-scale is not shown beside every image but may be found in Section 4.2.4 if required.
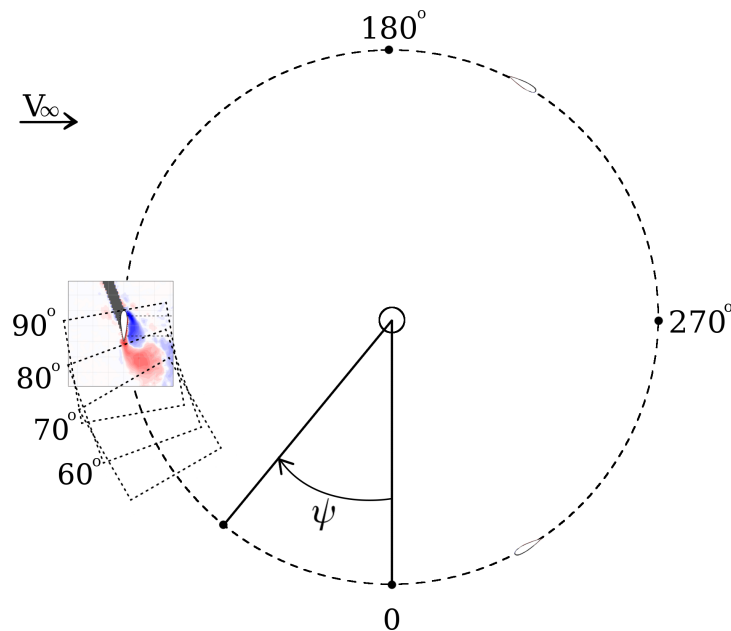


Figure 5.4: Diagram showing example PIV plots with reference to the overall rotor

The geometrically derived value of $\alpha$ becomes an increasingly poor estimate as $\lambda$ increases due to the greater impedance which is presented by the rotor to the flow. The rotor exerts a force on the incoming flow, slowing it down and forcing the streamtube to expand in order to conserve mass flow rate. The energy extraction by the blades in the upwind part of the rotation reduces the flow velocity in the downwind part of the rotation and lowering the angle of attack on the blades in this region. To account for this, the discussion of the flow physics are discussed relative to a corrected angle of attack $\alpha_c$ which has been obtained from a CFD solution (via the method detailed in Section 4.3.6) and has been shown to be reasonably well-matched to the experiment (later discussed in Section 5.5). For comparison and completeness, the geometrically derived value is also presented.

### 5.4.1 $\lambda = 2$

A plot of the change of angle of attack with azimuth angle shows the typical skewed sinusoidal variation (Figure 5.5), with a slightly lower range in $\alpha_c$ shown relative to $\alpha$ due to the rotor's effect on the flow. The flow speed is at its lowest for the downwind part of the rotation, due to the influence of the upwind blade passes and also the shaft, which results in a notable drop in $\alpha_c$. Overall, the corrected angle of attack shows only small changes from the geometrically-derived value at this condition, indicating there is minimal impedance on the flow and so the streamtube expansion is small. The $C_p$ performance at $\lambda = 2$ is shown to be low and is actually negative, and so a large momentum drop is not expected due to the lack of useful energy extraction by the VAWT. Some slight unevenness in the $\alpha_c$ curve is shown which is a product of the cut-out and interpolation process which is detailed in Section 4.3.6. The drop in $\alpha_c$ around $\psi = 270°$ is due to the presence of the drive shaft wake and resulting low wind velocity in this region.
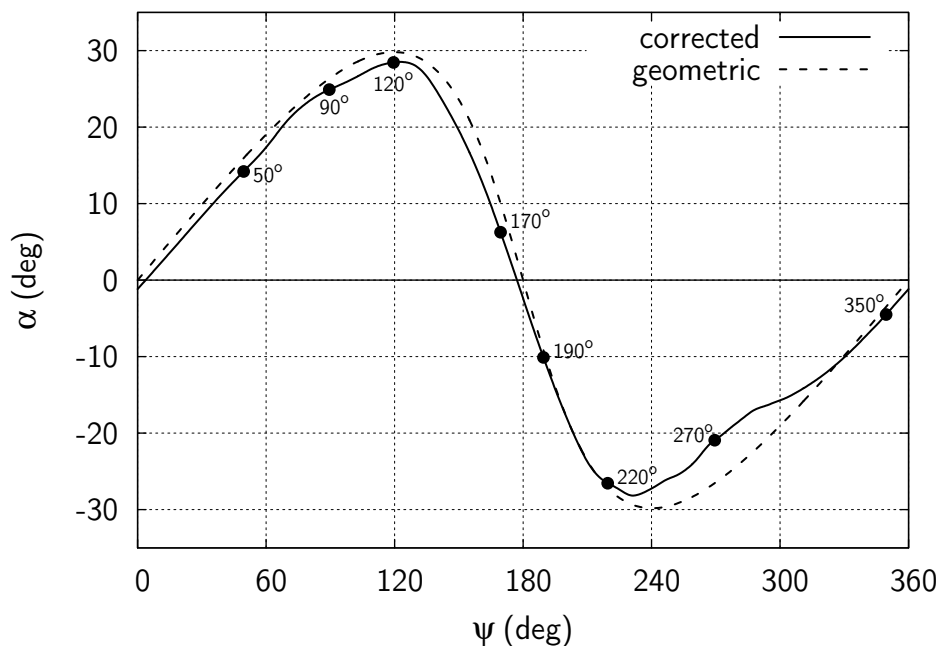


Figure 5.5: $\alpha$ vs $\psi$ for $\lambda = 2$.

PIV flow visualisations show the flow to be attached from the beginning of the rotation (Figure 5.6a) up to between $\psi = 50°$ and $\psi = 60°$, where the beginning of a leading edge roll-up (blue) is observed as part of the dynamic stall process (Figures 5.6b and 5.6c). Figure 5.5 shows $\alpha_c = 17.3°$ at $\psi = 60°$, which would certainly be above the static-stall angle for this aerofoil. Indeed, a CFD solution showed a stall angle of $11°$ for a static NACA0022 aerofoil. The rapid increase in $\alpha_c$ can be thought of as a 'pitch-up' motion; in tests on a pitching aerofoil such a motion is shown to increase the angle of attack at which stall occurs [58].
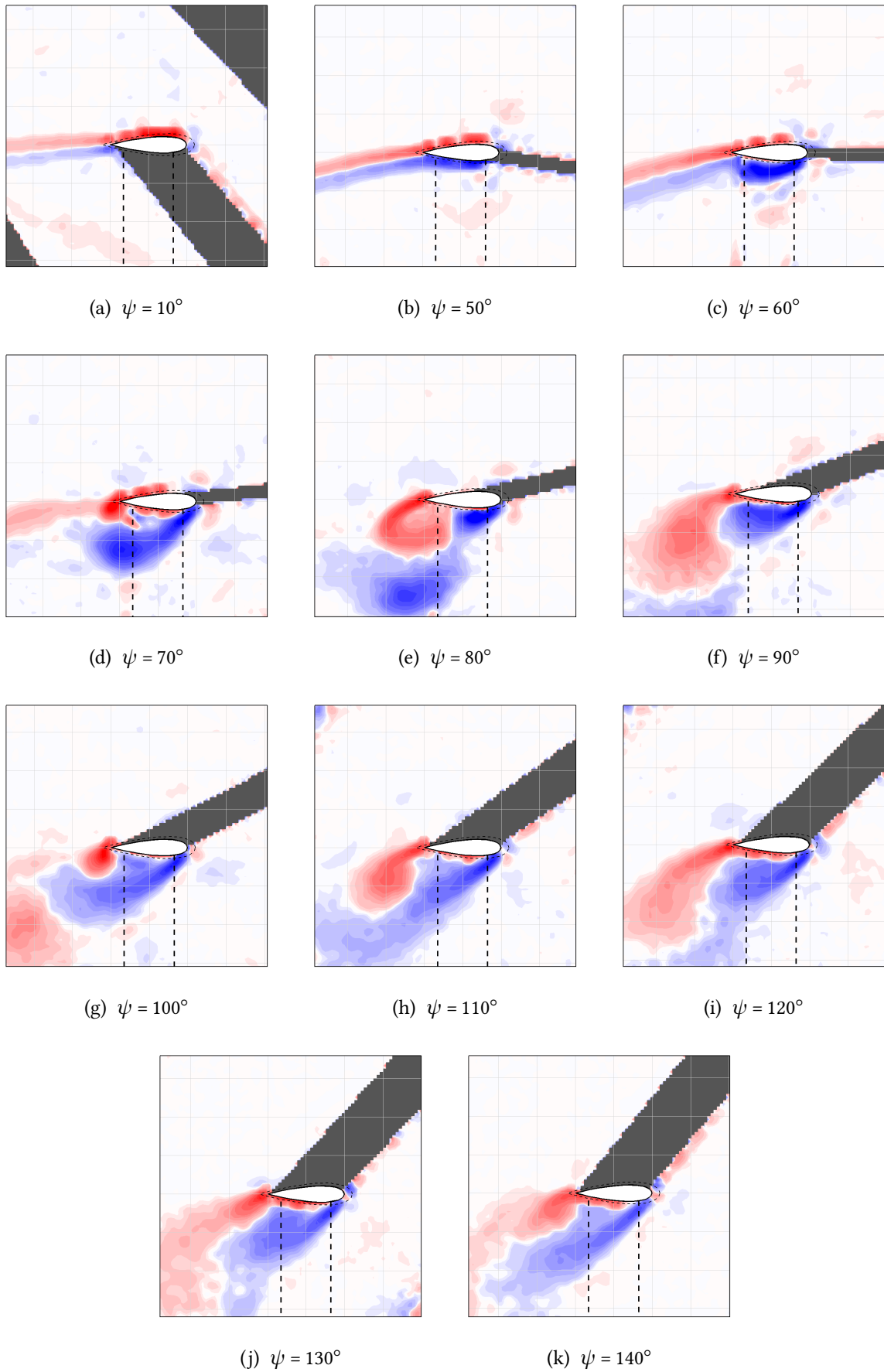
Approximately 10° later in the rotation, at $\psi = 70°$, the vortex originating from the leading edge is observed to have left the aerofoil surface, and the beginning of a trailing edge roll-up (red) is shown (Figure 5.6d). At $\psi = 80°$, a trailing edge vortex (red) is shed, and a second leading edge roll up (blue) is shown (Figure 5.6e). A further 10° later in the rotation, the second leading edge vortex is leaving the near-surface region at $\psi = 90°$ where $\alpha_c$ has now reached 25°(Figure 5.6f).

In the images from $\psi = 0°$ to 90°, clear structures have been shown in the averages of 100 ensembles. This suggests the stall point, roll-up and shedding pattern of the initial vortex-pair are similar between each rotation, which has already been shown for this case in Figure 4.21. Another pair of vortices are shed between $\psi = 90°$ and 110° (Figures 5.6f to 5.6h). Less defined structures show that the position of the secondary vortex pair is subject to more variation than the first pair, as is shown in Figure 5.7.

For the ensemble averages at $\psi = 120°$ to 140° the vortex positions vary greatly which results in two bands of vorticity being shown in the ensemble-averaged plots. The vorticity bands have some asymmetry which alternates between leading and trailing edges as shown in Figures 5.6i to 5.6k; this indicates the vortex shedding is continuing to alternate between leading and trailing edges of the aerofoil.

With $\alpha_c$ dropping to 5.9°, the flow has not yet attached by $\psi = 170°$ (Figure 5.8a) due to the rapid rate of drop in $\alpha_c$ from the deeply stalled condition. The rapid decrease in $\alpha_c$ can be thought of as a 'pitch-down' motion; in tests on a pitching aerofoil such a motion is shown to lead to a delayed reattachment of the flow as part of the dynamic stall process, which results in significant hysteresis in the aerodynamic forces [58].

Plots at $\psi = 180°$ and $\psi = 190°$ (Figures 5.8b and 5.8c) reveal a significant lag in the flow reattachment. At $\psi = 190°$ the flow is observed to be close to reattachment although $\alpha_c$ has dropped to -10.5°. Part of the wind tunnel structure prevented measurements at $\psi = 200°$ and 210°, and due to constraints of the laser position the laser shadow position obscures most of the view of the near-blade wake at $\psi = 220°$ (Figure 5.9a). Despite this, evidence of a leading edge roll up is shown by an area of high leading-edge vorticity, at this point $\alpha_c$ has already reached -26.7°. All of this shows that if the flow had reattached in the low $\alpha$ region of the mid-rotation, it did so only very briefly. At $\psi = 230°$ the leading-edge vortex (red) can be seen leaving the blade surface (Figure 5.9b), and is shortly followed by a vortex (blue) from the trailing edge at $\psi = 240°$ (Figure 5.9c). A second pair of vortices is shed between $\psi = 250°$ and $\psi = 270°$ (Figures 5.9d to 5.9f). As with the upwind shedding, the positioning of the first pair of vortices is close between each sample, and varies more for the second pair. Above $\psi = 231°$, $\alpha_c$ reduces and the depth of stall begins to reduce, vortices continue to be shed with little similarity across individual rotations (Figures 5.9f to 5.9i). Even by $\psi = 350°$, where $\alpha_c = -4.3°$ the flow has still not reattached to the blade surface (Figure 5.9j), it is only between $\psi = 350°$ and $\psi = 0°$, where $\alpha_c$ drops from -4.3° to -1.2° that the flow is again attached to the blade (Figure 5.9k), which would lead to a significant drop in drag.

(a) $\psi = 10°$

(b) $\psi = 50°$

(c) $\psi = 60°$

(d) $\psi = 70°$

(e) $\psi = 80°$

(f) $\psi = 90°$

(g) $\psi = 100°$

(h) $\psi = 110°$

(i) $\psi = 120°$

(j) $\psi = 130°$

(k) $\psi = 140°$

Figure 5.6: Plot of z-vorticity showing the upwind stalling process for $\lambda = 2$

(a) Sample 1          (b) Sample 2          (c) Sample 3
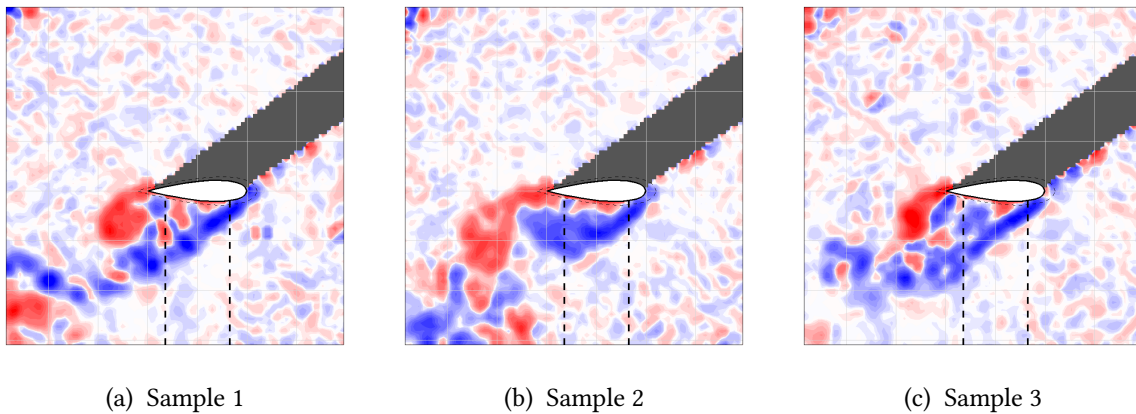
Figure 5.7: Plot of z-vorticity showing varying vortex positions for $\psi = 110°$, $\lambda = 2$



(a) $\psi = 170°$          (b) $\psi = 180°$          (c) $\psi = 190°$
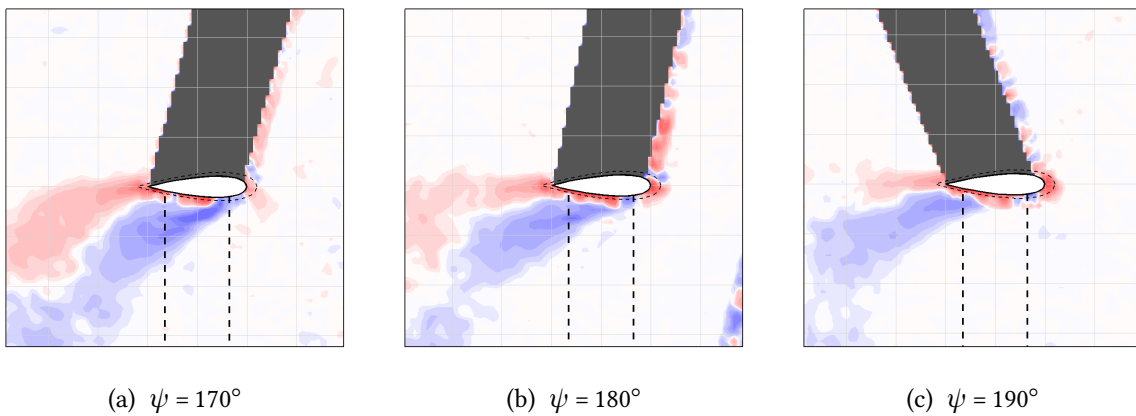
Figure 5.8: Plot of z-vorticity showing a delayed flow reattachment at low $\alpha$ for the mid-rotation positions for $\lambda = 2$

**Summary of Flowfield at $\lambda = 2$**

The PIV visualisations have shown that for $\lambda = 2$ the flow is detached from the blade surface for the majority of the rotation, it is only between $\psi = 0°$ to $50°$ that the flow is fully-attached. A characteristic dynamic stalling process is shown: the blade is observed to stall at a high angle of attack and there is a substantial delay in the reattachment of the flow. Shortly after stalling, chord-sized vortex pairs are shed from the blade at regular intervals in the rotation, before the non-deterministic element of the vortex shedding becomes more significant as $\psi$ increases. Towards the mid-point of the rotation the flow nears reattachment before a similar stalling process is shown for the downwind part of the rotation. Whilst lift and drag forces are not obtained from the PIV measurements, drag would certainly be high for most of the rotation due to the separated flow and it is understandable that such poor $C_p$ performance is measured. The lift and drag forces are examined using CFD simulations in later sections.
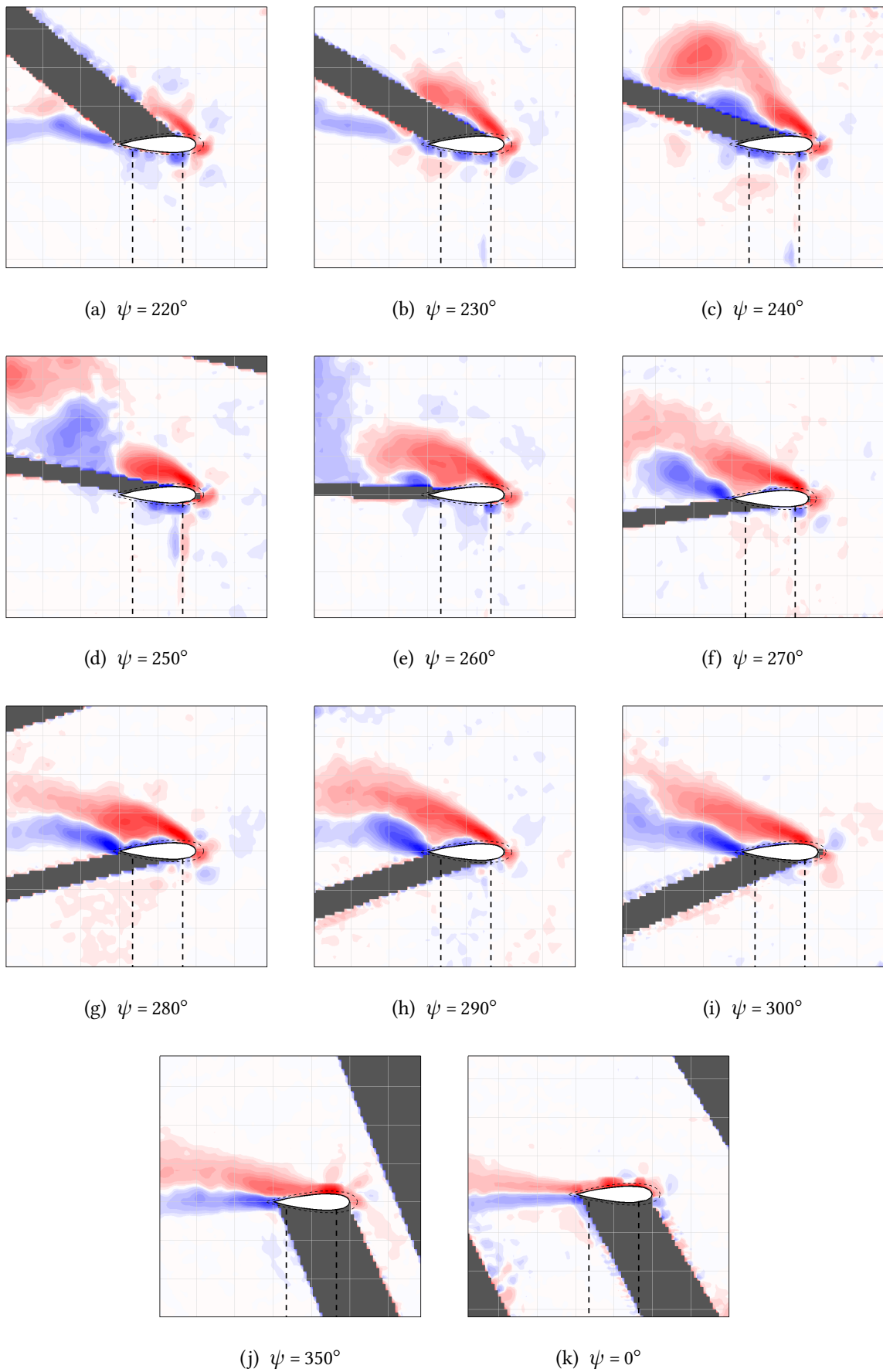
(a) $\psi = 220°$    (b) $\psi = 230°$    (c) $\psi = 240°$

(d) $\psi = 250°$    (e) $\psi = 260°$    (f) $\psi = 270°$

(g) $\psi = 280°$    (h) $\psi = 290°$    (i) $\psi = 300°$

(j) $\psi = 350°$    (k) $\psi = 0°$

Figure 5.9: Plot of z-vorticity showing the downwind stalling process and eventual reattachment for $\lambda = 2$

### 5.4.2 $\lambda = 3$

Figure 5.10 shows that for $\lambda = 3$, the increased $\lambda$ results in a higher flow impedance than at $\lambda = 2$. As a result, larger differences are shown between the corrected and geometrically-derived values of angle of attack. Again, a notable drop in $\alpha_c$ is observed for the downwind angles where the flow speed is at its lowest due to the influence of the upwind blade passage and the shaft.
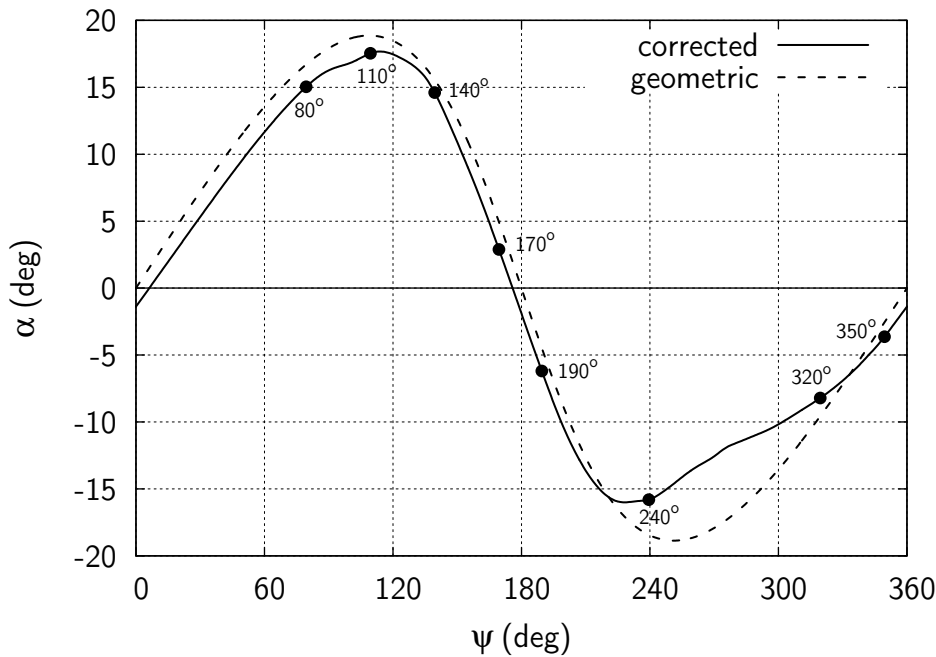


Figure 5.10: $\alpha$ vs $\psi$ for $\lambda = 3$.

PIV flow visualisations show the flow to be attached from the beginning of the rotation (Figure 5.11a) up to $\psi = 80°$, where the beginning of a leading edge roll-up (blue) is observed (Figure 5.11b and 5.11c). At the onset of stall $\alpha_c = 15.2°$, which is slightly lower than for $\lambda = 2$ condition; a drop in the rate of change of angle of attack would be expected to reduce the dynamic stall angle [58]). At $\psi = 100°$, the first vortex originating from the leading edge has left the aerofoil surface, and the beginning of a trailing edge roll-up (red) is shown (Figure 5.11d). At $\psi = 110°$, the trailing edge vortex is shed, and a second leading edge roll up is shown (Figure 5.11e), which has left the near-surface region by $\psi = 140°$ (Figure 5.6f), and now $\alpha_c = 26°$. As with the $\lambda = 2$ condition, the secondary vortex pairs have less similarity between rotations. In addition, the secondary structures are smaller than the primary vortex pair as $\alpha_c$ has begun to reduce; after reaching a maximum of $17.7°$ $\psi = 113°$, $\alpha_c$ has dropped to $14.5°$ at $\psi = 140°$.

As with the $\lambda = 2$ condition there is a significant delay in the reattachment of the flow; with $\alpha_c$ dropping to $2.7°$ at $\psi = 170°$, the flow has not yet attached (Figure 5.12a). The flow

(a) $\psi = 10°$

(b) $\psi = 80°$

(c) $\psi = 90°$

(d) $\psi = 100°$

(e) $\psi = 110°$
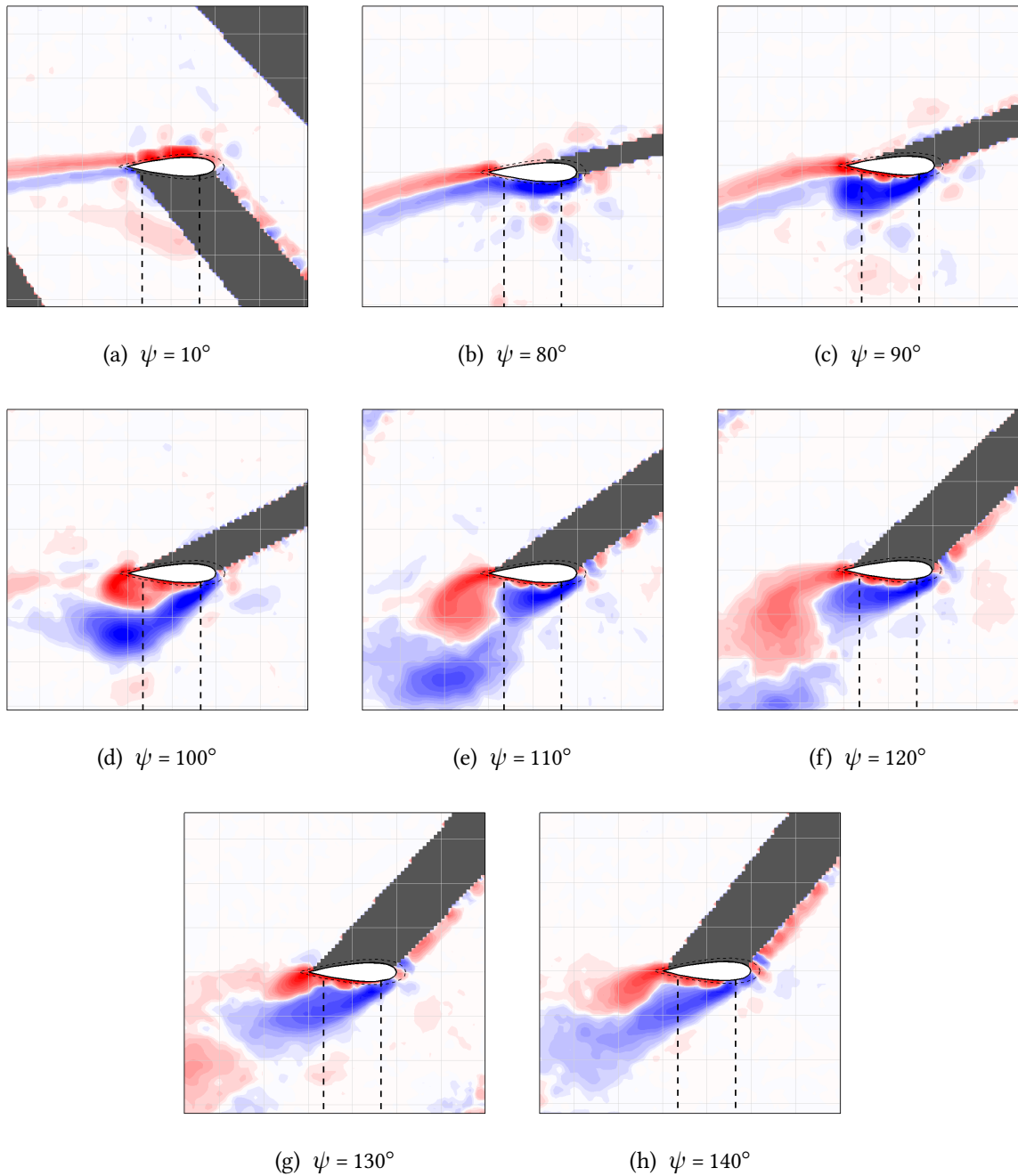
(f) $\psi = 120°$

(g) $\psi = 130°$

(h) $\psi = 140°$

Figure 5.11: Plot of z-vorticity showing the upwind stalling process for $\lambda = 3$

does appear to attach at $\psi = 190°$, where $\alpha = -6.4°$, which is an improvement over the $\lambda = 2$ condition and appears to have been assisted by the reduced rate of change of $\alpha_c$. However, this still shows a large stall to reattachment hysteresis, which results in separated high-drag flow for more of the rotation that might at first be expected.



(a) $\psi = 170°$        (b) $\psi = 180°$        (c) $\psi = 190°$
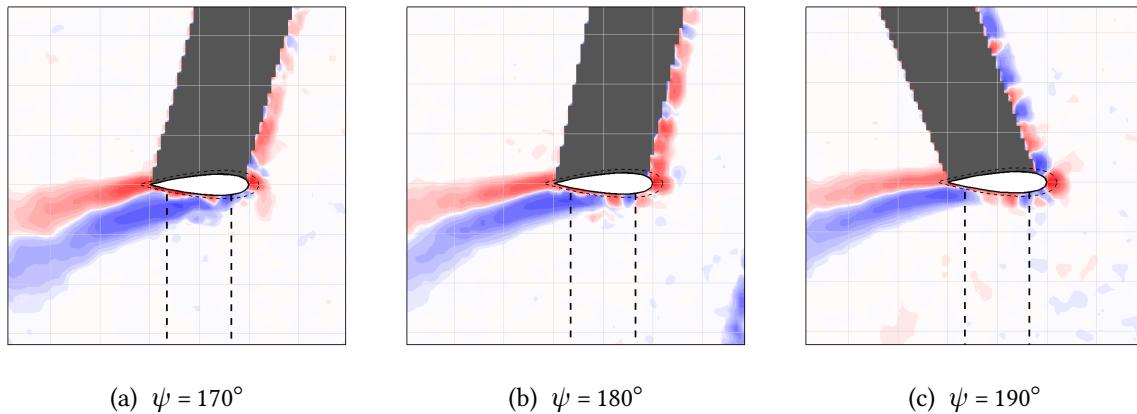
Figure 5.12: Plot of z-vorticity showing a delayed flow reattachment at low $\alpha$ for the mid-rotation positions for $\lambda = 3$

Although $\alpha_c$ reaches a maximum of $16°$ at $\psi = 228°$, the flow appears to remain attached until after $\psi = 230°$, as a leading edge separated flow is visible at $\psi = 240°$ in Figure 5.13c. However, the wake at $\psi = 220°$ (Figure 5.13a) and $230°$ (Figure 5.13b) looks much thicker that of the attached flow at low $\psi$. This suggests that the flow has not attached along the full chord-wise length of the blade surface. The stalling process from $\psi = 240°$ onwards does not feature any large repeated structures, instead small vortices are shed at random intervals (Figures 5.13d to 5.13g) which further suggests the flow was already partially separated. Again, full flow reattachment is delayed: occuring somewhere between $\psi = 320°$ to $350°$, where $\alpha_c$ drops from $8.2°$ to $3.5°$. As for the reattachment process around $\psi = 190°$, the second reattachment also occurs at slightly higher values of $\alpha_c$ than were observed for the $\lambda = 2$ condition. A drop in the rate of change of angle of attack would be expected to reduce the dynamic stall hysteresis, resulting in earlier reattachment, as well as the previously mentioned reduction in the overshoot of the stall point.

**Summary of Flowfield at $\lambda = 3$**

The flowfield images for the $\lambda = 3$ condition show that the flow is detached from the blade surface for much of the rotation, although to a lesser extent than has been shown for the $\lambda = 2$ condition. With $\alpha_c$ lower at stall and higher at reattachment, the dynamic stall hysteresis appears to be reduced when compared to the $\lambda = 2$ condition. Again, drag would certainly be high for most of the rotation due to the separated flow, but the larger region of attached flow allows an improved $C_p$ performance over the $\lambda = 2$ condition.

(a) $\psi = 220°$

(b) $\psi = 230°$

(c) $\psi = 240°$

(d) $\psi = 250°$

(e) $\psi = 270°$

(f) $\psi = 290°$

(g) $\psi = 310°$
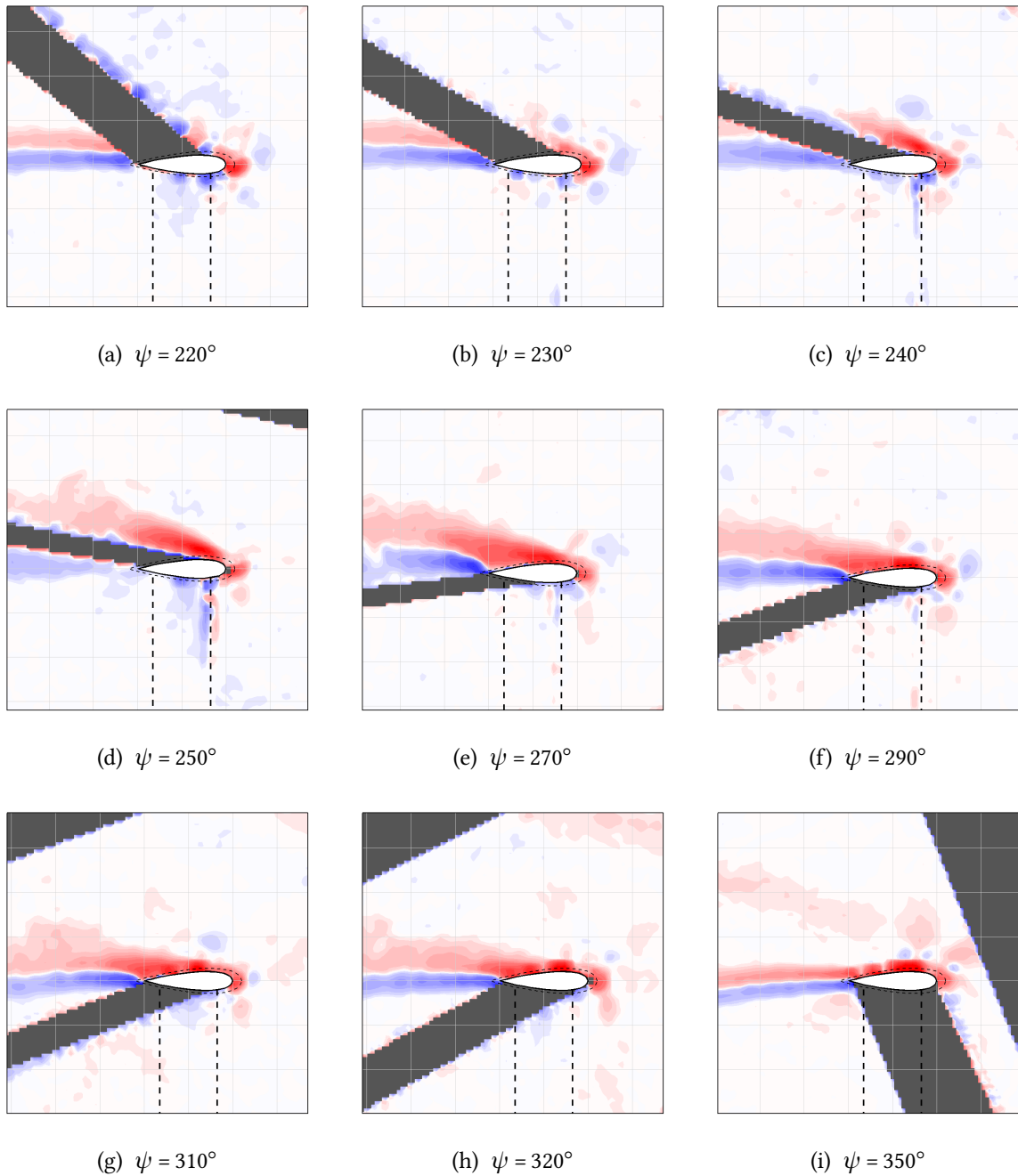
(h) $\psi = 320°$

(i) $\psi = 350°$

Figure 5.13: Plot of z-vorticity showing the downwind stalling process for $\lambda = 3$

### 5.4.3 $\lambda = 4$

When compared to the $\lambda = 2$ and 3 conditions, a plot of the change of angle of attack with azimuth angle shows the largest differences between the corrected angle of attack and the geometrically-derived value for $\lambda = 4$ (Figure 5.14). The upwind peak value reduces by 15% from 13.3° to 11.2° and the downwind peak by 35% from -13.3° to -8.6°. The increased $\lambda$ leads to a greater impedance and the positive $C_p$ performance results in a significant momentum drop across the streamtube. One effect of this is the largest non-zero value of $\alpha$ at $\psi = 0°$ and 180° of the three tested tip speed ratios.
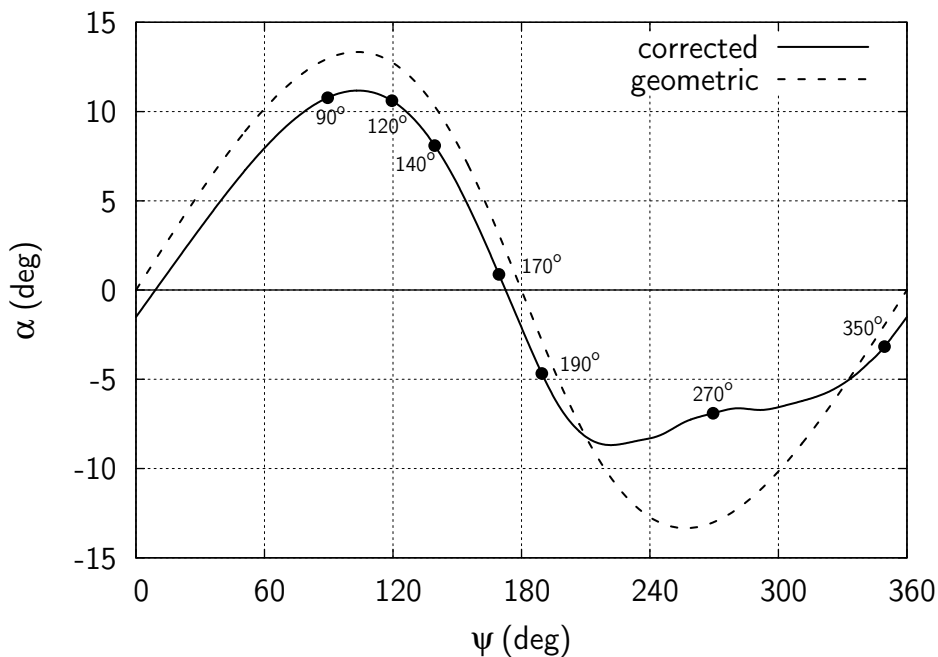


Figure 5.14: $\alpha$ vs $\psi$ for $\lambda = 4$.

PIV flowfield visualisations show the flow to be fully-attached from the beginning of the rotation (Figure 5.15a) up to approximately $\psi = 90°$. Between $\psi = 90°$ and $\psi = 120°$, despite a only small change in $\alpha_c$, which slightly rises and then falls in this region, a gradual separation from the trailing edge can be seen to moves forwards along the aerofoil suction surface as $\psi$ increases. At $\psi = 130°$, $\alpha_c$ is beginning to drop rapidly and a large vortex (blue) rolls up in the already separated flow as the 'pitch-down' motion occurs. The vortex is shed around $\psi = 140°$, although the exact position of this occurrence varies by a small amount between rotations and so the shed vorticity is spread over a small area in Figure 5.15g. A trailing edge vortex is also shown to roll up in $\psi = 140°$, but the lack of measurements at $\psi = 150°$ and 160° mean that the shedding behaviour is not fully captured.

There is again a significant delay in the reattachment of the flow, which occurs between $\psi = 180°$ to 190° (Figures 5.16b and 5.16c), where $\alpha_c$ drops from -2.1° to -4.8°. The vorticity

(a) $\psi = 10°$

(b) $\psi = 90°$

(c) $\psi = 100°$

(d) $\psi = 110°$

(e) $\psi = 120°$
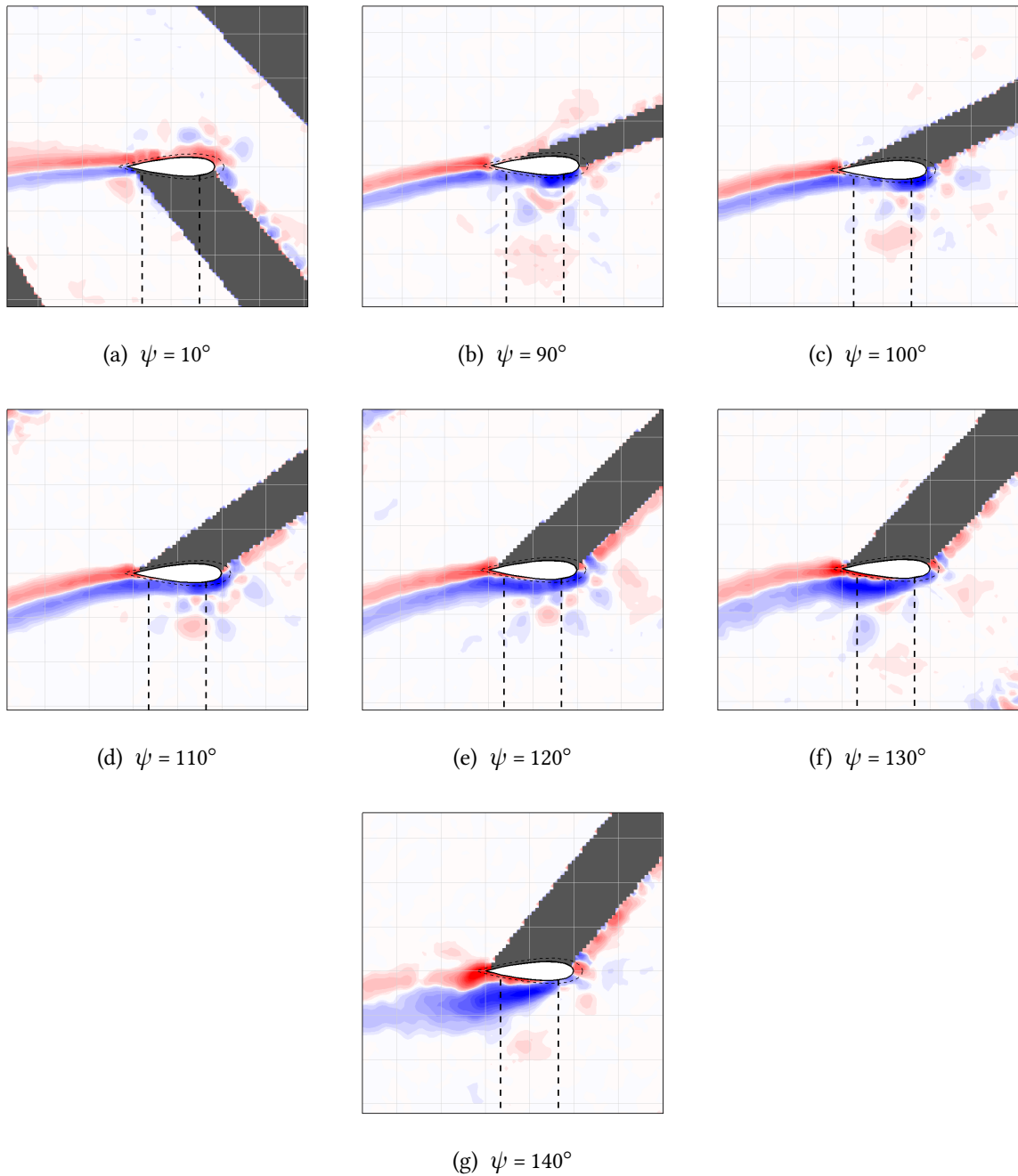
(f) $\psi = 130°$

(g) $\psi = 140°$

Figure 5.15: Plot of z-vorticity showing the upwind stalling process for $\lambda = 4$

shed from the stalling of the previous blade can also be seen ahead of the blade. As the blade speed is higher than the wind speed, the blade catches-up the previous blade's wake, which can also be seen to dissipate and move outward of the rotor centre due to the effect of the expansion of the streamtube (Figures 5.16a to 5.16c).



(a) $\psi = 170°$          (b) $\psi = 180°$          (c) $\psi = 190°$
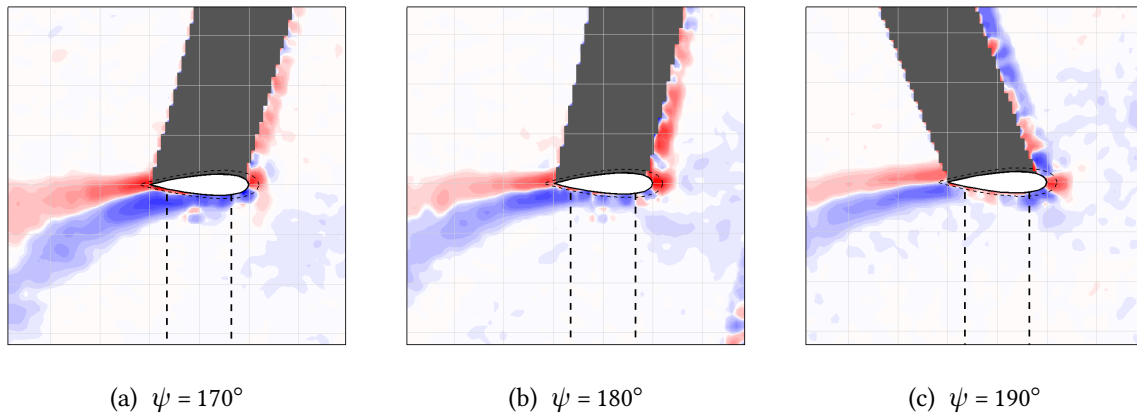
Figure 5.16: Plot of z-vorticity showing a delayed flow reattachment at low $\alpha$ for the mid-rotation positions for $\lambda = 4$

In the downwind part of the rotation, the flow remains attached at all the measured azimuth angles (Figures 5.17a and 5.17f) due to the higher effective tip speed ratio which results from the drop in wind speed through the rotor. In the images, the wake of the previous blade can be seen, which the inspected blade eventually passes through at $\psi = 0°$ (Figures 5.17a). This does not appear to significantly upset the flow which remains attached, as is shown by the visualisation at $\psi = 10°$ (Figure 5.15a).

**Summary of Flowfield at $\lambda = 4$**

The flowfield images for the $\lambda = 4$ condition show that the flow is attached to the blade surface for much of the rotation. $\alpha_c$ only just reaches the static stall angle, and separation occurs as part of the 'pitch-down' motion in the upwind part of the rotation. Some flow hysteresis is again shown as the flow reattachment does not occur until $\alpha_c$ has reached a small negative value. The downwind performance differs greatly from the upwind in that no significant separation is observed due to a reduced flow velocity which leads to a lower range in $\alpha_c$. For much of the rotation drag would certainly be lower than at the $\lambda = 2$ and 3 conditions, which were previously shown to feature highly separated flows, and the $C_p$ performance is expectedly much improved.

### 5.4.4   Comparison With Literature

Although PIV measurements were also carried out by Fujisawa and Shibuya [61], the only comparable study in the literature is provided by Ferreira et al. [7]. The study shows
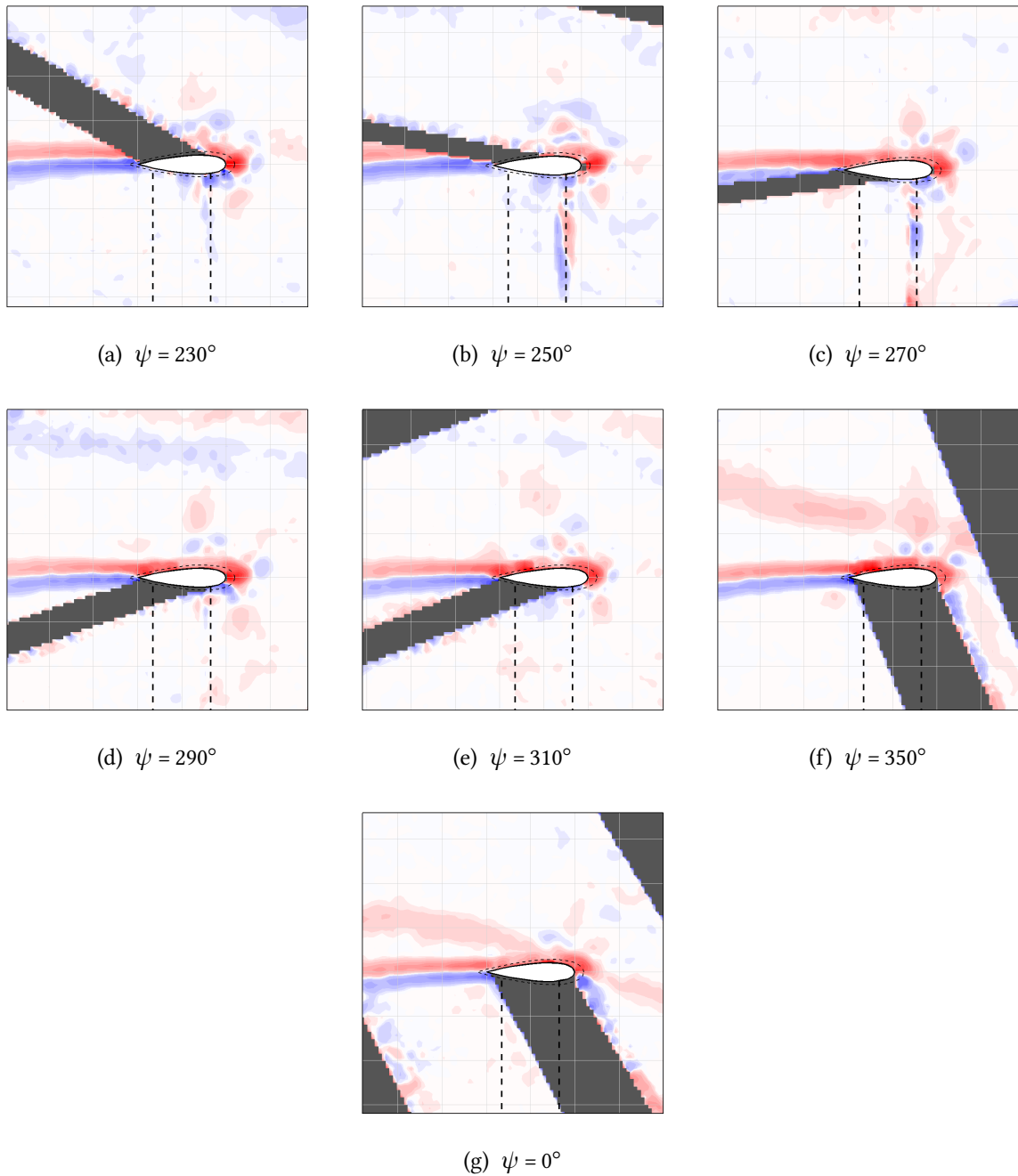
(a) $\psi = 230°$

(b) $\psi = 250°$

(c) $\psi = 270°$

(d) $\psi = 290°$

(e) $\psi = 310°$

(f) $\psi = 350°$

(g) $\psi = 0°$

Figure 5.17: Plot of z-vorticity showing the downwind stalling process for $\lambda = 4$

the evolution of the leading edge vortex for $\lambda$ = 2 on a one-blade VAWT rotor with similar geometry (NACA0015, $c$=50mm, $R$=0.2m) and at a similar Reynolds number to these experiments. Only one major leading edge vortex is shown leaving the blade which is then followed by a second vortex, shed from the trailing edge (Figure 5.18). This differs from the visualisations presented above, where a higher rate of vortex shedding has been shown. However, the vortex size relative to the blade size is comparable in each case. The onset of stall happens at approximately the same $\psi$, around 60° to 70°, although the aerofoil profiles have different thickness so an exact comparison cannot be made.
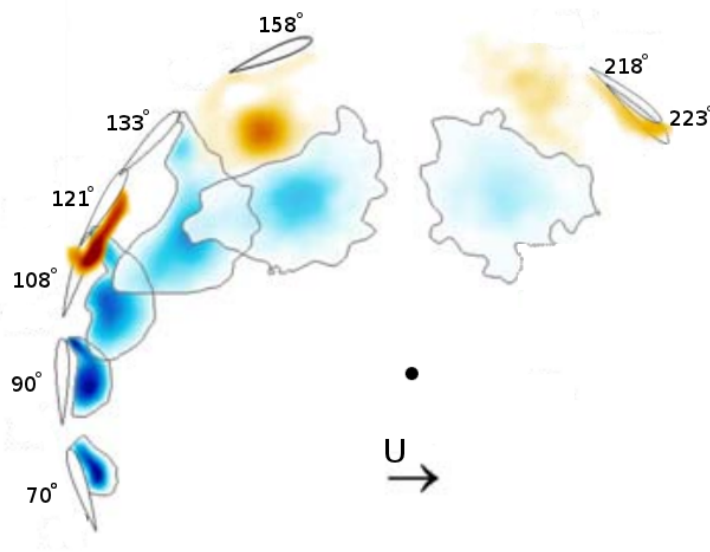


Figure 5.18: PIV vorticity contour plot of the results Ferreira et al. for $\lambda$ = 2 (two plots combined and adapted from [7]).

Other measurements by Ferreira et al. at $\lambda$ = 3 (Figure 2.30a) show the leading edge vortex to be separating from the surface at $\psi$ = 128°, with the trailing edge vortex following at $\psi$ = 163°. At $\lambda$ = 4, stall is limited to a slight separation that occurs at around $\psi$ = 127°, and results in small vortices being shed at $\psi$ = 163° (Figure 2.30b). Again, shedding frequency aside, this is comparable to what has been shown above.

So, for the upstream part of the rotation, PIV visualisations by Ferreira et al. show separated flow at a range of $\psi$ similar to this study's data for three tip speed ratios. However, the vortex shedding frequency differs significantly between the two datasets. Whilst the chord length and $Re$ are similar between the two cases, the VAWT rotor tested by Ferreira et al. has a $c/R$ ratio of more than twice that of the data presented in this study. This suggests that the vortex size and shedding rate may be dominated by the $c/R$ ratio, whist the stalled range of $\psi$ is dominated by $\lambda$. Without more than these two studies to compare, it is not possible for a firm conclusion to be drawn. Ferreira et al. only present visualisations showing the upwind

stall. So, as far as the Author is aware, there is currently no published data with which to compare the reattachment or downstream flow physics.

## 5.5   Comparison with CFD

The experimental work in this study provides performance data and flow visualisations, both of which can be used to form a validation case for the development of CFD modelling techniques. Within the same research group as the Author, a CFD model has been generated (see Section 4.3). The model was used by the Author to simulate the conditions tested in the Reference Case so that additional understanding could be gained. In order to evaluate the model, the comparison between simulated and experimental $C_p$ performance and flowfield visualisations is discussed in the following sections. Contour plots of vorticity are presented with the same levels used in each case (see Figure 5.19), the vorticity calculation in both the PIV and CFD cases is identical (see Section 4.2.4 for details).



(a)  PIV contour levels                         (b)  CFD contour levels
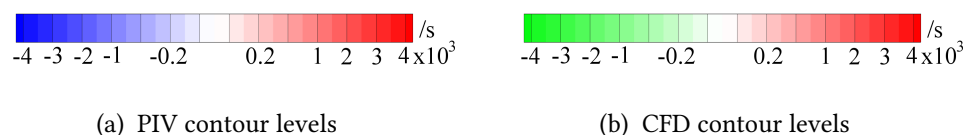
Figure 5.19: Contours used for Plotting PIV and CFD vorticity (i.e. green replaces blue to allow easy differentiation between PIV and CFD).

### 5.5.1   $\lambda = 2$

At the $\lambda = 2$ conditions, the experiment showed the onset of stall occurring between $\psi = 50°$ and $60°$, with the first leading-edge vortex leaving the surface at $\psi = 70°$ where roll-up at the trailing edge is also shown (Figures 5.20a to 5.20c). The CFD simulation shows a similar process with a slight lag behind the experiment (Figures 5.20d to 5.20f). The simulation shows the stall process originating from a gradual trailing edge separation, which differs from the experiment which appears to show a more sudden separation at the leading edge. The vortex shedding between $\psi = 80°$ and $\psi = 100°$ is also similar between the experiment (Figures 5.21a to 5.21c) and the simulation (Figures 5.21d to 5.21f), with the simulation continuing to lag slightly behind the experimental flowfield.

Towards the mid-rotation point ($\psi = 180°$), the CFD simulation also shows significant delay in the flow reattachment as the angle of attack rapidly decreases (Figure 5.22). As with the experiment, the reattachment of the flow occurs at around $\psi = 190°$. The simulation shows quite a sudden change from the shedding of large structures to a much smaller wake, whereas the PIV visualisations have shown this to be a more gradual process in the experiment.

At $\psi = 220°$, the CFD simulation shows the flow to be detached, as did the PIV measurements, and the shedding process is also shown to progress at similar rate between
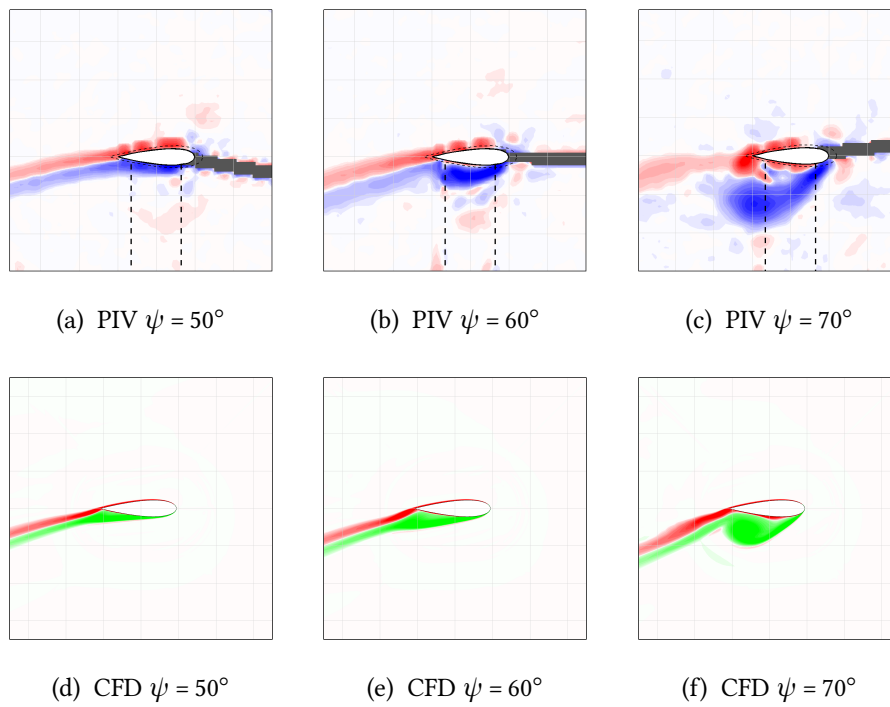
(a) PIV $\psi = 50°$     (b) PIV $\psi = 60°$     (c) PIV $\psi = 70°$

(d) CFD $\psi = 50°$     (e) CFD $\psi = 60°$     (f) CFD $\psi = 70°$

Figure 5.20: Plot of z-vorticity showing the onset of stall as shown by the PIV measurements and as predicted using the CFD model for $\lambda = 2$
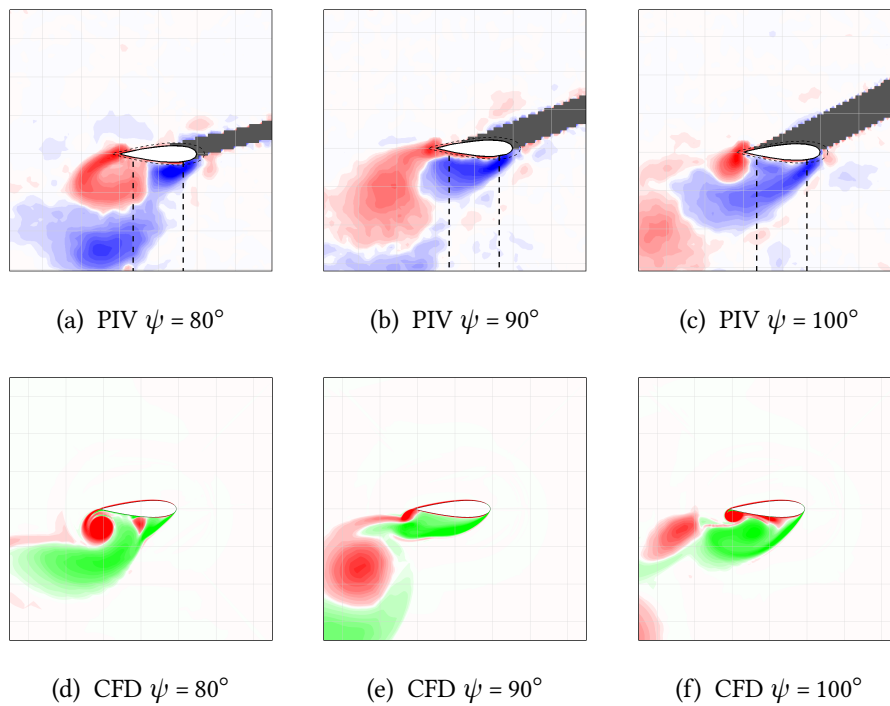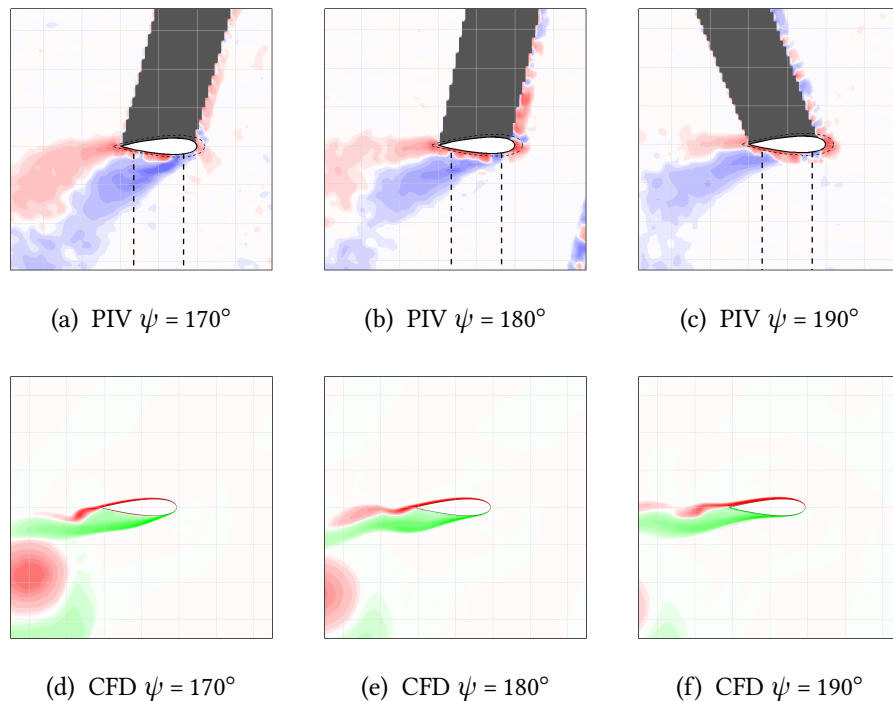


(a) PIV $\psi = 80°$     (b) PIV $\psi = 90°$     (c) PIV $\psi = 100°$

(d) CFD $\psi = 80°$     (e) CFD $\psi = 90°$     (f) CFD $\psi = 100°$

Figure 5.21: Plot of z-vorticity showing the upwind vortex shedding process as shown by the PIV measurements and as predicted using the CFD model for $\lambda = 2$

(a) PIV $\psi = 170°$      (b) PIV $\psi = 180°$      (c) PIV $\psi = 190°$

(d) CFD $\psi = 170°$      (e) CFD $\psi = 180°$      (f) CFD $\psi = 190°$

Figure 5.22: Plot of z-vorticity showing the mid-rotation reattachment process as shown by the PIV measurements and as predicted using the CFD model for $\lambda = 2$

the CFD and PIV visualisations (Figure 5.23). The only significant difference is that the path followed by the shed leading edge vortex is not matched in the CFD, which shows less downstream movement that the PIV measurements revealed (Figures 5.23c and 5.23f). This indicates that the flow velocity in the downwind portion of the rotor is higher in the experiment than in the CFD.

As the angle of attack reduces significantly from $\psi = 260°$ onwards (Figure 5.5), the CFD shows a gradually reducing depth of stall with the shed vortices also gradually reducing in size, which matches the PIV measurements well (Figure 5.24). The experimental flowfield is shown to vary in this region between rotations and so the individual vortex positions cannot be matched to the simulation. The downwind reattachment prediction in the CFD shows reattachment occurring before $\psi = 350°$ (Figure 5.25), which is earlier than the experimental flowfield. This would result in significantly lower drag being predicted for this part of the rotation.

**Summary of Simulated Flowfield at $\lambda = 2$**

The CFD-simulated flowfield and the PIV visualisations have been shown to be well-matched for $\lambda = 2$. The position that the flow detaches from the blade surface is closely matched for both upwind and downwind parts of the rotation, with only a small delay ($\ll 10°$ in $\psi$) being observed for the upwind part. However, the onset of stall appears to be different between

(a) PIV $\psi = 220°$    (b) PIV $\psi = 230°$    (c) PIV $\psi = 240°$

(d) CFD $\psi = 220°$    (e) CFD $\psi = 230°$    (f) CFD $\psi = 240°$
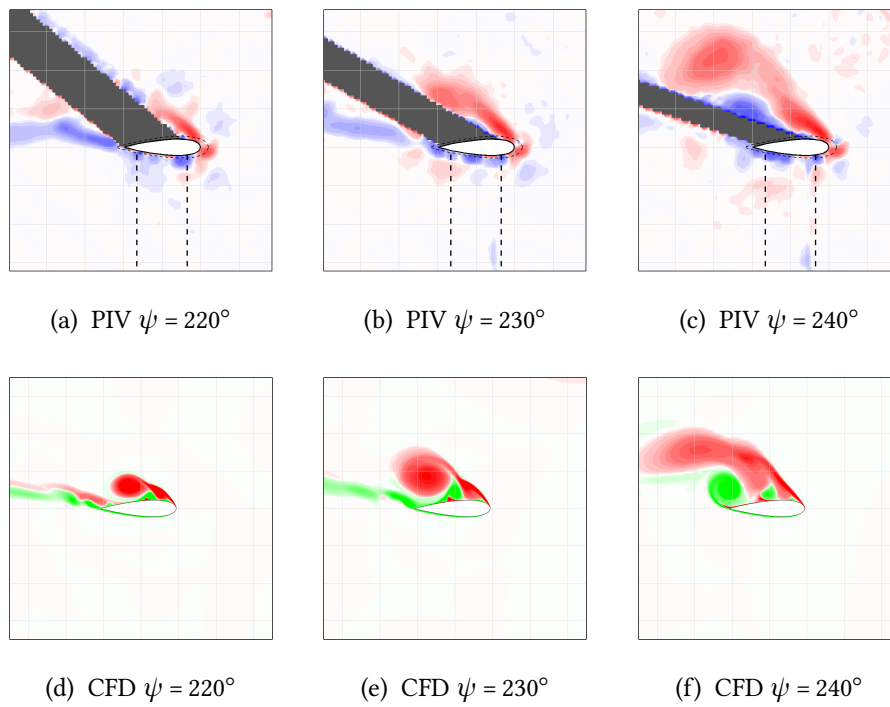
Figure 5.23: Plot of z-vorticity showing the downwind stalling process as shown by the PIV measurements and as predicted using the CFD model for $\lambda = 2$
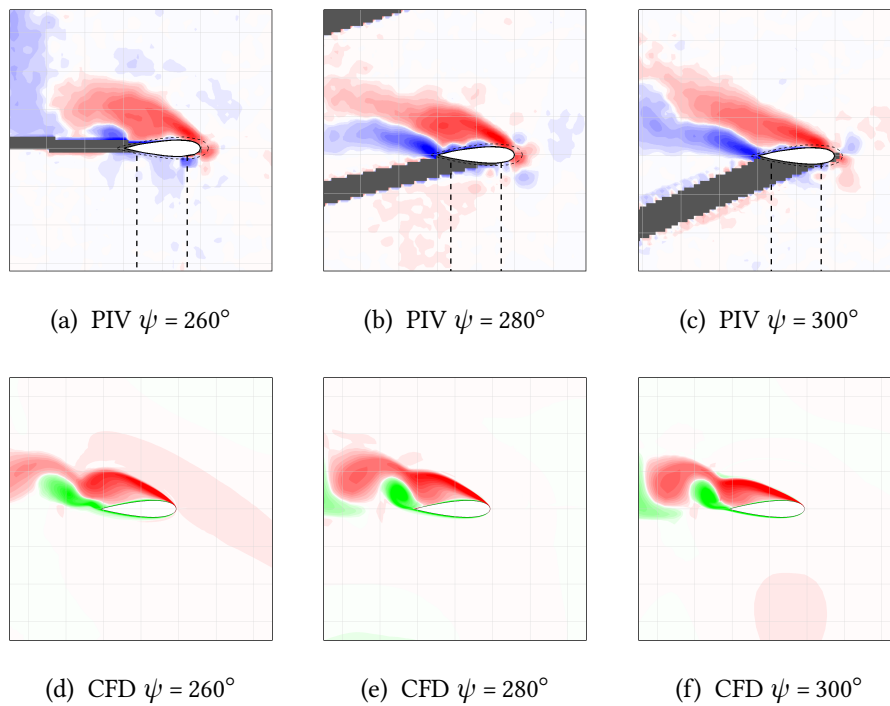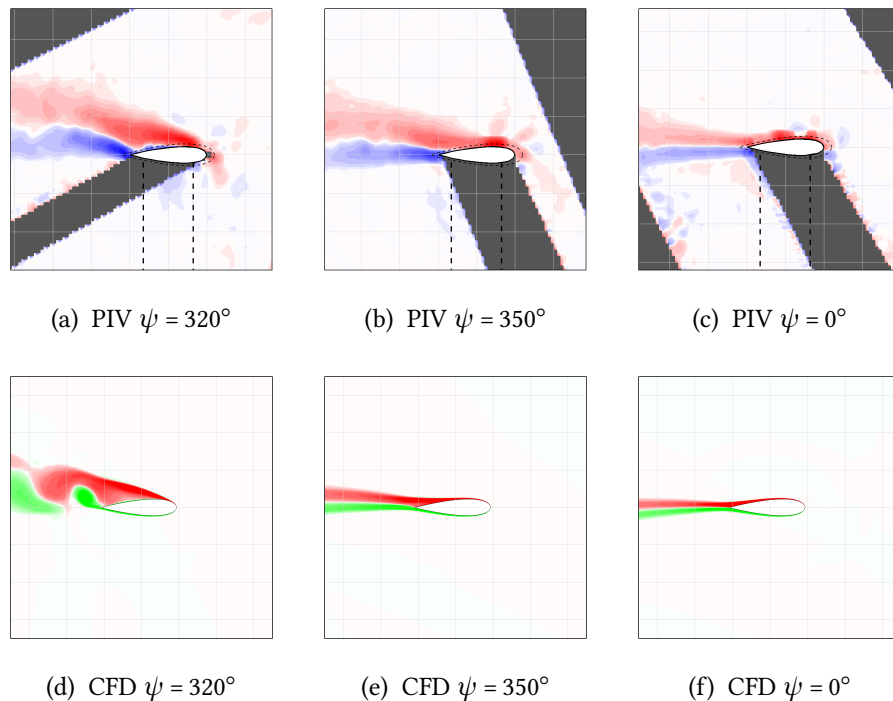


(a) PIV $\psi = 260°$    (b) PIV $\psi = 280°$    (c) PIV $\psi = 300°$

(d) CFD $\psi = 260°$    (e) CFD $\psi = 280°$    (f) CFD $\psi = 300°$

Figure 5.24: Plot of z-vorticity showing the downwind stall reduction as shown by the PIV measurements and as predicted using the CFD model for $\lambda = 2$

(a) PIV $\psi = 320°$      (b) PIV $\psi = 350°$      (c) PIV $\psi = 0°$

(d) CFD $\psi = 320°$      (e) CFD $\psi = 350°$      (f) CFD $\psi = 0°$

Figure 5.25: Plot of z-vorticity showing the downwind reattachment process as shown by the PIV measurements and as predicted using the CFD model for $\lambda = 2$

the experiment and simulation, with the simulation showing a gradual separation progressing forwards from the trailing edge, while the experiment shows a more sudden leading edge roll-up. The shedding behaviour is also well-matched, with similar scales of vortices being shed at a similar rate. The most significant CFD-PIV differences are observed in predicting reattachment: small differences are observed in the first reattachment at the mid-rotation, but a much earlier second reattachment is observed with the CFD showing earlier reattachment by at least $10°$ in $\psi$.

## 5.5.2 $\quad \lambda = 3$

At $\lambda = 3$, the CFD again shows stall beginning with a gradual separation from the trailing edge (Figures 5.26d to 5.26f), whereas the experiment reveals a more sudden separation from the leading edge (Figures 5.26a to 5.26c). The roll up of the first vortex is delayed relative to the PIV by an approximate $10°$ difference in $\psi$, which is likely to result in incorrect lift and drag predictions in this region. The subsequent vortex shedding is well-matched between $\psi = 120°$ and $140°$ in the experiment and simulation (Figure 5.27), with a similar vortex shedding rate observed, and similar reduction in the depth of stall shown as the angle of attack reduces in this region of the rotation.

As for the $\lambda = 2$ condition, the reattachment prediction is reasonably well matched between the PIV and CFD as is shown in Figure 5.28. Vortices shed by the upstream blade are visible
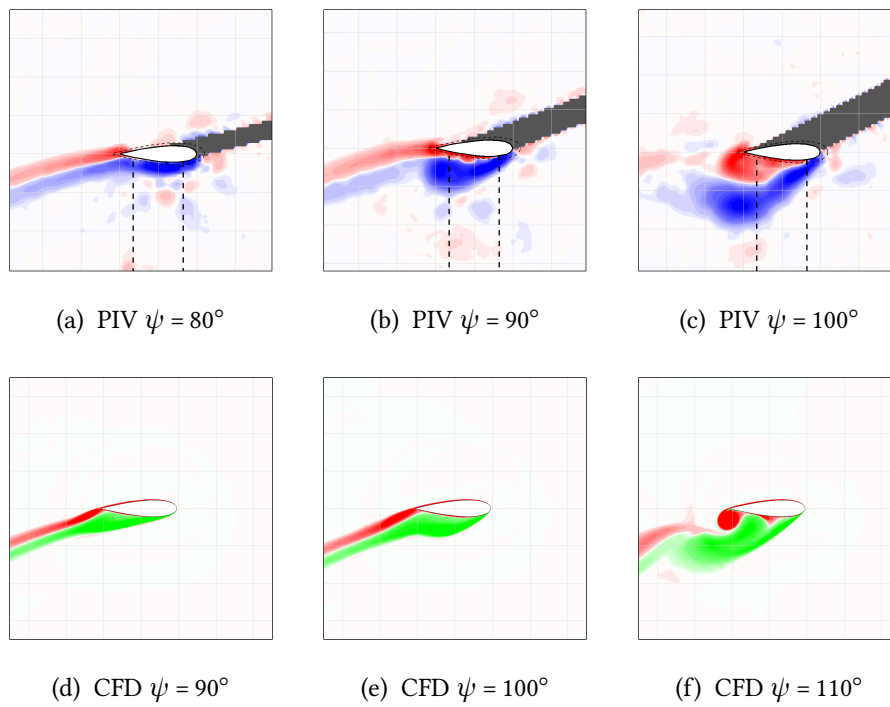
(a) PIV $\psi = 80°$  (b) PIV $\psi = 90°$  (c) PIV $\psi = 100°$

(d) CFD $\psi = 90°$  (e) CFD $\psi = 100°$  (f) CFD $\psi = 110°$

Figure 5.26: Plot of z-vorticity showing the onset of stall as shown by the PIV measurements and as predicted using the CFD model for $\lambda = 3$
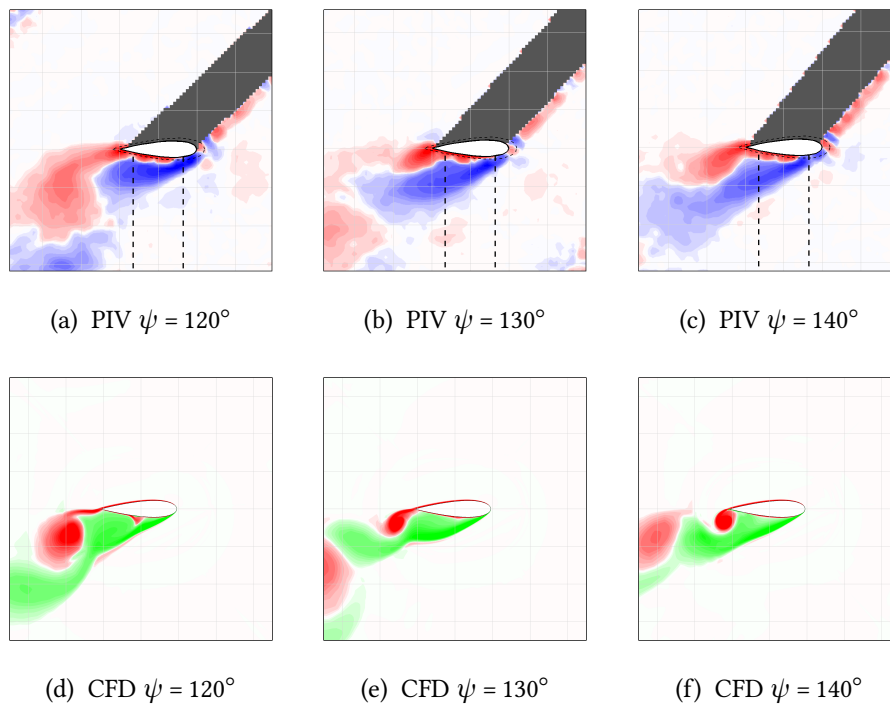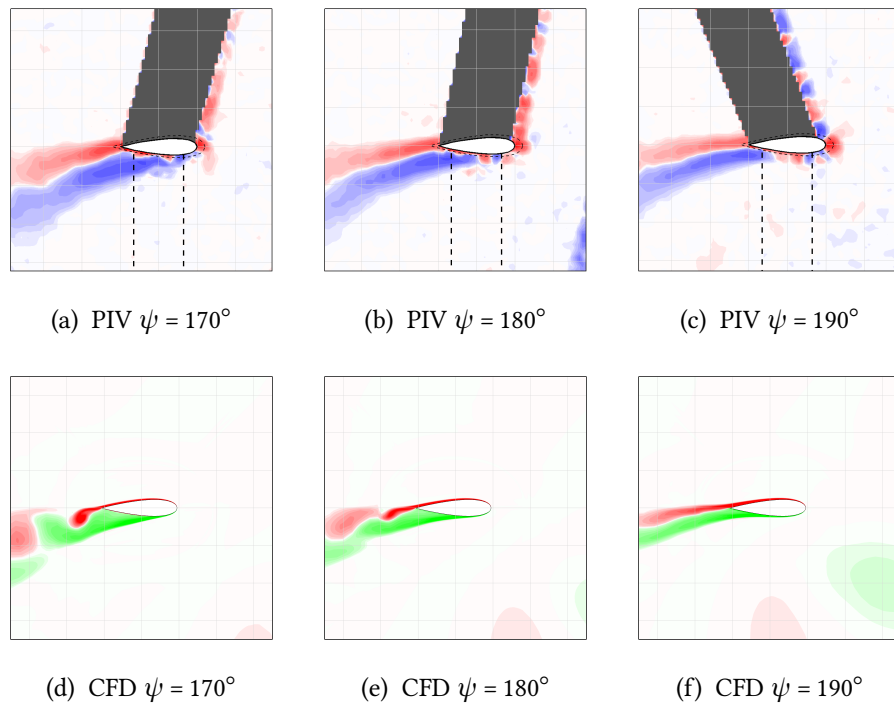


(a) PIV $\psi = 120°$  (b) PIV $\psi = 130°$  (c) PIV $\psi = 140°$

(d) CFD $\psi = 120°$  (e) CFD $\psi = 130°$  (f) CFD $\psi = 140°$

Figure 5.27: Plot of z-vorticity showing the upwind post-stall vortex shedding as shown by the PIV measurements and as predicted using the CFD model for $\lambda = 3$

in the CFD-predicted flowfield at $\psi = 190°$; some trace amounts vorticity of matching sign can also be seen in the equivalent PIV plot but the dissipation and collapse of the vortex structure in the experiment clearly happens at a higher rate, as would be expected versus a two-dimensional simulation.



(a) PIV $\psi = 170°$     (b) PIV $\psi = 180°$     (c) PIV $\psi = 190°$

(d) CFD $\psi = 170°$     (e) CFD $\psi = 180°$     (f) CFD $\psi = 190°$

Figure 5.28: Plot of z-vorticity showing the upwind post-stall vortex shedding as shown by the PIV measurements and as predicted using the CFD model for $\lambda = 3$

At $\psi = 220°$, the CFD predicts the flow to be attached (Figure 5.29d), as did the PIV measurement (Figure 5.29a); however, the experimentally observed thicker wake (relative to attached flow at other positions), indicating partially-separated flow, is not shown in the simulation. Vortices shed from the previous blade are also visible in the simulation, but not in the experimental flowfield. The experiment appeared to show significant stall beginning at $\psi = 240°$ (Figure 5.29b), and the simulation shows the same (Figure 5.29e). The larger wake shown by PIV at $\psi = 250°$ (Figure 5.29c) compared to the CFD simulation (Figure 5.29f) indicates that there is a delay in the predicted onset of stall, as was the case in the upwind part of the rotation.

As for the $\lambda = 3$ condition, as the angle of attack reduces significantly beyond $\psi = 270°$, the CFD shows a gradually reducing depth of stall with the shed vortices also gradually reducing in size, which matches the PIV measurements well. The reattachment of the flow in the simulation again precedes that which is shown by PIV in the experiment by around 20°.

(a) PIV $\psi = 220°$     (b) PIV $\psi = 240°$     (c) PIV $\psi = 250°$

(d) CFD $\psi = 220°$     (e) CFD $\psi = 240°$     (f) CFD $\psi = 250°$
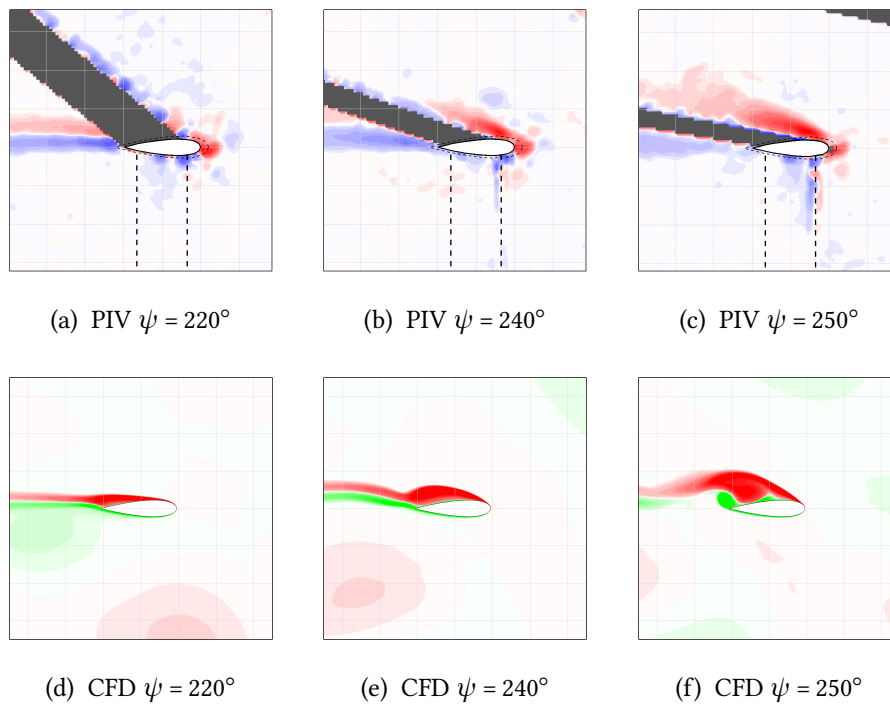
Figure 5.29: Plot of z-vorticity showing the onset of stall in the downwind part of the rotation as shown by the PIV measurements and as predicted using the CFD model for $\lambda = 3$
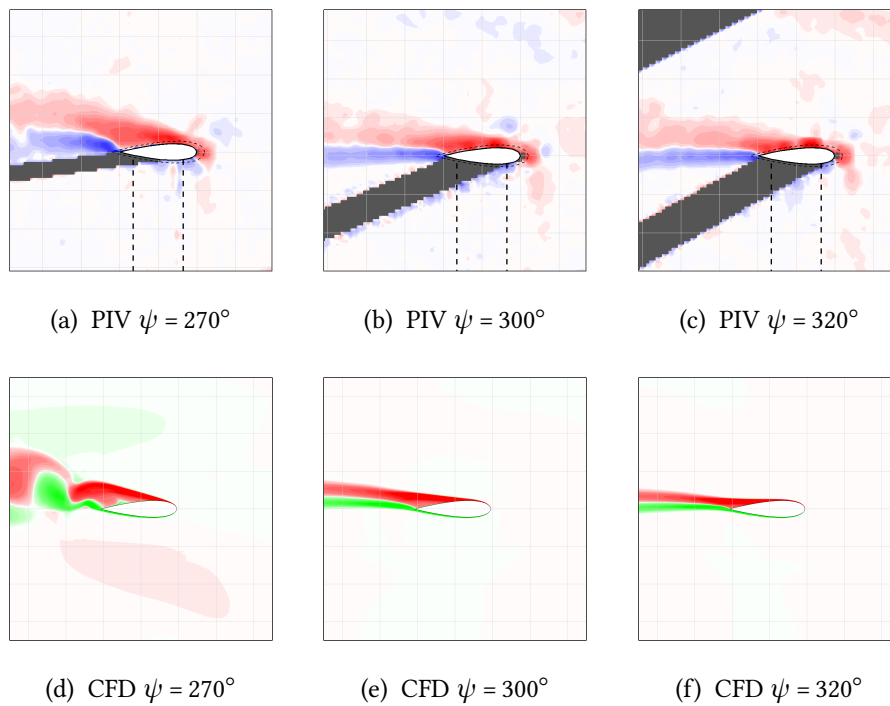


(a) PIV $\psi = 270°$     (b) PIV $\psi = 300°$     (c) PIV $\psi = 320°$

(d) CFD $\psi = 270°$     (e) CFD $\psi = 300°$     (f) CFD $\psi = 320°$

Figure 5.30: Plot of z-vorticity showing the downwind stall reduction and reattachment as shown by the PIV measurements and as predicted using the CFD model for $\lambda = 2$

**Summary of Simulated Flowfield at $\lambda$ = 3**

For the $\lambda$ = 3 condition, the match between the CFD-simulated flowfield and the PIV visualisations is reasonably good, although not at good as for the $\lambda$ = 2 condition. The position that the flow detaches from the blade surface is slightly delayed, more so than for the $\lambda$ = 2 condition, in both the upwind and downwind parts of the rotation. The shedding behaviour is again reasonably well-matched, with similar scales of vortices being shed at a similar rate. The most significant CFD-PIV differences are once again observed in predicting reattachment: although small differences are observed in the first reattachment at the mid-rotation, a much earlier second reattachment is observed in the downwind part of the rotation, with the simulation showing earlier reattachment by around 20°. With slightly delayed stall and earlier reattachment the simulation is likely to over predict the performance measured in the experiment, this is indeed the case as is shown in Section 5.6

### 5.5.3 $\lambda$ = 4

At the $\lambda$ = 4 condition, the CFD simulation shows a gradual detachment which moves forward from the trailing edge as indicated by the thickening area of high vorticy on the suction surface (Figures 5.31d and 5.31e), which is similar to the experiment (Figures 5.31a and 5.31b). However, as the angle of attack reduces beyond $\psi$ = 130°, the simulation (Figures 5.31f and 5.32d) does not show the same vortex shedding as is shown in the experimental flowfield observations (Figures 5.31c and 5.32a). In the experiment, the stalled flow eventually reattaches between $\psi$=170° and 180° (Figures 5.32b and 5.32b). For the CFD simulation, no large separation is shown and the separation point simply retreats back toward the trailing edge as the angle of attack reduces (Figures 5.32a to 5.32c). Attached flow is predicted for the full part of the downwind rotation, as was also shown in the wind tunnel experiment.

**Summary of Simulated Flowfield at $\lambda$ = 4**

The lack of a flow separation in the latter stages of the upwind part of the rotation is the only main point to note when comparing the simulation and experiment for the $\lambda$ = 4 condition. The performance in this region of the rotation would certainly be very different between the CFD simulation and the experiment, with the simulation very likely to be predicting lower drag and higher lift than would be actually be experienced by the blade in the wind tunnel experiment. For the rest of the rotation, the flow is attached in both the simulation and experiment due to the lowered angle of attack.

## 5.6 CFD Power Curve Comparison with Experiment

Comparison of the CFD flowfield with the experimental observations by PIV has revealed a fairly good match between the two. Certainly, the results have shown that it is possible
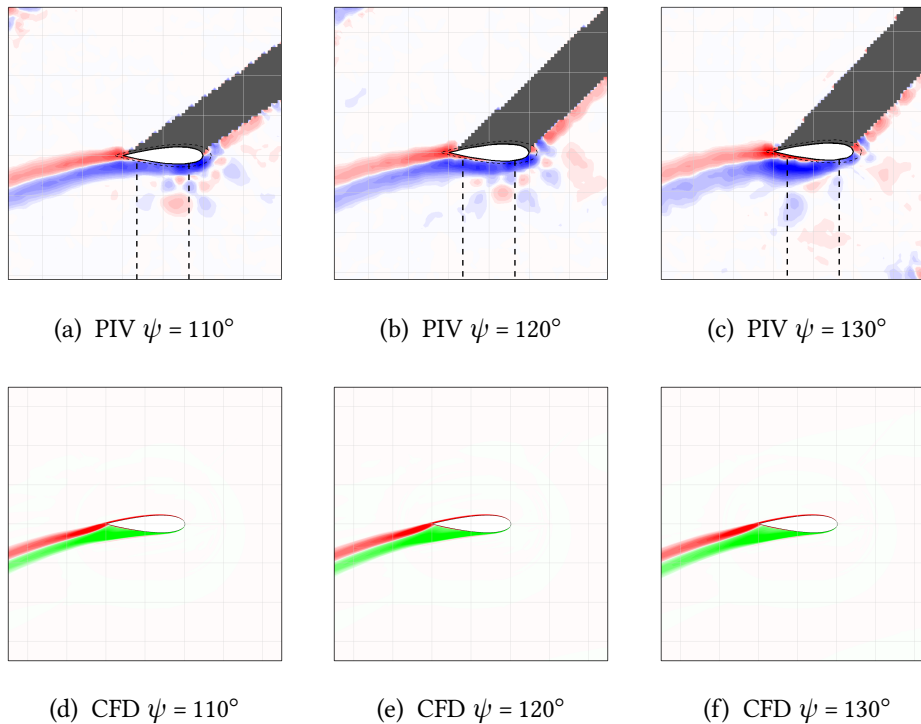
(a) PIV $\psi = 110°$      (b) PIV $\psi = 120°$      (c) PIV $\psi = 130°$

(d) CFD $\psi = 110°$      (e) CFD $\psi = 120°$      (f) CFD $\psi = 130°$

Figure 5.31: Plot of z-vorticity showing the upwind gradual separation as shown by the PIV measurements and as predicted using the CFD model for $\lambda = 4$

to simulate the basic VAWT-blade flow physics, including dynamic stall and reattachment. This is certainly a positive result when considering previously published attempts which have been discussed in Section 2.4.3. Correct simulation of the general flow physics is an important step on the way to a useful CFD VAWT model; however, a correct $C_p$ prediction is likely to be the ultimate goal for most future studies. With this in mind, a comparison of the CFD-predicted $C_p$-$\lambda$ relationship with the experiment is made by adding $C_p$ values from additional simulations to map-out the full curve.

Results of the CFD-predicted performance are shown alongside the experimental measurements in Figure 5.33. The first, and most obvious observation is that the maximum $C_p$ is over-predicted in the simulation by a significant margin. The simulation predicts $C_{p-max}$=0.35, whereas the experiment has measured $C_{p-max}$=0.14, clearly the predicted blade forces are quite different between the two cases. However, upon further inspection, the general curve shape is shown to be well represented: from $\lambda = 1$ the $C_p$ drops to form a negative trough in the performance curve just above $\lambda = 2$, and from here performance rapidly improves with increasing $\lambda$ until a maximum $C_p$ is encountered at around $\lambda = 4$ after which, with further increases in $\lambda$, a steep drop in performance in experienced.

The simulated $C_p$ matches the experiment closely for low tip speed ratios, and the flowfield has previously been shown to compare well compared for $\lambda$=2. However, the differences in the $C_p$ between CFD and experiment become more and more significant as $\lambda$ is increased.
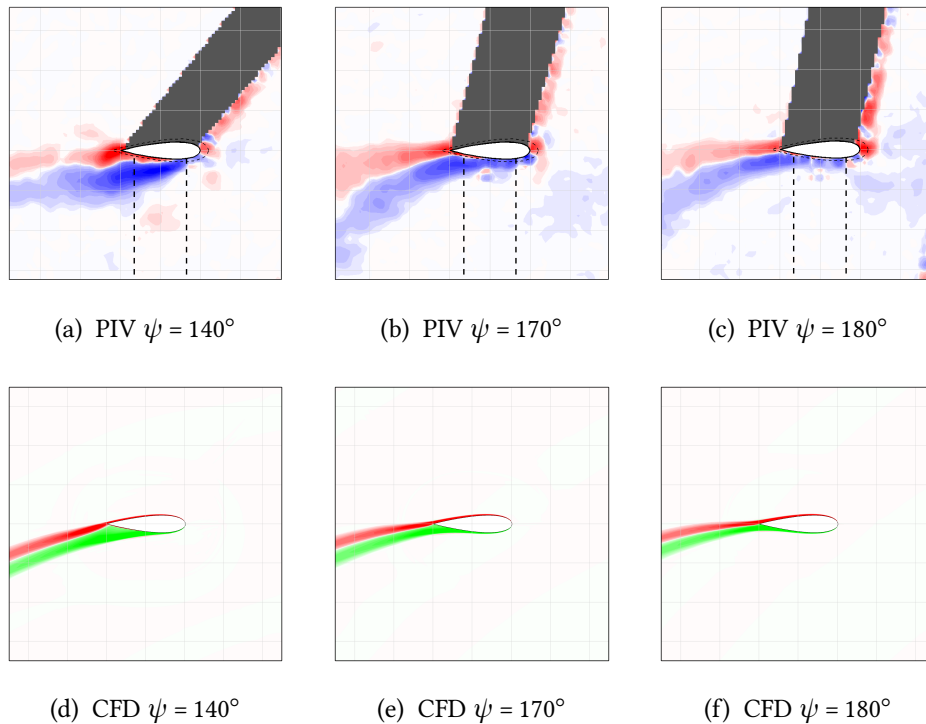
(a) PIV $\psi = 140°$      (b) PIV $\psi = 170°$      (c) PIV $\psi = 180°$

(d) CFD $\psi = 140°$      (e) CFD $\psi = 170°$      (f) CFD $\psi = 180°$

Figure 5.32: Plot of z-vorticity showing the upwind gradual separation as shown by the PIV measurements and as predicted using the CFD model for $\lambda = 4$

Increased stall delay and earlier flow reattachment were observed at $\lambda$=3, and understandably the CFD predicts higher $C_p$ at this tip speed ratio. Most significantly, no separation at all was predicted for $\lambda$=4, which would be expected to lead to a significant over-estimation of $C_p$ at this condition.

Certainly, some differences are expected due to 3D effects, the 2D CFD simulation takes no account of the interaction between the support arms and the blade, nor is the effect of a finite blade span simulated. Both of these effects have been shown to be significant in the PIV measurements taken along the blade length, as shown in Section 4.2.5. A similar comparison between experiment and 2D CFD is shown by Raciti Castelli et al. [71] (see Figure 5.34a), whose blades have a similar aspect ratio of 17. Howell et al. [51] show a much improved match between experimental results and their 3D CFD simulations (see Figure 5.34b), while their equivalent 2D CFD results are shown to give substantial over-prediction. However, the model used by Howell et al. has a very low aspect ratio of 4, and so the substantial 2D CFD versus 3D CFD differences are not surprising. Induced drag increases with the square of lift, and so the wing-tip effect would be expected to become more significant as the blade reaches an optimum $\lambda$ and the blade spends more of the rotation at a high-lifting condition. Results obtained by McIntosh [32] (Figure 5.35) show an increased effect of aspect ratio with $\lambda$, with a change in aspect ratio $AR$ from 160 to 15 leading to an approximate $C_p$ drop of 1/3 at $\lambda = 5$ and only 1/5 at $\lambda = 3$. This may, in part, account for why the flowfield visualisations match-up

reasonably well, yet the $C_p$ prediction does not. Further to this, a poor prediction of zero-lift drag, which has the most influence at high $\lambda$ [32] where the range in $\alpha$ is lowest, may also be at fault. Additional investigations would be required to better evaluate the model's ability to correctly predict the viscous drag, the contribution of which is most significant at low angle of attack.
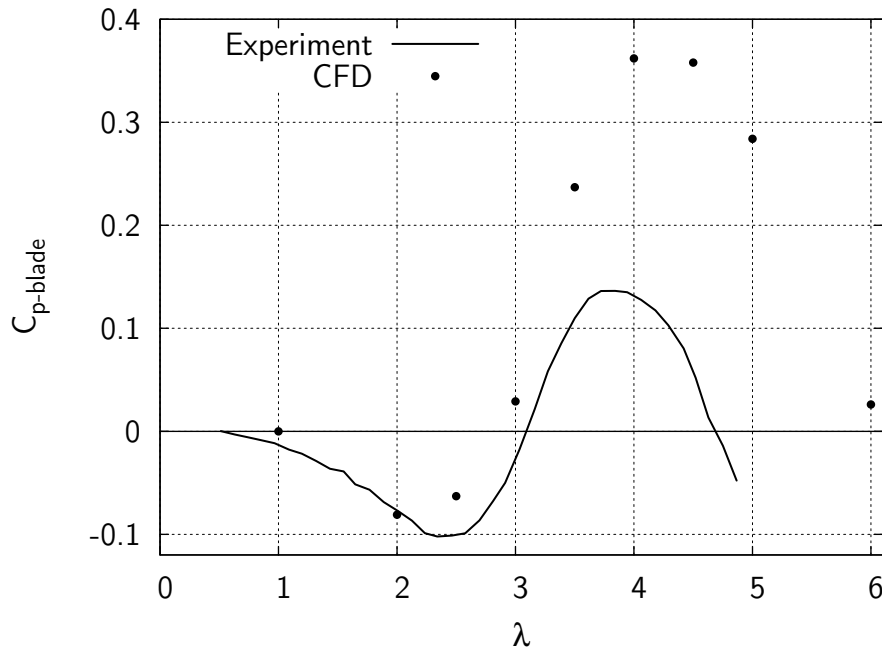


Figure 5.33: $C_{p-blade}$ vs $\lambda$ as predicted by the CFD and as measured in the experiments for the datum 7m/s case.

## 5.7 Summary

Using the PIV flowfield visualisations, much has been revealed about the flow conditions in the near-blade region:

- the azimuth angles at which separation and re-attachment occur are determined

- evidence of dynamic stall is clearly shown

- the nature of vortex generation and the scale and frequency of vortex shedding are revealed.

Basic theory (see Chapter 1) and the CFD solution results show that the VAWT operation is characterised by large variations in angle of attack, the experimental visualisations show that this can result in deep-stall vortex shedding, the extent of which increases with reducing tip
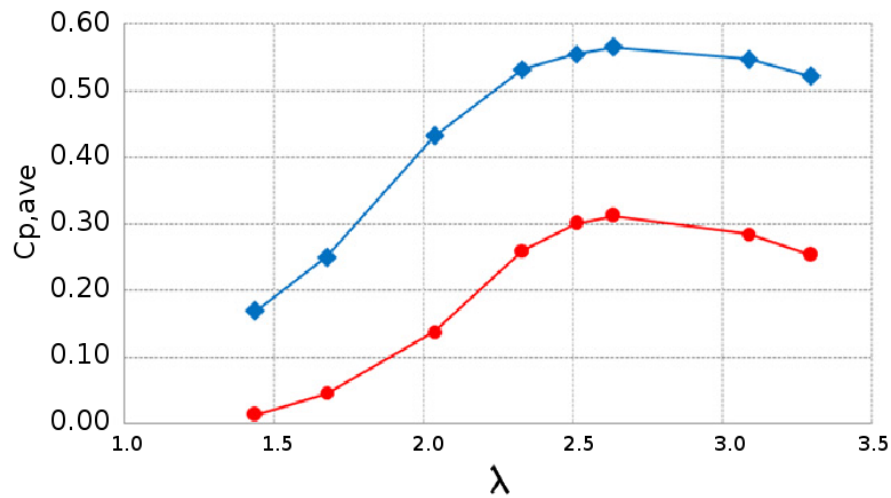
(a) Results from Raciti Castelli et al. [71] (Red=2D CFD, Blue=experiment)
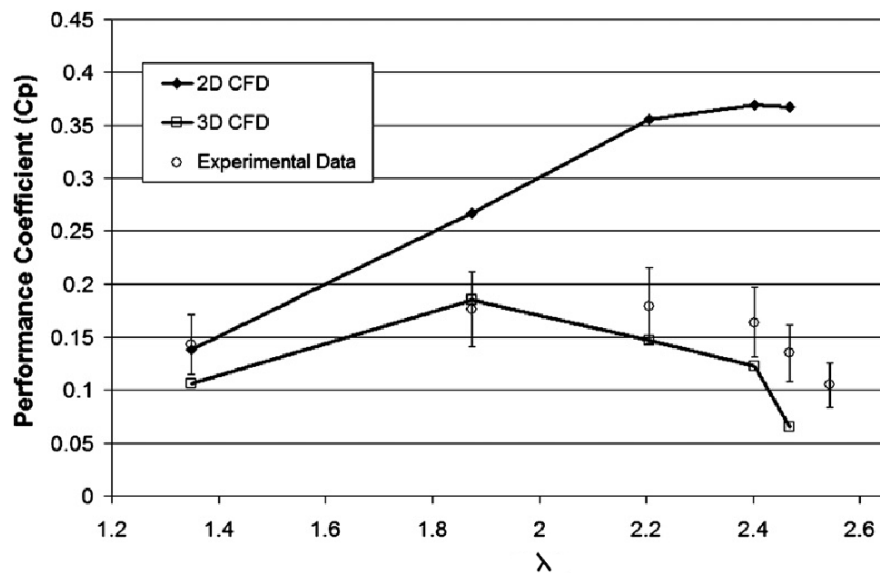


(b) Results from Howell et al. [51]

Figure 5.34: Results from other studies showing comparisons of CFD predictions and experimental results.

speed ratio. A significant hysteresis in the flow has also been observed. At $\lambda = 2$, stall occurs early in the upwind rotation, at $\psi \approx 60°$. At this point a sudden leading edge vortex was observed to roll up over the aerofoil suction surface (enhancing lift) before being shed from the blade, a series of vortices then followed, alternately shed from the trailing and leading edges. A delayed reattachment occurs at around $\psi = 180°$, where $\alpha \approx 0°$. A similar process was observed at $\lambda = 3$, with stall occurring later and reattachment earlier. At $\lambda = 4$, where the $C_p$ reaches the maximum value, a brief stall was observed in the upwind part of the rotation
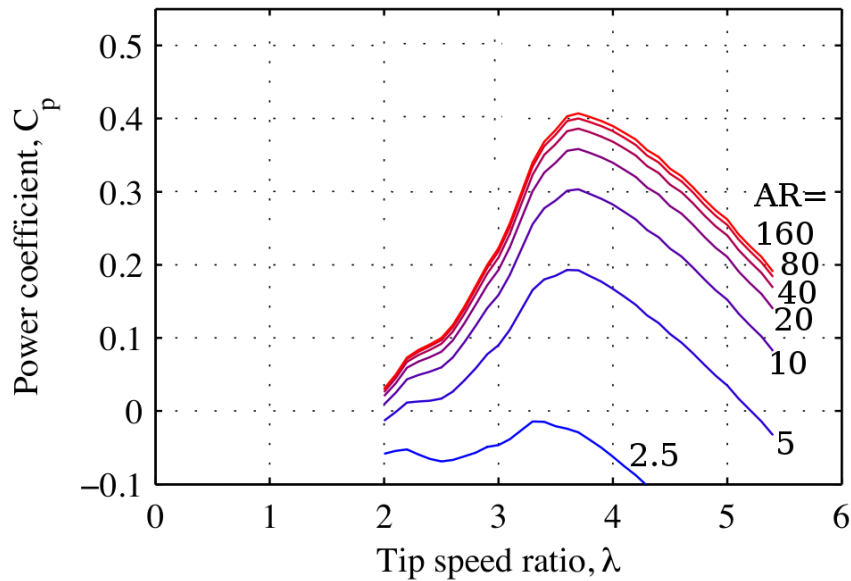
Figure 5.35: The effect of blade aspect ratio on VAWT $C_p$ vs $\lambda$ behaviour as predicted by the the vortex model of McIntosh (Figure adapted from [32]).

only. The lower downwind flow velocity leads to a higher effective tip speed ratio, and the lower range in $\alpha$ prevents stall.

When comparing CFD and experimental flowfields, the basic process of attached flow, stall, vortex shedding and reattachment is shown for the $\lambda = 2$ and 3 conditions, although the brief stall at $\lambda = 4$ is missing in the simulation. Some small delay in detachment and earlier reattachment is shown in the simulation, indicating the CFD flow is generally more inclined to be attached to the blade surface. Significant differences between simulated and experimental $C_p$ is noted at higher $\lambda$. However, in general, the curve is reasonably well-formed, the same basic trends are observed with changing $\lambda$ (albeit they are scaled by larger amounts) and the gradients in the curve at each of these points are similar. All of which suggests similar fundamental changes in the flow physics are contributing to the change in curve shape at each condition in both the simulation and the experimental case. As a result, the use of the CFD model to supplement the experimental data, as is done in the following Chapter, is well-justified.

# Chapter 6

# Reference Case: Lift and Drag Performance Through a Rotation

## 6.1 Introduction

This chapter aims to explain the effect of the aerodynamic forces on the previously observed changes in performance for the rotor at the three test tip speed ratios. The evaluation of a corrected angle of attack, using the technique discussed in Section 4.3.6, allows lift and drag polars to be determined. A performance discussion in traditional terms is then made from the point of view of one of the blades as it travels through the rotation.

Significant changes in the flowfield have been observed through the PIV measurements at different tip speed ratios. However, the flowfield visualisations do not reveal the blade forces at work, while the $C_p$-$\lambda$ curve represents only the product of the rotationally averaged tangential force. In order to form a full picture which allows the VAWT performance to be explained, the blade forces must be inspected. By understanding the performance impact of the changes in lift and drag, inferences as to possible aerofoil design alterations, or perhaps changes to the VAWT in general can be made.

Measuring the blade forces in the experiment or extracting them from the PIV data was considered to be practically difficult and also error prone. Instead, as the CFD has been shown to be reasonably well-matched with the experiment, tangential and normal blade forces are extracted from the simulation. Interpolation of the velocity field allows determination of the corrected angle of attack, $\alpha_c$ the variation of which has been presented in Figures 5.5, 5.10 and 5.14. The determination of $\alpha_c$ allows the tangential and normal forces to be more usefully resolved into lift and drag forces. This is done at the approximate aerodynamic centre (the quarter-chord position) to minimise the small contribution of the aerodynamic moment. This contribution to the overall torque is dependant on the aerofoil mounting position and the definition of azimuth position, both of which may vary from one VAWT to another. With the aerodynamic forces resolved, the lift and drag coefficients can be determined, and a better

evaluation of the blade performance then follows.

## 6.2   $\lambda = 2$

Flowfield visualisations have shown that the flow at $\lambda = 2$ is separated from the blade surface for a large portion of the rotation. Deep stall was encountered in both the upwind and downwind parts of the rotation and large scale vortex shedding was observed. A small negative power coefficient was measured in the experiment ($C_{p-blade} = -0.08$), which was closely simulated by the CFD simulation. The separation and reattachment of the flow from the blade surface appeared to follow a dynamic-stall type behaviour and, as is expected, plots of lift and drag coefficient show large hysteresis loops (Figures 6.2a and 6.2b) and a maximum lift coefficient far exceeding that predicted by a comparable static aerofoil simulation. To aid clarity, results are presented separately for four quadrants of the rotation, see Figure 6.1.



(a) first quadrant        (b) second quadrant        (c) third quadrant        (d) fourth quadrant
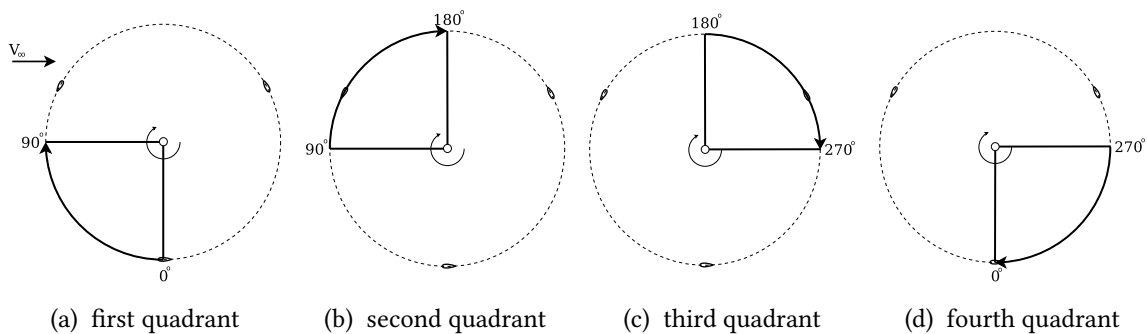
Figure 6.1: Rotation quadrants for subsequent force analysis.

### 6.2.1   First Quadrant

In the experiment, the onset of stall was shown to begin with a leading edge roll-up at $\psi = 50°$, with the corresponding vortex being shed at $\psi = 70°$. The roll-up in the simulation was different: originating and moving forwards from the trailing edge before the vortex roll-up, convection and shedding progressed at a similar rate to the experiment (Figure 5.20). The plot of $C_l$ vs $\alpha_c$ (Figure 6.2a) shows enhanced lift (relative to a static aerofoil) for this region of the rotation, where $\alpha_c$ increases in a 'pitch-up' manner, which is shown to increase the angle of attack at which stall occurs in pitching aerofoil tests [58]. The corresponding torque contribution from lift, $T_{lift}$, (Figure 6.2c) is shown to increase accordingly at lift increases. In addition, as $\alpha_c$ increases, the direction of the lift has a greater contribution to the tangential (torque) direction. Lift begins to drop as the vortex is shed between $\psi = 70°$ and $80°$. Drag is shown to rise dramatically between $\psi = 60°$ and $70°$ (Figure 6.2b) as full separation occurs. The corresponding torque contribution from drag, $T_{drag}$, rises and the overall rotor torque, $T$ is quickly effected as the direction of the drag force is more closely aligned with the tangential

direction, and the result of this is a significant drop in torque, despite the enhanced lift. In fact, the alignment of the drag force is such that the small drag increase during the initial roll-up of the vortex results in the rotor torque actually falling from $\psi = 55°$ onwards.

Although the flow is attached during the early part of the rotation, $\alpha_c$ is very small, and so lift makes very little contribution to rotor torque, which only becomes positive beyond $\psi = 22°$, where $\alpha_c$ has already reached 5.8° (Figure 5.5).

### 6.2.2  Second Quadrant

The flowfield visualisations in both the experiment and simulation showed the vortex shedding continues into the second rotation quadrant, with vortices of alternating sign being shed from the leading and trailing edges. Oscillations in the lift and drag forces result (Figures 6.3a and 6.3b) and an unsteady overall torque is clearly shown in Figure 6.3c. There are low troughs in $T_{drag}$ as large vortices separate from the suction surface, such as at $\psi = 100°$. As each leading edge vortex rolls up a corresponding peak in $T_{lift}$ is noted, such as at $\psi = 120°$. Figure 6.3a shows similar values of lift coefficient are being reached as for the initial blade stalling at $\psi = 70°$. However, the corresponding drag coefficient values are higher and prevent the peaks in torque reaching that of the onset of stall. The overall result is a largely negative overall rotor torque for the region of large vortex shedding between $\psi = 70°$ to 150°.

As $\alpha_c$ reduces beyond $\psi = 160°$, the flow begins to reattach and the drag drops but remains higher than the previous value at the same angle of attack due to the incomplete reattachment, the lift also drops rapidly in this region of the rotation, but does not recover to the previous values for the same reason. The flow speed relative to the blade is much reduced in this region (Figure 6.4) and so the aerodynamic forces are small and the overall torque is therefore close to zero.
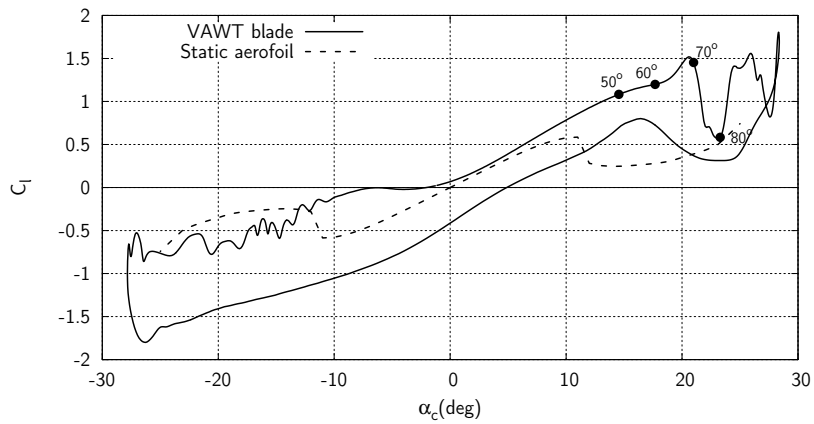
(a) $C_l$ versus $\alpha_c$
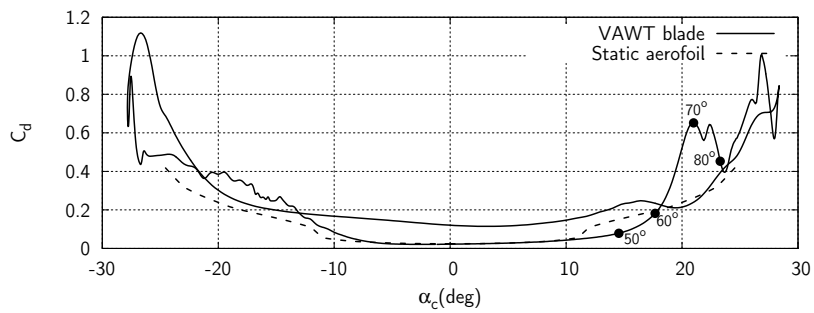


(b) $C_d$ versus $\alpha_c$
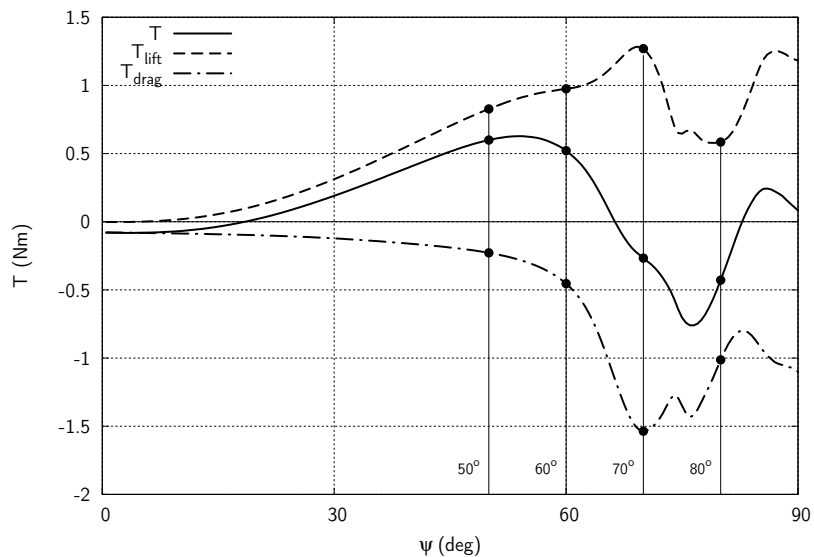


(c) $T$ versus $\alpha_c$

Figure 6.2: $C_l$ and $C_d$ versus $\alpha_c$, and $T$ versus $\psi$ for the first quadrant as predicted by the CFD simulation, at $\lambda = 2$ for the reference 7m/s case.
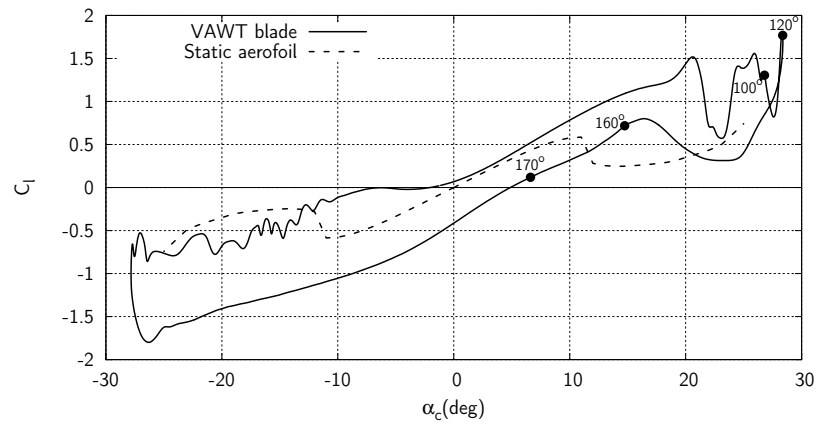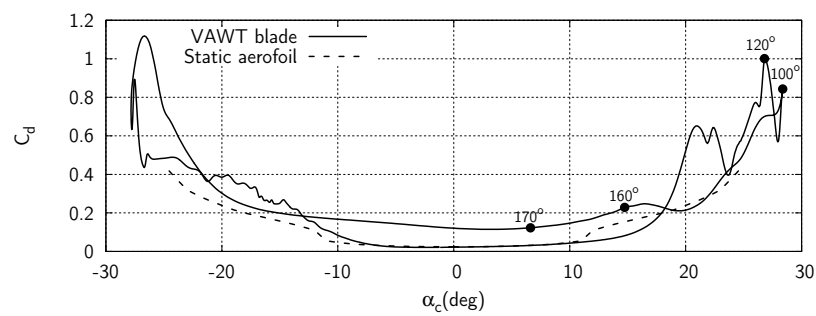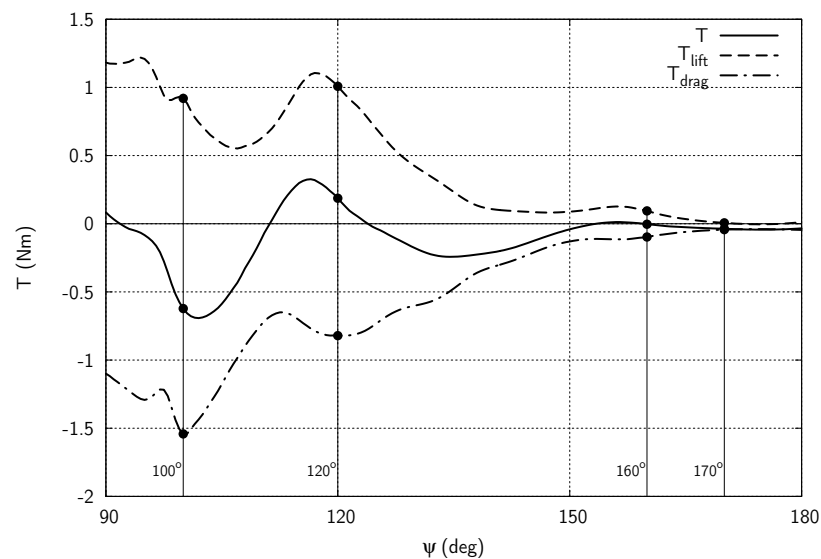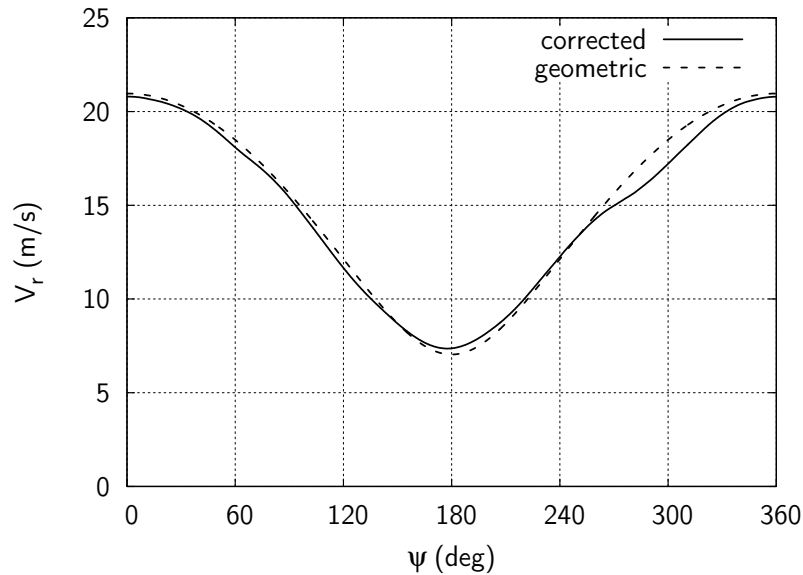
(a) $C_l$ versus $\alpha_c$



(b) $C_d$ versus $\alpha_c$



(c) $T$ versus $\alpha_c$

Figure 6.3: $C_l$ and $C_d$ versus $\alpha_c$, and $T$ versus $\psi$ for the second quadrant as predicted by the CFD simulation, at $\lambda = 2$ for the reference 7m/s case.

Figure 6.4: Relative blade velocity through a rotation at $\lambda = 2$.

### 6.2.3 Third Quadrant

At the mid-rotation point similar flowfields were observed in both the simulation and the experiment, with both showing a significant lag in the flow reattachment. As the blade moves past $\psi = 180°$, $\alpha_c$ is small but $C_l$ is enhanced above static values due to the separation which remains from the upwind stall but is now on the pressure-side of the aerofoil due to the reversal of the angle of attack direction. However, although lift is unexpectedly enhanced in this early part of the downwind rotation, $\alpha_c$ is small, as is $V_r$, and so the effect on the overall torque is not significant.

Beyond $\psi = 180°$, $\alpha_c$ increases at a higher rate than for the first quadrant due to the skewed sinusoid form of the $\alpha_c$-$\psi$ curve (Figure 5.5). As a result $C_l$ reaches a maximum of 1.85 (negative), which is higher than the maximum value of 1.5 that was simulated for the upwind part of the rotation (Figure 6.5a). A similar pattern of vortex roll-up and shedding was shown in the visualisations as compared to the upwind part of the rotation, and the enhanced lift again struggles to make a useful contribution to torque over the increased drag. However, the drag curve does show that the drag increase is delayed to higher (negative) angles relative to the upwind stall (Figure 6.5b). As a result, $T$ is not pulled down to such negative values as were observed around $\psi = 70°$ (Figure 6.5c). Beyond the initial dynamic stall, vortex shedding is observed causing oscillations in the torque curve as was experienced in the upwind part of the rotation. In general, the lower relative blade speed (Figure 6.4) results in both the lift and drag forces being lower, which results in the third quadrant's torque peaks and troughs being much smaller than those of the first quadrant.
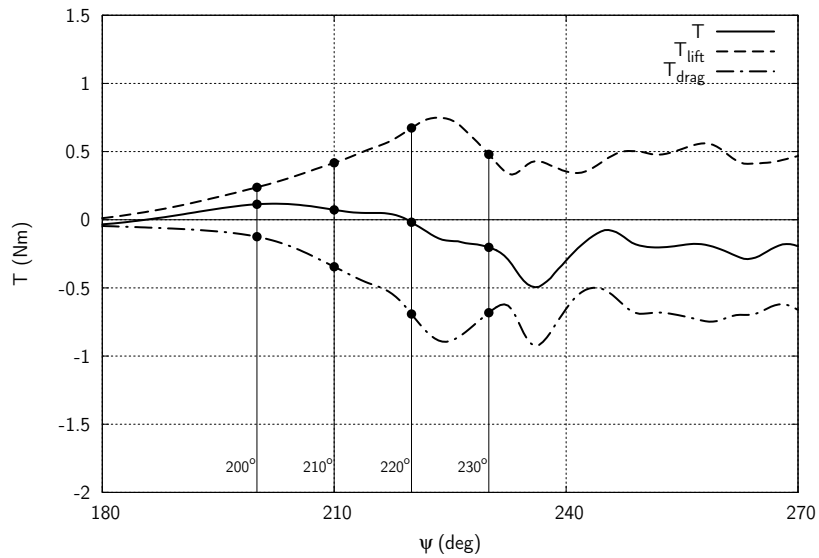
### 6.2.4 Fourth Quadrant

Both experimental and CFD visualisations showed vortex shedding to continue for much of the downstream portion of the rotation before the flow begins to reattach as $\alpha_c$ reduces. This occurs at around $\psi = 330°$ in the simulation which is slightly ahead of the experiment which showed reattachment process starting at around $\psi = 350°$. As $\alpha_c$ reduces beyond $\psi = 230°$, the flow separation from the aerofoil results in a large hysteresis present in the $C_l-\alpha_c$ curve (Figure 6.6a) and $T_{lift}$ is small. The flow separation also leads to high drag (Figure 6.6b). $V_r$ is also higher in this region as the blade heads into the wind, and so the delayed reattachment is more significant in this region than it was for the latter part of the second quadrant. Drag reduces significantly from around $\psi = 310°$, as the depth of stall reduces and the flow gradually begins to reattach. This increases the overall torque (Figure 6.5c); however, the overall rotor torque remains negative for the whole fourth quadrant of the rotation. The reduced rate of change of $\alpha_c$ compared to the mid-rotation results in a reduced amount of lag in the reattachment, and the lift at $\psi = 0°$ is only slightly enhanced by a small amount of separation which remains on what becomes the pressure-side of the blade in the upwind part of the rotation.
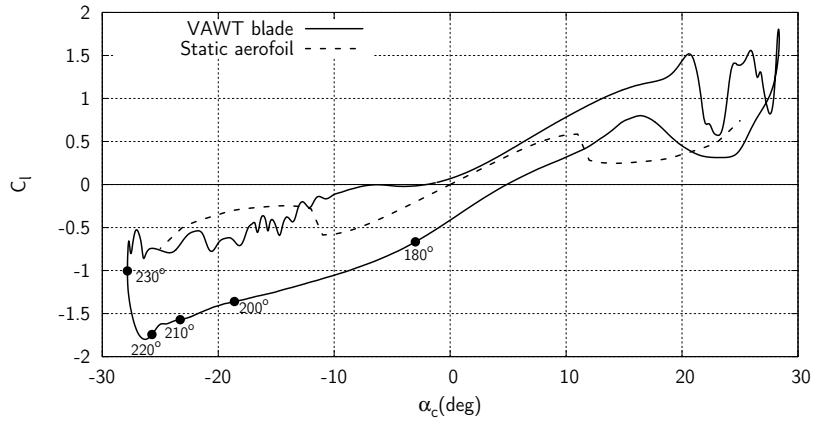
(a) $C_l$ versus $\alpha_c$
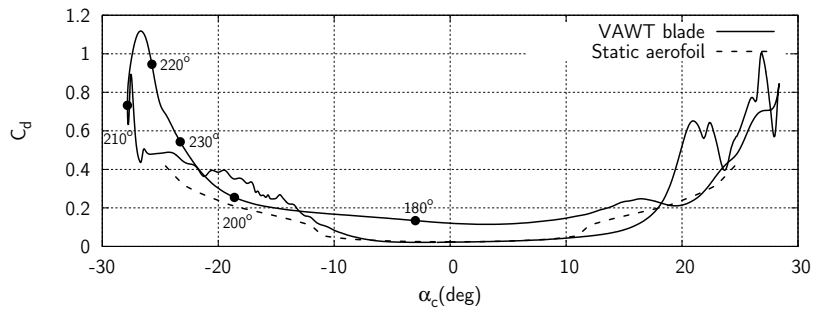


(b) $C_d$ versus $\alpha_c$



(c) $T$ versus $\alpha_c$

Figure 6.5: $C_l$ and $C_d$ $\alpha_c$, and $T$ versus $\psi$ for the third quadrant as predicted by the CFD simulation, at $\lambda = 2$ for the reference 7m/s case.
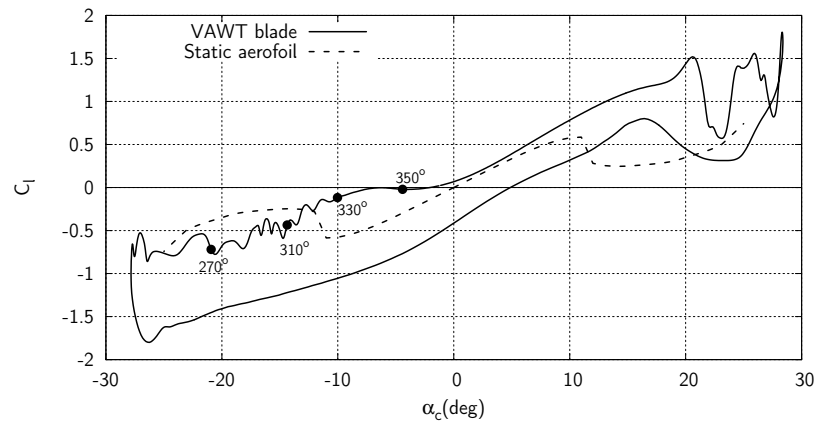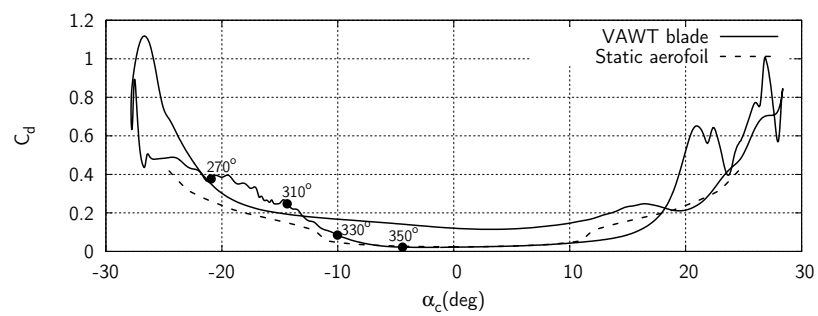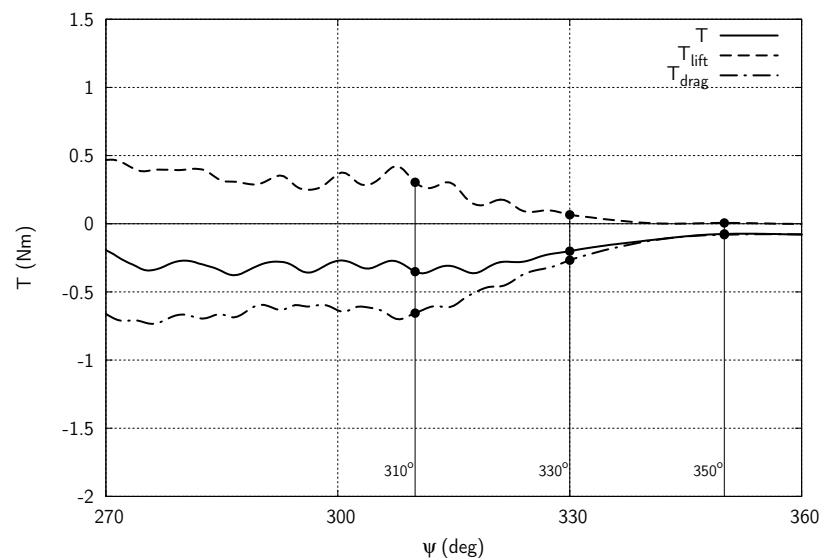
(a)  $C_l$ versus $\alpha_c$

(b)  $C_d$ versus $\alpha_c$

(c)  $T$ versus $\alpha_c$

Figure 6.6: $C_l$ and $C_d$ versus $\alpha_c$, and $T$ versus $\psi$ for the fourth quadrant as predicted by the CFD simulation, at $\lambda = 2$ for the reference 7m/s case.

## 6.2.5 Summary

For the $\lambda = 2$ condition, the analysis of the forces extracted from the simulation has shown that the rotor torque is only positive for a limited range between $\psi = 20°$ and $66°$ and for two brief moments during vortex shedding around $\psi = 90°$ and $120°$. In the downwind portion of the rotation, a small positive torque is shown between $\psi = 185°$ and $220°$. The trends observed in lift and drag are characteristic of an aerofoil experiencing rapid sinusoidal oscillations in $\alpha_c$: enhanced lift is shown during the onset of dynamic stall as $\alpha_c$ increases beyond $\alpha_{ss}$. Delayed reattachment then results in a lower lift and higher drag as $\alpha_c$ reduces. Similar curves are shown in pitching aerofoil studies, such as the study by Lee and Gerantakos [58].

Higher torque due to enhanced lift during the onset of dynamic stall is shown to be quickly overpowered by increases in drag, which is more aligned to the tangential rotor direction. Halfway through the rotation, delay in flow reattachment further contributes to high drag and low lift, and negative torque results. Toward the end of the rotation, a second period where delayed reattachment is predicted which leads to another large portion of the rotation where negative torque is produced.

The overall rotor torque change through the rotation is plotted alongside the flowfield visualisations in Figure 6.7 and the large regions of negative torque are clearly shown. The relative blade velocity is at its highest at $\psi = 0°$, and its lowest at $\psi = 180°$ and this is reflected in the overall rotor torque: The period of attached flow in the first quadrant contributes much more to rotor torque than that of the third quadrant. Similarly, the period of large scale vortex shedding between $\psi = 70°$ and $120°$ yields larger oscillations in the aerodynamic forces than the similar behaviour which is exhibited at around $\psi = 210°$ and $270°$. The delayed reattachment in the fourth quadrant can also be seen to yield a larger negative torque than the same behaviour in the second quadrant.

The benefit of a delayed stall which leads to enhanced lift is outweighed by the large drag forces which result from the flow separations which the blade does not recover quickly from due to the rapid changes in angle of attack. Overall, the flow is detached for $\approx 70\%$ of the rotation and negative torque is produced for $\approx 75\%$ of the rotation, which clearly explains the negative $C_p$ which is recorded for the $\lambda = 2$ condition.
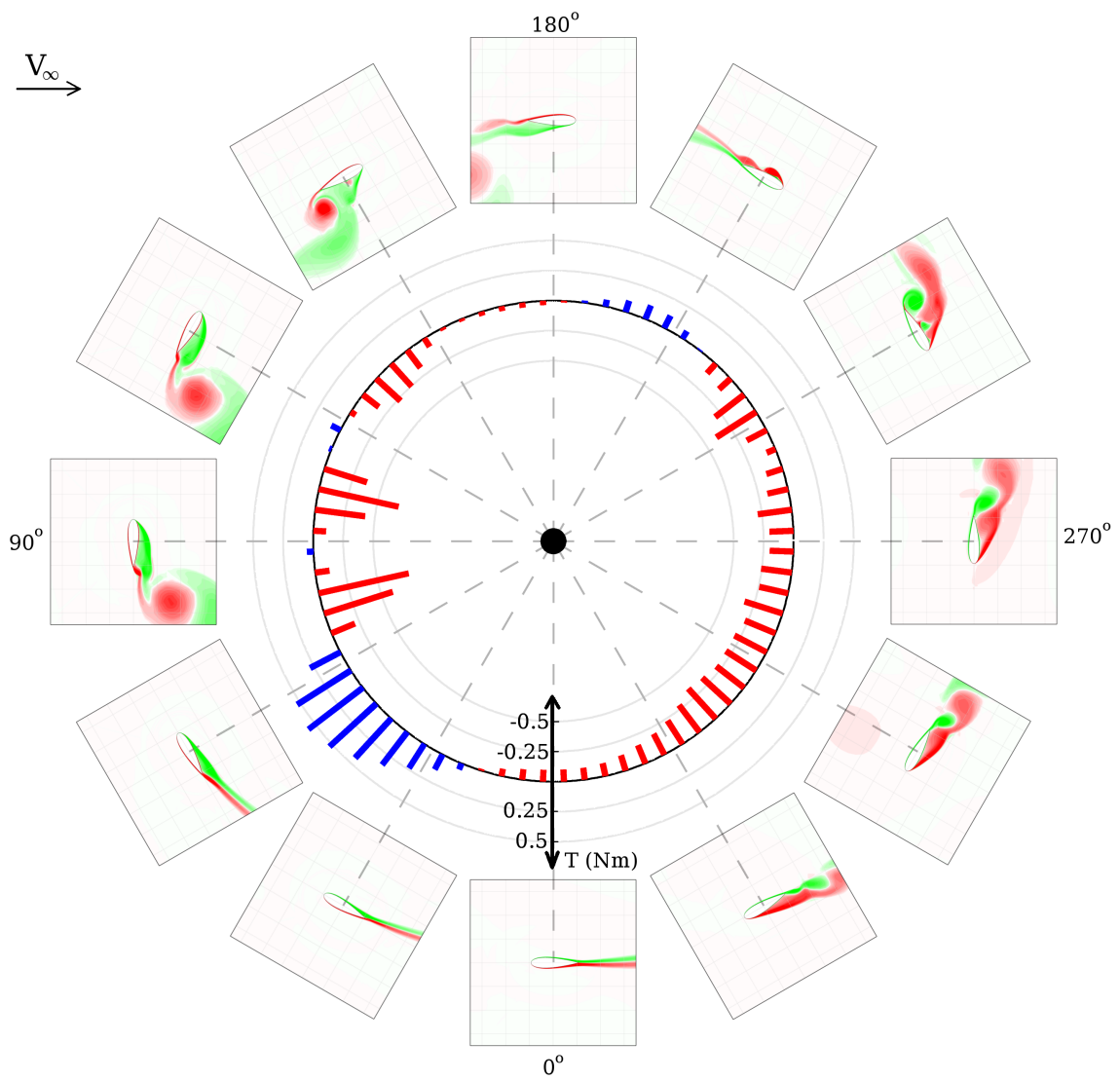
Figure 6.7: A plot showing the rotor torque and flowfield changes with azimuth angle at $\lambda = 2$ for the reference 7m/s case. Positive torque is represented by blue bars, negative torque by red bars.

## 6.3  $\lambda = 3$

Flowfield visualisations have shown that the flow at $\lambda = 3$ separates later in the rotation in both the upwind and downwind parts of the rotation than at $\lambda = 2$. Again, deep stall was encountered and large scale vortex shedding was observed for both the upwind and downwind parts of the rotation, and hysteresis loops are shown in the $C_l$–$\alpha_c$ and $C_d$–$\alpha_c$ curves (Figures 6.8a and 6.8b). A small negative power coefficient was measured in the experiment ($C_{p-blade} = -0.02$), which was slightly below the small positive value of 0.025 predicted in the CFD simulation. The CFD simulation showed slightly delayed stall and earlier reattachment in the downwind part of the rotation to which the small difference in $C_{p-blade}$ is attributed. Again, the aerodynamic force analysis is presented separately for four quadrants of the rotation, see Figure 6.1.

### 6.3.1  First Quadrant

The simulation shows the onset of stall beginning with a separation at the trailing edge which progresses gradually forwards as $\psi$ ranges from 60° to 90°. As with the $\lambda = 2$ condition, this is different the more sudden leading edge roll-up which was shown by the experimental PIV visualisations. The simulation stall is also delayed by nearly 10° in $\psi$. However, the post stall vortex convection and shedding behaviour again progresses at a similar rate to the experiment, and the general flow behaviour is a good representation of what was experimentally observed.

The plot of $C_l$ (Figure 6.8a) shows a maximum lift coefficient above the value shown by the static aerofoil solution, with the lift beginning to drop-off as the separation progresses forwards. $T_{lift}$ is shown to increase accordingly at lift increases (Figure 6.8c). Drag coefficient is shown to treble between $\psi = 60°$ and 90° (Figure 6.2b), although the delay in separation leads to the drag remaining below static values. The result of this is a drop in torque past $\psi = 75°$, although the torque remains positive. With the experiment not showing the gradual separation from the trailing edge it may be that the drag rise before full stall is not as large as the simulated change.

As was observed at the $\lambda = 2$ condition, although the flow is attached during the early part of the rotation, $\alpha_c$ is small, and so lift makes very little contribution to rotor torque. Rotor torque only becomes positive beyond $\psi = 25°$, where $\alpha_c$ has already reached 4° (Figure 5.10).
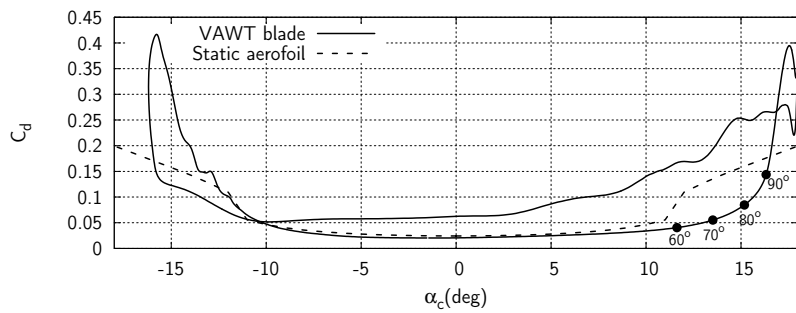
### 6.3.2  Second Quadrant

The flowfield visualisations in the simulation showed the first vortex leaving the surface at around $\psi = 100°$ after which further vortices of alternating sign being shed from the leading and trailing edges. The experimental visualisation showed similar flow patterns occurring around 10° earlier in the rotation.

As the stall vortex rolls up at $\psi = 100°$ in the simulation, the lift briefly increases from an already high value (Figure 6.9a); however, drag has continued to rise dramatically (Figure

6.9b) resulting in the overall rotor torque being negative at this point. At $\psi = 110°$ lift drops dramatically, as the stall vortex leaves the blade surface region, and the overall rotor torque drops to its lowest level for the rotation (Figure 6.9c). Roll up of the second leading edge vortex causes a short-lived increase in lift at $\psi = 120°$; after which, smaller vortices are shed as $\alpha_c$ reduces and the flow begins the process of reattaching. Between $\psi = 150°$ and $170°$ the lift coefficient remains low, and the drag coefficient high; as a result, the overall rotor torque remains negative but is small as the flow speed relative to the blade is much reduced in this region (Figure 6.10) and so the aerodynamic forces are small.
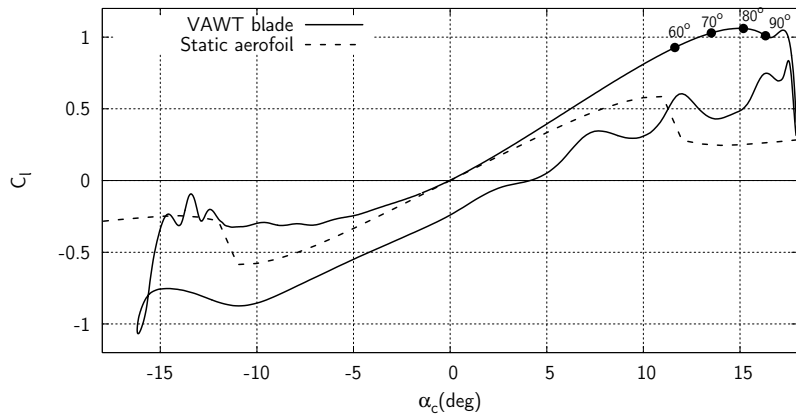
(a)  $C_l$ versus $\alpha$
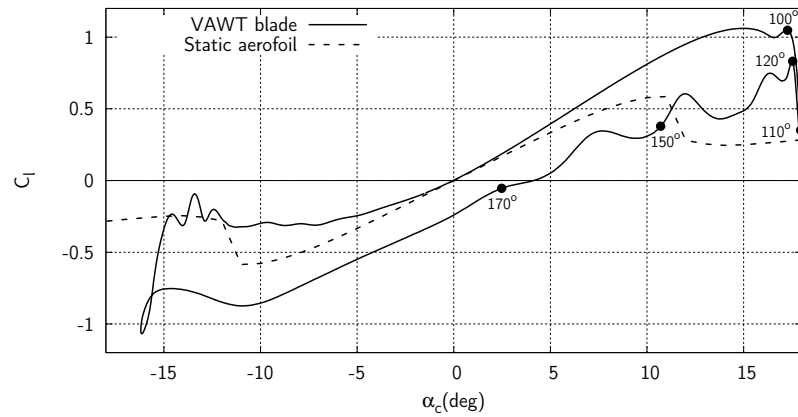


(b)  $C_d$ versus $\alpha_c$
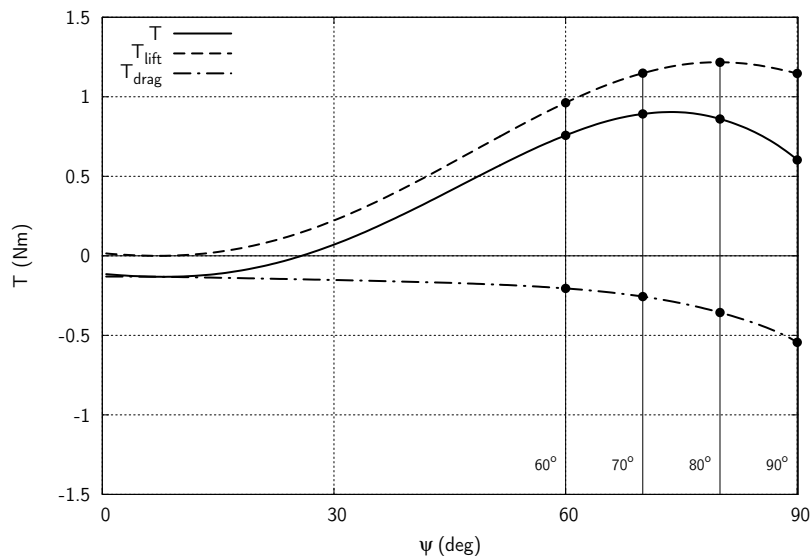


(c)  $T$ versus $\alpha_c$

Figure 6.8: $C_l$ and $C_d$ versus $\alpha_c$, and $T$ versus $\psi$ for the first quadrant as predicted by the CFD simulation, at $\lambda = 3$ for the reference 7m/s case.

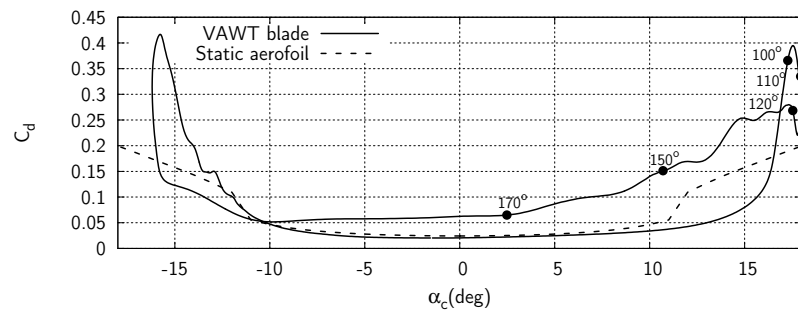(a) $C_l$ versus $\alpha_c$
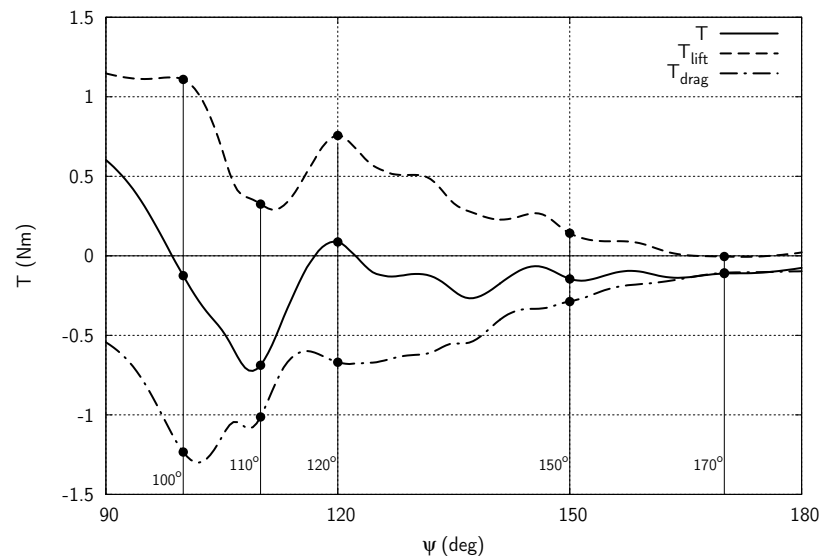


(b) $C_d$ versus $\alpha_c$



(c) $T$ versus $\alpha_c$

Figure 6.9: $C_l$ and $C_d$ versus $\alpha$, and $T$ versus $\psi$ for the second quadrant as predicted by the CFD simulation, at $\lambda = 3$ for the reference 7m/s case.
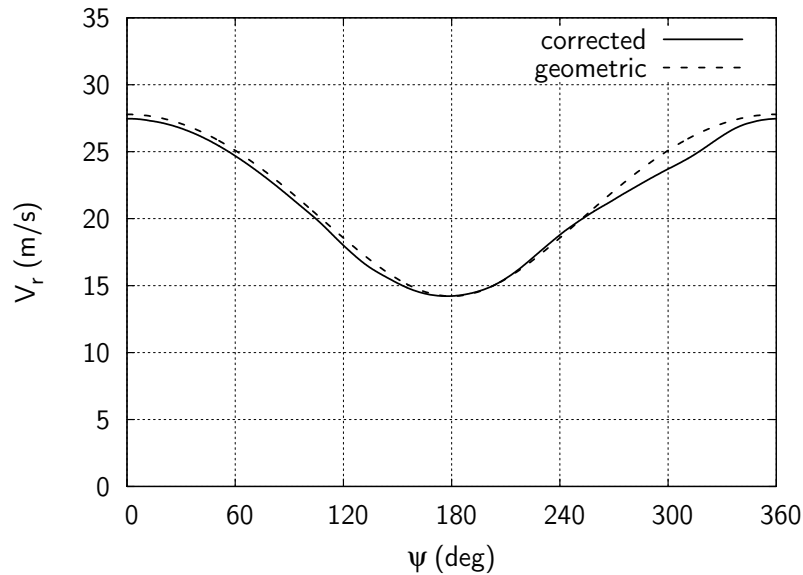
Figure 6.10: Relative blade velocity through a rotation at $\lambda = 3$.
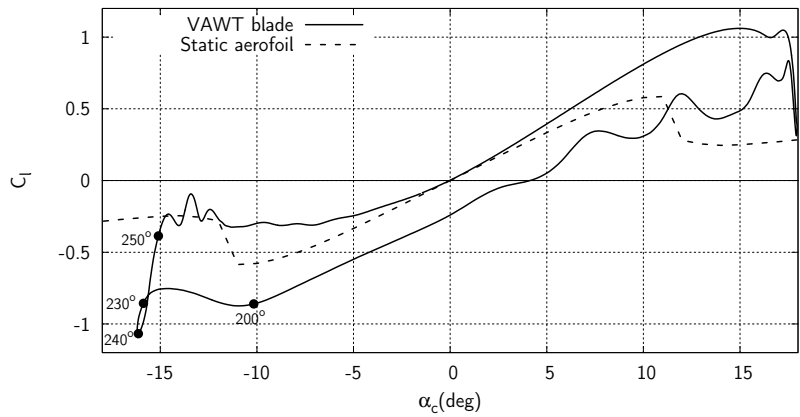
### 6.3.3   Third Quadrant

At the mid-rotation point similar flowfields were observed in both the simulation and the experiment, with both showing a significant lag in the flow reattachment. As with the $\lambda = 2$ condition, $C_l$ is enhanced above static values as the blade moves past $\psi = 180°$, due to an effective-camber resulting from the upwind stall separation which is still present on the pressure-side of the aerofoil. Due to the lower tip speed ratio the pitching rate is slower and the reattachment lag is reduced, the resulting lift enhancement is therefore lower: $C_l = 0.25$ at $\alpha_c = 0°$ rather than 0.45 as in the $\lambda = 2$ case. Again, $\alpha_c$ is small around the mid-rotation point, as is $V_r$, and so the effect on the overall torque is not particularly significant.

Beyond $\psi = 180°$ the flow is attached, and $\alpha_c$ increases rapidly up to $\psi = 200°$ where the flow begins to separate and a relatively slow roll-up is observed to occur between $\psi = 220°$ and $\psi = 240°$. In this region the resultant $\alpha_c$ actually changes very little, although $C_l$ and $C_d$ continue to change as the flow recovers from the recent rapid change in $\alpha_c$ (Figures 6.11a and 6.11b). The resulting torque contributions of lift and drag increase but outweigh each other resulting in a fairly flat peak in the rotor torque curve (Figure 6.11c). As the vortex leaves the blade surface region at $\psi = 250°$, lift drops significantly resulting in a further drop in rotor torque to an even lower negative value. Beyond $\psi = 250°$, $\alpha_c$ is decreasing and the stall depth begins to reduce, with reduced vortex shedding observed in the flowfield visualisations, and a corresponding increase in rotor torque is shown in Figure 6.11c.
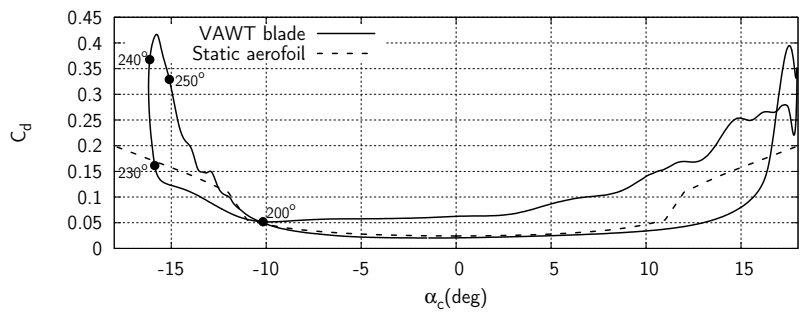
### 6.3.4 Fourth Quadrant

The experimental PIV visualisations showed vortex shedding to continue for much of the fourth quadrant before the flow begins to reattach as $\alpha_c$ reduces. The exact position was not determined due to a lack of measurements due to structural obstructions but was somewhere between $\psi = 320°$ and $350°$. The simulation showed reattachment to be almost completed by $\psi = 320°$.

The simulated flowfield shows the flow to begin attaching from $\psi = 270°$ onwards, with a significant drag reduction shown between $\psi = 270°$ and $300°$ (Figure 6.11b) and a small increase in lift (Figure 6.11a) resulting in the overall rotor torque returning to positive above $\psi = 288°$ (Figure 6.11c). Between $\psi = 300°$ and $330°$, lift falls as $\alpha_c$ reduces; however, as the flow attaches to more of the blade surface, drag reduces significantly in this region which results in a small increase in overall rotor torque. Beyond $\psi = 330°$, $\alpha_c$ drops leading to further reduced lift which results in the rotor torque dropping again to negative values. The reduced rate of change of $\alpha_c$ compared to the mid-rotation results in a reduced amount of lag in the reattachment, and the flow has recovered such that $C_l = 0$ at $\psi = 0°$.

(a) $C_l$ versus $\alpha_c$



(b) $C_d$ versus $\alpha_c$
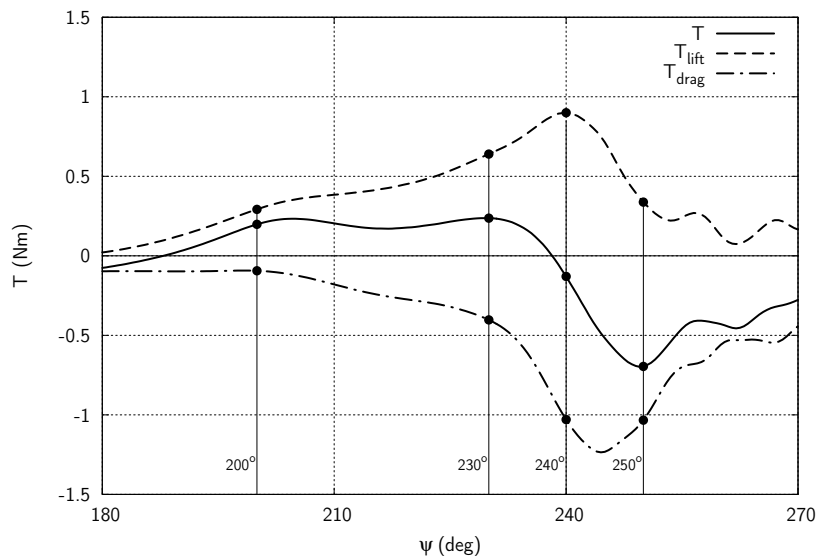


(c) $T$ versus $\alpha_c$

Figure 6.11: $C_l$ and $C_d$ versus $\alpha_c$, and $T$ versus $\psi$ for the third quadrant as predicted by the CFD simulation, at $\lambda = 3$ for the reference 7m/s case.

(a) $C_l$ versus $\alpha_c$



(b) $C_d$ versus $\alpha_c$



(c) $T$ versus $\alpha_c$

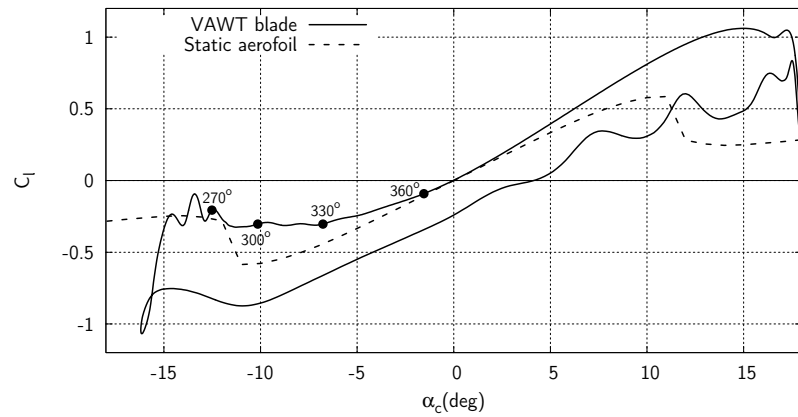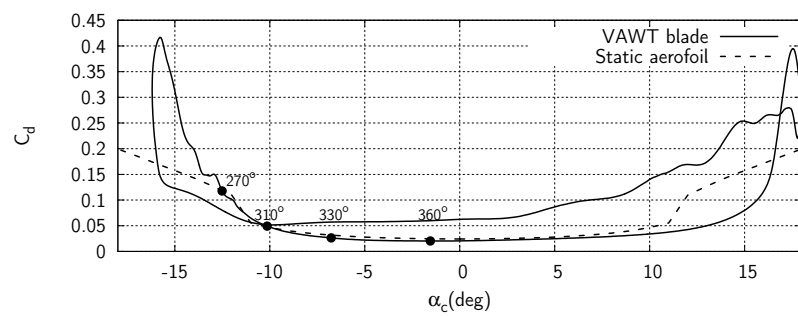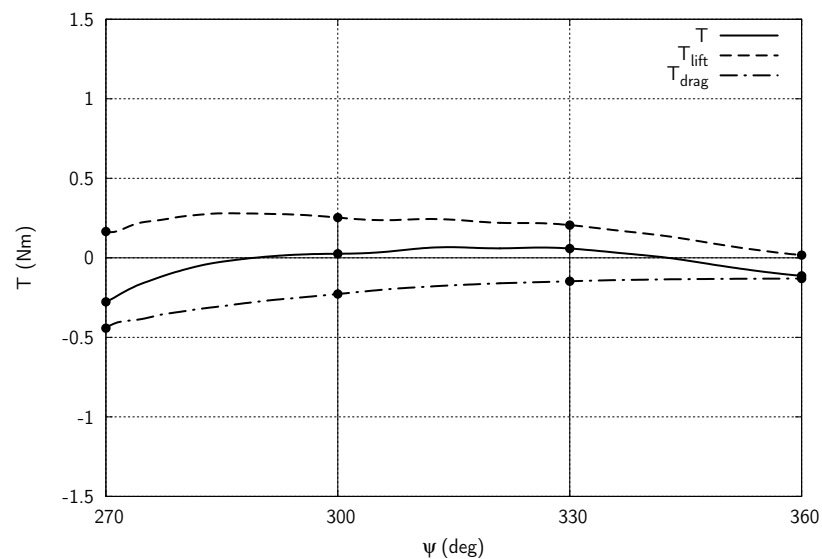Figure 6.12: $C_l$ and $C_d$ versus $\alpha_c$, and $T$ versus $\psi$ for the fourth quadrant as predicted by the CFD simulation, at $\lambda = 3$ for the reference 7m/s case.

### 6.3.5 Summary

For the $\lambda = 3$ condition, the flowfield visualisations have shown wider regions of attached flow and the simulation has shown an increased amount of positive torque as a result. Analysis of the forces extracted from the simulation have shown that the rotor torque is positive for between $\psi = 25°$ and $75°$ and in the downwind portion of the rotation, a smaller positive torque is shown between $\psi = 190°$ and $238°$. Deep stall was again observed in the flowfield visualisations and is shown to cause large troughs in the torque curve which have a significant impact on the average torque for the rotation. Delay in flow reattachment following the upwind and downwind stalling further contributes to high drag and low lift, and negative torque results.

In Figure 6.13 the overall rotor torque change through the rotation is plotted alongside the flowfield visualisations, the increased regions of positive torque are clearly shown. The dependence of the small positive $C_p$ on the upwind region of attached flow is clear, and the post stall regions of high drag are shown to give the largest regions of negative drag. Almost equally significant are the regions of delayed flow reattachment which prevent a recovery of the lift in the latter part of the second quadrant and the fourth quadrant. Overall the flow is detached for $\approx 45\%$ of the rotation and negative torque is produced for a similar percentage which explains the improvement over the negative $C_p$ which was recorded for the $\lambda = 2$ condition. In the experiment, the slightly earlier upwind stall and later downwind reattachment understandably yield a lower $C_p$ when compared to the simulation.
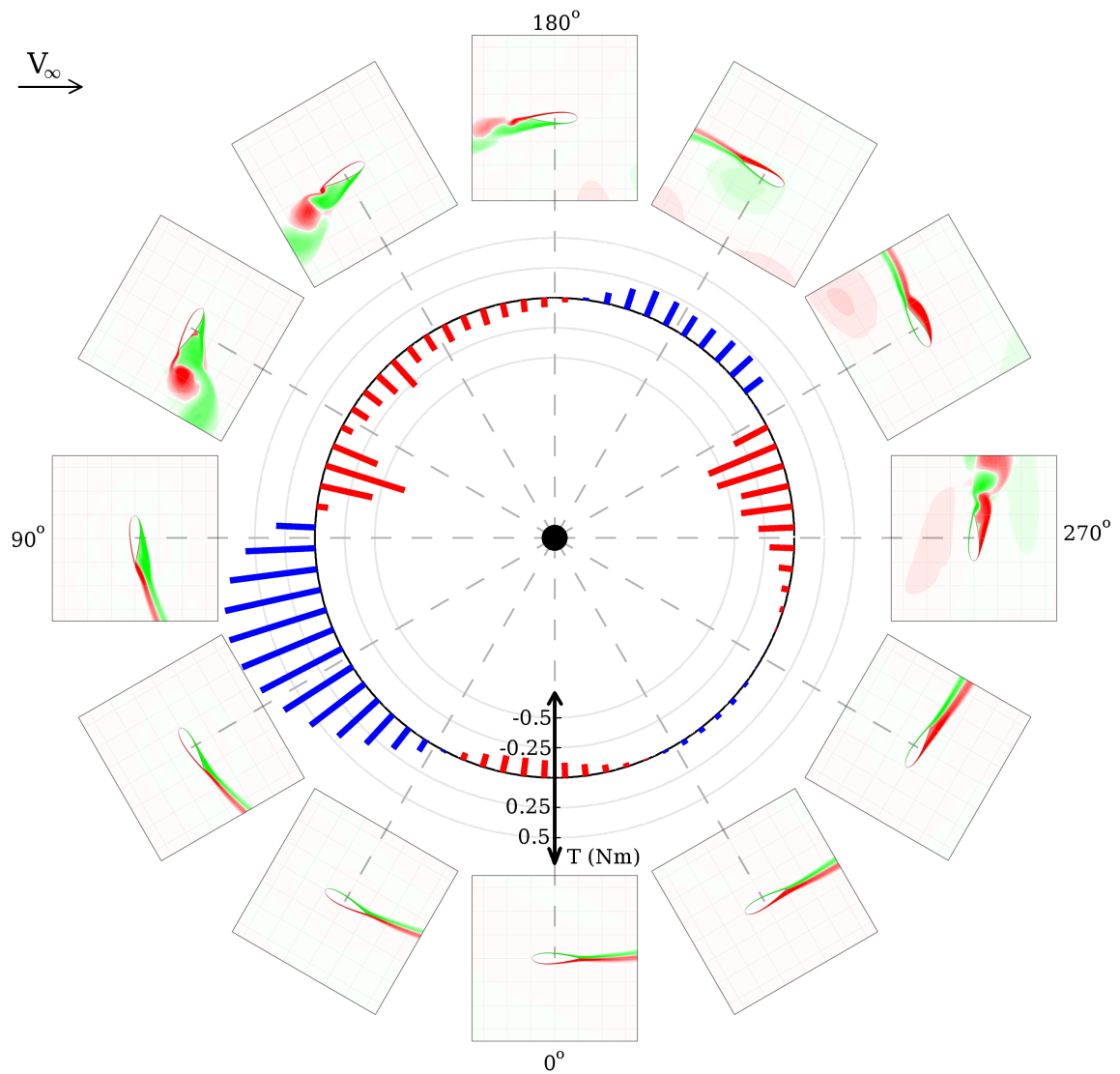
Figure 6.13: A plot showing the rotor torque and flowfield changes with azimuth angle at $\lambda = 3$ for the reference 7m/s case. Positive torque is represented by blue bars, negative torque by red bars.

## 6.4  $\lambda = 4$

The CFD flowfield visualisations have shown that the flow at $\lambda = 4$ does not experience deep stall and no large vortices are shed at any point in the rotation. Some partial separation is shown in the regions of the rotation which experience the highest angles of attack. As a result, hysteresis loops shown in the $C_l - \alpha$ and $C_d - \alpha$ curves are much reduced relative to the other conditions. The experiment showed separation in the upwind part of the rotation, in a similar manner to the CFD a gradual detachment, moving forwards from the trailing edge, was visible in the PIV visualisations. Some vortex shedding was shown in the experiment after $\psi = 130°$ where $\alpha_c$ is actually reducing, this was not the case in the simulation. As a result, the experimental flow had to recover around the mid-rotation point whereas the simulated flowfield did not. The likely result of this is that drag in the second quadrant would be much higher in the experiment and goes to show that not all the difference between the $C_{p-blade} - \lambda$ curves is due to 3D effects.

### 6.4.1  First Quadrant

At $\psi = 0°$, due to the effect of the rotor impedance on the incoming flow $\alpha_c$ starts at a small negative value of $-1.5°$. Lift between $\psi = 0°$ and $30°$ is therefore low (Figure 6.14a), and although drag is low (Figure 6.14b), the low value of $\alpha_c$ allows little useful contribution from the lift to the rotor torque, which is negative up to $\psi = 33°$ (Figure 6.14c).

Between $\psi = 30°$ and $60°$ there is a steady rise in both lift and drag as $\alpha$ increases, lift increase at a higher rate with $C_l$ at $\psi = 60°$ being 2.5 times the value at $\psi = 30°$. The increase in $\alpha_c$ in this region results in an increased lift contribution to the tangential direction and so $T_{lift}$ at $\psi = 60°$ is around 4 times the value at $\psi = 30°$. Similarly, although drag has increased, the reduced contribution due to higher $\alpha_c$ actually results in a slight drop in $T_{drag}$ between $\psi = 30°$ and $60°$. This results in the overall rotor torque going from a negative to a positive value in this region.

Between $\psi = 60°$ and $90°$ there is a further increase in lift and drag. The simulation and experimental visualisations showed that the flow begins to separate from the trailing edge, towards the end of the first quadrant. As a result, the rate of change of $C_l$ is observed to fall, whilst the rate of change of $C_d$ begins to rise, this leads to the overall rotor torque curve flattening out in the $\psi = 60°$ and $90°$ region.

### 6.4.2  Second Quadrant

Visualisations from the simulation show the trailing edge separation to progress slowly forwards before beginning to go backwards at $\psi = 140°$. This demonstrates a lag in the flow behaviour, as $\alpha_c$ actually reaches its maximum value at $\psi = 105°$. This shows dynamic effects are still present, although dynamic stall is not encountered in the simulation.

Figure 6.15a shows a 15% drop in $C_l$ for a tiny change in $\alpha_c$ across the $\psi = 90°$ to $120°$

region which actually results in a one third drop in $T_{lift}$. In the same portion of the rotation, $C_d$ increases by 25% (Figure 6.15b), although $T_{drag}$ increases only slightly (Figure 6.15c). Figure 6.16 shows that the resultant blade velocity actually falls in this region from 28m/s to 25m/s, which accounts for a 20% drop in the aerodynamic forces ($\propto V_r^2$), and when added to the fall in $C_l$ and rise in $C_d$ the changes in $T_{lift}$ and $T_{drag}$ are explained.

Between $\psi = 120°$ and $150°$ lift falls significantly, due to a much reduced $\alpha_c$, although the flow hysteresis also means that $C_l$ values are below those predicted in the static aerofoil simulation. The reduced $\alpha_c$ also reduces $C_d$ but the flow hysteresis leads to values remaining above those measured on the 'pitch-up' part of the curve. The net effect on rotor torque is an overall reduction to $T = 0$ by $\psi = 154°$. Between $\psi = 150°$ and $180°$, $\alpha_c$ drops significantly from small positive to a small negative value, $C_l$ and $C_d$ fall to low values, and the resultant rotor torque is negative. The reduced relative blade velocity results in the negative torque at $\psi = 180°$ being around half of that at $\psi = 0°$, despite the similar flow physics between the two positions.

The experimental and simulated flowfield visualisations differed greatly in this region, the experimental case featured a higher degree of separated flow and would undoubtedly have much higher drag. Although, the reduced relative blade velocity in this region may mean that this is not as significant as it first appears.
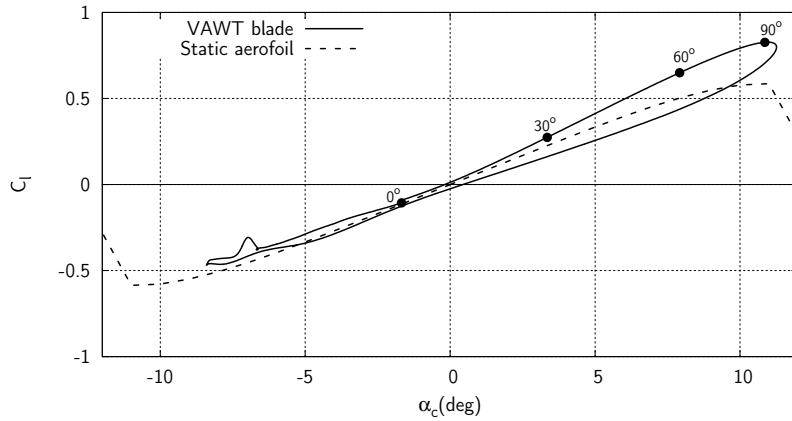
(a) $C_l$ versus $\alpha_c$
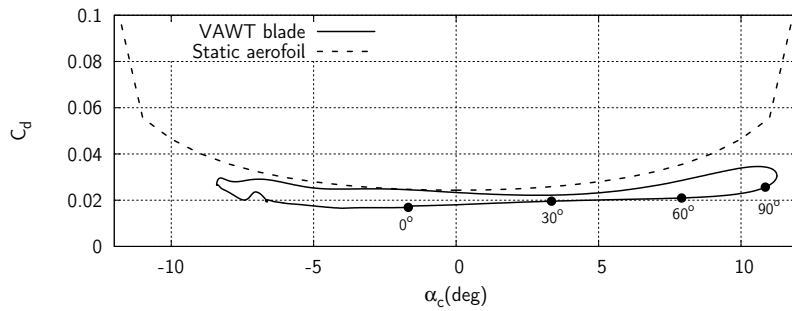


(b) $C_d$ versus $\alpha_c$
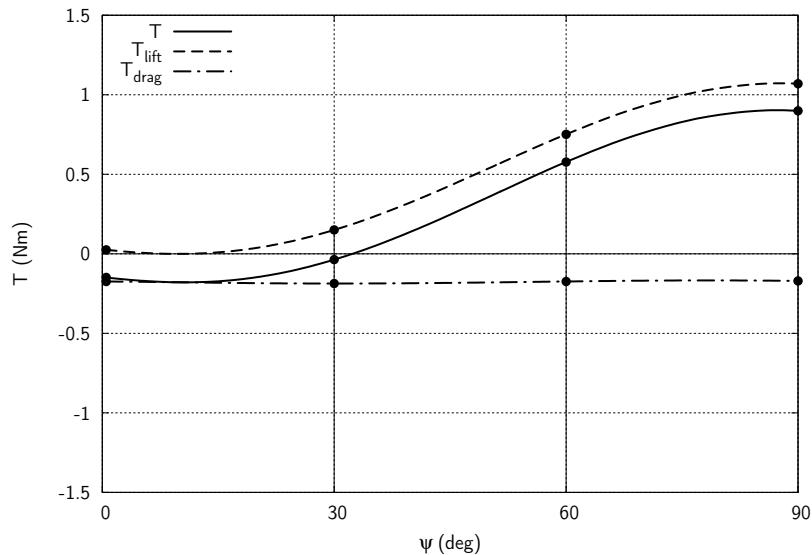


(c) $T$ versus $\alpha_c$

Figure 6.14: $C_l$ and $C_d$ versus $\alpha_c$, and $T$ versus $\psi$ for the first quadrant as predicted by the CFD simulation, at $\lambda = 4$ for the reference 7m/s case.
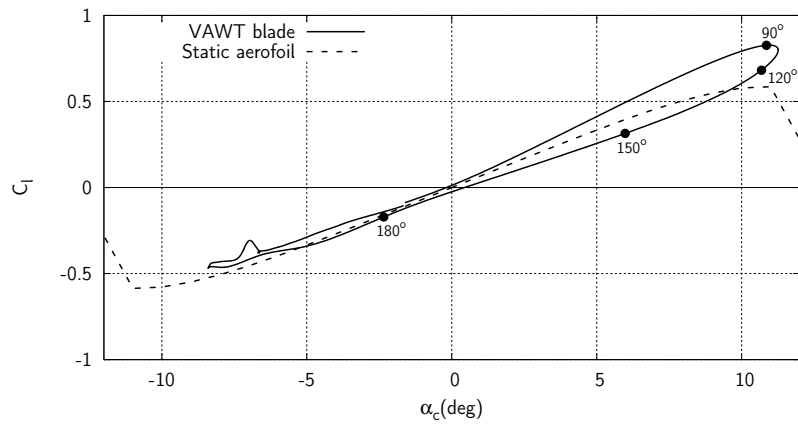
(a)  $C_l$ versus $\alpha_c$



(b)  $C_d$ versus $\alpha_c$



(c)  $T$ versus $\alpha_c$

Figure 6.15: $C_l$ and $C_d$ versus $\alpha_c$, and $T$ versus $\psi$ for the second quadrant as predicted by the CFD simulation, at $\lambda = 4$ for the reference 7m/s case.
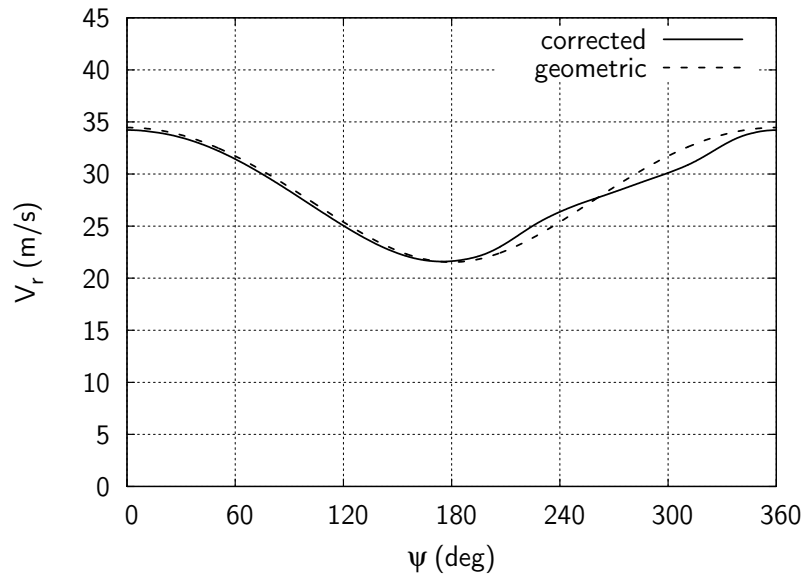
Figure 6.16: Relative blade velocity through a rotation at $\lambda = 4$.

### 6.4.3 Third Quadrant

Both the simulation and experimental PIV visualisations showed attached flow for the whole of the third quadrant. With no large separation in the upwind part of the rotation, lift in the early part of the third quadrant is not enhanced as it was for the $\lambda = 2$ and 3 conditions, and $C_l$ lies close to static values.

Beyond $\psi = 180°$, $\alpha_c$ increases rapidly and an increase in $C_l$ is shown in Figure 6.17a with little increase in drag shown for the same region in Figure 6.17b. Around $\psi=210°$, the blade begins to encounter a region of flow which has been significantly slowed down by the upstream part of the rotor. The freestream velocity decrease is such that the resultant value of $\alpha_c$ changes very little between $\psi=210°$ and $250°$, $C_l$ and $C_d$ remain fairly steady (Figures 6.17a and 6.17b), giving a fairly flat peak in the rotor torque curve (Figure 6.17c).

Near $\psi = 270°$ the blade encounters the wake of the shaft resulting in a drop in $\alpha_c$ which results in small drop in lift and a small increase in drag, with the net result being a small drop in overall rotor torque.

### 6.4.4 Fourth Quadrant

Past $\psi = 270°$ the blade leaves the wake of the shaft resulting in a small increase in $\alpha_c$ which results in small increase in lift, which gives a small rise in overall rotor torque. Between $\psi = 300°$ and $330°$, lift falls as $\alpha_c$ reduces, drag remains fairly constant. and the overall rotor torque drops but remains positive. Beyond $\psi = 330°$, $\alpha_c$ drops leading to further reduced lift which results in the rotor torque dropping again to negative values. The range in $\alpha_c$ is reduced

in this region due to the strong influence of the upwind blade pass in the first quadrant, where significant energy extraction has taken place and the flow velocity has been reduced. The effect on the relative blade velocity can also be seen in Figure 6.16. As a result, the torque produced in this region is low when compared to the first quadrant.
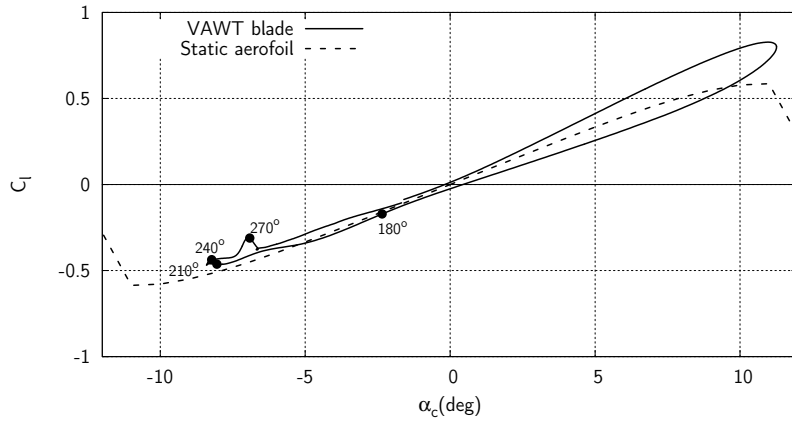
(a) $C_l$ versus $\alpha_c$
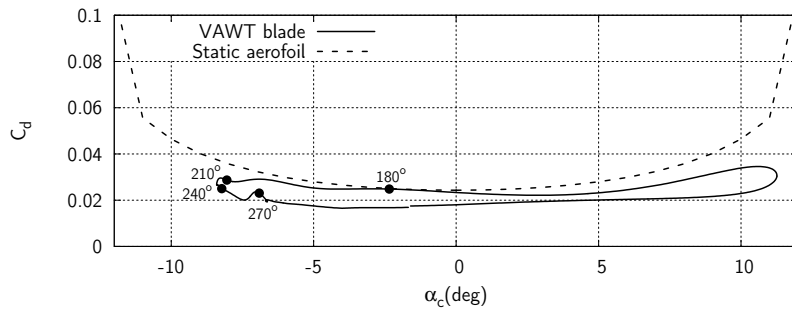


(b) $C_d$ versus $\alpha_c$
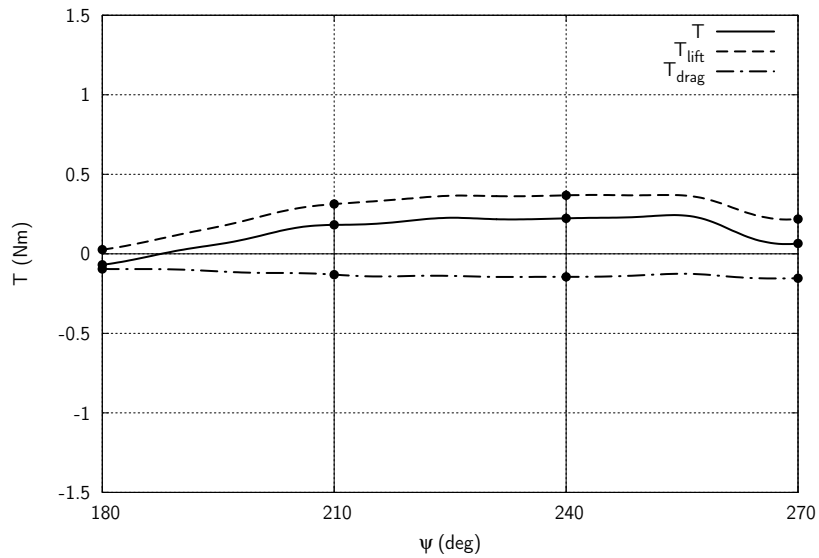
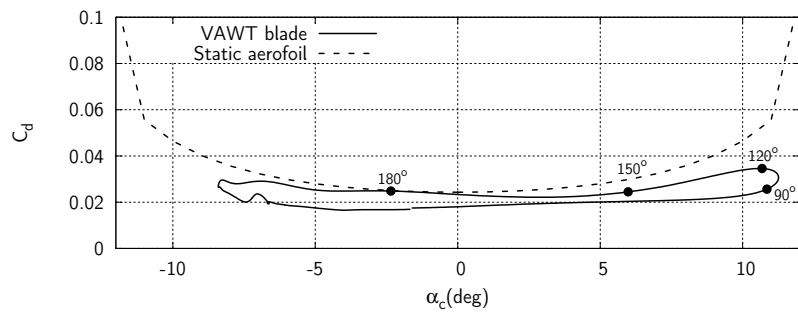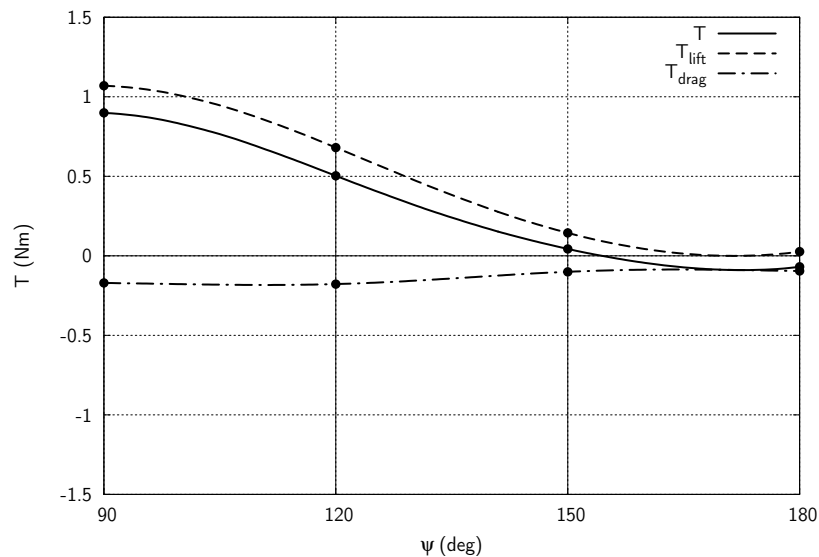

(c) $T$ versus $\alpha_c$

Figure 6.17: $C_l$ and $C_d$ versus $\alpha_c$, and $T$ versus $\psi$ for the third quadrant as predicted by the CFD simulation, at $\lambda = 4$ for the reference 7m/s case.
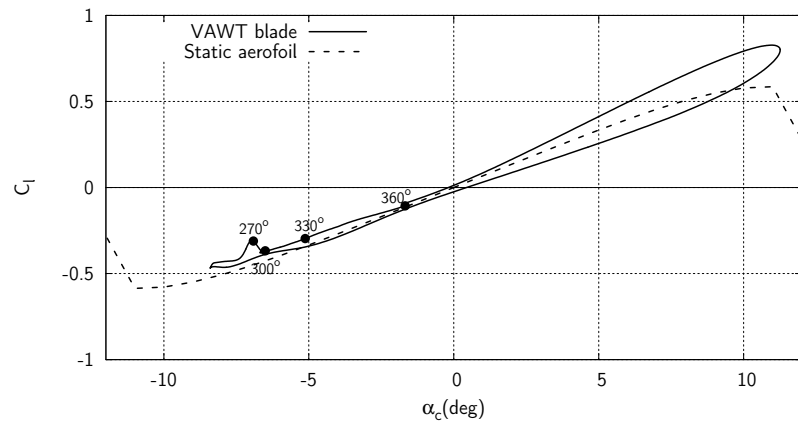
(a)  $C_l$ versus $\alpha_c$
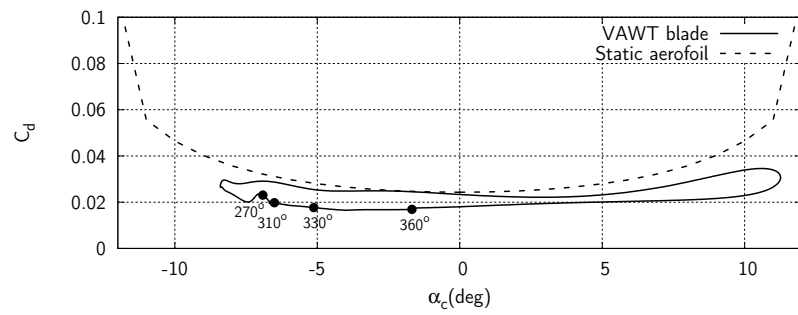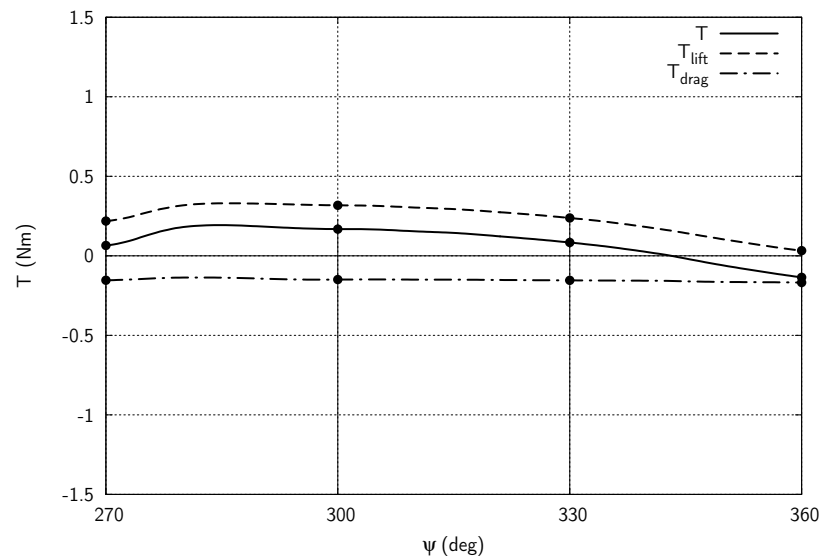
(b)  $C_d$ versus $\alpha_c$

(c)  $T$ versus $\alpha_c$

Figure 6.18: $C_l$ and $C_d$ versus $\alpha_c$, and $T$ versus $\psi$ for the fourth quadrant as predicted by the CFD simulation, at $\lambda = 4$ for the reference 7m/s case.

### 6.4.5   Summary

For the $\lambda = 4$ condition, the flowfield visualisations from the simulation show attached flow for the whole rotation. The torque curve only falls to negative values for around 20% of the rotation, between $\psi = 342°$ and 33° and also between $\psi = 154°$ and 186°. These are regions where the blade experiences a small $\alpha_c$ which results in a low amount of lift and a small $T_{lift}$ which is unable to outweigh the contribution $T_{drag}$ makes to overall rotor torque.

In Figure 6.19 the change in $T$ through the rotation is plotted alongside the flowfield visualisations, the large regions of positive torque are clearly shown. The effect of the variation in relative blade velocity is clearly shown in the different levels of negative torque shown between the start of the rotation, where $V_r$ is highest, and the mid-rotation, where $V_r$ is lowest. The effect of the reduced downwind flow velocity results in a low and flattened peak in the $T$-$\psi$ curve. The further flow velocity reduction due to the shaft wake causes a notable drop in the torque around $\psi = 270°$. Overall, two-thirds of the overall power comes from the upwind portion of the rotation, which has a broad peak in torque around $\psi = 90°$. The remaining positive contribution is spread over most of the downwind rotation, with the third quadrant giving a greater proportion due to the higher flow velocity.

The experiment was shown to stall around $\psi = 130°$, and reattach around $\psi = 180°$. Figure 6.19 shows the forces in this region are relatively low due to the lower relative blade velocity. So the effect may not be as severe as first anticipated, and is expected to lead to an approximate 10% reduction in the overall torque.
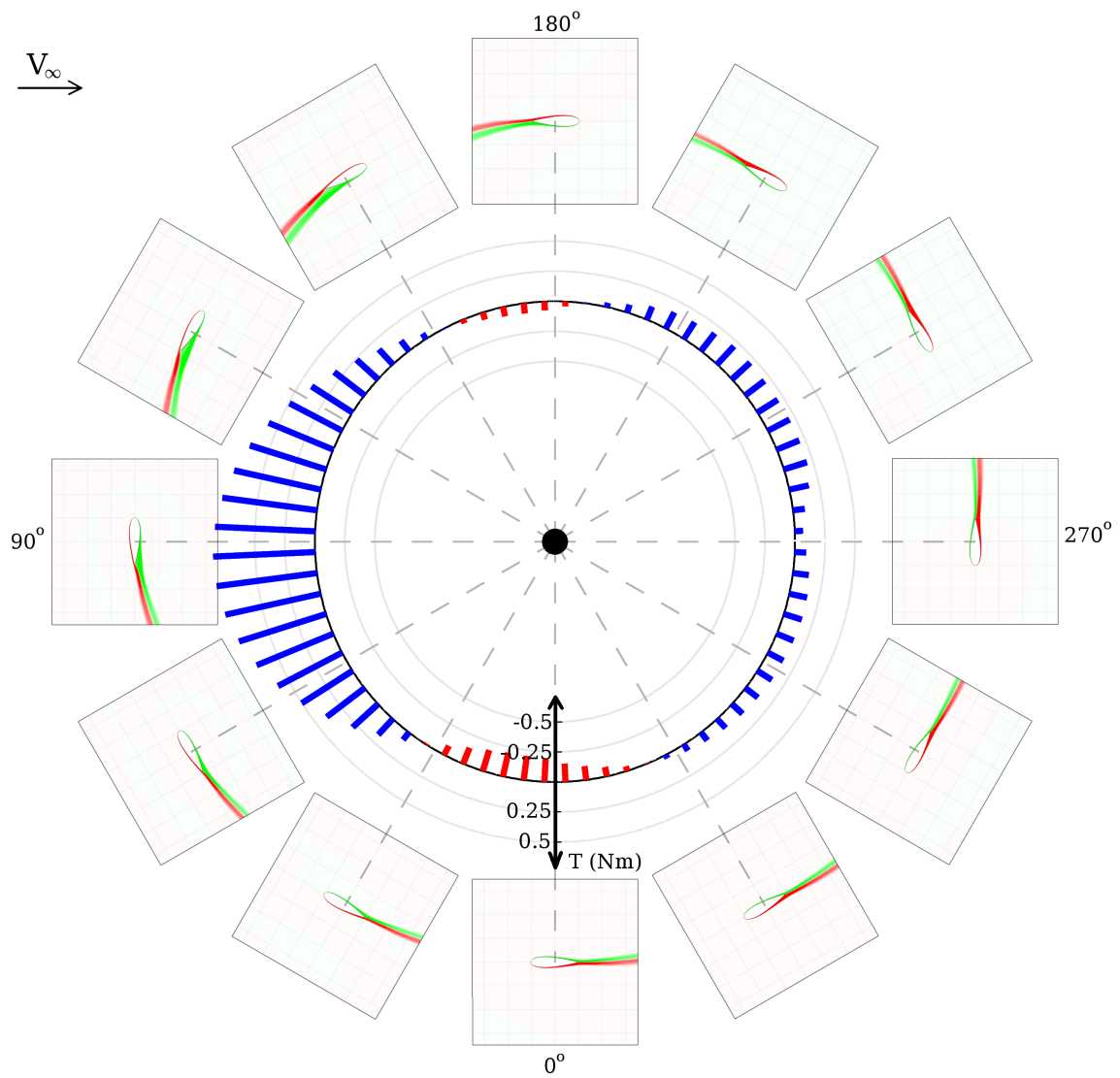
Figure 6.19: A plot showing the rotor torque and flowfield changes with azimuth angle at $\lambda = 4$ for the reference 7m/s case. Positive torque is represented by blue bars, negative torque by red bars.

## 6.5 Summary

A significant flow hysteresis was observed in the visualisations presented previously in Chapter 5, and predictably, large loops were revealed in the lift and drag curves presented in this chapter. The effect of dynamic stall on the aerodynamic forces has been clearly shown, with larger values of $C_{l-max}$ shown over static data for the same aerofoil. The highest lift coefficient was shown for the $\lambda = 2$ condition where a lift coefficient of (-)1.8 was shown to be the result of the highest rate of change of $\alpha$. However, higher torque due to enhanced lift during the onset of dynamic stall was shown to be quickly overpowered by the corresponding increase in drag, which is more aligned to the tangential direction. As $\alpha$ reduces, the delayed flow reattachment then further contributes to high drag and low lift, and negative torque results.

At $\lambda = 2$, the flow is detached for 70% of the rotation and negative torque is produced for 75% of the rotation, explaining the negative $C_p$. At $\lambda = 3$, the flow is detached for 45% of the rotation and negative torque is produced for a similar percentage which explains the improvement over the $\lambda = 2$ condition. At $\lambda = 4$, the torque curve only falls to negative values for around 20% of the rotation, in regions where the blade experiences a small angle of attack and a resulting low amount of lift which is unable to outweigh the contribution from drag. Two-thirds of the overall power is generated in the upwind portion of the rotation at $\lambda = 4$.

The post stall regions of high drag are shown to give the most significant regions of poor performance. However, almost equally significant are the regions of delayed flow reattachment which prevent a recovery of the lift in the latter part of the second quadrant and the fourth quadrant at $\lambda = 2$ and 3. This shows that the use of an aerofoil that encourages post-stall flow reattachment, as well as generally high lift and low drag characteristics, would likely be beneficial to overall performance.

# Chapter 7

# The Effect of Fixing Angle Adjustment

## 7.1   Introduction

Previous research (discussed in Section 2.3.1) has shown that small changes to the blade fixing angle can have a significant impact on the performance of the VAWT. Positive pitch (defined as pitching the leading edge away from the VAWT shaft, see Figure 3.5a) reduces the angle of attack in the upwind part of the rotation, delaying stall to higher azimuth angles where the orientation of the lift is such that it may make a larger contribution to torque. Whilst in the downwind part of the rotation stall is reached earlier, as the fixing angle has the opposite effect on the angle of attack. However, as the previous chapter has shown, the stalling behaviour is not the only concern, the reattachment behaviour may also have a strong effect on performance. Due to the direct effect that fixing angle has on stalling behaviour of the VAWT, a study of fixing angle is the next logical step.

The main difficulty in assessing the effect of fixing angle adjustment is that any change has both positive and negative impacts throughout the rotation. The particular trade off of earlier or later stall and reattachment in the upwind and downwind parts of the rotation eventually determines the overall effect on $C_p$. Assessment of this overall outcome involves good modelling of the whole rotation, and so mathematical models which lack a proper modelling of upwind and downwind behaviour are not suited to the evaluation of fixing angle effects.

As the downwind part of the rotation has a lower wind speed it may be more beneficial to enhance the upwind torque peak. However, this benefit is said to only exist for small positive fixing angles, with Coton et al. [26] showing a slight increase in performance for a +2deg fixing angle. Published experimental data on the effect of fixing angle is currently limited to the comparison of $C_p$ values, such as that by Klimas [25], this chapter goes beyond this by using PIV visualisations to explain the reasons behind the observed changes in measured

181

power coefficient.

## 7.2 $C_p$ Performance

Using the previously detailed experimental set-up, the $C_p$ performance with changing $\lambda$ was measured for two blade fixing angles: $\beta = -2°$ and $2°$ (as defined in Figure 3.5a). The same spin-down method (detailed in Section 3.4) and test conditions were used as for the Reference Case (see Section 5.3). Again, for each data point both the calculation of $C_p$ and $\lambda$ were corrected for the relevant drop in wind speed. The results are presented in Figure 7.1 alongside the comparable data from the Reference Case where $\beta = 0°$.

The results show that relative to the $\beta = 0°$ case:

- $\beta = -2°$ leads to:

    - a very similar performance below $\lambda = 2$

    - improved performance between $\lambda = 2$ and 3.2, giving a reduced negative trough.

    - a much-reduced $C_{p-max}$ of 0.05 is generated at a slightly lower $\lambda$.

    - a performance which tends toward that of the $\beta = 0°$ case when $\lambda > 4.6$.

- $\beta = +2°$ gives:

    - a very similar performanc below $\lambda = 2$

    - a much reduced performance between $\lambda = 2$ and 4, leading to a deeper negative trough.

    - a similar $C_{p-max}$ of 0.145 is generated at a slightly higher $\lambda$.

    - a much sharper peak in the $C_{p-blade}$ curve.

    - a performance tending toward that of the $\beta = 0°$ case when $\lambda > 4.3$.

The results have some comparisons with the results of Klimas (Figure 2.12) in that Klimas' results show positive angles have the most significant negative effect at lower tip speed ratios and that there appears to be very little increase in $C_p$ achievable from adjusting the fixing angle. Although, the results are have limited comparison potential as Kilmas' results are from an outdoor test of a Darrieus turbine, at a larger scale and with a different blade profile (NACA0015).

## 7.3 PIV Visualisation

Significant changes are observed in the $C_p$ measurement with small positive and negative fixing angles. PIV measurements were again taken to aid the understanding of the performance curves and reveal the details of the changes to the flow physics through the rotation
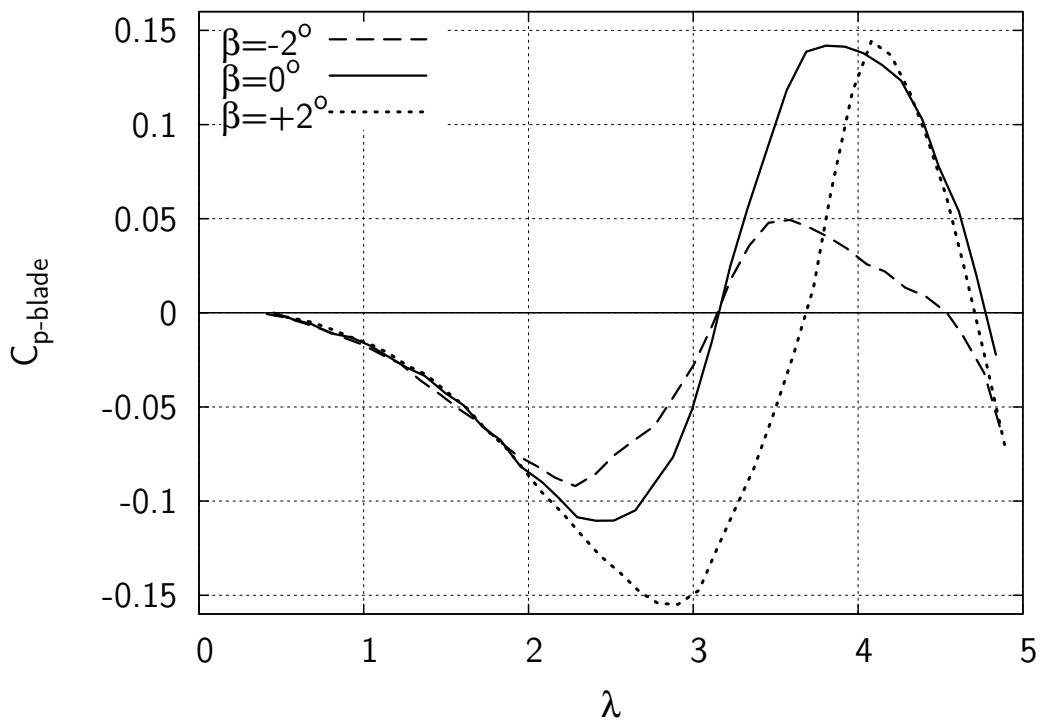
Figure 7.1: A plot of $C_{p-blade}$ vs $\lambda$ showing the effect of small fixing angle changes relative to the zero fixing angle Reference Case.

which result from altering the blade fixing angle. The same test conditions were used as for the Reference Case (see Section 5.4), with $\lambda = 2$, 3 and 4. Measurements were taken at $10°$ $\psi$ intervals, matching the $\psi$-positions and field of view for the $\beta = 0°$ case.

### 7.3.1 $\beta = -2°$, $\lambda = 2$

PIV flow visualisations show the flow to be attached from the beginning of the rotation (Figure 7.2a) up to $\psi = 50°$, where the beginning of a leading edge roll-up is observed as part of the dynamic stall process (Figure 7.2b). This shows that the onset of the upwind stall occurs around $10°$ earlier in the rotation than for the $\beta = 0°$ case (see Figures 5.6a to 5.6c). Following the onset of stall, a similar large-scale vortex shedding process is shown, with the approximate $10°$ phase-difference being maintained (Figures 7.2b to 7.2f).

The mid-rotation reattachment behaviour is shown to lag behind the reduction in $\alpha$ at $\psi = 170°$ to $190°$ (Figures 7.3a to 7.3c). Similar plots were shown for the $\beta = 0°$ case (Figures 5.8a to 5.8c) indicating that the small change in fixing angle has little effect in this part of the rotation where the rate of change of $\alpha$ is at its most rapid.

The visualisations show the downstream stall to occur in a very similar manner to the $\beta = 0°$ case, again the flow appears to have stalled before $\psi = 230°$ (Figure 7.4a) as reattachment

(a) $\psi = 10°$     (b) $\psi = 50°$     (c) $\psi = 60°$



(d) $\psi = 70°$     (e) $\psi = 80°$     (f) $\psi = 90°$
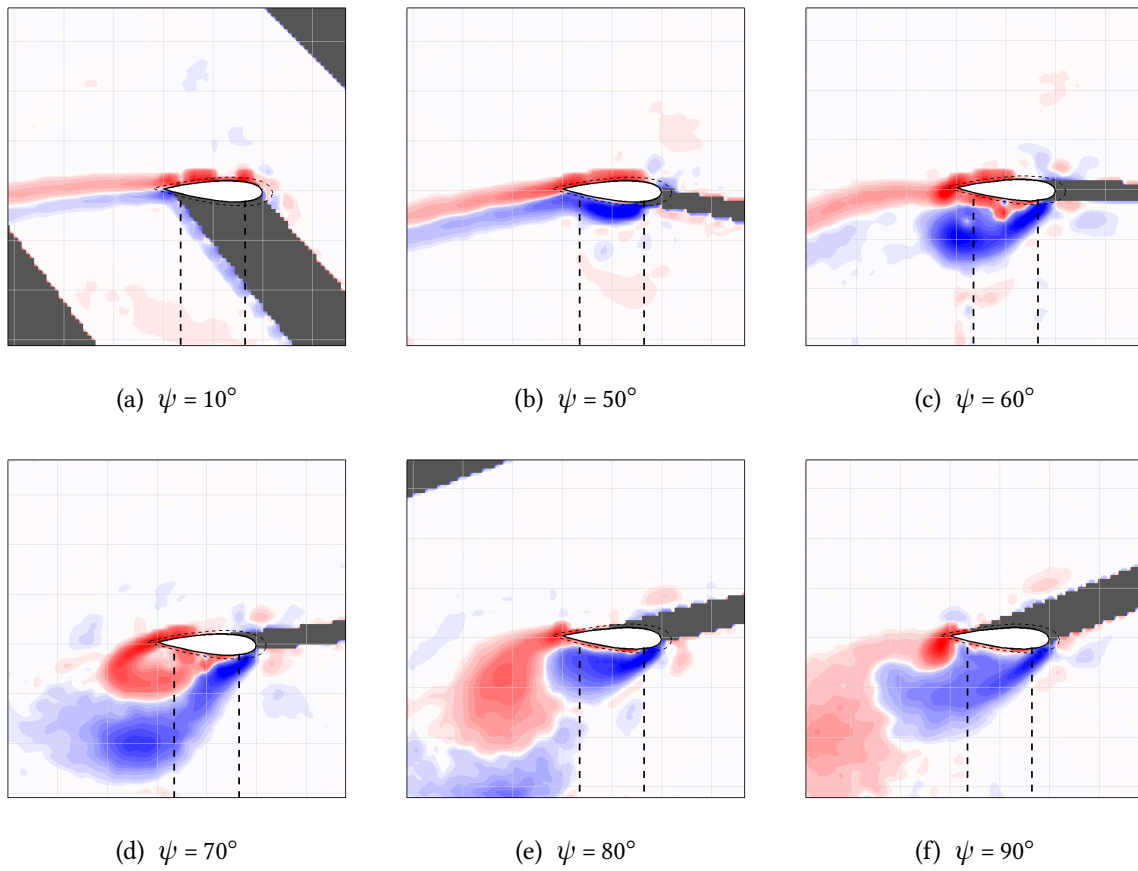
Figure 7.2: Plot of z-vorticity showing the upwind stalling process for $\beta = -2°$, $\lambda = 2$



(a) $\psi = 170°$     (b) $\psi = 180°$     (c) $\psi = 190°$

Figure 7.3: Plot of z-vorticity showing a delayed flow reattachment at low $\alpha$ for the mid-rotation positions for $\beta = -2°$, $\lambda = 2$

is perhaps not completed after the upwind stall. Once stalled, a similar large-scale vortex shedding process is shown to the $\beta = 0°$ case. (Figures 7.4b to 7.4c). The major difference that the fixing angle change makes is that it leads to an earlier reattachment of the flow in the fourth quadrant of the rotation. For $\beta = 0°$, visualisation of the wake at shows that the flow had reattached just before $\psi = 0°$ (Figures 7.4f). For the $\beta = -2°$ case the flow is fully reattached at $\psi = 350°$ indicating reattachment took place at least 10° earlier in the rotation than for the $\beta = 0°$ case. Drag in this region would therefore be much reduced, which would somewhat offset the penalty of the earlier stall observed for the upwind part of the rotation. The force analysis of the previous chapter has shown that the magnitude of the positive torque around the onset of the upwind stall is not significantly greater than that of the negative torque around the downstream reattachment (Figure 6.7). As a result, only a slightly higher $C_p$ performance is measured for the $\beta = -2°$ case relative to the $\beta = -2°$ case at this tip speed ratio.



(a)  $\psi = 230°$         (b)  $\psi = 240°$         (c)  $\psi = 250°$

(d)  $\psi = 300°$         (e)  $\psi = 350°$         (f)  $\psi = 0°$
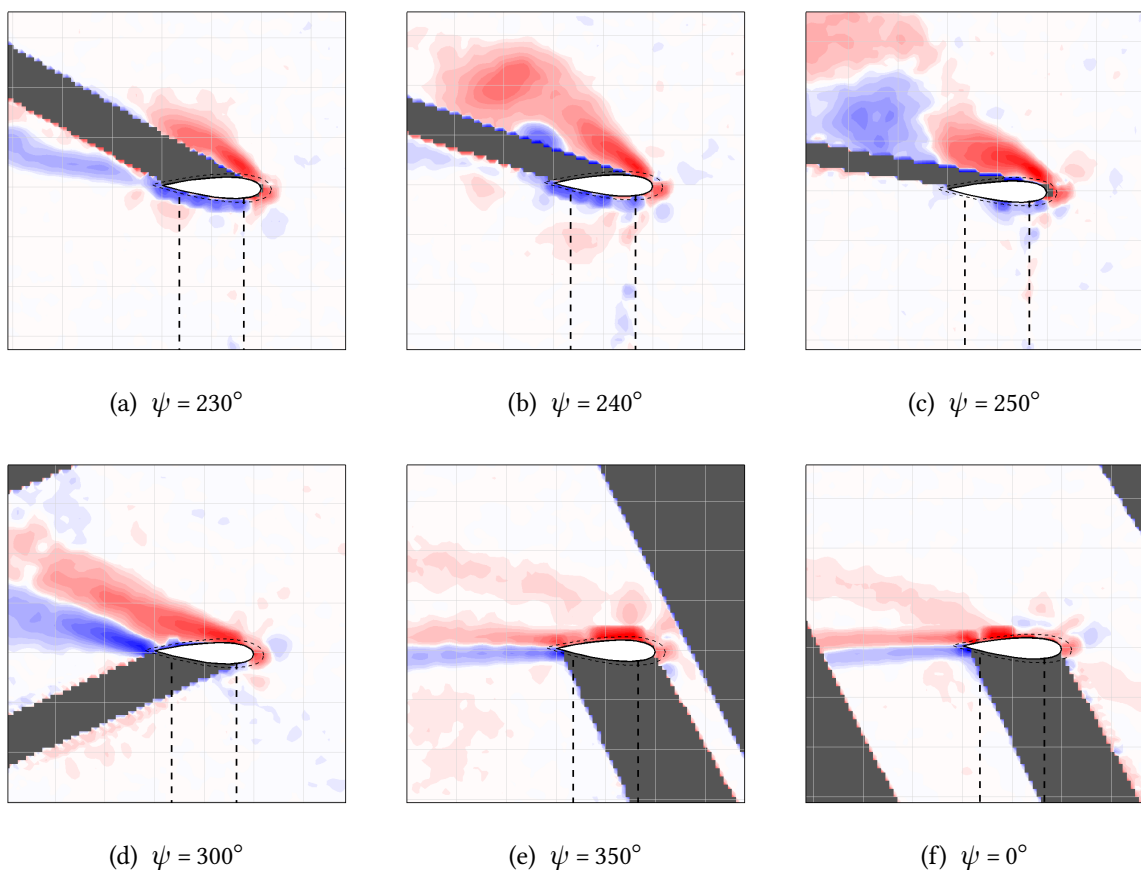
Figure 7.4:  Plot of z-vorticity showing the downwind stalling process and eventual reattachment for $\beta = -2°$, $\lambda = 2$

### 7.3.2  $\beta = -2°$, $\lambda = 3$

At $\lambda = 3$, the PIV flow visualisations show the flow to be attached from the beginning of the rotation (Figure 7.5a) up to $\psi = 70°$, where the beginning of a leading edge roll-up is observed (Figure 7.5b). As for the $\lambda = 2$ condition, this is around $10°$ earlier in the rotation than for the $\beta = 0°$ case (see Figure 5.11b). A very similar large-scale vortex shedding process is shown, with the $10°$ out of phase images of $\beta = -2°$ case (Figures 7.5c to 7.5f) being almost identical to those of the $\beta = 0°$ case showing that the phase difference is maintained (Figures 5.11b to 5.11e).



(a)  $\psi = 10°$  (b)  $\psi = 70°$  (c)  $\psi = 80°$

(d)  $\psi = 90°$  (e)  $\psi = 100°$  (f)  $\psi = 110°$
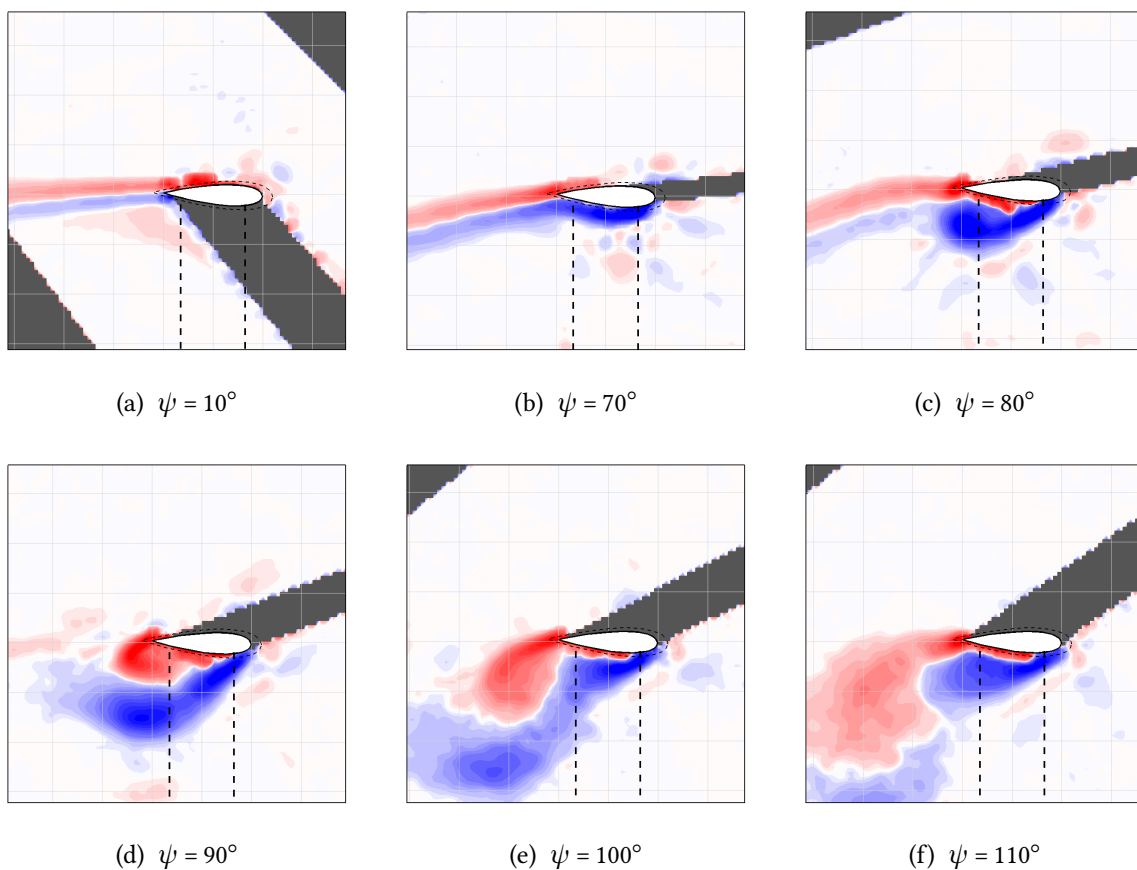
Figure 7.5: Plot of z-vorticity showing the upwind stalling process for $\beta = -2°$, $\lambda = 3$

As for the $\lambda = 2$ condition, similar plots are shown for the mid-rotation reattachment behaviour when $\beta = -2°$ (Figures 7.6a to 7.6c) or $\beta = 0°$ (Figures 5.12a to 5.12c) again indicating that the small change in fixing angle has little effect in this part of the rotation where a rapid rate of change of $\alpha$ is experienced.

In the downwind part of the rotation the PIV visualisations show that the $-2°$ fixing angle results in a reduced depth of stall relative to the $\beta = 0°$ case. Between $\psi = 220°$ and $240°$ (Figures 7.7a to 7.7b) the thickness of the wake suggest the flow has not fully-reattached, although the shadow region prevents more conclusive analysis. At $\psi = 270°$ (Figure 7.7c) the

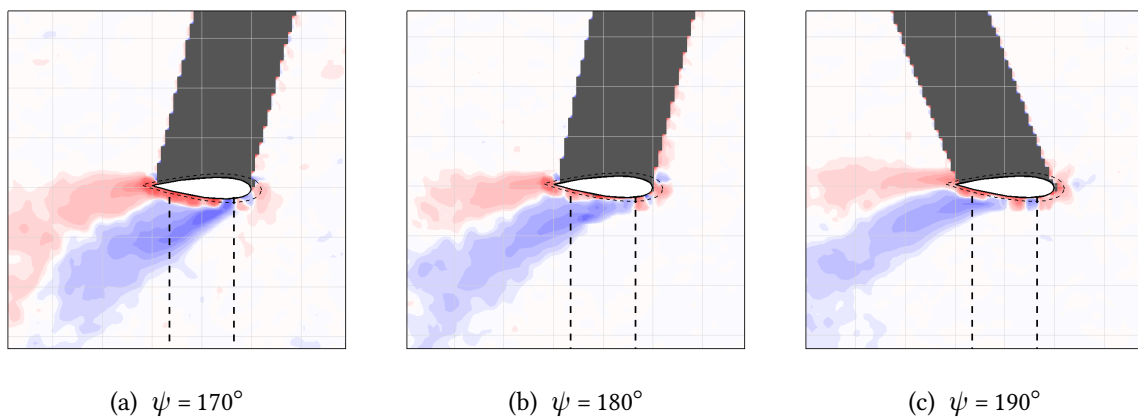(a) $\psi = 170°$       (b) $\psi = 180°$       (c) $\psi = 190°$

Figure 7.6: Plot of z-vorticity showing a delayed flow reattachment at low $\alpha$ for the mid-rotation positions for $\beta = -2°$, $\lambda = 3$

flow is shown to be separated from the blade surface; the depth of stall is certainly reduced relative to that shown for the $\beta = 0°$ case (Figure 5.13e). From $\psi = 290°$ onwards the flow is fully attached, which differs greatly from the $\beta = 0°$ case for which the flow was shown to be separated beyond $\psi = 320°$.

The force analysis of the previous chapter shows the region of vortex shedding encountered for the $\beta = 0°$ case during the deep stall between $\psi = 240°$ and $270°$ leads to a large region of substantial negative torque (Figure 6.7). The $-2°$ fixing angle would therefore lead to a reduced drag for this region due to the reduced depth of stall which is shown in the PIV visualisations. In addition, the earlier reattachment in the fourth quadrant will also lead to additional gains over the $\beta = 0°$ case. So, despite the earlier upwind stall, the $C_p = -0.028$ measured for the $\beta = -2°$ case is shown to be above that of the $\beta = 0°$ ($C_p = -0.05$) due to a reduced level of separation in the downwind part of the rotation.

### 7.3.3   $\beta = -2°$, $\lambda = 4$

At $\lambda = 4$, the PIV flow visualisations show the flow to be attached from the beginning of the rotation (Figure 7.8a) up to around $\psi = 100°$ at which point the beginning of a leading edge roll-up is observed (Figure 7.8c). This differs greatly from the flow physics shown for the $\beta = 0°$ condition, where a gradual forward progression of a trailing edge separation was shown to lead to a brief full-separation when the 'pitch-down' change in $\alpha$ occurred beyond $\psi = 140°$ (Figure 5.15g). For the $\beta = -2°$ case, deep stall is encountered and a chord-sized pair of vortices are shed between $\psi = 110°$ to $130°$ (Figures 7.8d to 7.8f), after which smaller vortices are more randomly shed as $\alpha$ reduces and the flow begins the process of reattachment. The force analysis of the previous chapter shows that for the $\beta = 0°$ case the upwind performance generated two-thirds of the total turbine torque, and this was shared between the first and second quadrants (Figure 6.19). The occurrence of stall early in the second quadrant would

(a) $\psi = 220°$

(b) $\psi = 240°$

(c) $\psi = 270°$

(d) $\psi = 290°$

(e) $\psi = 310°$

(f) $\psi = 350°$
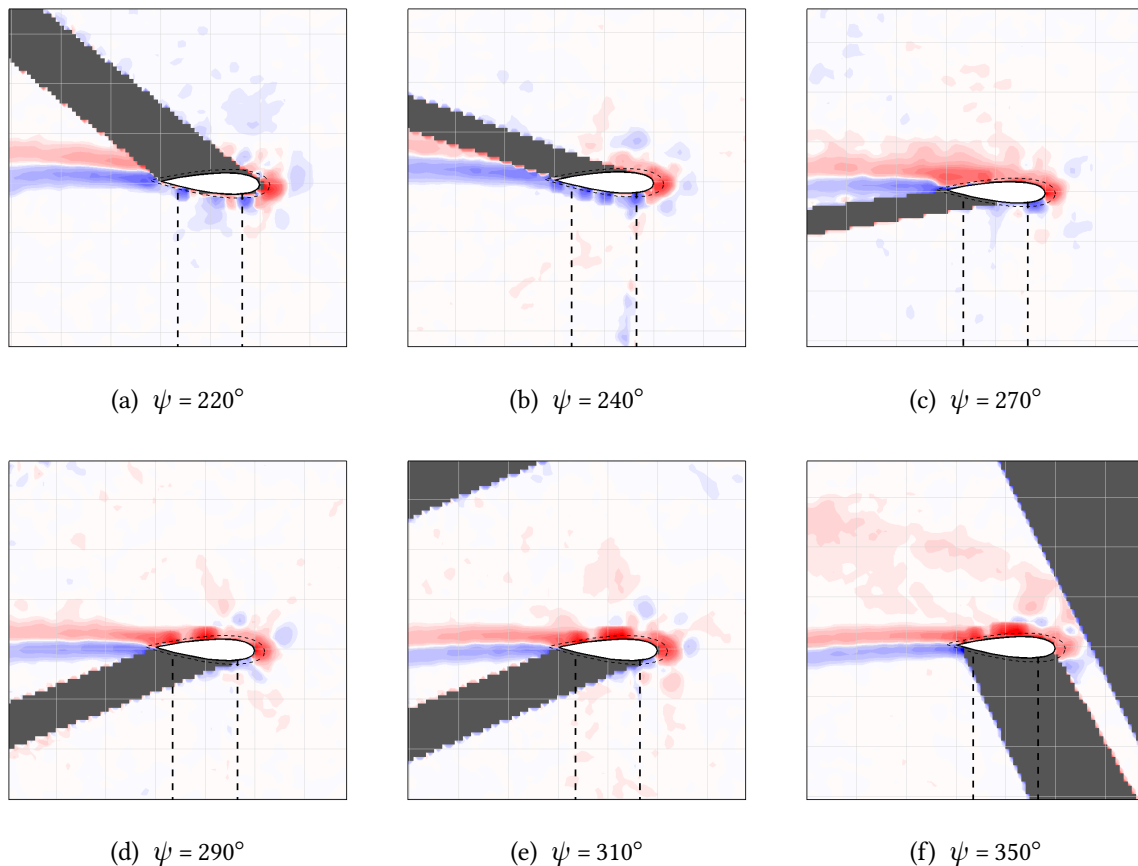
Figure 7.7: Plot of z-vorticity showing the downwind stalling process for $\beta = -2°$, $\lambda = 3$

therefore result in a large drop in torque.

As for both the $\lambda = 2$ and 3 conditions, similar plots are shown for the mid-rotation reattachment behaviour when $\beta = -2°$ at $\lambda = 4$ (Figures 7.9a to 7.9c). However, due to the much deeper stall, the reattachment does appear to be slightly lagging when compared to the $\beta = 0°$ condition (Figures 5.16a to 5.16c), and the wake shows a higher amount of vorticity. Even so, relative to the dramatic changes in the stalling process revealed for the upwind part of the rotation, the small change in fixing angle has again had relatively little effect on the mid-rotation reattachment.

In the downwind part of the rotation, the flow remains attached at all the measured azimuth angles (Figures 7.10) due to the higher tip speed ratio resulting from the drop in wind speed through the rotor, as was the case for the $\beta = 0°$ condition. With both cases showing attached flow in this region, the reduction in $\alpha$ due to a negative fixing angle will lead to reduced lift and performance is also likely to be lower here.

The wake of the previous blade can be seen in Figures 7.10c to 7.10f), the downstream convection of which is notably faster than that shown for the $\beta = 0°$ case. This shows that the reduced performance in the upwind part of the rotation has lead to increased flow velocity in

(a) $\psi = 10°$

(b) $\psi = 90°$

(c) $\psi = 100°$

(d) $\psi = 110°$

(e) $\psi = 120°$

(f) $\psi = 130°$

(g) $\psi = 140°$
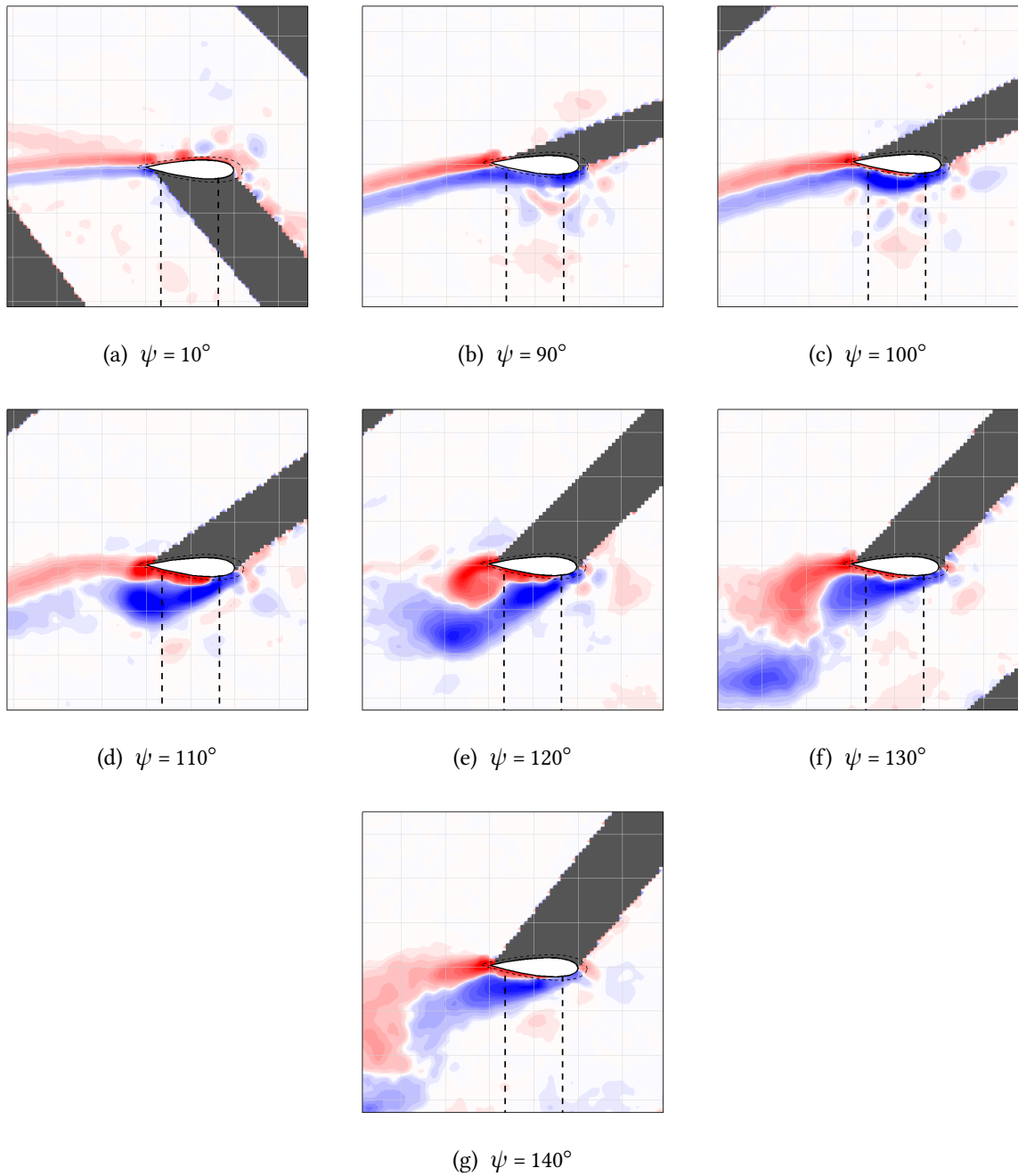
Figure 7.8: Plot of z-vorticity showing the upwind stalling process for $\beta = -2°$, $\lambda = 4$

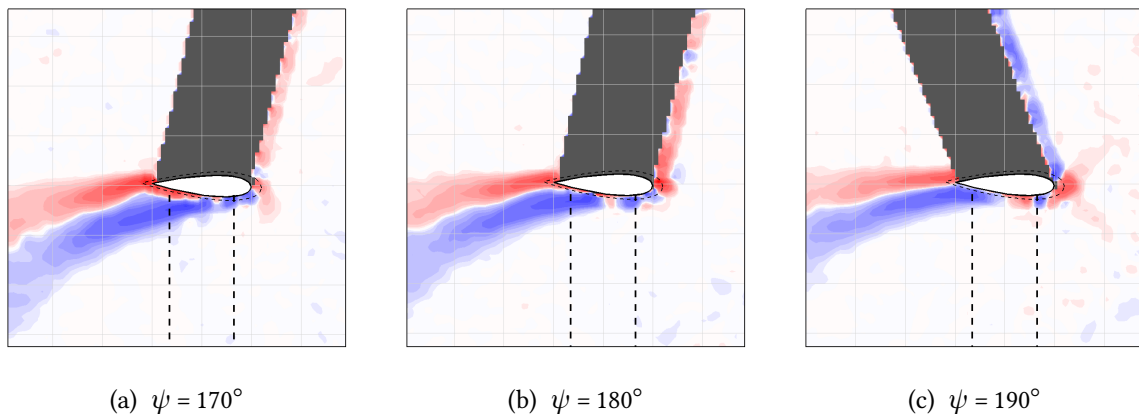(a) $\psi = 170°$          (b) $\psi = 180°$          (c) $\psi = 190°$

Figure 7.9: Plot of z-vorticity showing a delayed flow reattachment at low $\alpha$ for the mid-rotation positions for $\beta = -2°$, $\lambda = 4$

the downwind part, with a possible downwind performance resulting. The size of the fixing angle change becomes more significant with increasing tip speed ratio, as at higher tip speed ratios the range in angle of attack is smaller. Crucially, at $\lambda = 4$, this has had the effect of pushing the blade flow into deep stall in the upwind part of the rotation, which requires some time to recover from and results in large hysteresis in the aerodynamic forces. The significantly increased stall is shown to have the greatest influence on performance with a much lower $C_p$ being measured for the $\beta = -2°$ case, compared to the $\beta = 0°$ case, at $\lambda = 4$.

### 7.3.4    $\beta = +2°$, $\lambda = 2$

For the $\beta = +2°$ case, PIV flow visualisations show the flow to be attached at the beginning of the rotation (Figure 7.11a) although a slightly thicker wake is visible than for the $\beta = 0°$ case (Figure 5.6a), this suggests the downwind reattachment has been slightly delayed by the small positive fixing angle. At $\psi = 60°$, the beginning of a leading edge roll-up is observed as part of the dynamic stall process (Figure 7.11b. The roll-up is shown to be slightly behind that of the $\beta = 0°$ case (Figure 5.6c) which shows that the onset of the upwind stall is occurring slightly later in the rotation due to the small positive fixing angle change. Following the onset of stall, a similar large-scale vortex shedding process is shown in Figures 7.11c to 7.11f. The differences between the $\beta = +2°$ and $\beta = 0°$ cases are small at each $\psi$ position, indicating that the phase difference is less than 5° in $\psi$.

The mid-rotation reattachment behaviour is shown to lag behind the reduction in $\alpha$ at $\psi = 170°$ to 190° (Figures 7.12a to 7.12c). Very similar plots were shown for both the $\beta = -2°$ and $\beta = 0°$ cases (Figures 5.8a to 5.8c). This shows that both small positive and negative changes in fixing angle have had little effect. In this part of the rotation, the rate of change of $\alpha$ is at its most rapid and so a small change in fixing angle becomes insignificant.

PIV flow visualisations show the downstream stall to occur in a very similar manner to

(a) $\psi = 230°$      (b) $\psi = 270°$      (c) $\psi = 290°$

(d) $\psi = 310°$      (e) $\psi = 350°$      (f) $\psi = 0°$
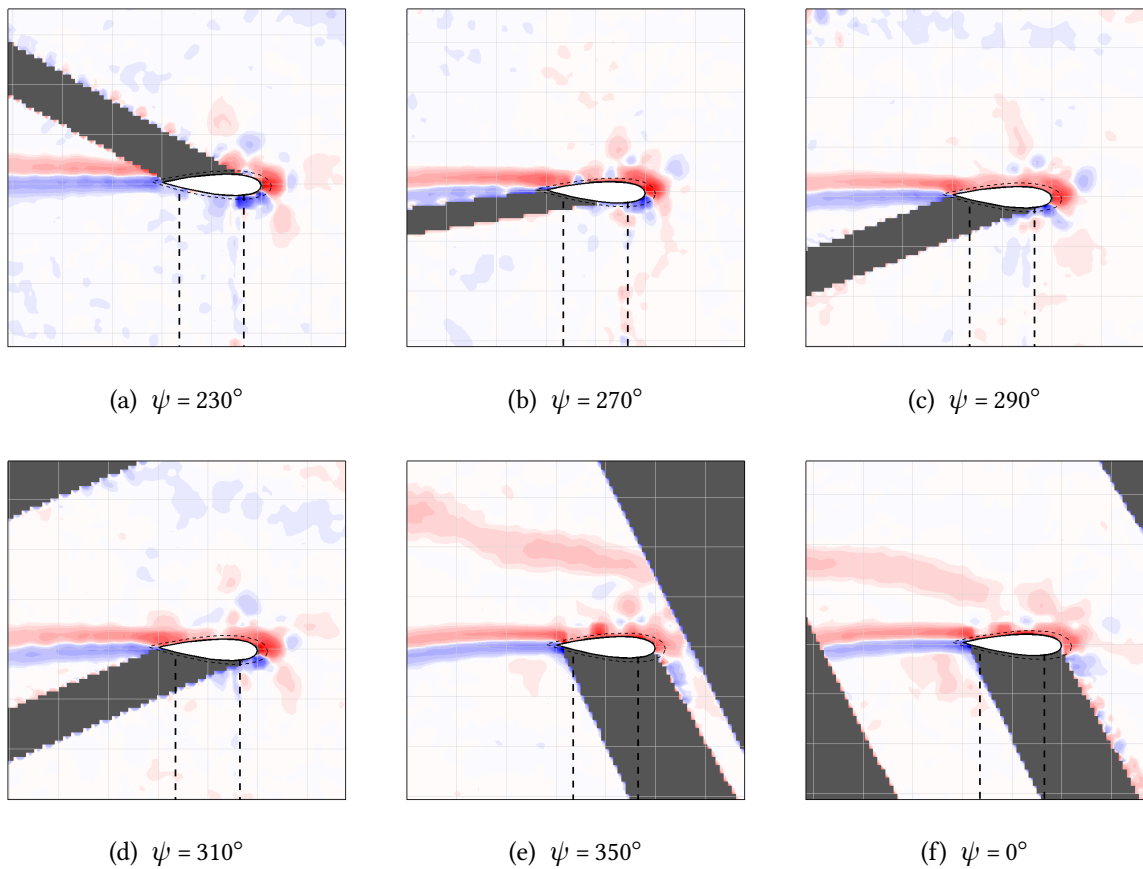
Figure 7.10: Plot of z-vorticity showing the downwind stalling process for $\beta = -2°$, $\lambda = 4$

the $\beta = 0°$ case, the flow appears to stall before $\psi = 230°$ (Figure 7.13a) and a similar large-scale vortex shedding process (Figures 7.13b to 7.13e). The vortices are shown to be in slightly advanced positions relative to the $\beta = 0°$ case, which indicates that the small positive fixing angle has slightly advanced stall in the downwind part of the rotation. The reattachment of the flow toward the end of the rotation appears to be slightly delayed when comparing PIV visualisations for $\psi = 350°$ and $\psi = 0°$ for the $\beta = -2°$ case (Figures 7.13f to 7.13g) against equivalent $\beta = 0°$ case images (Figures 5.9j to 5.9k). Drag in the downwind portion of the rotation would therefore be slightly higher, which would somewhat offset the slightly delayed stall observed for the upwind part of the rotation. The upwind and downwind changes are small, and have opposing effects on performance, so it is understandable that a similar $C_p$ performance is measured for the both $\beta = +2°$ and $\beta = 0°$ cases at $\lambda = 2$.

## 7.3.5   $\beta = +2°$, $\lambda = 3$

At $\lambda = 3$, the PIV flow visualisations show the flow to be attached from the beginning of the rotation (Figure 7.14a) up to $\psi = 90°$, where the beginning of a leading edge roll-up is observed (Figure 7.14b). This is around 10° later in the rotation than for the $\beta = 0°$ case (see Figure 5.11b).

(a) $\psi = 10°$

(b) $\psi = 60°$

(c) $\psi = 70°$

(d) $\psi = 80°$

(e) $\psi = 100°$

(f) $\psi = 120°$
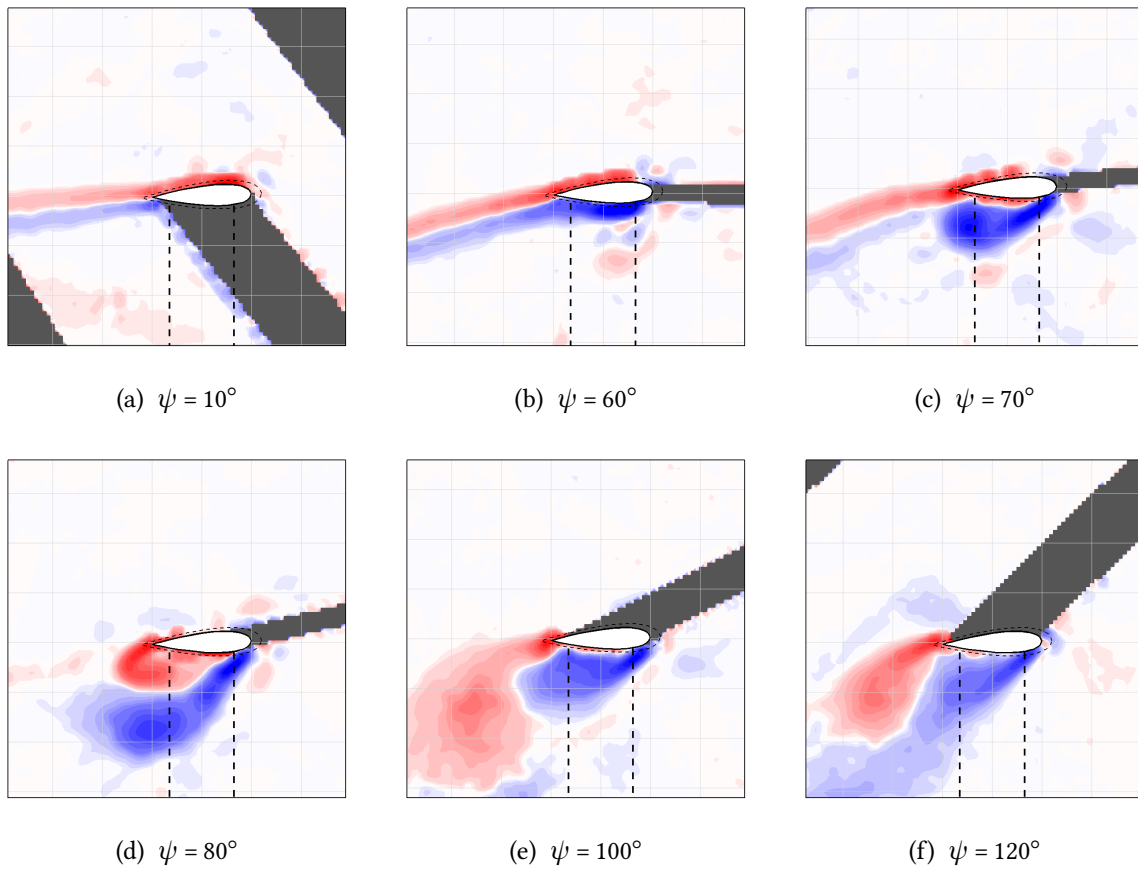
Figure 7.11: Plot of z-vorticity showing the upwind stalling process for $\beta = +2°$, $\lambda = 2$
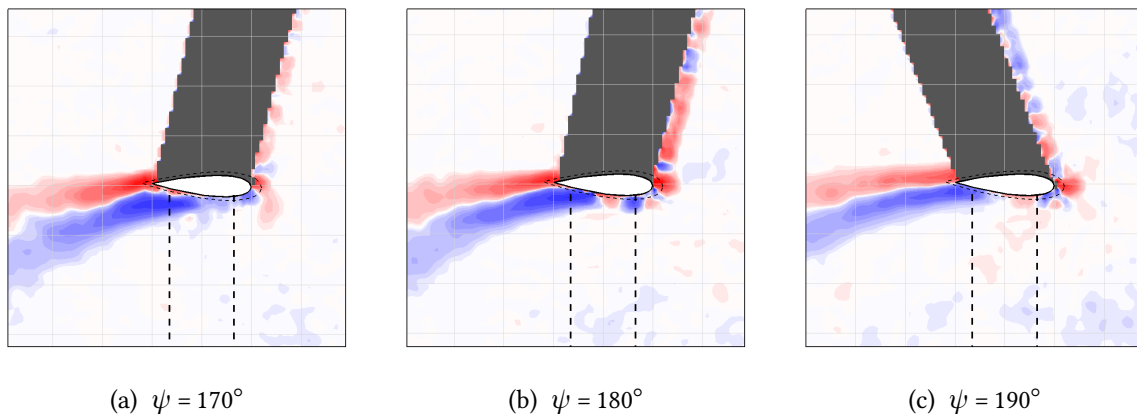


(a) $\psi = 170°$

(b) $\psi = 180°$

(c) $\psi = 190°$

Figure 7.12: Plot of z-vorticity showing a delayed flow reattachment at low $\alpha$ for the mid-rotation positions for $\beta = +2°$, $\lambda = 2$

(a) $\psi = 230°$

(b) $\psi = 240°$

(c) $\psi = 250°$

(d) $\psi = 260°$

(e) $\psi = 270°$

(f) $\psi = 350°$

(g) $\psi = 0°$

Figure 7.13: Plot of z-vorticity showing the downwind stalling process and eventual reattachment for $\beta = +2°$, $\lambda = 2$

A very similar large-scale vortex shedding process is shown, with the 10° out of phase images of $\beta = +2°$ case (Figures 7.14b to 7.14d) being closely-matched to those of the $\beta = 0°$ (Figures 5.11b to 5.11e).



(a)  $\psi = 10°$            (b)  $\psi = 90°$            (c)  $\psi = 100°$

(d)  $\psi = 110°$            (e)  $\psi = 120°$            (f)  $\psi = 130°$
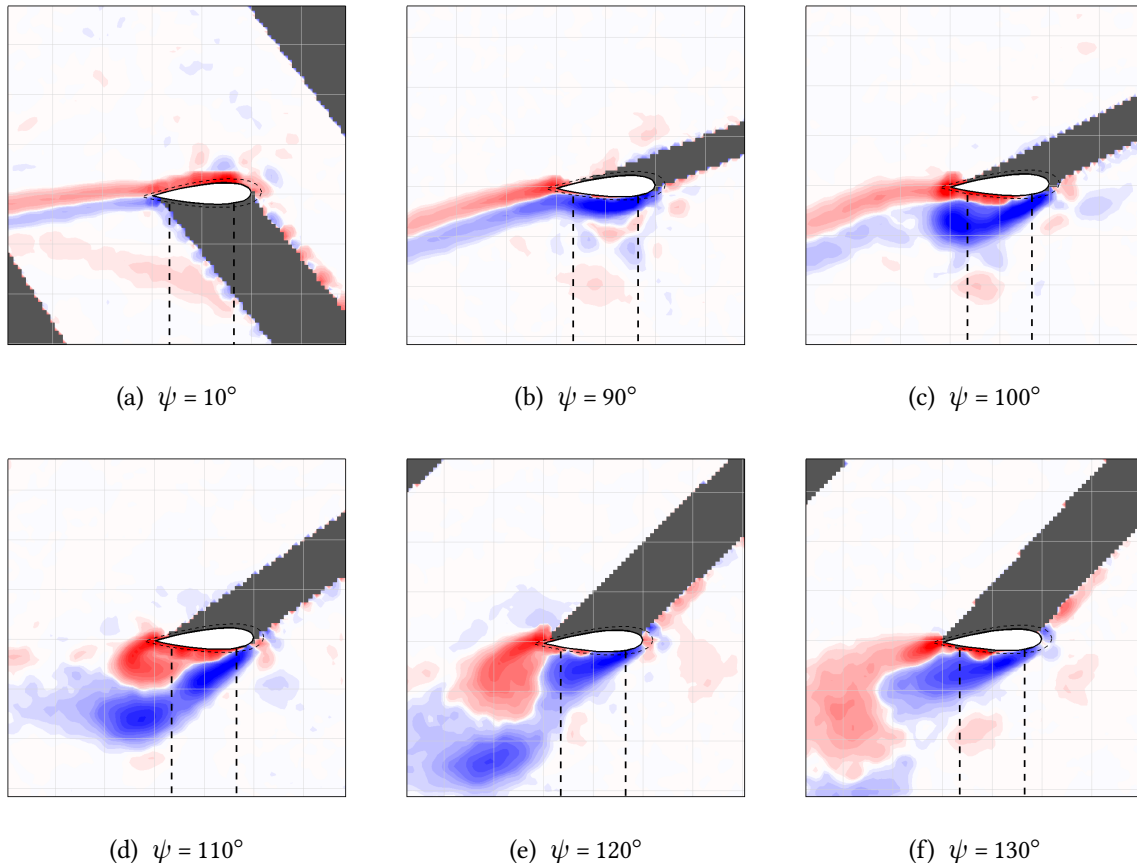
Figure 7.14: Plot of z-vorticity showing the upwind stalling process for $\beta = +2°$, $\lambda = 3$

As for the $\lambda = 3$ condition, very similar plots are shown for the mid-rotation reattachment behaviour when $\beta = +2°$ (Figures 7.15a to 7.15c) as compared to the $\beta = 0°$ case (Figures 5.12a to 5.12c). The small change in fixing angle has had little noticeable effect in this part of the rotation.

In the downwind part of the rotation the PIV visualisations show that the $+2°$ fixing angle results in an increased depth of stall relative to the $\beta = 0°$ case. The roll-up of a larger leading edge vortex is shown at $\psi = 240°$ (Figure 7.16a), with a smaller trailing edge vortex then being shed at $\psi = 250°$ (Figure 7.16b). This differs from the $\beta = 0°$ case which showed no large structures being shed in the downwind part of the rotation. Between $\psi = 270°$ and $320°$ (Figures 7.16c to 7.16f) a more random shedding pattern of smaller structures is shown, with the depth of stall clearly still increased over the $\beta = 0°$ case. Reattachment is shown to occur between $\psi = 320°$ and $\psi = 350°$ (Figures 7.16f and 7.16g), as measurements were not possible between these angles an exact comparison between $\beta = 0°$ and $\beta = +2°$ cases is not possible.

(a) $\psi = 170°$        (b) $\psi = 180°$        (c) $\psi = 190°$

Figure 7.15: Plot of z-vorticity showing a delayed flow reattachment at low $\alpha$ for the mid-rotation positions for $\beta = +2°$, $\lambda = 3$

However, the wakes do suggest that when $\beta = 0°$ the flow reattaches toward the beginning of this region, closer to $\psi = 320°$, where as for $\beta = +2°$ the flow reattaches closer to $\psi = 350°$. At $\psi = 350°$, the visible wakes from the previous blades are shown to be closer to the centre of the rotor, indicating that the less streamtube expansion has occurred and that the early upwind performance is not as high in the $\beta = +2°$ case.

The force analysis of the previous chapter shows the region of vortex shedding encountered for the $\beta = 0°$ case during the deep stall leads to a large region of substantial negative torque (Figure 6.7). The $+2°$ fixing angle results in an increased depth of stall, as shown in the PIV visualisations. The delayed reattachment in the fourth quadrant will also lead to additional losses over the $\beta = 0°$ case. For the $\beta = +2°$ case, $C_p = -0.15$ which is well below that of the $\beta = 0°$ ($C_p = -0.05$). So, despite the delayed upwind stall, the increased level of separation in the downwind and the reduced performance close to $\psi = 0°$, where $V_r$ is highest, contributes to a large reduction in the overall $C_p$.

### 7.3.6   $\beta = +2°$, $\lambda = 4$

At $\lambda = 4$, the PIV flow visualisations show the flow to be attached all the way through the upwind part of the rotation (Figure 7.17). For the $\beta = 0°$ case, a small separation was shown at $\psi = 130°$, so the drag in the latter part of the second quadrant for the $\beta = +2°$ case would be expected to be much reduced.

As there is no significant upwind separation, the flow between $\psi = 170°$ to $190°$ is also attached to the blade surface (Figures 7.18b and 7.18c). Again this would be expected to contribute to lower drag in this region than was experienced for the other fixing angle tested. As has been shown in the force analysis of the previous chapter, the relative blade velocity in this region is low, and so the resulting aerodynamic forces are also low. The result of this is that changes to performance in this region are of low significance to the overall value of $C_p$.

(a) $\psi = 240°$

(b) $\psi = 250°$

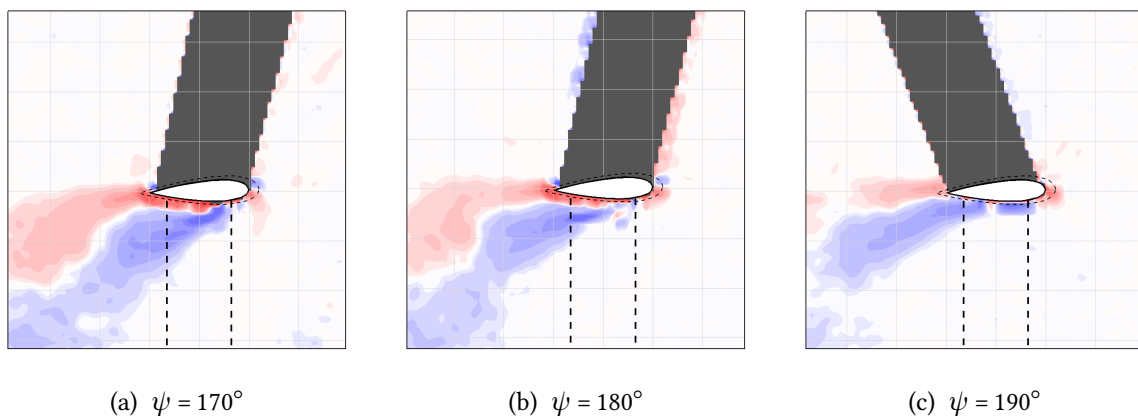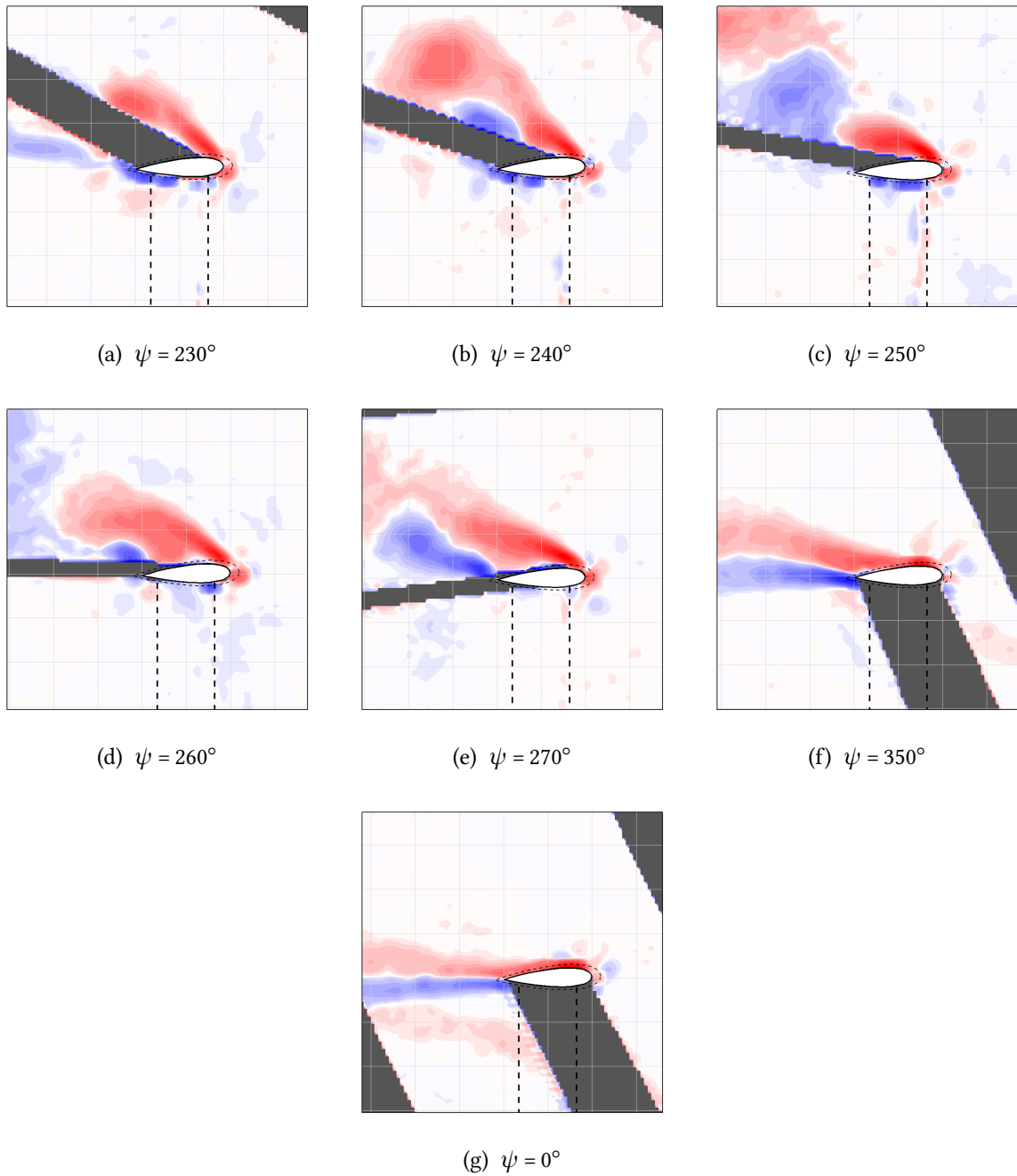(c) $\psi = 270°$

(d) $\psi = 290°$

(e) $\psi = 310°$

(f) $\psi = 320°$

(g) $\psi = 350°$
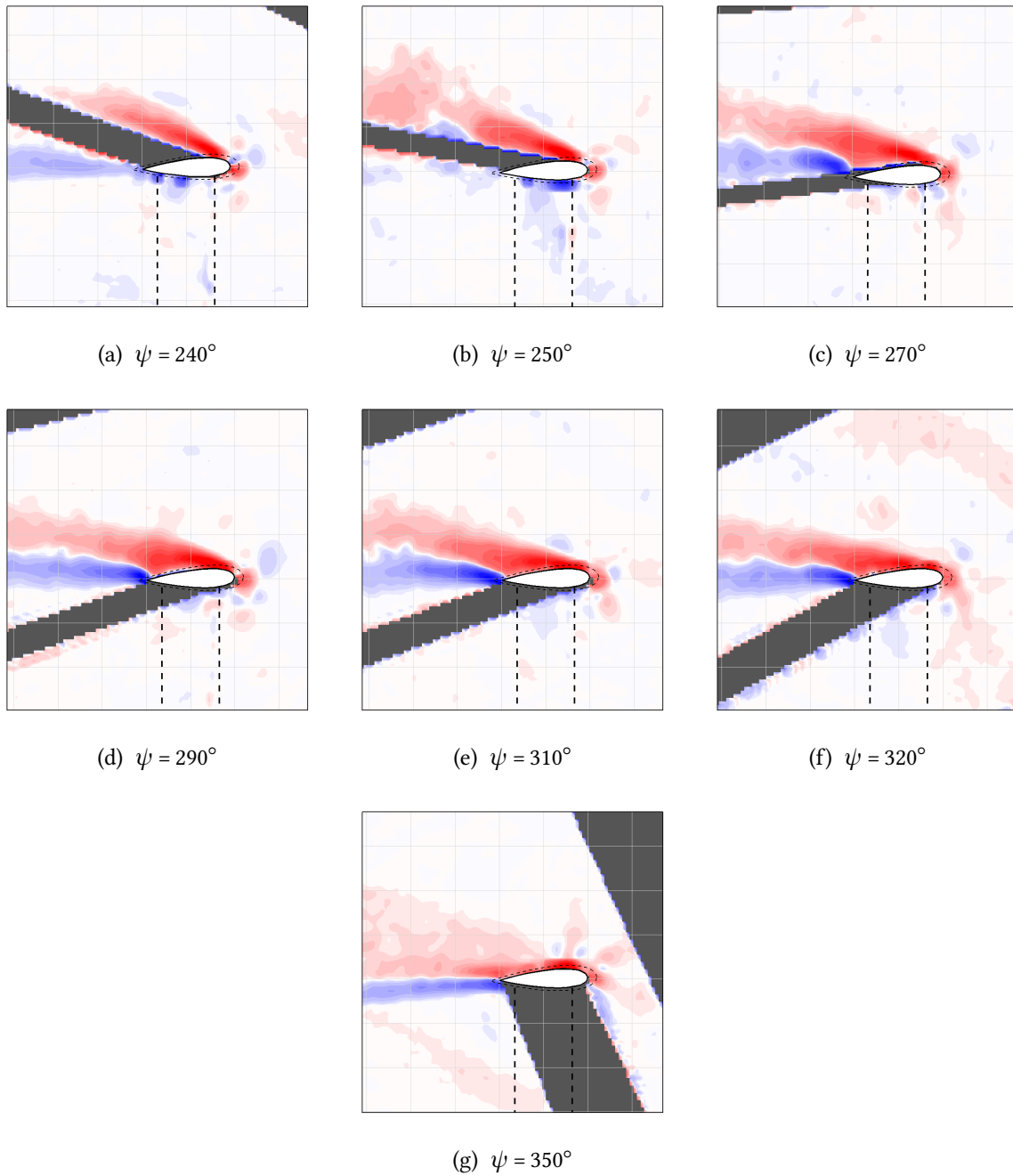
Figure 7.16: Plot of z-vorticity showing the downwind stalling process for $\beta = +2°$, $\lambda = 3$

(a) $\psi = 10°$    (b) $\psi = 90°$
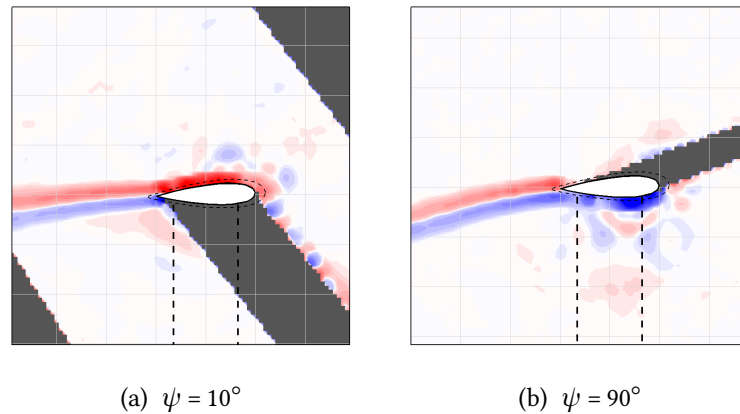
Figure 7.17: Plot of z-vorticity showing attached flow for the upwind part of the rotation at $\lambda = 4$
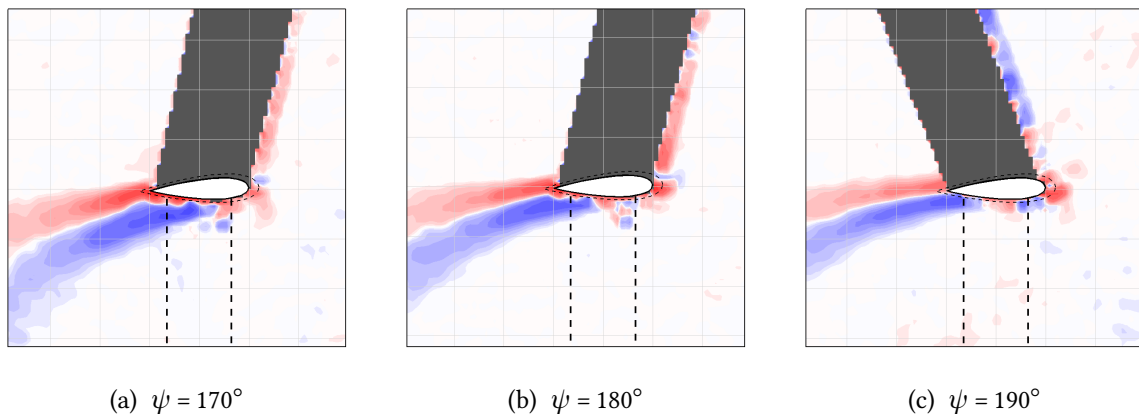


(a) $\psi = 170°$    (b) $\psi = 180°$    (c) $\psi = 190°$
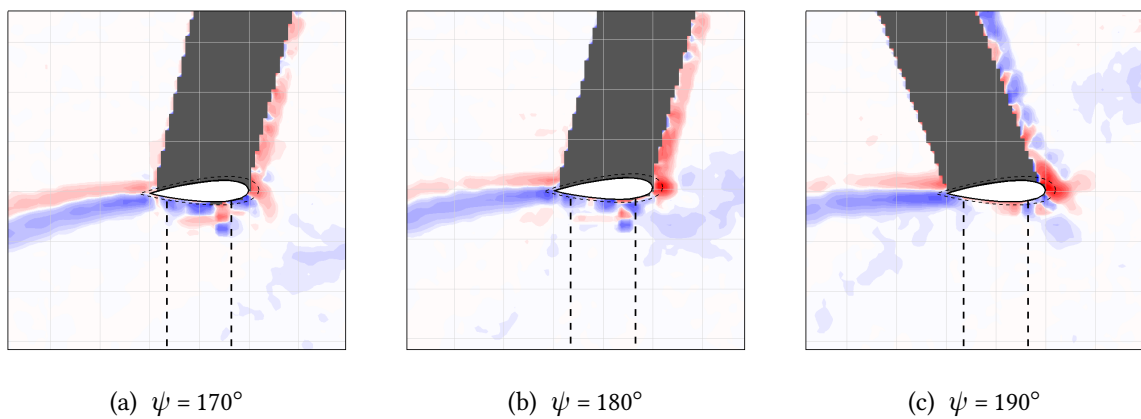
Figure 7.18: Plot of z-vorticity showing a delayed flow reattachment at low $\alpha$ for the mid-rotation positions for $\lambda = 4$

In the downwind part of the rotation the flow remains attached at all the measured azimuth angles (Figures 5.17a and 5.17f). In the images the wake of the previous blade can be seen, at $\psi = 250°$ to $290°$ less downstream movement of the wake can be seen, which indicates that the flow velocity has been reduced due to the improved upstream performance. However, as for the $\lambda = 3$ condition, toward the end of the rotation the wake of the previous blade shows less out-bound movement is observed, indicating that the less streamtube expansion has occurred and that the early upwind performance is not as high in the $\beta = 0°$ case. Overall, the much-improved flow attachment in the second quadrant appears to be cancelled out by the reduced angle of attack in the first quadrant and the reduced flow velocity in the downwind portion of the rotation. The result of this is that a very similar $C_p$ is measured for both the $\beta = +2°$ and $\beta = 0°$ cases.

(a) $\psi = 230°$

(b) $\psi = 250°$

(c) $\psi = 270°$

(d) $\psi = 290°$

(e) $\psi = 310°$

(f) $\psi = 350°$

(g) $\psi = 0°$
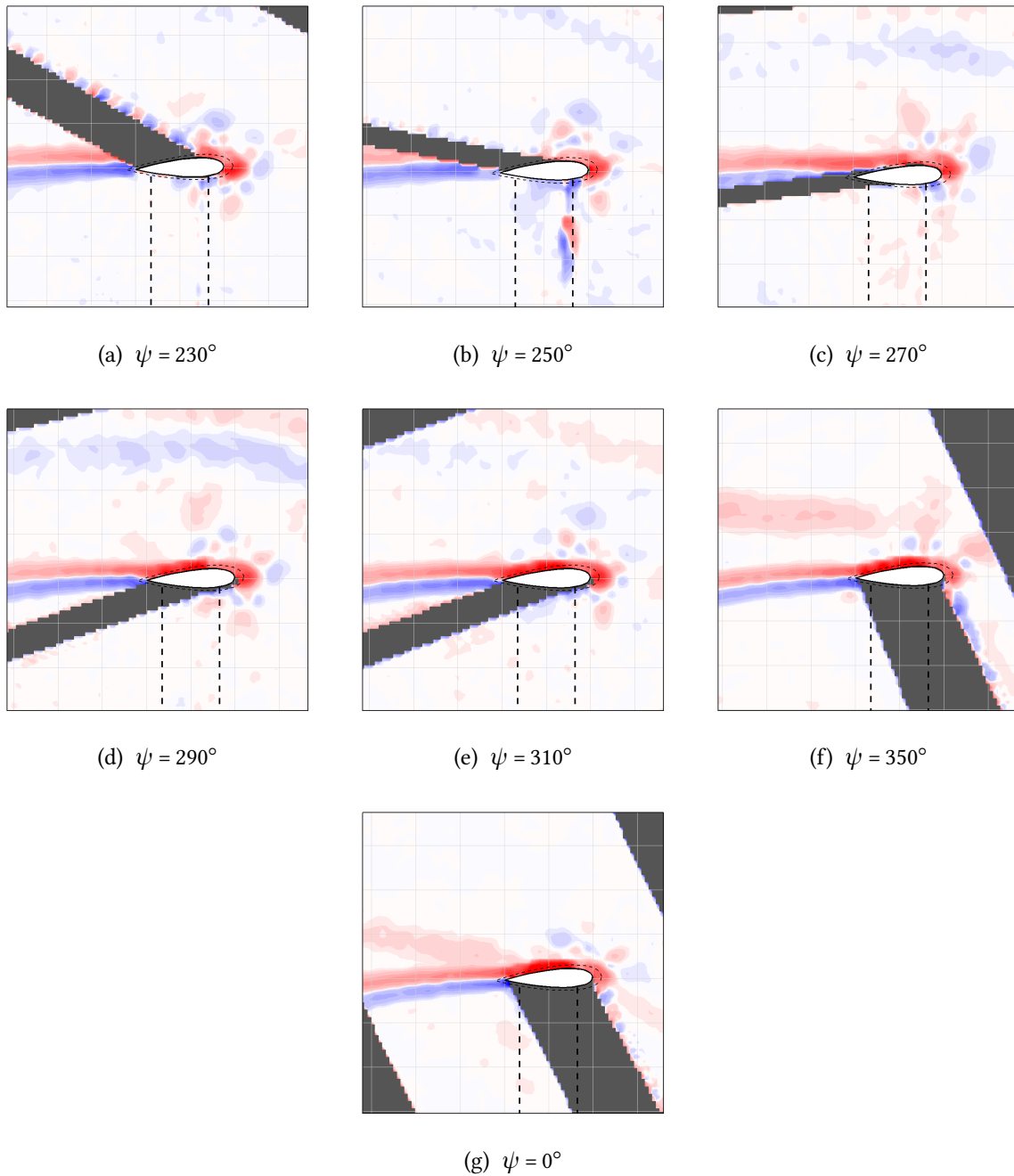
Figure 7.19: Plot of z-vorticity showing the downwind stalling process for $\lambda = 4$

## 7.4  Summary

Visualisations by PIV have shown that the performance changes due to an altered fixing angle result from the overall effect of a number of changes occurring throughout the rotation. The PIV visualisations showed that, relative to the $\beta = 0°$ case:

- for $\lambda = 2$:

    - $\beta = -2°$ leads to earlier stall in the upwind region, and earlier reattachment in the fourth quadrant. $C_{p-blade}$ increases slightly.

    - $\beta = +2°$ gives a slightly later stall in the upwind region, and slightly later reattachment in the fourth quadrant. $C_{p-blade}$ change is negligible.

- for $\lambda = 3$:

    - $\beta = -2°$ leads to earlier stall in the upwind region, and a reduced depth of stall and earlier reattachment in the downwind portions of the rotation. $C_{p-blade}$ increases.

    - $\beta = +2°$ results in poor performance near $\psi = 0°$, stall occurs later in the upwind region, and a deeper stall and later reattachment occur in the downwind region. $C_{p-blade}$ reduces quite significantly.

- for $\lambda = 4$:

    - $\beta = -2°$ leads to much earlier upwind stall and deep stall is encountered in the second quadrant. $C_{p-blade}$ reduces quite significantly.

    - $\beta = +2°$ gives a poor performance near $\psi = 0°$, but stall is avoided throughout the rotation. $C_{p-blade}$ change is negligible.

The various changes which have occurred at different positions in the rotation and at different tip speed ratios, indicate that the trade-off between the performance of one part of the rotation versus another is quite likely to change with different aerofoil profiles and different turbine configurations. Consequently, identical changes to the shape $C_p - \lambda$ curve which have been presented in this chapter, are not necessarily expected to occur on a VAWT with a different profile, c/R ratio, Re, or any other difference which may influence stall or reattachment. The few studies in the literature would seem to agree with this: Klimas' results (Figure 2.13) show no clear effect of positive versus negative angles. The vortex code analysis of Coton et al. (Figure 2.15) shows no difference between the $C_p$ for different fixing angles at low $\lambda$, which is hard to believe given the various consequences of stall that have been shown throughout this chapter, and the previous two. The $C_p$ curves of Coton et al. then tend away from each other at higher $\lambda$. The opposite trend has been shown in the results of this study. For the changes to the stalling behaviour shown in this chapter, it is clear that a very good dynamic stall model is needed to assess the effects of fixing angle changes at low $\lambda$, this may explain the results of Coton et al. The only consensus between this study and those of Klimas and Coton et al. is that there appears to be little gain possible if attempting to increase the value of $C_{p-max}$ through the adjustment of fixing angle. It appears that an adjustment of the fixing angle may be used to alter the shape of the power curve, perhaps to improve starting performance.

Although the material in this chapter has added considerably to the understanding of the reasons behind a performance change due to an altered blade fixing angle, the overall literature available is limited, and the study is still not complete. The complexity of a trade-off of the performance at various points in a rotation, suggests a 'complete' study of the effect of fixing angle is difficult to achieve. As a result, a VAWT designer would be advised that the exact effect of a fixing angle change is probably best evaluated on a case-by-case basis.

# Chapter 8

# Conclusions and Further Work

The literature review concluded that, in order to advance the understanding of the VAWT, the following areas of research required further investigation:

- A better understanding of the blade aerodynamics is required in order to feed into aerofoil selection, because current understanding is often based on models which employ data from 2D static aerofoil tests.

- The effect of flow induction and upstream shed vortices needs to be understood before upwind versus downwind performance can be properly assessed.

- Further development of CFD modelling techniques is required as the models may prove very useful for the detailed assessment of the flow physics.

- The improvement of experimental techniques is a priority for improving understanding of the VAWT operation. Some of the downfalls of mathematical models can then be addressed, and those models improved.

This study contributes to the key areas of required research, stated above, in three main ways:

1. A variety of methods and apparatus were designed and utilised during the study, these are documented in detail in two chapters and include a new method for the experimental determination of the power curve.

2. The near-blade flow physics were interrogated using both experimental PIV measurements and CFD simulations, yielding details of the effect of changes in azimuthal position, tip speed ratio and fixing angle.

3. A new methodology for determining flowfield-corrected lift and drag polars from a CFD solution allowed detailed examination of the performance-impact of the changes in the aerodynamic forces with azimuthal position and tip speed ratio.

The results, impact and conclusions of the contributions of this study to these key areas are summarised in the following sections.

# 8.1 Advancement of VAWT Research Techniques

Much of the literature was found to be based on results drawn from mathematical models, whilst many of the models are shown to give reasonable matches to experimental performance curves, the models are not useful for investigation of the detailed VAWT flow physics. A need for improved research methods, centred around experimental techniques, was clearly identified. This study has added to the general understanding of the apparatus and methods required for VAWT testing, with significant advances made in a number of areas.

## 8.1.1 VAWT Performance Testing

The new spin-down method is shown to be a useful method for determining the change of performance with tip speed ratio. A full-curve is shown to be determined using a short test taking a few minutes. In addition, a detailed description of the general apparatus and methods has been given that is hopefully of use to other researchers wishing to carry-out wind tunnel testing of VAWTs.

## 8.1.2 PIV Visualisation

So far, only a small number of studies have been published showing PIV measurements of the VAWT flow physics. The experimental campaign added significantly to the published measurements with images shown for a full rotation, at three different tip speed ratios, and for three fixing angles. Again, the general equipment, settings and methods are well-documented and would be easily transferred to another VAWT set-up.

## 8.1.3 Modelling of the VAWT by CFD

CFD study of the VAWT is an emerging area of VAWT research; the VAWT is a challenging case due to a performance which is strongly dependant on the accurate prediction of flow separation and reattachment and also upon low-Re operation, which most rotors will encounter at low $\lambda$ or low $V_\infty$.

The results of a CFD model are presented alongside experimental measurements and visualisations. A new methodology has been presented which allows the determination of blade forces and a corrected angle of attack. This is very important as it allows the assessment of the aerodynamic behaviour of the VAWT blade to be made in traditional terms. This allows comparison with aerofoil tests and more easily associates results gained from pitching aerofoil tests with the dynamic behaviour of the VAWT blade.

## 8.2 Understanding of the Near-Blade Flow Physics

### 8.2.1 Reference Case

The experimental visualisations showed that the VAWT operation is characterised by large variations in angle of attack that result in deep-stall and vortex shedding, the extent of which increases with reducing tip speed ratio. A significant hysteresis in the flow was observed, as is characteristic of a dynamic stall process. Stall was shown to be delayed to much higher angles of attack than would be possible for a static aerofoil, and, as a result of the continuous changes in angle of attack, a substantial delay in reattachment was also observed.

At $\lambda$ = 2 the visualisations showed stall occurring early in the upwind rotation, $\psi \approx 60°$, where a leading edge vortex was observed to occur, which rolled up over the aerofoil suction surface (enhancing lift) before being shed from the blade. A series of vortices then followed, being alternately shed from the trailing and leading edges. Reattachment did not occur until past $\psi$ = 180°, where $\alpha$ is expected to be close to 0°. Due to the skew in the $\alpha$-$\psi$ curve, the blade stalled relatively earlier in the third rotation quadrant, and again a delayed reattachment was observed to occur just before the end of the rotation. A similar process was observed at $\lambda$ = 3, but stall occurred later and reattachment earlier. At $\lambda$ = 4, where the $C_p$ was at its highest, a brief stall was observed in the upwind part of the rotation only. The lower downwind flow velocity clearly lead to a higher effective tip speed ratio for the downwind part of the rotation, and the lower range in $\alpha$ prevented stall here at this tip speed ratio.

The results show the importance of correctly modelling dynamic stall of the VAWT, which has a significant influence at the three tip speed ratios tested (covering a large part of the power curve). The delayed-reattachment effect of dynamic stall shows that aiding reattachment is possibly as important as delaying stall. Analysis of the forces, summarised in the following section, adds further to this point.

### 8.2.2 The Effect of Fixing Angle Adjustment

A change in the fixing angle was shown to have a number of effects throughout the rotation, the overall result of which determined the resulting power output of the rotor. A positive change in the fixing angle was shown to lead to delayed stall in the upwind part of the rotation, while reattachment (around $\psi$ = 180°) was not significantly effected. In the downwind part of the rotation, a positive change in the fixing angle leads to stall occurring earlier in the rotation, and most significantly reattachment was delayed.

A negative fixing angle led to opposing changes in the stalling and reattachment behaviour. In addition, the point at which optimum lift coefficient occurred in the rotation was delayed which effected the contribution to torque, and also the relative blade velocity relationship with $\alpha$ - which effected the magnitude of the lift force. At $\lambda$ = 2, performance measurements showed a positive fixing angle of 2° to yield a small improvement in $C_p$, at $\lambda$ = 3 the same angle reduced the $C_p$, and at $\lambda$ = 4 it had little effect.

A negative fixing angle of $-2°$ had a small detrimental effect on performance at $\lambda = 2$. At $\lambda = 3$, performance was significantly improved, while at $\lambda = 4$ $C_p$ was greatly reduced. The most significant changes in performance appeared to be where the blade was close to stalling or only-just stalled. In these regions, a change in fixing angle either just prevented stall or resulted pushed to blade into a deep stall which otherwise would not have occurred. The most significant examples of this were shown at $\lambda = 3$, $\beta = +2°$ and $\lambda = 4$, $\beta = -2°$

It was concluded that it is difficult to make an assessment of the effects of a fixing angle change on a particular VAWT design, as the overall result depends on the trade-off of a number of changes to the flow behaviour. Other published studies seemed to agree with this, as the performance trends with adjusting fixing angle are different in each case. The data in this study also agrees with the literature in showing that it does not appear that there is much to gain in terms of possible increases in $C_{p-max}$. Instead, a change in fixing angle should be viewed as a way to adjust the shape of the performance curve, perhaps for the improvement of starting performance, for example.

### 8.2.3 Flowfield and $C_p$ Comparison with the CFD Simulation

A reasonable match was shown between the CFD-simulated flowfield and the PIV visualisations, with the match being closest for the lowest tip speed ratio, where the performance prediction was also closely matched. On the whole, the position that the flow detaches from the blade surface is closely matched for both upwind and downwind parts of the rotation, a small delay ($< 10°$ in $\psi$). The vortex shedding behaviour is also well-matched. However, the flow-behaviour at the onset of stall appears to be different between the experiment and simulation, with the simulation showing a gradual separation progressing forwards from the trailing edge, while the experiment shows a more sudden leading edge roll-up. A separation of this nature is more characteristic of a higher-Re aerofoil, and it is not surprising that the full-turbulent CFD simulation results in this incorrect stall-initiation prediction. At higher tip speed ratios the CFD over-predicted $C_p$ by quite a large margin, although the general well-matched shape of the curve was maintained and peak performance was shown at a similar tip speed ratio. Overall, the simulation was considered to match to basic operation of the VAWT well-enough to justify its further use for the analysis of the aerodynamic forces, discussed in the following section...

## 8.3 Effect of Stall on Blade Forces

Measuring the blade forces in the experiment was considered to be practically very difficult, particularly as aluminium blades were used resulting in the centrifugal loads dwarfing the aerodynamic forces. Instead, as the CFD was shown to be reasonably well-matched with the experiment, tangential and normal blade forces were extracted from the simulation. Interpolation of the velocity field allowed determination of the corrected angle of attack, which

in turn allowed the tangential and normal forces to be resolved into lift and drag. This was considered important as it allows the assessment of the aerodynamic behaviour of the VAWT blade to be made in traditional terms. This is useful for a number of reasons, such as evaluating the use of static aerofoil test data for performance prediction.

Large hysteresis loops were revealed in the lift and drag curves. The effects of dynamic stall on the aerodynamic forces were clear, with larger values of $C_{l-max}$ shown over static data for the same aerofoil. The highest lift coefficient was shown for the highest pitching rate of the three simulated tip speed ratios, this occurred in the downwind portion of the rotation of the $\lambda$ = 2 condition where a lift coefficient of (-)1.8 was calculated. However, at $\lambda$ = 2 and 3, higher torque due to enhanced lift during the onset of dynamic stall was shown to be quickly overpowered by increases in drag, which was more aligned to the tangential rotor direction. The delay in flow reattachment further contributed to high drag and low lift, and negative torque resulted. This was particularly significant in the fourth quadrant where the relative blade velocity was high.

At $\lambda$ = 2, the flow is detached for 70% of the rotation and negative torque is produced for 75% of the rotation, which clearly explains the negative $C_p$. At $\lambda$ = 3, the flow is detached for 45% of the rotation and negative torque is produced for a similar percentage which explains the improvement over the $\lambda$ = 2 condition. At $\lambda$ = 4, the torque curve only falls to negative values for around 20% of the rotation, this occurs in regions where the blade experiences a small angle of attack which results in a low amount of lift and a small contribution of torque which is unable to outweigh the contribution from drag.

The dependence of the $C_p$ on the upwind region of attached flow was clearly shown at $\lambda$ = 3 and 4. At $\lambda$ = 4, two-thirds of the overall power is generated in the upwind portion of the rotation, which has a broad peak in torque around $\psi$ = 90°. The remaining positive contribution is spread over most of the downwind rotation, with the fourth quadrant giving a greater proportion due to the higher flow velocity. Parts of the rotation featuring high post-stall drag are shown to give the most significant regions of negative performance. However, almost equally significant are the regions of delayed flow reattachment which prevent a recovery of the lift in the latter part of the second quadrant and the fourth quadrant at $\lambda$ = 2 and 3.

The strong dynamic effects, leading to large hysteresis loops, clearly show that correctly modelling the VAWT depends on an understanding of an aerofoils dynamic performance, and that the stall and recovery behaviour must be understood, particularly for low tip speed ratios. Modification of static aerofoil data to the point at which low tip speed ratios are correctly assessed will be a difficult task. This is the likely reason that mathematical models have often been found to yield poor results at low tip speed ratios. The operating tip speed ratio of a simple VAWT would likely be chosen to be at a better-performing higher tip speed ratio, where dynamic effects become less severe, and it is understandable that mathematical model-based predictions would give a reasonable estimate of the energy output.

Whilst different aerofoils have not been assessed, the results of Chapters 5 and 6 show that

the use of an aerofoil that discourages stall and/or encourages post-stall flow reattachment would likely be beneficial to overall performance. The results of Chapter 6 have shown that efforts should not necessarily concentrate on preventing stall (which may be unavoidable at low tip speed ratios), encouraging earlier reattachment may be just as beneficial to overall performance. An aerofoil with generally high lift and low drag characteristics is obviously desirable. Furthermore, the results of Chapter 6 clearly indicate that efforts to reduce drag are likely to be highly beneficial. So, at least in the first instance, aerofoil design optimisation should concentrate on the reduction of drag rather than seeking an increase in lift.

## 8.4   Further Work

Despite the reasonable quantity of research published over the last 40 years there are a number of fundamental issues which need to be properly addressed in order for VAWT performance to be more fully understood, and for effective designs to emerge. The work in the thesis has made good progress on this front although, a reliable transfer of the results to other design configurations or larger scale VAWTs cannot yet be confidently made.

Historically, substantial effort has been dedicated to mathematical modelling; the literature and the work is this study shows the flow physics are complex and are not properly understood, which has prevented fully-adequate models from being developed. The attempts to use inadequate models to address design issues has lead to inconclusive studies.

The complex problem of understanding and improving the VAWT still requires additional work in a number of areas, which are detailed in the following subsections. The following suggestions concentrate on experimental aspects and the VAWT flow physics.

### 8.4.1   Performance Measurements

**Transfer of Understanding to...**

**...Larger Scale VAWTS**

A significant amount of additional work is required to transfer the findings of this study to the point where the same assessments of the performance flow physics can be made for a wide range of VAWTs. The rotor in this study was small and so the resultant blade Reynolds number was low. Some attempts were made to simulate the effect of a higher-Re (large scale) operation by raising the freestream turbulence level, which showed some significant changes to the performance curves. However, this was not investigated in detail due to various practical, time and funding constraints. Possible future studies might include larger scale tests as well as further tests using some additional means to simulate higher-Re operation, such as boundary layer trips.

**...VAWTs in Real Situations**

One area of testing that has not been addressed by this study, or adequately assessed in other published studies, is that of wind tunnel blockage. In order for $C_p$ measurements to be transferred to a real-wind environment the effect of the wind tunnel walls, such as an effectively raised flow velocity, needs to be quantified. This is also important when comparing the results with CFD models. An approximate measure was taken in this study to try to match significance of the experimental 3D blockage in a 2D CFD simulation. Exactly how adequate this was has not been established. One way to do this would be through the use of 3D CFD models, which are very computationally expensive. Experimentally, an open-section wind tunnel or a blow-type tunnel with porous walls could be used, if available.

**...Other Design Configurations**

As was shown in the review of the literature, the influence of VAWT design parameters has yet to be properly determined and there are numerous possible studies that could be carried out in this area. It would be very interesting to repeat the tests carried out in this study with different aerofoil profiles. A comparison of the behaviour of the VAWT blade with some reliable tests of a static or pitching aerofoil might be a useful way to extend the knowledge regarding the modification of static aerofoil data, and would ultimately feed into aiding the choice of suitable VAWT blade profiles based on traditional aerofoil datasets.

Other parameters such as solidity, c/R ratio and fixing angle all warrant further investigation. The complex flowfield revealed in this study suggests this work would be best undertaken, initially using experimental or perhaps CFD methods. Once the resulting flow physics understanding is improved a revisit of mathematical models would be wise. such models usually need a relatively small amount of time required to obtain a solution, and so are much more suited to optimisation studies where the comparison of a large number of VAWT configurations may be necessary.

**Improvement of Apparatus and Techniques**

The apparatus and methods in this study were found to work effectively, although a number of improvements could be made:

- Lighter blades would be very beneficial, and would allow smaller bearings and supporting structure to be used which would low the parasitic drag of the rig. With very light blades it is possible that the spin-down method could be extended to torque measurements within a rotation using high-resolution rotational speed measurements. This might be more-suited to one or two blade designs which would have a larger torque ripple. With light (and stiff) blades, the VAWT could also be safely spun to higher rotational speeds which would allow measurements to be taken at higher Re and/or higher $\lambda$

- Obtaining measurements of the force variations within a rotation would be very desirable, providing data ideal for comparison to models of all kinds. Lighter blades would aid this, as currently the deduction of relatively small aerodynamic forces from a much larger total force (due to centrifugal and vibrational forces) would be error-prone and would require highly accurate force data at high-resolution to overcome this.

- To truly validate the spin-down method a comparison of spin down with a shaft-mounted torque sensor should be made. This was not possible in this study due to practical and funding constraints.

### 8.4.2 Visualisations

Visualisation of the near-blade flowfield were found to be very useful in this study and there are a number of ways in which the work could be furthered:

- In this study, the separation and reattachment behaviour was shown to be highly important to performance. More detailed visualisations could be taken of the near-surface flow, although this is difficult due to surface reflections. This would aid the understanding of the mechanisms of separation and reattachment, potentially improving design and also allowing useful comparison with CFD models.

- So far visualisations have been made assuming a strong 2D-behaviour of the flow. PIV measurements along the blade length showed 3D effect may be significant near the support arms and blade tips and more investigation of this should be carried out. A good assessment of the reliability of the comparison of 2D CFD with experimental measurements requires improved knowledge in this areas.

- The possibility of determining the blade loading from PIV data, as featured in one published study, should be further explored. Ideally, this would be combined with experimental force measurements for the best possible validation of the methods.

# Appendices

# Appendix A

This appendix contains some additional design calculations and equipment calibrations.

## A.1   Estimating the Rotor Loading

Spinning a VAWT rotor to high rotational velocities is a potentially dangerous experiment. So, although the study was concerned only with the aerodynamic performance, the loading on the rotor needed to be investigated and determined to be safe before any experiments could proceed. As the design was bespoke this involve some estimations and some 'engineering judgement' along the way. By far the most significant load on the rotor was the centrifugal load due to the blades, $F_\omega$, so the structural assessment concentrated on this. As the blade was mounted at a constant radius, this force was simply calculated from the mass of the blades, $m$ the turbine radius, $R$ and the rotational speed, $\omega$:

$$F_\omega = mR\omega^2 \tag{A.1}$$

Consideration of the rotor design allowed the most-likely modes of failure to be determined, these were:

1. severe bending of the blade resulting from the distributed centrifugal loading.

2. failure of the bolts fixing the blade to the support arm, through either:

   - tensile fracture
   - or a shear failure of the aluminium thread in the support arm

It is important to note that a partial failure during operation would likely lead to some unbalancing of the rotor and, in all likelihood, the resulting vibrations would be severe and could increase the loading by a large amount - rapidly leading to a catastrophic failure. Therefore, the structural safety calculations aimed to prevent failure within generous factors of safety. It should also be noted that the likelihood of failure and the severity of the consequences would be much easier to contend with if lighter blades (e.g. carbon fibre) were used, unfortunately this was not possible with the manufacturing facilities and funding available.

The bending of the blade was assessed by approximating the free end of the blade as a cantilevered beam, the maximum deflection, $\delta x_{max}$ of which is given by:

$$\delta x_{max} = \frac{8wL^4}{8EI} \tag{A.2}$$

where $w$ is the distributed loading (= $F_\omega/B$), $L$ is the length of the free blade end (= $B/4$), $E$ is the material Young's modulus and $I$ is the second moment of area for the section - this was calculated by approximating the aerofoil as an ellipse. Due to the approximations used, the calculation is likely to under predict deflection. However, at 1000RPM a deflection of 2mm was calculated, which was not thought to be alarming. Images taken during the PIV tests showed a deflection of a few millimetres at rotational velocities up to 800RPM, showing the estimation used in the rotor design stage was adequate.

The tensile load on the bolts was simply calculated by dividing $F_\omega$ equally between the four M4 bolts, this lead to a tensile bolts stress prediction of 28MPa (at 1000RPM) which is less than 10% of the yield stress of the steel bolt.

The shear strength of the 6mm deep aluminium thread in the support arm was calculated for the M4 bolts. Data tables (ISO 724 (DIN 13 T1)) gave the pitch diameter $d_0$ of an M4 bolt as 3.3mm, yielding a shear area of $A_{shear} = 3.1 \times 10^{-5} m^2$ ($A_{shear} = 0.5\pi d_0 L$, where L is the thread length in metres). The force required to strip the thread was then calculated, using tabulated material data from [? ], as $F_{shear} = 9kN$, which was substantially more than the 350N shared between the bolts at 1000RPM.

The calculations of the most significant rotor loadings showed that the rig should be able to withstand loading several factors higher than that which occurred at 1000RPM. The deflection of the blade tips is the main limiting factor. Aside from the material stress due to bending, if the blades were to bend significantly, the change in rotor geometry would be difficult to account for and the loading on the joints may become more complex and severe. The calculations were approximate, and several additional effects could not be easily accounted for, such as the effect of repeatedly taking the blade off and on during the experimental campaign. For safety, it was decided that the rotational speed should not be allowed to exceed 1000RPM.

## A.2 Torque Brake

### A.2.1 Torque Capacity Estimation

To specify the torque brake, the range of required applied torque needed to be estimated. Bearing resistance would oppose the rotor torque; however, at the design stage the bearing resistance was hard to quantify and so it was neglected for the torque brake range calculation. This meant the torque brake was slightly over-sized. The wind tunnel speed was limited to 10m/s, and the rotor area was $0.4 m^2$, this allowed the maximum power into the rotor to be determined:

$$P_{wind} = \frac{1}{2}\rho A V_w^3 = \frac{1}{2}*1.2*0.4*10^3 = 240\,W \tag{A.3}$$

Assuming a highest possible $C_p$ = 0.4 allowed the maximum possible rotor power to be determined as $P_{T-max}$ = 96 $W$. For a VAWT of solidity of 0.33, $C_{p-max}$ would be expected around $\lambda$ = 0.4 (see Figures 2.16 and 2.17). So, for the maximum power condition, the maximum rotor rotational velocity, $\omega_{max}$, could be estimated:

$$\lambda = \frac{R\omega}{V_w} \quad \therefore \quad \omega_{max} = \frac{\lambda V_w}{R} = \frac{10*4}{0.35} = 114\, rad/s \tag{A.4}$$

Using the estimates of $P_{T-max}$ and $\omega_{max}$, the corresponding maximum torque, $T_{max}$ could easily be calculated:

$$P_{T-max} = T_{max}\omega_{max} \tag{A.5}$$

$$T_{max} = \frac{P_{T-max}}{\omega_{max}} = \frac{96}{114} = 0.84 Nm \tag{A.6}$$

Once the brake model was selected, springs of a suitable strength could be specified for the torque balance. The length and strength of the spring was such that the expected range of displacements would be within the Hookes Law region of the spring this would make for ease of measurement, giving a linear relationship between applied torque and the measured displacement of the torque arm. A calibration test was carried out to determine this relationship so that the applied torque could be known to a determined degree of accuracy.

## A.2.2   Balance Calibration

The balance was calibrated by loading the arm of the spring balance with a series of masses. The torque arm rotated in a horizontal plane, a string suspended over a pulley was used to apply a horizontal load using the vertically suspended masses. The friction of the pulley was a possible source of error; an alternative method would have been to turn the measurement box on its side, so that the spring balance rotated in a vertical plane and a load could be applied directly to the torque arm. However, the change in bearing loads when turning the box on its side was judged to be a far more significant source of error than the pulley friction. An attempt was made to quantify the pulley friction by suspending a two different masses across it. However, it soon became clear the required mass difference was very small relative to the size of mass being applied for the spring balance calibration and so it was decided that the pulley friction was insignificant and could be neglected.

For the test, mass was incrementally added to load the balance and the corresponding displacement sensor voltage was noted for each case. The measurements were then repeated as the load was removed in the same increments, this gave an indication of an hysteresis present in the system. At each loading case, the brake shaft was spun so that static bearing friction was overcome, as the shaft would always be rotating when the system was being used. The loading and unloading test was repeated four times, results are shown in Figure A.1. It can be seen that the relationship between applied torque and displacement sensor voltage is linear, as expected, and a line of best fit is added and used as the calibration relationship. The maximum error in applied torque measurement was determined to be ±0.01 $Nm$.
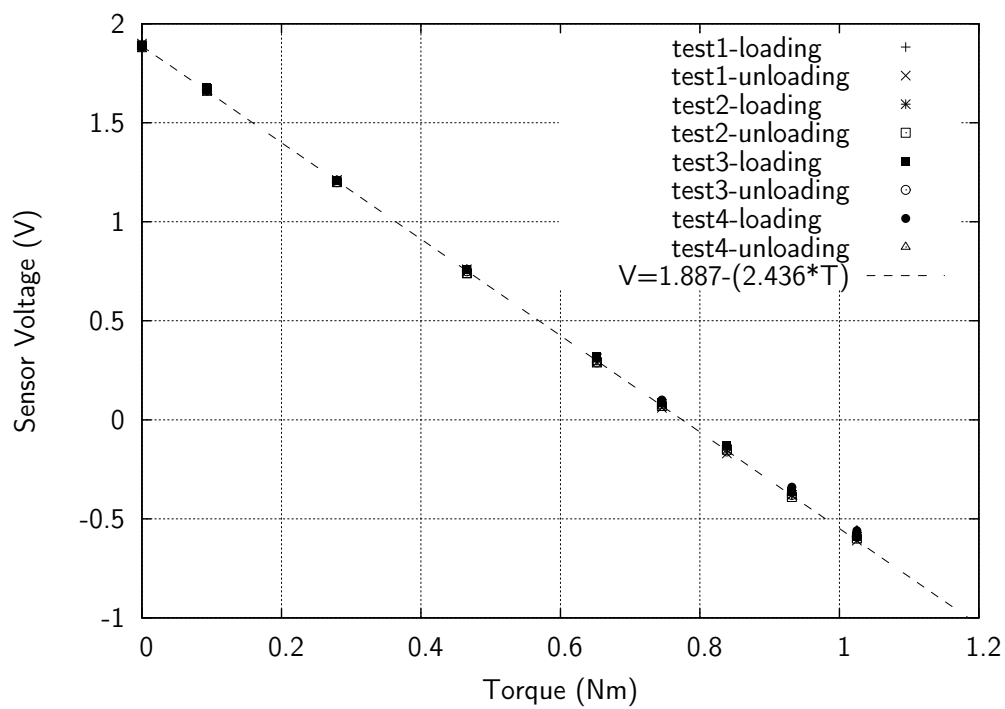
Figure A.1: Measurements of applied torque versus displacement sensor voltage for the spring balance, showing line of best fit used for calibration.

# References

[1] Department of Energy Change and Climate. Renewable energy in 2010, 27/11/2011 June 2010.

[2] Department of Energy Change and Climate. Uk small-scale wind survey, aea/ed02438/issue 1, May 2009.

[3] Cleveland Abbe. The aims and methods of meteorological work, 1899.

[4] Sandia National Laboratories. The history of the doe program, 1990.

[5] Akiyoshi Iida, Akisato Mizuno, and Keiko Fukudome. Numerical simulation of aerodynamic noise radiated from vertical axis wind turbines. In *16th Australasian Fluid Mechanics Conference*.

[6] S Mertens. The energy yield of roof mounted wind turbines. *Wind Engineering*, Issue 2003-27-6, 2003.

[7] C J Simao Ferreira, Gijs van Kuik, Gerand J W Van Brussel, and Fulvio Scarano. Visualization by piv of dynamic stall on a vertical axis wind turbine, 26/11/08 2008.

[8] S Eriksson, H Bernhoff, and M Leijon. Evaluation of different turbine concepts for wind power. *Renewable and Sustainable Energy Reviews*, 12:1419–1434, 2008.

[9] R J Templin. Aerodynamic performance theory for the nrc vertical-axis wind turbine. Technical report, 1974.

[10] H Glauert. *The Elements of Aerofoil and Airscrew Theory, 2nd ed.* Cambridge Universtiy Press., 1948.

[11] James H Strickland. The darrieus turbine: A performance prediction model using multiple streamtubes. Technical report, Sandia National Laboratories, 1975.

[12] R E Wilson and PBS Lissaman. Applied aerodynamics of wind power machines. Technical report, 1974.

[13] Ion Paraschivoiu. Double-multiple streamtube model for darrieus wind turbines, February 1981 1981.

[14] MH Worstell. Measured aerodynamics and system performance of the 17-m research machine. In *Vertical-Axis Wind Turbine (VAWT) Design Technology Seminar for Industry*.

[15] Ion Paraschivoiu. Predicted and experimental aerodynamic forces on the darrieus rotor. *Journal of Energy*, 7(6):610–615, 1983.

[16] S C McIntosh and H Babinsky. Aerodynamic modeling of swept bladed vertical axis wind turbines, 5 - 8th January 2009 2009.

[17] H C Larsen. Summary of a vortex theory for the cyclogiro, 1979 1975.

[18] R. E. Walters, J. B. Fanucci, J. L. Loth, P. G. Migliore, N. Ness, G. M. Palmer, W. Squire, and S. Yusuff. Innovative wind machines. executive summary and final report. Technical report, West Virginia Univ., Morgantown. Dept. of Aerospace Engineering., 1976. Export Date: 12 May 2011 Source: Scopus.

[19] R E Wilson. Wind-turbine aerodynamics. *Journal of Industrial Aerodynamics*, 5:357–372, 1980.

[20] Mazharul Islam, David S K Ting, and Amir Fartaj. Aerodynamic models for darrieus-type straight-bladed vertical axis wind turbines. *Renewable and Sustainable Energy Reviews*, 12:1087–1109, 2008.

[21] J H Strickland, B T Webster, and T Ngyuyen. A vortex model of the darrieus turbine: An analytical and experimental study. *Journal of Fluids Engineering*, 101:500–505, 1979.

[22] F B Blackwell. Wind tunnel performance data for the darrieus wind turbine with naca0012 blades. Technical report, 1976.

[23] R. E. Wilson and S. N. Walker. Fixed wake theory for vertical axis wind turbines. *Journal of Fluids Engineering, Transactions of the ASME*, 105(4):389–393, 1983. Cited By (since 1996): 5 Export Date: 12 May 2011 Source: Scopus.

[24] B. Basuno, F. N. Coton, and R. A. Galbraith. Prescribed wake aerodynamic model for vertical axis wind turbines. *Proceedings of the Institution of Mechanical Engineers, Part A: Journal of Power and Energy*, 206(3):159–166, 1992. Cited By (since 1996): 1 Export Date: 12 May 2011 Source: Scopus.

[25] Paul C Klimas. Effects of blade preset pitch/offset on curved-blade darrieus vertical axis wind turbine performance. Technical report, 1981.

[26] F N Coton, R A Mc D Galbriath, and D Jiang. The influence of detailed blade design on the aerodynamic peformance of straight-bladed vertical axis wind turbines. *Proceedings of the Institution of Mechanical Engineers, Part A: Journal of Power and Energy*, 210(1):65–74, 1996.

[27] Robert E Sheldahl, P C Klimas, and Louis V Feltz. Aerodynamic performance of a 5m diameter darrieus turbine with extruded aluminium naca0015 blades. Technical report, 1980.

[28] C A Consul, R H J Willden, E Ferrer, and M D McCulloch. Influence of solidity on the performance of a cross-flow turbine, 2009.

[29] MH Worstell. Aerodynamic performance of the 17-m-diameter darrieus wind turbine in the three-bladed configuration: An addendum. Technical report, 1982.

[30] John C Vassberg, Arathi K Gopinath, and Antony Jameson. Revisiting the vertical-axis wind-turbine design using advanced computational fluid dynamics, 10-13th January 2005 2005.

[31] Brian Kinloch Kirke. *Evaluation of Self-Starting Vertical Axis Wind Turbines for Stand-Alone Applications*. Phd, 1998.

[32] S C McIntosh. *Wind Energy for the Built Environment*. PhD thesis, 2009.

[33] FloWind Corporation. Final project report: High-energy rotor development test and evaluation. Technical report, 1996.

[34] PG Migliore, WP Wolfe, and JB Fanucci. Flow curvature effects on darrieus turbine blade aerodynamics. *Journal of Energy*, 4(2):49–55, 1980.

[35] D E Berg, P C Klimas, W A Stevenson, and Sandia National Laboratories. Aerodynamic design and initial performance measurements for the sandia 34m diameter vertical axis wind turbine. In *The Ninth ASME Wind Energy Symposium*, volume 9.

[36] Paul C Klimas. Tailored airfoils for vertical axis wind turbine. Technical Report SAND84-1062 UC60, Sandia National Laboratories, 1992.

[37] Christian Masson, Christophe Leclerc, and Ion Paraschivoiu. Appropriate dynamic-stall models for performance predictions of vawts with nlf blades. *International Journal of Rotating Machinery*, 4(2):129–139, 1998.

[38] J R Baker. Features to aid or enable self starting of fixed pitch low solidity vertical axis wind turbines. *Journal of Wind Engineering and Industrial Aerodynamics*, 15:369–380, 1983.

[39] J V Healy. The influence of blade camber on the output of vertical-axis wind turbines. *Wind Engineering*, 2(3):146–155, 1978.

[40] Mazharul Islam, David S K Ting, and Amir Fartaj. Desirable airfoil features for smaller capacity straight bladed vawt. *Wind Engineering*, 31(3):165–196, 2007.

[41] Mark Drela. Xfoil - subsonic airfoil development system, 01/07/2011.

[42] Mazharul Islam, Ruhul M Amin, Rupp Carriveau, and Amir Fartaj. Investigation on low reynolds number airfoils for fixed-pitch straight-bladed vawt, 5 - 8th January 2009 2009.

[43] M Islam, A Fartaj, and R Carriveau. Design analysis of a smaller-capacity straight-bladed vawt with an asymmetric airfoil. *International Journal of Sustainable Energy*, 30(3):179–192, 2011.

[44] J V Healy. The influence of blade thickness on the output of vertical axis wind turbines. *Wind Engineering*, 2(1):1–9, 1978.

[45] S J Miley. A catalog of low reynolds number airfoil data for wind turbine applications. Technical report, Department of Aerospace Engineering, Texas A and M University., 1982.

[46] N. V. C. Swamy, P. A. Aswatha Narayana, and K. Chandrasekhar. Parametric studies of parabolic vertical axis wind rotors. *Renewable Energy*, 3(8):947–949, 1993.

[47] MS Selig and BD McGranahan. Wind tunnel aerodynamic tests of six airfoils for use on small wind turbines. *Journal of Solar Energy Engineering*, 126:986–1001, 2004.

[48] N Cao, S-K Ting, and R Carriveau. The performance of a high-lift airfoil in turbulent wind. *Wind Engineering*, 35(2):179–196, 2011.

[49] T D Ashwill. Measured data for the sandia 34m vertical axis wind turbine. Technical report, 1992 1992.

[50] H H Dodd, T D Ashwill, D E Berg, Mark E Ralph, W A Stevenson, P S Veers, and Sandia National Laboratories. Test results and status of the doe/sandia 34m test bed. In *The Canadian Wind Energy Association Conference*.

[51] Robert Howell, Ning Qin, Jonathan Edwards, and Naveed Durrani. Wind tunnel and numerical study of a small vertical axis wind turbine. *Renewable Energy*, 35(2):412–422, 2010.

[52] D E Berg. An improved double-multiple streamtube model for the darrieus-type vertical axis wind turbine., 1983.

[53] I. Paraschivoiu and A Allet. Aerodynamic analysis of the darrieus wind turbines including dynamic-stall effects. *Journal of Propulsion*, 4(5):472–477, September 1988.

[54] A Allet and I Paraschivoiu. Viscous flow and dynamic stall effects on vertical-axis wind turbines. *International Journal of Rotating Machinery*, 2(1):1–14, 1995.

[55] W J McCroskey, L W Carr, and K W McAlister. Dynamic stall experiments on oscillating airfoils. *AIAA Journal*, 14(1):57–63, 1976.

[56] R B Noll and N D Ham. Effects of dynamic stall on swecs. *Journal of Solar Energy Engineering, Transactions of the ASME*, 104(2):96–101, May 1982.

[57] J G Leishman. Dynamic stall experiments on the naca23012 aerofoil. *Experiments in Fluids*, 9(1-2):49–58, January 1990.

[58] T Lee and P Gerontakos. Investigation of flow over an oscillating airfoil. *Journal of Fluid Mechanics*, 512:313–341, August 2004.

[59] W J McCroskey. The phenomenon of dynamic-stall. Technical report, 1981.

[60] C J Simao Ferreira, G van Kuik, and G J W van Brussel. Wind tunnel hotwire measurements, flow visualisation and thrust measurements of a vawt in skew, 9-12th January 2006 2006.

[61] Nobuyuki Fujisawa and Satoshi Shibuya. Observations of dynamic stall on darrieus wind turbine blades. *Journal of Wind Engineering and Industrial Aerodynamics*, 89(2001):201–214, 2000.

[62] Kristian Dixon, C J Simao Ferreira, Claudia Hofemann, G J W van Brussel, and G van Kuik. A 3d unsteady panel method for vertical axis wind turbines. In *European Wind Energy Conference and Exhibition (EWEC) 2008*, pages 1–10.

[63] Claudia Hofemann, C J Simao Ferreira, Kristian Dixon, G J W van Brussel, G van Kuik, and Fulvio Scarano. 3d stereo piv study of tip vortex evolution on a vawt. In *European Wind Energy conference and Exhibition (EWEC)*, pages 1–8.

[64] C J Simao Ferreira, G J W van Brussel, Fulvio Scarano, and G van Kuik. Piv visualization of dynamic stall vawt and blade load determination, 7 - 10 January 2008 2008.

[65] C J Simao Ferreira, H Bijl, G J W Van Brussel, and G van Kuik. Simulating dynamic stall in a 2d vawt: Modeling strategy, verification and validation with particle image velocimetry data, 2007 2007.

[66] K Horiuchi, I Ushiyama, and K Seki. Straight wing vertical axis wind turbines: A flow analysis. *Wind Engineering*, 29(3):243–252, 2005.

[67] C J Simao Ferreira, G J W van Brussel, and G van Kuik. 2d cfd simulation of dynamic stall on a vertical axis wind turbine: Verification and validation with piv measurements. In *45th AIAA Aerospace Sciences Meeting and Exhibit*. AIAA.

[68] VR Klaptocz, GW Rawlings, Y Nabavi, M Alidadi, Y Li, and SM Calisal. Numerical and experimental investigation of a ducted vertical axis tidal current turbine. In *7th European Wave and Tidal Energy Conference*.

[69] S Tullis, A Fiedler, K McLaren, and S Ziada. Medium-solidity vertical axis wind turbines for use in urban environments, 24 - 26 June 2008 2008.

[70] H Beri and Y Yao. Effect of camber airfoil on self starting of vertical axis wind turbine. *Journal of Environmental Science and Technology*, 4(3):302–312, 2011.

[71] M Raciti Castelli, A Englaro, and E Benini. The darrieus wind turbine: Proposal for a new performance prediction model based on cfd. *Energy*, 36(8):4919–4934, August 2011.

[72] P Vittecoq and A Laneville. The aerodynamic forces for a darrieus rotor with straight blades: Wind tunnel measurements. *Journal of Wind Engineering and Industrial Aerodynamics*, 15:381–388, 1983.

[73] A Laneville and P Vittecoq. Dynamic stall: The case of the vertical axis wind turbine. *Journal of Solar Energy Engineering*, 108(2):140–145, 1986.

[74] G J W van Brussel, H Polinder, H F A Sidler, and TU Delft. The development of turby, a small vawt for the built environment, 2004.

[75] Tamas Bertinyi and Paul Penna. Full-scale wind tunnel testing of the qr5 vertical axis wind turbine, 7th-10th January 2008.

[76] G J W Van Brussel, H Polinder, and H F A Sidler. Turby: Concept and realisation of a small vawt for the built environment, 19-21 April 2004 2004.

[77] Robert E Sheldahl. Comparison of field and wind tunnel darrieus wind turbine data. Technical report, 1981.

[78] S Armstrong and S Tullis. Power performance of canted blades for a vertical axis wind turbine. *Journal of Renewable and Sustainable Energy*, 3(1), 2011.

[79] A Fielder and S Tullis. Blade offset and pitch effects on a high solidity vertical axis wind turbine. *Wind Engineering*, 33(3):237–246, 2009.

[80] J Kjellin, F Bulow, F Eriksson, P Deglaire, M Leijon, and H Bernhoff. Power coefficient measurement on a 12 kw straight bladed vertical axis wind turbine. *Renewable Energy*, 36(11):3050–3053, 2011.

[81] J O Dabiri. Potential order-of-magnitude enhancement of wind farm power density via counter-rotating vertical-axis wind turbine arrays. *Journal of Renewable and Sustainable Energy*, 3(4), 2011.

[82] S C McIntosh, H Babinsky, and T Bertinyi. Optimizing the energy output of vertical axis wind turbines for fluctuating wind conditions, 2007 2007.

[83] T C Smith. *Aerodynamic Design of Wind Turbine Blades for Maximum Wind Power Extraction.* Masters, 2006.

[84] Kenichi Hamada. *Aerodynamic Design of Vertical Axis Wind Turbine Blade for Urban Rooftop Applications.* PhD thesis, 2007.

[85] L A Danao. Personal communication, 2011.

[86] Alan Pope and John J Harper. *Low-Speed Wind Tunnel Testing.* John Wiley and Sons, 1966.

[87] M Raffel, C Willert, S Wereley, and J Kompenhams. *Particle Image Velocimetry: A Practical Guide.* Springer, second edition edition, 2007.

[88] A P Broeren and M B Bragg. Spanwise variation in the unsteady stalling flowfields of two-dimensional airfoil models, 2001.

[89] W G Bastedo and T J Mueller. Spanwise variation of laminar separation bubbles on wings at low reynolds numbers. *Journal of Aircraft*, 23(9):687–694, September 1986.

[90] J M Edwards, L A Danao, and R J Howell. Novel experimental power curve determination and computational methods for the performance analysis of vertical axis wind turbines. *Journal of Solar Energy Engineering*, page accepted for publication 05/12/11, 2012.

[91] ANSYS Inc. Fluent 12.1 user guide and manual. released 01/10/2009.

[92] Kenichi Hamada, Tomos C Smith, Naveed Durrani, Ning Qin, and Rob Howell. Unsteady flow simulation and dynamic stall around vertical axis wind turbine blades. In *46th AIAA Aerospaces Sciences Meeting and Exhibit*. AIAA.

[93] W Z Shen, J H Zhang, and J N Sorenson. The actuator surface model: A new navier-stokes based model for rotor computations. *Journal of Solar Energy Engineering*, 131(1):0110021–011002, February 2009.

[94] F Scheurich, T M Fletcher, and R E Brown. Simulating the aerodynamic performance and wake dynamics of a vertical-axis wind turbine. *Wind Engineering*, 14(2):159–177, March 2011.

[95] BH Carmichael. Low reynolds number airfoil survey. Technical Report HC AO6/MF A01, Low Energy Transportation Systems, 7th January 1981.

[96] PBS Lissaman. Low-reynolds-number airfoils. *Annual Review of Fluid Mechanics*, 15:223–239, 1983.

[97] R E Shedahl and P C Klimas. Aerodynamic characteristics of seven symmetrical airfoil sections through 180-degree angle of attack for use in aerodynamic analysis of vertical axis wind turbines. Technical report, Sandia National Laboratories, 1981.